Synthesis of Metal, Semiconducting Metal Oxide and Sulfide Nanomaterials for Catalysis and Photocatalysis

THESIS

Submitted in partial fulfillment of the requirements for the degree of

Doctor of Philosophy

by

Pragati Fageria

2012PHXF0017P

Under the Supervision of

Dr. Surojit Pande

BIRLA INSTITUTE OF TECHNOLOGY & SCIENCE

PILANI, PILANI CAMPUS (RAJASTHAN), INDIA

August 2018

Birla Institute of Technology & Science
Pilani – 333 031 (Rajasthan) INDIA

Dr. Surojit Pande
Associate Professor
Department of Chemistry

Phone: +91-1596-515709(O)
+91-9468646542(M)
Fax: +91-1596-244183
Email: surojitpande@gmail.com / spande@pilani.bits-pilani.ac.in

CERTIFICATE

This is to certify that the thesis entitled **"Synthesis of Metal, Semiconducting Metal Oxide and Sulfide Nanomaterials for Catalysis and Photocatalysis"** submitted by **Pragati Fageria** ID No **2012PHXF0017P** for the award of Ph. D. Degree of the Institute embodies the original work done by her under my supervision.

Name: **Dr. Surojit Pande**

Date: /   / 2018

Designation: Associate Professor

Dedicated

To *Mummy & Papa* who offered

me endless support.

To *Didi & Dinu* who gave me all

the strength.

To those who believe in hard

work and never-give-up on their

DREAMS…

Acknowledgements

anger in a grateful manner. I definitely would not have made it this far without them and I dedicate this milestone to them. Sweet thanks to our beautiful little angels *Dhruv* and *Arihant* for their puerile support. I consider myself lucky for having them in my life. My hearty thanks to didi *Dr. Snehlata* and adorable *Simmu* for their extraordinary care and love. I wish to place on record the encouragment and strong support given by my better half *Mukesh Kumar Mitharwal*, without which I would not have been able to succeed in this endeavor. I would like to state my inexplicable gratitude for all the family members for suspending the family priorities for me to facilitate my research work. It is my journey- rather than the thesis that matters to them and I hope I have not disappointed them.

I was taught that the way of progress is neither swift nor easy; the words of *'Marie Curie'* always inspire me to get crumbled, struggled and move ON. Whenever I failed to do, my belief in the immense hard work provoked me to hustle in silence and try hard. I am thankful for my inner strength that always pushed me to spend nights in the lab, to stick with the chair, to cry alone and to laugh publicly. It was really a memorable saga of a journey and thanks, everyone who has been a part of this. May God shower his choicest blessings and prosperity on all those who assisted me in any way during completion of my Ph.D.

Thanks to All!

Date: /   / 2018

Place: Pilani, India   *Pragati Baldev Fageria*

Table of Contents

Abstract

The thesis entitled "*Synthesis of Metal, Semiconducting Metal Oxide and Sulfide Nanomaterials for Catalysis and Photocatalysis*" deals with the synthesis of semiconductor nanostructures for the rapid developments in science and engineering that are evolving at a very fast pace in the field of nanoscience and nanotechnology. The synthesized nanomaterials were used in different applications such as photocatalysis and electrocatalysis. First chapter of the thesis describes a literature overview about the fundamentals of semiconductors, hybrid nanostructures, metal nanoparticles, properties, and applications of nanomaterials. Additionally, the chapter describes the history of nanoscience and various synthetic method used for the synthesis of nanomaterials. Overall, the background of the present research work has been explained in this chapter. Second chapter of the thesis gives a brief account of the chemicals, methods, and instrumentation techniques are used to furnish the whole thesis work. Chapter three delineates the synthesis of zinc oxide nanoflower in alkaline medium via hydrothermal route using CTAB surfactant. The synthetic strategy also involves the preparation of ZnO/Au and ZnO/Ag by depositing silver and gold nanoparticles on nanoflower using hydrazine hydrate as a reducing agent. The comparative efficiency and reusability of ZnO/Au and ZnO/Ag for the methylene blue and phenol degradation under irradiation of visible and UV light have been presented in the chapter. Chapter four demonstrates the synthesis of cone and dumbbell-shaped ZnO nanoparticles on the surface of graphitic carbon nitride ($g-C_3N_4$) using hexamethylenetetramine and ammonia as hydrolyzing agents. The control experiments were performed to clarify the different morphologies. The visible light activity and recyclability of the as-prepared semiconductor heterostructure have been explored by degradation of phenol and methylene blue pollutants. Chapter five provides insight into the synthesis of both mono- (Au and Pd) and bimetallic (AuPd) nanoparticles using photoexcited electron of carbon nitride quantum dots via the photochemical routes. The synthetic procedure eliminates the necessity of any extra stabilizer or reducing agent. To explore the catalytic activity of mono- and bimetallic nanoparticles, the reduction of 4-nitrophenol with excellent performance has been investigated. Chapter six depicts decoration of porous MoS_2 nanostructures on $g-C_3N_4$ surface, results in the formation of $MoS_2/g-C_3N_4$ heterostructure. The use of $MoS_2/g-C_3N_4$ in electrochemical hydrogen evolution reaction and rhodamine B dye degradation in solar light has been studied in this chapter. The study presents an efficient and cost effective transition metal-based heterostructure for hydrogen evolution reaction. Chapter seven embodied preparation of

semiconductor hybrid hollow nanostructure of ZnO/ZnS and its catalytic application for adsorptive dye removal involving three dye molecules, methylene blue, rhodamine B and malachite green. The synthetic procedure involves 'Kirkendall effect' which has been explained in detail in the chapter. Finally, the last chapter summarizes the main results obtained from the study of different semiconductor metal oxide and sulfide nanomaterials. Future avenues and directions using new semiconductor metal oxide and sulfide nanocomposites are also discussed.

Keywords: Hybrid nanocomposite, heterostructure, photocatalysis, hydrogen evolution, quantum dots, photochemical route, Kirkendall effect.

List of Abbreviations

AU	Arbitrary Unit
BE	Binding Energy
BET	Brunauer-Emmett-Teller
C	Cone
CD	Cyclodextrin
CPS	Cycles per Second
CTAB	Cetyltrimethylammonium Bromide
CTR	Charge transfer resistance
CV	Cyclic voltammetry
D	Dimension
D	Dumbbell
DR	Diffusion Resistance
DRS	Diffuse Reflectance Measurement
DSC	Differential Scanning Calorimetry
DTA	Differential Thermal Analysis
ECSA	Electrochemical Active Surface Area
EDS	Energy Dispersive Spectroscopy
EDX	Energy Dispersive X-ray
EIS	Electrochemical Impedance Spectroscopy
eV	Electron Volt
FTIR	Fourier Transform Infrared Spectroscopy
FESEM	Field Emission Scanning Electron Microscopy
GCE	Glassy Carbon Electrode
H	Hour
HMT	Hexamethylenetetramine
HRTEM	High Resolution Transmission Electron Microscopy
LMB	Leuco Methylene Blue
LSV	Linear Sweep Voltammetry
M	Molar
MA	Milli Ampere
MB	Methylene Blue

MG	Malachite Green
Min	Minute
mL	Milliliter
mM	Millimolar
Mn	million
μM	Micromolar
mW	Milliwatt
NIR	Near-infrared Radiation
nm	Nanometer
NP	Nanoparticle
NF	Nanoflower
NR	Nanorod
PED	Potential Energy Distribution
PXRD	Powder X-ray Diffraction
QSE	Quantum Size Effect
RhB	Rhodamine B
Sec	Second
SAED	Selected Area Electron Diffraction
SDS	Sodium Dodecyl Sulfate
SEM	Scanning Electron Microscopy
SPB	Surface Plasmon Band
SPR	Surface Plasmon Resonance
STEM	Scanning Transmission Electron Microscopy
TEM	Transmission Electron Microscopy
UV	Ultra Violet
XPS	X-ray Photoelectron Spectroscopy

List of Symbols

α   Absorption coefficient

Å   Size

β   Beta

°C   Degree celcious

δ   Delta

ε   Molar extinction coefficient

E_g Band gap

η   Overpotential

γ   Gamma

λ   Wavelength

μ   Mu

ν   Nu

ω   Omega

π   Pi

h   Planck's constant

σ   Sigma

τ   Tau

θ   Diffraction angle

List of Tables

List of Schemes

List of Figures

Chapter 1

Introduction and Future Scope

✿ *This chapter contains the insights of the thesis and summarizes the different aspects of nanomaterials in terms of its properties, applications, and modes of synthesis.*

✿ *The chapter emphasizes the band theory, type of materials, semiconductor nanoparticles and highlights their significance in the field of catalysis.*

✿ *The motivation towards the thesis has been presented in the chapter.*

1.1 Nanoscience and Nanotechnology: The Perspective

Everything, when miniaturized to the sub-100-nanometer scale has new properties in spite of what it is. Based on the lecture of Richard Feynman at an annual meeting of the American Physical Society at Caltech, called as "*There's Plenty of Room at the Bottom*", the concepts and perceptions behind nanoscience and nanotechnology has been started [1-4]. The word "*nano*" originates from the Greek word 'dwarf', which means something *very small*. As a prefix for a unit of time or length, it means one billionth of that unit i.e. a nanometer or 10^{-9} meter. Nature has been executed various assemblies at nanoscale very well in the creation of the complicated molecular machinery that supports the life of human being on earth such as DNA helix (2 nm), water spheres etc. Over more than a decade, Nanoscience and Nanotechnology are being emerged, and scientists have done dynamic research in the area. It has become a buzzword among science and technology circles and comes to a level of maturity where the scientific community has observed an explosion of interest and investment in the field of nanoscience and nanotechnology. There is a fundamental difference between both the terms. Nanoscience is the study of objects at ~ 1-100 nm scale in one of the dimension, whereas, nanotechnology is the technique to devise and organize objects on ~ 1-100 nm scale with the aim of fabricating novel materials with specific chemical and physical properties and, consequently, functions [4-8]. Hence, it is justified that nanoscience is a prerequisite to nanotechnology and should obtain long-term elementary support.

The current nanotechnology research is primarily focused on the benefits and applications of nanotechnology for the human being. However, incessant efforts have been made to fabricate, analyze and explore novel nanomaterials by many researchers all over the world. Nanomaterials now emerged as one of the focal points of modem research because they are probably used in diverse applications depends upon their exceptional optical, electrical, biological, mechanical, magnetic, and catalytic properties [1-6]. The fascinating world of these nanomaterials and their manifold applications becomes part of our life. The issue ultimately is what "nanoscience and nanotechnology" do and what potential does it have to improve our lives? In what follows, these questions will be addressed in an expansive overview of the present state of the field.

1.1.1 The Origin of Nano

The origin of nanotechnology could be argued to have their roots in the fourth century AD in the Lycurgus cup shown in **Figure 1.1.a** which is made from a glass impregnated with nanometre-sized gold (about 40 parts per million) and silver (about 300 parts per million) particles that give rise to its famous dichroic effect. The glass contains 70 nm particles as seen in the transmission electron micrograph. Later, nanotechnology was used extensively by the medieval craftsmen who produced the stained glass by mixing gold chloride into the molten glass which embellished many of Europe's cathedrals. The diameter of tiny, uniformly sized gold spheres was found 50 nm which impart the deep ruby-red color [1-3]. "Damascus Sword' containing the nanoscale carbon particles is also a paradigm of the use of nanoparticles in ancient time (**Figure 1.1.b**) [4]. In 1857, Faraday demonstrated the synthesis of colloidal gold and called it "divided state of gold", the solutions are preserved in Royal Institution (**Figure 1.1.c**) [1-2].

Figure 1.1 Uses of the nanomaterials in prehistoric times a. The Lycurgus Cup, b. Damascus Sword and c. Michael Faraday's gold colloid preserved in Royal Institution (http://www.thebritishmuseum.ac.uk)

The anticipation of many of the potential benefits of nanotechnology was highlighted in the Feynman's lecture [5-8]. The formal term 'nanotechnology' was defined in the mid-1970s by Norio Taniguchi as 'it is the processing by which materials are separated, consolidated, and deformed by one atom or one molecule' [9-11]. Subsequently, this basic definition was explored in greater depth by Eric Drexler, who vigorously endorsed the technological significance of nanoscale phenomena and devices [2,3].

1.1.2 Nanomaterials: Different from Bulk Materials

The physical properties exhibited by materials in micrometer scale are generally analogous to that of the bulk form; yet, materials in the nanometer scale display distinctively different properties from their bulk counterpart. The origin of special behavior of nanomaterials from their bulk counterpart can be attributed with two important factors, first, surface to volume ratio and second, quantum size effect [7-12]. The changes in the surface to volume ratio at nanoscale lead to the change in the properties of nanomaterials. The electronic configurations of nanoscale materials are also different from bulk and show different optical and electrical properties. The tailoring in the dimension of the nanomaterials results in the formation of discrete energy levels unlike to the continuous energy bands in bulk materials, called as *quantum size effect* shown in **Figure 1.2** [12]. The Figure shows that due to the decrease in confining dimension of the particle, discretization of energy levels found and this widens up the band gap and consequently increases the band gap energy. The energy shift can be derived by $E = n^2h^2/8ma^2$, where, n = principle quantum no., h = Plank's constant, m = effective mass and a = length, which clearly shows that energy is reciprocal with a dimension of the particle. This causes a spectacular alteration in size and shapes dependent properties such as electrical, thermal, mechanical, magnetic, and optical properties [5-9].
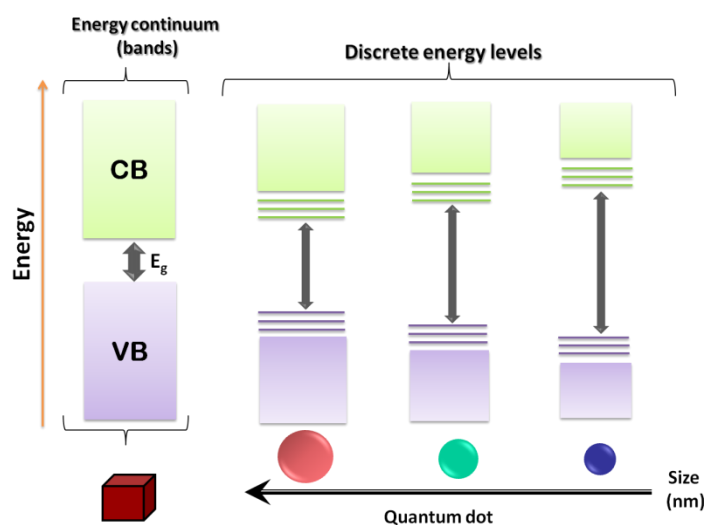
Figure 1.2 Discretization of electronic energy levels (quantum size effect) with the variation in size

1.2 Synthetic Methods

Nanomaterials are synthesized using two different routes: top-down or physical and bottom-up or chemical [14-25].
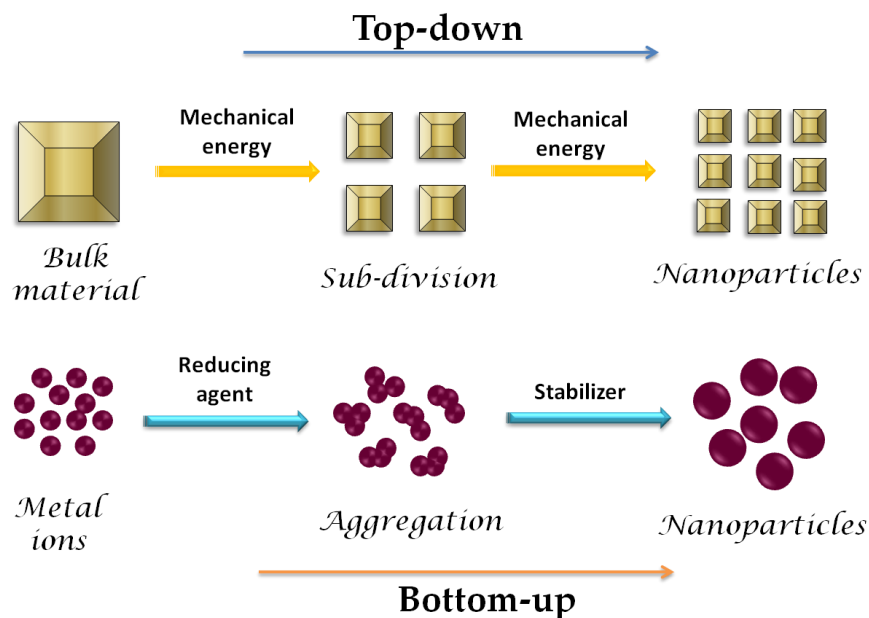
Figure 1.3 Top-down (or physical) and bottom-up (chemical) approaches for the synthesis of nanomaterials

1. *Top-down approach*: This is a physical approach, where the bulk material or constituent material is taken from which nanomaterials are synthesized. The "top-down" approach is a traditional method for the fabrication of nanoscale materials, suggested by Feynman in his lecture in 1959 [1-3]. It begins with the bulk piece of material (macroscopic), which gradually or step-by-step reduced to form objects in the nanometer-size regime ($\sim 10^{-9}$ m) shown in **Figure 1.3**. These methods are very effective for the production of large quantities of materials. However, the principal problem with this process is the large particle size variation. Various top-down approaches are used for the synthesis of nanomaterials, such as lithography, anodization, high-energy ball milling, inert gas condensation, arc discharge, wire explosion, ion sputtering and ion- and plasma etching (PE) etc. [7-12].

2. *Bottom-up approach*: This is a chemical approach of synthesis that initiates with metal ions, leading to the formation of nanostructures shown in **Figure 1.3**. The method comprises of miniaturization of the materials up to atomic level. Atoms are formed from ions, generally in solutions, and they are assembled to large nanostructures. Michael Faraday was the first used *bottom-up technique* to study the formation of gold sols using red phosphorus as a reducing agent to reduce the $[AuCl_4]^-$ ions. Some examples are commonly encountered such as chemical reduction, hydrothermal synthesis, solvothermal synthesis, photochemical synthesis, electrochemical synthesis, thermolysis, sonochemical routes, micelles and microemulsions, interfacial synthesis, biological methods, hybrid methods, solvated metal atom dispersion, and arrested precipitation [7-9]. In recent times, significant effort has been made for the synthesis of surface modified nanoparticles of several metal oxides. Many synthetic approaches are available for the synthesis of metal oxides, such as microwave refluxing [13], sol-gel [14], hydrothermal [15], wet-chemical [16-17], co-precipitation [18], and spray pyrolysis [19-20] etc.

Our research work mainly focuses on the wet chemical synthesis of metal, metal oxide and sulfide nanoparticles which includes hydrothermal, solvothermal, and co-precipitation methods.

1.2.1 Hydrothermal Synthesis

The synthesis takes place in an autoclave which is a pressurized vessel where the temperature can be increased above the boiling point of water, and the pressure up to the vapor pressure. Hydrothermal synthesis is extensively utilized to synthesize various metal oxide and sulfide nanoparticles. In this method, hydrothermal treatment of metal precursor in aqueous medium takes place [14-18]. This synthetic approach is helpful to control the size, morphology, crystalline phase and surface chemistry of the particle via regulating the solution composition, temperature and pressure of reaction, solvent properties, additives and aging time [15-17].

1.2.2 Low-temperature Wet-chemical Synthesis or Precipitation Method

Another conventional technique to prepare metal oxide and sulfide nanoparticles is the precipitation method. In this process metal salts such as $ZnCl_2$, $ZnSO_4$, and $Zn(NO_3)_2$ can be used to synthesize ZnO [15-16]. The metal salt is dissolved in a solvent and the corresponding

hydroxide precipitated via addition of a base solution such as ammonium hydroxide, hexamethylenetetramine (HMT), or sodium hydroxide. To achieve metal oxide, the chloride salts, i.e. NaCl or NH_4Cl, are washed carefully and the remaining hydroxides are calcined [14-18]. In the same solution, different metal oxide composites also can be synthesized via co-precipitation of the different metal hydroxides. Using this synthetic procedure it is very hard to control the particle size in a desirable dimension [20-23].

1.2.3 Solvothermal Method

The solvothermal method is similar to the hydrothermal technique excluding the use of water as solvents. Various nanoparticles with narrow dimensions have been synthesized using this approach in organic solvents with high boiling points. The method is used to control dimensions, shape, crystallinity, and to synthesize metal oxide and sulfide nanoparticles with or without the accumulation of surfactant additives [19-23].

1.3 Stabilization of Nanoparticles

Stability is one of the important factors that determines the potential application of the nanoparticles. Stability of nanoparticles especially as dispersion can be achieved by two methods
(I) Electrostatic stabilization
(II) Steric stabilization (using ligand/surfactants)

One of the significant characteristics of nanoparticles is their small size. Synthesis of smaller size metallic nanoparticles without the addition of a stabilizer is unstable and aggregated towards bigger particle as shown in **Figure 1.4**. The figure shows that the presence of stabilizer confines the particle in the nanometer scale and after complete growth stabilizer restricts the nanoparticles to get agglomerate. If the stabilizer is not added in the reaction it leads to the formation of bigger particles and due to this agglomeration the properties of nanoparticles linked with the colloidal state of these small-size metallic particles will lose.

Numerous reports already exist on the stability of colloids and nanoclusters [23-30]. The van der Waals forces of attraction exist between two metallic nanoparticles due to a shorter distance. The presence of a repulsive force is required to oppose the attraction force and to restrict the aggregation of colloidal particles. The repulsive force can be induced by the addition

of stabilizer which is essential to synthesize small-size nanoparticles. The stabilization strategies of colloidal materials have been illustrated in Derjaguin-Landau-Verwey-Overbeek theory [27-28]. The stabilization of Nanoclusters is frequently discussed in terms of (i) charge stabilization (ii) steric stabilization (iii) the combination of steric and charge stabilization with the electrostatic stabilization such as surfactants, and (iv) the stabilization using ligand [26-31].
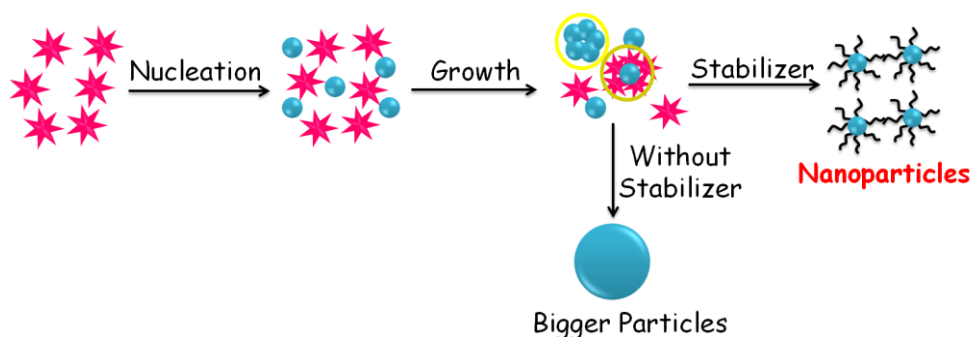
Figure 1.4 The role of a stabilizer to stabilize the nanoparticles, stabilizer restricts particle size in nanometer length scale

1.3.1 Electrostatic Stabilization

The aqueous solution of ionic compounds like halides, carboxylates, or polyoxoanions can generate the electrostatic stabilization. When more than one molecule or ion comes closer to the nanoparticles, the system becomes more complex. For example, if two adsorbates having similar charge approached nanoparticles from opposite sides, according to basic algebra the overall dipole moment decreases to zero and it increases if adsorbates have the opposite charge. When ions having positive and negative charge approach the metal particles, it induces δ+ and δ-image charge on the surface shown in **Figure 1.5** and due to these charges the particle acquire multiple moments [32-33]. The cations and anions are of different chemical nature and thus have distinct interactions with the metal sphere. Generally, the surface of metal is surrounded by one kind of ions and counterpart is present as a shell. Therefore, as long as the number of ions surrounding the nanoparticles is lesser, a single ion strongly interacts with the neutral metal particles. The metal nanoparticle interaction with cation and anion is different and this results in the formation of a double layer with oppositely charged ion's. This double layer creates the repulsive forces between two vicinal nanoparticles [27,31-32]. It is noteworthy that the change in

the magnitude of the dipole moments can be employed to control the agglomeration and re-dispersion of the corresponding nanoparticles [32-35].
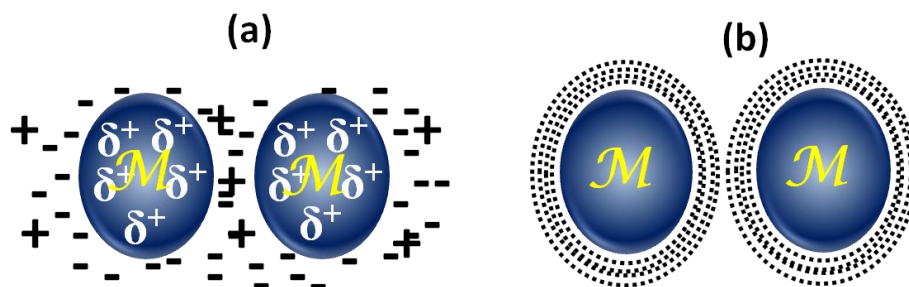
Figure 1.5 Schematic representation of (a) Coulomb repulsion between partially charged metal particles and generation of electrostatic stabilization and (b) dipole-dipole interaction between neutral metal spheres

1.3.2 Steric Stabilization

The aggregation of metal colloids can also be prohibited using macromolecule stabilizers such as polymer or oligomer [35-36]. These molecules get adsorbed on the particle surface and create a protective layer around the particle as shown in **Figure 1.6**. However, the width of the protective layer can be affected by length and nature of macromolecules. By visualizing the interaction of two metallic colloids the stabilization strategy in presence of large adsorbed molecules can be elucidated. The movement of adsorbed molecules will be hindered in interparticle space and the entropy will reduce and free energy will increase. The steric stabilization is mainly used in organic or aqueous phase [35-38].
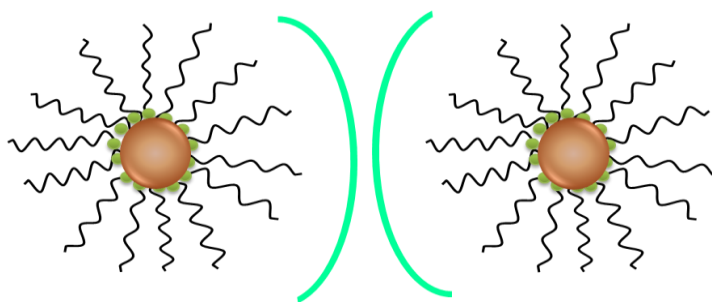
Figure 1.6 Steric stabilization: elongated molecules adsorbed via anchoring centers hinder nanoparticles from close contact

1.3.3 Electrosteric Stabilization

The materials, which are ionic, strongly adsorbed on the surface of metal particle and assemble the concept of steric and electrostatic stabilization simultaneously, used to sustain the stability of metallic nanoparticles in the solution [7,12]. Generally, ionic surfactants bearing polar head group and lipophilic side chain provide this type of stabilization. The polar head group produces electrical double layer and a non-polar side chain offers steric repulsion. Polyoxoanions such as the couple ammonium (Bu_4N^+)/polyoxoanion $(P_2W_{15}Nb_3O_{62}^{9-})$ also provides the electrosteric stabilization and prevent the agglomeration of the nanoparticles in the solution [39].

1.3.4 Stabilization by Ligand or Solvent

When the traditional ligands are used to stabilize the transition metal colloids, it is termed as ligand stabilization. The ligands like phosphene $(-PH_2)$, thiols $(-SH)$, amine $(-NH_2)$, carbonyl $(=CO)$ etc. coordinate with the transition metal nanoparticles and stabilize it [40-44]. Amiens and co-workers reported the selective synthesis of Pt and Pd particles using carbonyl and phosphines ligands as a stabilizer [40]. Vidoni *et al.* reported the synthesis of Ru nanoparticles using organic solvents without adding any additional steric or electrostatic stabilizers [41].

1.3.4.1 Ligand as a Shape and Size Directing Agent for Nanoparticles

Ligands are also known to direct the shape of nanoparticles leading to the formation of anisotropic nanoparticles. Murphy and co-workers have extensively synthesized gold nanorods of different aspect ratio using a method called 'seed-mediated method'. The same group also concluded that CTAB (Cetyltrimethylammonium bromide) is the most suitable surfactant for the formation of gold nanorods and nanowires [42-44]. Detail study on the role of CTAB in nanorods and wires synthesis can be shown in **Figure 1.7**. CTAB has CTA^+ head group and a non-polar tail. The head group CTA^+ binds to the surface of nanorods preferentially and this binding is based on the steric stabilization. In the nanorod of Au atom, the side face {100} spacing is more equivalent to the CTA^+ head group in contrast to the spacing of close-packed {111} face of gold, at the end. Hence, this binding preferentially stabilizes the side faces. This

face has comparatively large surface energy and stress than other faces [43-47].
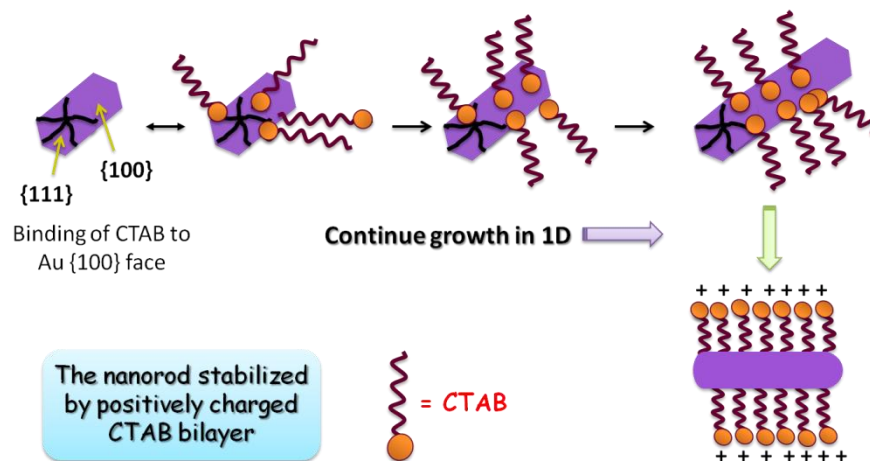
Figure 1.7 Preferential binding of CTAB on (100) and (111) surface of gold nanoparticles

Detailed investigation of the formation of different shapes on nanoparticles has been carried out by Sau and co-workers [45-46]. Methods like preformed-seed-mediated growth, high-temperature reduction, spatially confined medium/template approach; electrochemical synthesis, photochemical and biosynthesis which result in different anisotropic nanoparticles in presence of various ligands have been demonstrated [45-51]. They have concluded that surfactants and ligands play a major role to govern the shape of nanoparticles [52-54].

1.3.4.2 Surface Plasmon Resonance

In nanomaterials the absorption band results when the incident photon frequency is resonant with the collective oscillation of the conduction electrons and is known as the localized surface plasmon resonance (LSPR). The resonance frequency of the LSPR is highly dependent upon the size, shape, dielectric properties, and local environment of the nanoparticles [56]. The creation of a surface plasmon oscillation is shown. The electric field of an incoming light wave induces a polarization of the (free) conduction electrons with respect to the much heavier ionic core of a spherical nanoparticle. The positive charges in the particle are assumed to be immobile and the negative charges, that is, the conduction electrons, move under the influence of external

fields. Therefore, a displacement of the negative charges from the positive ones occurs when the metallic nanoparticle is placed in an electric field, that is, there results in a net charge difference at the nanoparticle boundaries. This, in turn, gives rise to a linear restoring force to the system. As a consequence, a dipolar oscillation of the electrons is created (within a particular time period), and this is known as the surface plasmon oscillation. The metallic nanoparticles show this SPR phenomenon when interacted with the electric field of incoming light.

1.3.5 Applications of Nanomaterials

The fields where nanoparticles are used to have a wide spectrum. Nanoparticles are extensively used in advanced materials, pharmaceuticals, environmental detection, and drug sciences [7-9]. Nanoparticles are being used in catalysis, sensors, electronic devices, photocatalysis, optics, data storage, surface enhanced Raman spectroscopy substrate etc. Nanoparticles also applied in surface coating, construction of scratch-proof eyeglasses, crack-resistant paints, anti-graffiti wall coatings, visible sunscreens, stain-repellent fabrics, and ceramic coatings in solar cells. Nanoparticles are also used in ultra-fine wiring, efficient solar cell, doping for metal, ceramic, epoxy-material, fiber, semiconductor etc. and coating for surfaces of glass, lance, film, electrode etc. purposes [55-60].

1.4 Classification of Materials

On the technical ground, materials can be classified as metals, semiconductors, insulators, ceramics, glasses, composites, biomaterials, polymers, etc. On the basis of the capacity to conduct current, the materials are categorized as conductors, insulators and the semiconductors, shown in **Figure 1.8**. The conduction of current depends upon the forbidden gap present between valence and conduction band. The details about conduction band, valence band, and forbidden gap have been elucidated in the band theory section.

1. Conductors: In conductors, conduction and valence bands overlap with no forbidden gap or energy gap. Thus a large number of free electrons are available to conduct the electrical current at room temperature. Examples are metallic copper, aluminum, gold, silver etc.

2. Insulators: A large energy gap (> 9 eV) is found between the conduction band and valence

band. Practically, it is not feasible for an electron to move from the valence to conduction band by crossing this large energy gap. Hence, such materials cannot conduct electricity and called insulators. If the high voltage or high-temperature conditions have been applied, the insulator also can conduct electricity. For example diamond, plastics, glass, paper, rubber, wood, mica, etc.
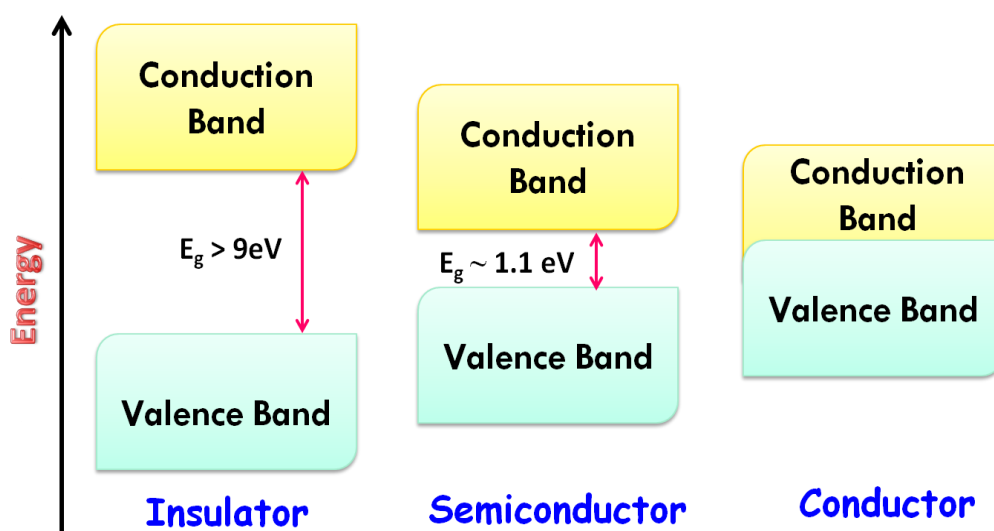
Figure 1.8 Type of materials on the basis of the energy gap between valence and conduction band

3. Semiconductors: The narrow band gap (~1.1 eV) materials as shown in **Figure 1.8**, called semiconductors. The conduction of electricity is possible in such materials after the absorption of energy. The adequate energy is provided to semiconductors at room temperature so that electrons can move from the valence to the conduction band. Example: silicon, germanium etc.

On the basis of the charge carrier semiconductors can be classified into two types: *p and n-type*. The charge carried by p-type is positive, and n-type is negative. The larger hole concentration is found in p-type, while the larger electron concentration is present in n-type.

1.4.1 Band Theory

In molecules there are two types of energy bands are present, fully occupied or bonding orbital (σ-band) and empty or antibonding orbital (σ*-band). The valence band is the result of

bonding orbital, while an anti-bonding orbital form the conduction band of the molecule. The thickness of an individual band is called bandwidth. The valence band (VB) signify the highest occupied molecular orbital (HOMO) and the conduction band (CB) characterize the lowest unoccupied molecular orbital (LUMO) of a molecule [60]. Likewise, the gap between the HOMO and LUMO is called band gap or energy gap or forbidden gap (Eg). This band gap shows the energy which is necessary for the electrons to cross the energy gap. The level of electrons in a material at absolute zero temperature is called the Fermi level, also termed as occupied highest energy state [61]. In a *p-type* semiconductor, there is an increase in the density of empty energy states. Thus, more electrons can be accommodated at lower energy states means Fermi level is lower and close to VB. In an *n-type* semiconductor, the density of filled energy states increased and thus, electrons have to be accommodated at higher energy levels and Fermi level is present closer to CB. According to the atomic and molecular orbital theory, the electronic properties of metals, semiconductors, and insulators can be determined by the energy band gap as shown in **Figure 1.2 and 1.8** [62-63].

Electrons must have a certain energy to occupy a given band and require extra energy to move from the valence band to the conduction band. Furthermore, the bands should be partially filled to conduct electricity, as empty and fully occupied bands cannot conduct the electricity. Due to the presence of partially filled energy bands and a number of free electrons metals are conductors. Owing to the existence of completely filled or empty energy levels material become insulators. However, in the semiconductors, the electricity can be conducted by the absorption of energy which leads to the wide variety of the application of semiconductors.

1.4.2 Semiconductor Nanomaterials

Semiconducting materials have band gap (> 0 eV and < 4 eV) and electrical conductivity (10^2 Scm^{-1} - 10^{-9} Scm^{-1}) at room temperature. Semiconductors occur in many different chemical compositions in a variety of crystal structures. They are classified as elemental semiconductors (Si, Ge, Se) and compound semiconductors (GaAs, ZnO, CdS, ZnS, MoS$_2$) based on their constituent elements [64]. Some manifestations of semiconductor technology can be easily seen in daily life appliances such as radio, television, electronic balance, video games, smartphones, watches, CD player, stereo, computer, digital lights, calculator, diagnostic equipment,

refrigerator, security devices, toys and many more [64-65].

1.4.3 Electronic Structure of Semiconductor

To understand the electronic structure of a semiconductor, it is essential to elucidate some fundamental definitions. There are four quantum numbers, n (principal electron shell), l (s, p, d, and f subshells), m_l (number of orbitals and orientation within each subshell) and m_s (electron spin, +1/2 and −1/2) used to illustrate the movement and trajectories of each electron within an atom. When two isolated atoms get close to each other, their electric fields start to interact and cause a splitting of the energy levels. Each original energy level splits into two, one is higher and other one is lower. Wolfgang Pauli in 1925 stated that no two electrons in an atom, molecule or crystal can have the same values of all four quantum numbers, simultaneously referred as Pauli Exclusion Principle [7-10]. A solid material consists of a large no. 'N' of atoms. When N atoms are brought in close proximity the energy levels that were indistinguishable in isolation, split into N closely spaced but discrete energy levels [64-68].
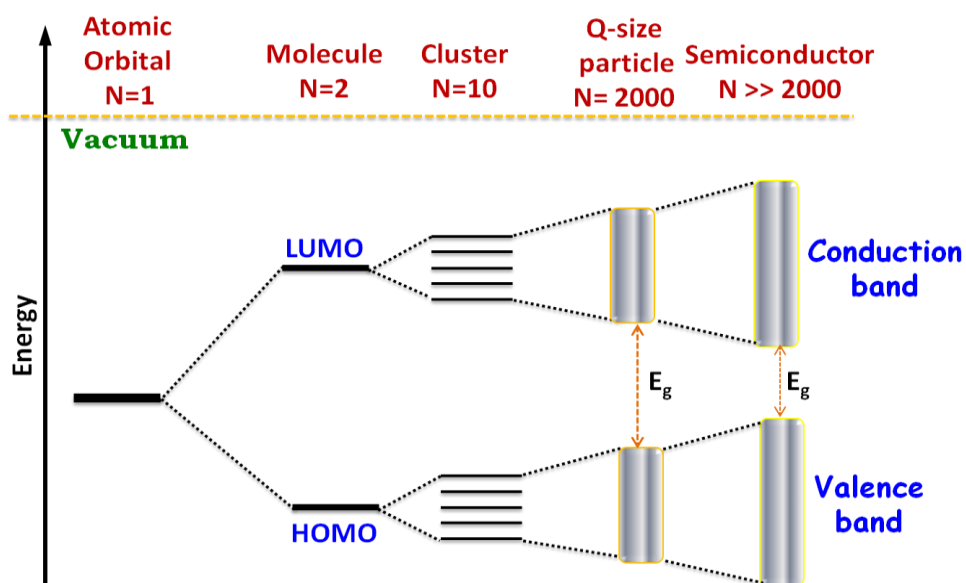
Figure 1.9 Electronic band structures in a semiconductor when the number of N increases from one to more than 2000

Figure 1.9 demonstrates the modification of energy levels in a semiconductor compound

as the number N varies from one to more than 2000 units [67-68]. The large no. of closely spaced energy levels present when N increases and set of that closely spaced energy levels form "electronic energy band". In case of a semiconductor, N becomes much higher (>2000) so a continuum of energy states forms and two types of distinguished energy band found i.e. the conduction band and the valence band. There is a region between both the levels called as "forbidden band" represents that energy states only exist above and below this gap.

With reference to the energy levels of an electron, the higher energy level is identified as conduction band and lower energy level is termed as valence band. The energy difference between both the bands is called "band gap (Eg)". In case of semiconductor materials, the valence band is completely filled with the electrons and conduction band is vacant. Upon excitation with a source of energy the electrons in lower energy valence band move into the conduction band. The absorption of the energy depends upon the band gap of the semiconductor. According to the difference in the band gap of each semiconductor, the energy required for the electron to move from valence to conduction band is also different. The effect of the size of the material on the band gap of a semiconductor can be explained by the *quantum size effect*, which is explained in **Figure 1.2**. This effect is basically due to changes in the atomic structure when the material is of sufficiently small size - usually from 1 to 25 nm for typical semiconductor groups of IV, III-V and II-VI. In which the spatial extent of the electronic wave function is comparable with the dimension of the particle. The phenomenon results from geometrically constraints of electrons and holes into a dimension that is near to Bohr exciton radius which causes unique size depended on properties and increase the band gap [6-9]. Semiconductor nanoparticles demonstrate distinctive size-dependent properties (explained in **Figure 1.2**) that modify its photochemical, photophysical, optical, and electrochemical responses [60-68]. Charge carrier generation, retardation, retention, and transfer between a semiconductor interface are also affected [67-68]. Both the large (e.g., ZnO, ZnS, TiO_2, SnO_2 and WO_3), and lower bandgap semiconductor (e.g., CdSe, CdS, $g-C_3N_4$), display the diverse optical, electrical and physical properties [14-16,64-70].

1.4.4 Semiconductor Heterostructures

Recently, Semiconductor heterostructures have become a cornerstone in applicative and

fundamental researches in the field of catalysis. A structure consists of two or more than two kinds of semiconductors with unique electrical properties and suitable band alignment is called heterostructure. As shown in **Figure 1.10**, depending on the band offsets of the two semiconductors, the heterostructure is of three types, *straddling alignment* (type-I), *staggered alignment* (type-II) and *broken alignment* (type-III) [69-72].
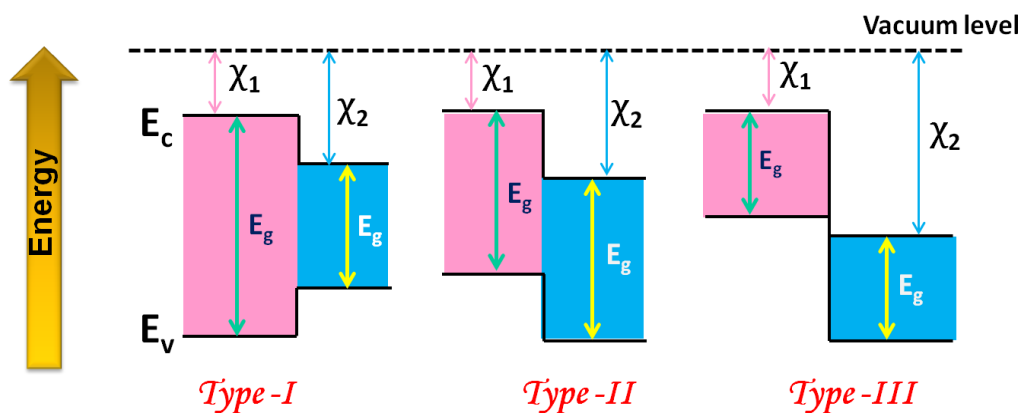
Figure 1.10 Type I, II and III of semiconductor heterostructures according to their band alignment design

Type-I and type-II alignments are useful for photon energy conversion. Three properties which established the heterostructure and movement of charge carrier at a heterojunction are known as band gap, electron affinity, and work function. The band-alignment design of a semiconductor also depends on the difference between the electron affinities (χ_1 and χ_2) of both the semiconductors shown in **Figure 1.10**. The heterostructure is generally adopted for three significant reasons: to promote the dissociation of photogenerated charge carriers (electron and hole), to facilitate the successive collection and to separate the excitons at the interfaces of two semiconductors to minimize charge recombination [69-74].

1.5 Applications of Semiconductor Nanomaterials

The semiconductor nanomaterials have used extensively in nanoelectronics, nanophotonics, fabricate computer chips, energy conversion, optics, sensors, imaging devices, solar cells, catalysis, detectors, photography, diodes, biological sciences etc. [75-79]. Our main

goal is to apply the as-synthesized semiconductor material for the photo and electrocatalysis application.

1.5.1 Catalysis

Catalysis can be described as the phenomenon where the rate of a process or reaction accelerated due to the participation of an extra material called catalyst, usually present in small quantities. Catalysts interact with the reactants in several ways which vary from providing a surface for the reaction to occur. Catalyst also offers an alternative path way for the reaction with lower activation energy thereby allowing reaction to occur at conditions which have been previously not favorable for the reaction. A catalyst doesn't have any effect on thermodynamics and equilibrium composition of a reaction; it only affects the rate of reaction.

$$A+B \xrightarrow{\text{catalyst}} C+D$$

The key property of a catalyst lies in the fact that despite interacting with the reaction the substance returns to its original state at the end of the reaction which allows it to catalyze the subsequent reactions as well. The catalyst is vital not only to the chemical industry but also to daily life itself.

1.5.2 History

The industrial catalyst technology begins in 1875 when a platinum catalyst has been used for large-scale production of sulfuric acid. In following years, a variety of major catalytic processes have been discovered. In 1903, Ostwald did ammonia oxidation on Pt gauge for nitric acid production. The development of iron catalyst during ammonia synthesis has been reported by Mittasch, Bosch, and Haber in 1908-1914. A major development in the energy zone has come in 1920-1940 with the conversion of synthesis gas to liquid hydrocarbons by hydrogenation of CO. Furthermore, the energy scenario has been changed with the development in petroleum industry during 1935-1940 [80-84].

The finding of *Ziegler-Natta catalyst*, the polymer industry developed appreciably. In 1960, the first large-scale industrial homogeneous catalytic process started with the production of acetaldehyde from ethylene called *Walker process*. Furthermore, noble metals have been used as

a catalyst to control the emission of environmental pollutants such as CO, NO_x, and hydrocarbons from automobiles. Vanadia-titania and shape-selective catalyst zeolites were developed for the selective reduction of NO_x. Moreover, modified noble metal catalysts have been used to degrade the environmental pollutants in the recent years which lead to the discovery of the catalyst with large efficiency and vast usability. Catalysis is a constantly rising field and discovery of new catalysts and their applications in several chemical reactions have led to the major advancements in chemical industry [80-84].

1.5.3 Types of Catalysis

In catalysis it is desirable to fasten the rate of chemical reactions and to recognize the mechanism of the reaction. The catalysts are accessible in the form of solid, liquid and gas phases. There are largely two types of catalysis in literature, homogeneous and heterogeneous catalysis [83-86].

1.5.3.1 Homogeneous Catalysis

If reactants and catalyst both are in the same physical state i.e. gas, liquid, or solid, called homogeneous catalysis. For example, it can be solubilized in a solvent like water or they may all be gases in our atmosphere. Homogenous catalysts generally react with one or more reactants to form an intermediate and then react to form the end reaction product, in the process restoring the catalyst.

1.5.3.2 Heterogeneous Catalysis

Heterogeneous catalysts when reactants and products are present in a dissimilar physical state. For example, the catalyst may be solid while the reactants and products are in liquid phase. In the field of nanoscience, a wide variety of semiconductor nanomaterials have been prepared which are used as photocatalysts and electrocatalysts. The heterogeneous photocatalysis is much advantageous rather than the other conventional processes, the reasons can be précised as follows [85]:

The ambient temperature and pressure conditions are required to carry out the processes.

For these processes, the atmospheric oxygen is used as oxidant avoiding the association of any additional oxidizing chemical. The environmental oxygen is a strong oxidant and less selective which results degradation of all organic contaminants (dyes, phenols, nitro compounds etc.) present in wastewater.

1. This photocatalysis process is "green and environmentally benign" since the degraded products are less toxic.

2. Low concentration is required for the process because the contaminants are strongly adsorbed on the catalyst surface, even in parts per million concentrations.

3. The catalysts are cost-effective, stable, chemically and biologically inert, easily separable and recyclable.

By examining all these advantages of heterogeneous photocatalysis which offers an economical and efficient substitute to clean wastewater and environmental remediation.

1.5.4 Photocatalysis

1.5.4.1 Background

Recently, the extensive presence of toxic chemicals such as heavy metals, herbicides, pesticides, detergents, arsenic compounds, solvents, degreasing agents, volatile organics, and chloro and nitrophenols pose a severe threat to the environment. These chemicals exert harmful effects when liberated in the water bodies [86-89]. For instance, effluents from textile industries contain azo dyes, phenols, nitrophenols etc. which are less biodegradable and chemically stable water pollutants. Chemical structure of a few common dyes is given in **Figure 1.11** [89-91]. This wastewater causes a severe impact on natural water and land in the surrounding area and also cause serious health issues [89-90].

These organic pollutants can be degraded using metal oxides, metal sulfides as a catalyst via photocatalysis process. In photocatalysis, light energy is provided to the catalyst to generate charge carriers which participate in redox processes. It is a vital chemical approach which is extensively used in water or air purification, water splitting reaction and in solar cells [91]. In 1977, Frank and Bard used titania for cyanide decomposition, which shows interest in photocatalysis using semiconductor materials [86]. A range of semiconductor materials are found but only a few are suitable for photocatalysis. The semiconductor to be used as photocatalyst for

degradation of dye pollutants must be (i) photoactive in UV or visible light (ii) inert and (iii) photostable [70-72,92-97].

The wide range applications of a photocatalyst are constrained due to recombination of photogenerated charges. In semiconductors also the probability of electron-hole pairing is very high [97-101]. For that, it is required to design a semiconductor photocatalyst which can inhibit the recombination rate and provide large-scale applications in remediation of pollutants with high efficiency.
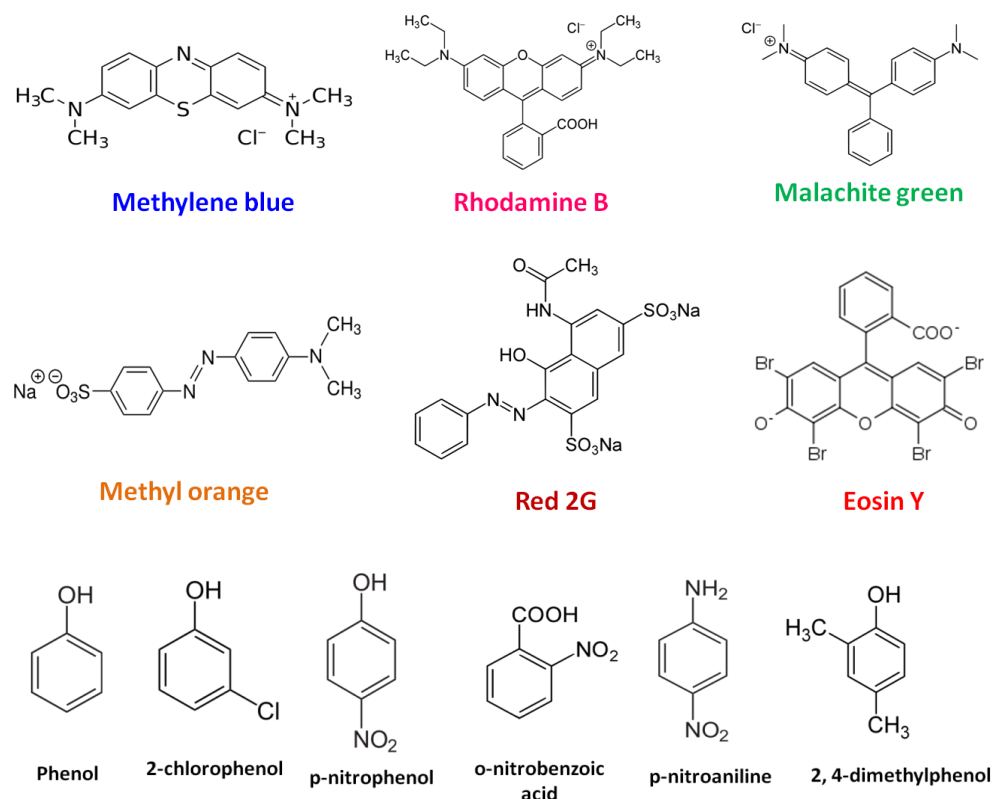
Figure 1.11 Examples of environmental pollutants (textiles dyes, phenols, and nitro compounds)

1.5.4.2 Water Pollution and Water Treatment

Water is the most essential fluid on the earth for all the living beings. Water covers 75% of the earth's area but fresh water is only 3% and two third is in frozen condition. The accessible water which is used for human and animal is only 0.25% [101-102]. So far the world's supply of

groundwater is gradually declining and it has become more complicated to conciliate the requirements for water supply for human consumption. Therefore, saving water is a key concern for modern societies to save the earth and to make the future of mankind secure.

The rapid growth in the industrial area, population escalation, and development in scientific technology have dragged our world to new perspectives but the cost which we have to pay is too high [102-107]. The faster industrial development and the worldwide population outburst results in the large requirement for fresh water, both for the household works and for agriculture. In addition, the consumption of accessible fresh water has increased tremendously in the domestic sectors and the quantity of contaminated water has also increased. The foremost water pollutant is the textile dyes which are toxic and non-biodegradable [86-88,102].

On a global level, over 0.7 million tons of organic synthetic dyes are produced annually which are essential in the textile manufacturing, leather, painting, food, plastics, cosmetics, photographic and paper industries [87-88]. It is estimated that 1-20% of the total worldwide production of dyestuff is released into the environment as dye effluent during the textile processing due to inefficiencies [88,103-105]. These dyes are not biodegradable and demonstrate hazardous effects specifically carcinogenic, DNA damage, allergic dermatoses and mutagenic effects, hence the effects of dyes on the environment is a matter of concern [91]. The colorants present in the water stream can block both sunlight and oxygen, which are essential for aquatic life. Low concentrations of dyestuff in wastewater do not usually impart any major environmental hazard but because of the presence of the higher concentration of these chemicals, there is a significant requirement to destroy efficiently these dyes before disposing them to the water receiving bodies.

1.5.4.3 Semiconductor-based Photocatalysis

In current times, various approaches to clean the water bodies including conventional methods have been reported in the literature by innovators [105-107]. These methods of wastewater treatment are of three types: biological, chemical and physical. These processes are not entirely effective because either they fail to accomplish complete color removal or inertness of contaminants that are not easily absorbable or volatile. In addition, they merely convert the contaminants to a different phase which again causes disposal harms.

Now, it is essential to discover more effective systems to purify water than the conventional water purification processes. As a response, the development of newer environmentally benign techniques of degrading hazardous waste became a crucial concern. Thus, over the past decade, research exertion has been dedicated to manufacturing a newer, more efficient and photoactive semiconductor nanostructures to transform the pollutants existing in the sewage into safe end products devoid of any toxic hazardous for environment [97-102].

In particular, there has been an incredible improvement over the past decade in the synthesis of semiconducting metal oxides and sulfides nanoparticles of different sizes and with good yield [64,68,70-75]. Semiconductor photocatalysts (TiO_2, ZnO, ZnS, CuO, CuS etc.) have widely been studied and have utilized in photocatalysis [88,108-112]. The electronic structure of semiconductor nanomaterials reveals that these materials have scope to modify and the general mechanism of photocatalysis shows that these materials can be used efficiently as a photocatalyst [79].

1.5.4.4 Requirement of a Semiconductor Material to be used as a Photocatalyst

The band potential of a semiconductor and the values of the redox potential of surface adsorbed species decide the capability of the semiconductor to undergo photoinduced charge transfer. The energy of band or band edge potential depicts the thermodynamic limitations for the photoreactions that accomplished by photogenerated charge carrier species. The energy level of the conduction band determines the reduction potential of the electrons and the energy level of the valence band establishes the oxidizing potential of the holes. In actual, both the conduction and valence band edge potentials indicate the ability of a semiconductor to perform the reduction and oxidation reactions [71,74]. From the thermodynamic perspective, the electrons of conduction band can reduce the adsorbed species if they have the more positive redox potential values than the band edge potential of the conduction band, the higher the conduction band edge the larger the reductive power of the electrons. Similarly, adsorbed couples can be oxidized by the holes of valence band if they have more negative redox potential than the band edge potential of the valence band [70,102,113-114].

The band edge positions of some frequently used semiconductors are illustrated in **Figure 1.12** [113-114]. However, the electronic structure in bulk semiconductor influenced by pressure, temperature and the pH of electrolyte used during the reaction. The main constraint for a wide

bandgap (3 eV) photocatalyst is that the band gap restricts their reactivity to the small UV-region of the sunlight, i.e. less than 5% of sunlight can be harvested by these materials. So, the narrow bandgap semiconductors are preferred but they also have lower stability issues [70-74].
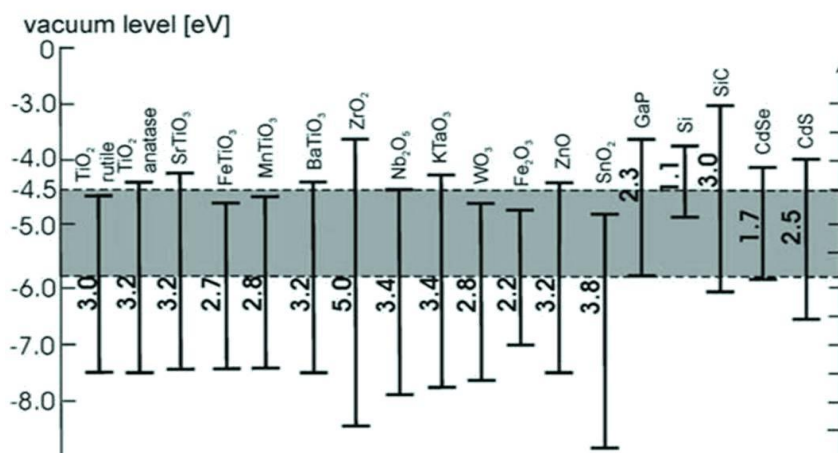
Figure 1.12 The band gaps and band-edge positions of various semiconductors with respect to the vacuum level [114]

The semiconductor is shown in **Figure 1.12**, an example of a metal oxide which has sufficient band gap energies to be excited in UV or visible region, and the redox potentials of the CB and VB edges can encourage a series of oxidative and reductive reaction. However, some of the semiconductor materials do not have durability in aqueous media [86,97]. Metal oxides and sulfides (TiO_2, ZnO, ZnS, Cu_2O, Fe_3O_4, SnO_2, CeO_2, Bi_2O_3, SnO, NiO etc.) have been the subject of an extensive investigation from the last couple of years [115-120]. The other class of semiconductors is metal chalcogenides (MoS_2, CdS, $CdSe$, PbS, $MoSe_2$, and $PbSe$), which offers a noteworthy advantage because of their tunable reactivity under visible light [71-72,107,116]. Consequently, a lot of research and attention have been focused towards the development of a visible light active material which shows prolonged stability during photocatalysis.

1.5.4.5 Mechanism of Dye Degradation

This thesis work includes mainly the synthesis of heterogeneous catalysts of semiconductor metal oxide and sulfide nanomaterials and their applications in photocatalysis. A semiconductor can be excited by light energy higher than the bandgap energy with the generation

of electron-hole pairs which involves photoreduction and photooxidation reactions shown in **Figure 1.12** [99,102,109].

Photocatalysis is a chemical process catalyzed by a solid catalyst where the external energy source is used to excite the electrons [113-115]. A material can be used as an ideal photocatalyst, if it owns the following characters: (i) photoactive, (ii) chemically and biologically inactive and photostable, (iii) inexpensive and (iv) environment-friendly [71-76,116].

The heterogeneous photocatalytic process is a surface phenomenon that pursues the following steps when a semiconductor material is used as a catalyst and shown in **Figure 1.12** and **1.13**: [99,112-116].

❖ Photoexcitation of semiconductor with light absorption, having energy equivalent to or higher than the band gap energy.

❖ Transfer of electron from the filled VB to the empty CB of the semiconductors and creation of the electron-hole pairs.

❖ Separation of the electrons and holes or prevention of the photogenerated charge pairing. Therefore, the rate of reaction must be higher than the rate of the recombination of electrons and holes, to avoid deactivation of the catalyst.

❖ Various environmental pollutants (synthetic dyes, phenolic compounds, nitro compounds etc.) adsorb on the catalyst surface via chemical or physical adsorption.

❖ Redox reactions carried out on the catalyst surface between the electrons, holes and the adsorbed molecules; are important in the formation of ultimate reaction products.

❖ Desorption of the end products from the catalyst surface in the degraded forms (CO_2 and H_2O).
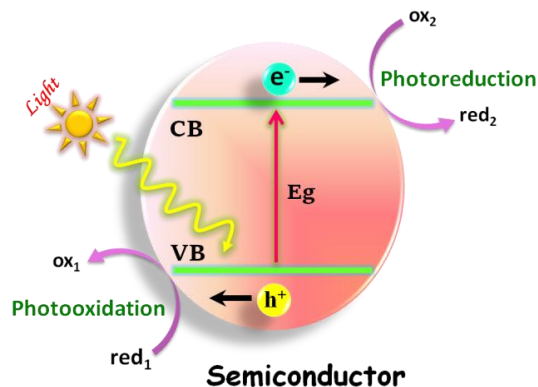
Figure 1.13 General photocatalysis mechanism in a semiconductor under light illumination
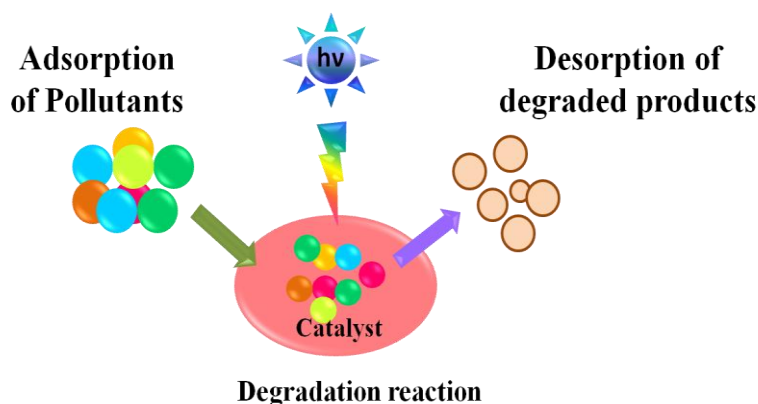
Figure 1.14 Degradation of pollutants on a catalyst surface under visible light irradiation

Dye degradation by the semiconductor nanomaterials under light carried out by two processes. In the *first step*, when a semiconductor nanomaterial absorbs the light energy higher or equal to the energy gap, the electrons get excited. These photogenerated electrons jump from the valence to conduction band with the simultaneous generation of the holes in the valence band. Holes can take part in the various oxidative reactions with the formation of reactive intermediates. These intermediates give the final products and the reaction steps can be shown as [70,74,102].

$$MO/MS + h\nu \rightarrow MO/MS \ (e_{CB}^- + h_{VB}^+) \qquad (1)$$
$$e_{CB}^- / h_{VB}^+ + dye \rightarrow dye^* \rightarrow degraded\ product \qquad (2)$$
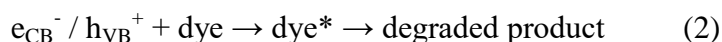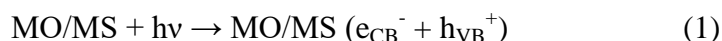
The holes react with the surface bounded hydroxyl species and generate hydroxyl ($OH^\bullet$) free radicals in the presence of aqueous solution. These species are highly reactive and responsible for the dye degradation as follows:

$$h_{VB}^+ + H_2O \rightarrow H^+ + OH^\bullet \qquad (3)$$
$$h_{VB}^+ + OH^- \rightarrow OH^\bullet \qquad (4)$$

The band edge potential of the conduction band (e_{CB}^-) is sufficient negative and the electrons of the CB can reduce the surface absorbed oxygen molecules with the subsequent generation of superoxide free radical ($O_2^{-\bullet}$).

$$e_{CB}^- + O_2 \rightarrow O_2^{-\bullet} \qquad (5)$$

The radical again react with surface adsorbed water molecules to form peroxide (H_2O_2) which is eventually generate $OH^{\bullet}$.

$$O_2^{-\bullet} + H^+ \rightarrow HOO^{\bullet} \qquad\qquad (6)$$

$$HOO^{\bullet} + HOO^{\bullet} \rightarrow H_2O_2 \rightarrow OH^{\bullet} + O_2 \qquad\qquad (7)$$
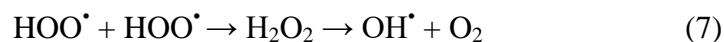
The successive reactions of the reactive chemical species ($OH^{\bullet}$ and $O_2^{-\bullet}$) degrade dye molecules entirely and simple molecules as end products are formed [70,74,99,102].

The *second step* is the dye sensitization mechanism where surface adsorbed dye molecules absorb light and get excited [121-122]. In this process, dye molecule absorbs an energy and the existing electrons go through excitation from HOMO to LUMO. The excited electrons present in the LUMO of dye are inserted into the conduction band of the catalyst. The dye is converted to cationic dye radical [120-124]. These dye radicals degraded via generation of the similar oxidative species ($O_2^{-\bullet}$ and $OH^{\bullet}$) as explained in the first mechanism [74,118-121]. The absolute degradation of dye takes place and produce degraded end products. This mechanism is important when dye molecules are adsorbed directly on the photocatalyst surface [86,74-75]. These two mechanisms are depicted in **Figure 1.15**.
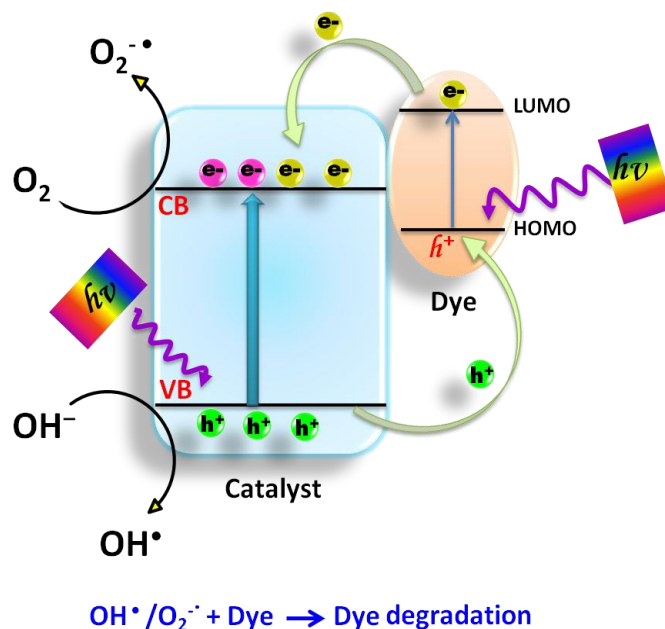
Figure 1.15 Dye degradation mechanism in presence of semiconductor material as a catalyst

1.5.4.6 Limitations of a Photocatalyst

In spite of several semiconducting metal oxide and sulfide combinations reported in the literature with high photocatalytic activities, still, there is a huge demand for new nanomaterials. The major problem of a large bandgap semiconductor is the recombination of electron and holes and restricted light-harvesting capacity. This leaves a vast scope for the development of new heterostructures with different combinations of improved optical properties, photocatalytic efficacies, and thermal stability.

A semiconductor can be sensitized using an additional semiconductor material while charge recombination can be reduced using noble metal deposition (Ag, Pt, Au, Pd etc.). Another challenging problem is to fabricate catalysts that can excite under visible light, which is 43% of sunlight. The disadvantage of using bare metal oxide and sulfide nanomaterials like TiO_2, ZnO, ZnS, SnO_2, CeO_2, Bi_2O_3, SnO, NiO, Cu_2O, Fe_3O_4 etc. as photocatalysis is that these nanomaterials can absorb mainly UV light thus significantly restricts the practical application of these photocatalysts. Therefore, the modification of a catalyst surface is essential with other visible light active nanomaterials. Further obstacles and disadvantages associated with nanomaterials are instability, non-reusability, and toxicity. There is also a scope to synthesize nanoparticles which are durable, cost-effective, reusable and environmentally benign.

1.5.5 Approaches to Enhance the Photocatalytic Activity of Semiconductor Nanomaterials

1.5.5.1 Deposition of Metal Nanoparticles

Photocatalytic reactivity of nanoparticles boosted to many folds when assisted by metals like Au, Ag, Pt, and Pd due to the electron scavenging property of metal nanoparticles [108,125-126]. There is a lot of scopes to develop various combinations of semiconducting metal oxide and sulfide nanoparticles and modify their surfaces by using different noble metals to enhance the photocatalytic reactivity. It will effectively increase the lifetime of photoexcited electrons and therefore the recombination of the electron and hole is delayed [71,108,127-130]. Previous studies discovered that metal deposited semiconductor nanocomposite improves the effectiveness of the photocatalytic reactions, in which metal nanoparticles behave as an inert sink for electrons or holes and obstructed the recombination. Owing to the dissimilar work function of

the metal nanoparticles and semiconductor, a space charge region is originated upon their contact and an in-built potential promote the separation and easy transportation of photogenerated charges analogous to the coupled semiconductor heterostructures [127-136].

The role of a metal associated with a semiconductor can vary depending upon their oxidation state. A metal nanoparticle of zero valency can be used along with a semiconductor to prevent recombination of photogenerated charges. A metal ion (cation) can be doped into a semiconductor and can be used to expand the photoreactivity of the semiconductor nanomaterials under visible light [86,127-136]. Along with various metal nanoparticles, used for the synthesis of the metal-semiconductor composite, noble metal nanoparticles have been established to be more beneficial to facilitate the efficiency of semiconductor nanomaterials for catalytic reactions [70-75]. Non-noble metals like Cu, Mn, and Fe are used more often as chromophores to harvest light. Platinum-based compounds have also been used for enhancing the catalytic properties of semiconductors [36]. Previously, TiO_2 or doped TiO_2 (with anions, cations, and metal ions) were used to improve photocatalytic efficiency, which normally absorbs at UV wavelength region [86].
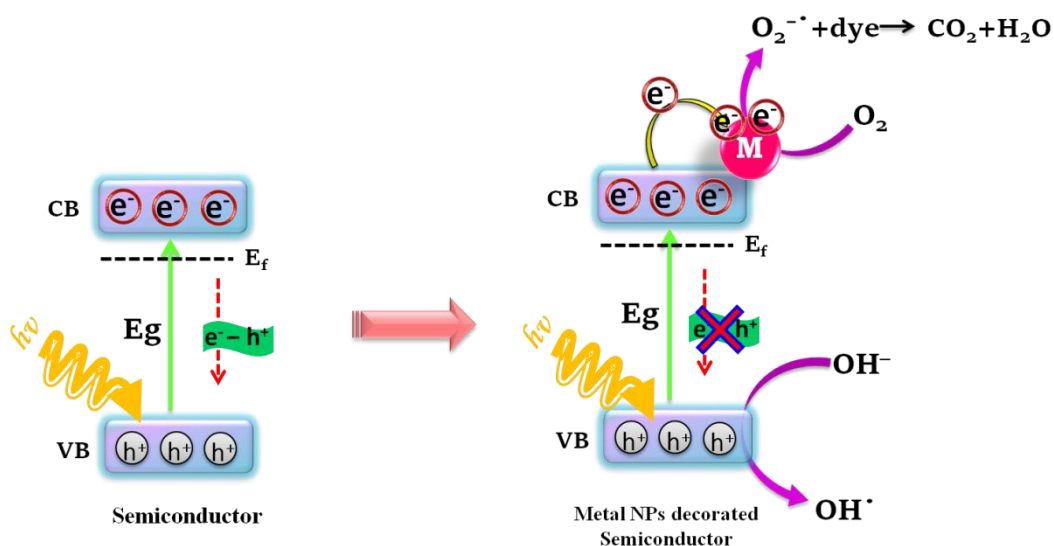
Figure 1.16 Schematic representation showing photocatalytic process using metal decorated metal oxide nanoparticles

Kamat and co-workers showed the charge and discharge of electrons in between TiO_2 and Ag nanoparticles in the presence and absence of UV light. The same group explained the VB

electrons of metal oxide nanoparticles get excited with a light source and jump from VB to CB. The metal nanoparticles scavenge electrons from CB of metal oxide nanoparticles [127]. These electrons on the metal surface were used in the dye degradation reaction. The overall process is shown in **Figure 1.16**.

Chiou *et al.* reported the connection between electronic structures and photocatalytic activities during a photocatalysis process. They have explained Au, Ag, and Pt metal nanoparticles on the ZnO nanorod surface act as a sink, facilitating the interfacial charge transfer and effective separation of photoinduced electron and hole. Therefore, the photocatalytic performance of bare ZnO has improved after decorating with metal nanoparticle [130]. Zheng *et al.* reported the synthesis of Ag/ZnO nanocrystals using a varied amount of silver and without using any extra stabilizer via the solvothermal method. The correlation of morphology with the photocatalytic performance has been investigated and results revealed that the photocatalytic property is associated with its structure, oxygen defects, and crystalline nature. They have shown that the silver nanoparticles and oxygen vacancies on the ZnO nanorods surface enhance the charge separation and thus boost the photocatalytic efficiency [132]. Chang and co-workers reported the synthesis of Pd/ZnO with different Pd contents using a facile one-pot hydrothermal approach. The results demonstrated that the partial Pd loading is present on the surface of ZnO and the remaining is doped in the lattice of ZnO. It has also found that the loading of Pd modulates the electronic structure of ZnO and also affect the content of surface hydroxyl resulting in the promotion of photodegradation efficiency [135]. The dimer-type heterostructure of Ag-ZnO nanofibers and photodegradation of RhB dye under the UV light has been reported by Lin and co-workers. The heterojunction structure endorsed the separation of electrons and holes and the photon efficiency, allowing both charges to contribute in the overall photocatalytic reaction. It has also been observed that in Ag-ZnO the photocatalytic activity is exceeded by a factor of more than 25 as compared to pure ZnO [134].

1.5.5.2 Coupled Semiconductors

To promote the charge separation and reduce/hinder the charge-carrier recombination for superior photocatalytic activity, the coupling of two semiconductors having different band gap energies is a successful approach. Countless efforts have been made to design the different

heterostructures such as ZnO/CdS, CuS/ZnS, CuS/ZnO, ZnO/ZnS, SnO$_2$/TiO$_2$, ZnO/TiO$_2$ or CdS/TiO$_2$ [137-140]. The heterostructure significantly inhibits the recombination of charges and facilitate electron transfer due to the inducement of the internal static electric field and the potential difference between VB and CB resulting in the enhancement of photocatalytic efficiency [116-119]. The heterostructure replaces the drawbacks of the bare material and stimulate a synergistic effect between both the semiconductors [117]. If there are two semiconductors which have dissimilar electron affinities, the possibilities of different types of heterostructure have been shown in **Figure 1.10**.

Considering a type-II (**Figure 1.10**) band alignment, it is apparent that the energy gradient existing at the interface of heterostructure is inclined in such a way that electrons and holes are separated on the different sides of the heterojunction. Due to this electrons will be restricted to the CB of one semiconductor and holes may be into VB of another. The mechanism of the electron and hole separation in a semiconductor heterostructure is schematically depicted in **Figure 1.17**.
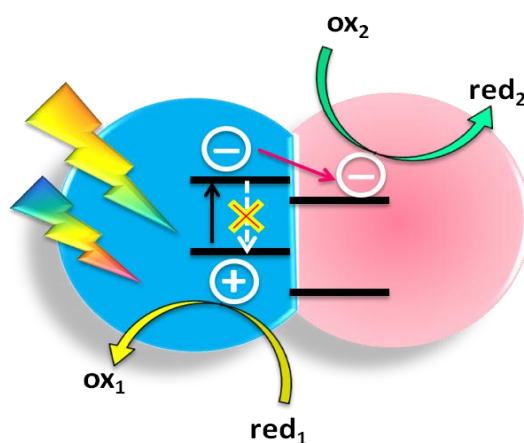
Figure 1.17 Schematic diagram demonstrating photocatalysis mechanism in coupled semiconductor type-II heterostructure

When a semiconductor heterostructure nanomaterial is irradiated with UV light, VB electrons are excited and jump to the CB with the immediate generation of the holes in the VB. The generation of electrons takes place in the UV-active material as it only absorbs the photons. Afterward, from the higher CB edge semiconductor, electrons are transferred to the lower CB

edge semiconductor as shown in **Figure 1.17**. In sequence, the holes present in opposite direction involves in the oxidative reactions that raise the rate of charge separation [71-74]. The similar kind of charge transfer can happen in case of visible light active materials.

Serpone *et al.* reported the coupling of two semiconductors (CdS and TiO$_2$) and showed the significant increase in photocatalytic efficiencies (degradation of dyes and organic pollutants) due to interparticle electron transfer between TiO$_2$ and CdS [140]. Dandan *et al.* reported the activity toward photocatalysis, which enhanced by synthesizing the semiconductor heterostructure (ZnO-ZnS) [15,16,141]. The band gap energy values for ZnO and ZnS nanoparticles are 3.37 and 3.70 eV, respectively. When ZnS-ZnO heterostructure illuminated by light then electron gets excited from VB to CB and there will be excess of electrons in the CB of ZnO, which helps in the photoreduction and excess of holes in VB of ZnS for photooxidation reaction [141-143]. Therefore, the photocatalytic reactivity enhanced as compared to bare metal oxide/sulfide semiconductor nanoparticles.

Various semiconductor assemblies with different kinds of morphologies such as nanoflowers, nanotubes, nanorods, nanoleaves, etc. have been used to exhibit high photocatalytic efficiency [144-147]. Zhang and co-workers explained the synthesis of flower-like ZnO nanostructure using a surfactant. They used a surfactant as a stabilizer and explained the role of surfactant in the formation of ZnO [144]. Yong and co-workers reported a facile approach to the fabrication of CuS/ZnO heterostructure nanowire arrays and their successful application as visible light photocatalysis using acid orange dye (AO7). They have explained the higher photocatalytic reactivity in presence of heterostructure as compared to the pure semiconductor. This enhanced photocatalytic activity is due to the interfacial charge transfer (IFCT) from the VB of the ZnO nanowires to the CuS nanoparticles. They mentioned the reusability of the catalyst particles without any significant loss of activity for photodecolorization of acid orange [145]. This photoinduced interfacial charge transfer in CuS/ZnS heterostructure has been also reported by Gong and co-workers [146].

Serpone *et al.* explained the heterogeneous photocatalysis and the idea about the semiconductor materials used in photocatalysis. Countless studies are available to illustrate the pathway of electron transfer in dye photosensitization process, and in photosensitization of semiconductor in presence of another semiconductor called coupled heterostructure [147-148]. Li and co-workers reported the ZnO/CdS heterostructure and its use in the photodegradation of

rhodamine B (RhB) dye under sunlight, and the photocatalytic performance signifies that the heterostructure exhibits better photocatalytic efficiency, which can be attributed to the extensive photoresponse range and the improved charge separation rate [149]. Yu *et al.* reported the synthesis of monodisperse CuS/ZnS nanocomposite and the enhanced photocatalytic activity in heterostructure has been used for the decolorization of RhB dye under visible-light illumination [150].

1.5.5.3 Scavenging of Photogenerated Electrons and Holes

Scavenging of photogenerated charges using any charge acceptor or donor in the VB and CB respectively is another technique to inhibit the electron-hole recombination and enhance the photocatalytic activity [64-68,147]. During photocatalysis, the recombination step is predominant in the lack of an electron acceptor, and thus it confines the effectiveness of photocatalysis [151-155]. The involvement of external oxidants or electron acceptors into photocatalysis lead to progress the photocatalytic degradation of organic pollutants as (i) it accepts the electrons present in CB and reduce the electron-hole pairs recombination; (ii) increasing the concentration of hydroxyl radical in the reaction mixture which accelerates the rate of oxidation of transition species; and (iii) produce supplementary radicals and supplementary oxidizing species to increase the degradation of intermediates [70-74]. Numerous researchers have been investigated that hydroxyl radicals play a considerable role in the photodegradation reactions. The consequences of electron acceptors or scavengers have been well studied in the photocatalytic degradation of contaminants and mostly hydrogen peroxide (H_2O_2), potassium bromate $(KBrO_3)$, and potassium persulfate $(K_2S_2O_8)$ have been reported and shown in **Figure 1.18**. To decompose the pesticides and herbicides, these acceptors provide an excess of hydroxyl radicals and slowed down the electron-hole pair recombination [14,15,115]. For example, H_2O_2 can scavenge the photogenerated electrons to stabilize the electron-hole pairs [155].

$$H_2O_2 + e^- \rightarrow OH^\bullet + OH^- \qquad (8)$$
$$H_2O_2 + O_2^{-\bullet} \rightarrow OH^\bullet + OH^- + O_2 \qquad (9)$$
$$H_2O_2 + OH^\bullet \rightarrow H_2O + OH_2^\bullet \qquad (10)$$
$$OH_2^\bullet + OH^\bullet \rightarrow H_2O + O_2 \qquad (11)$$
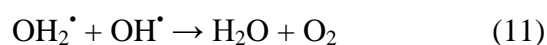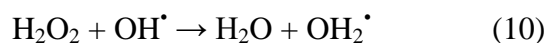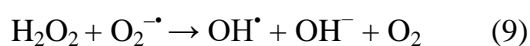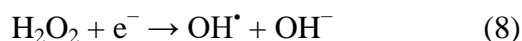
In presence of H_2O_2 extra $OH^\bullet$ radicals generated via the reaction (8) and (9), which probably endorse the degradation of pollutants as it is the key species in photocatalysis. Generally, molecular oxygen present in dissolved condition behaves as electron acceptor and produce superoxide radicals ($O_2^{-\bullet}$) which also plays a key role during photocatalysis. Though, the excess addition of H_2O_2 would capture the $OH^\bullet$ radicals via reaction (10) and (11) and suppress the photocatalytic activity.
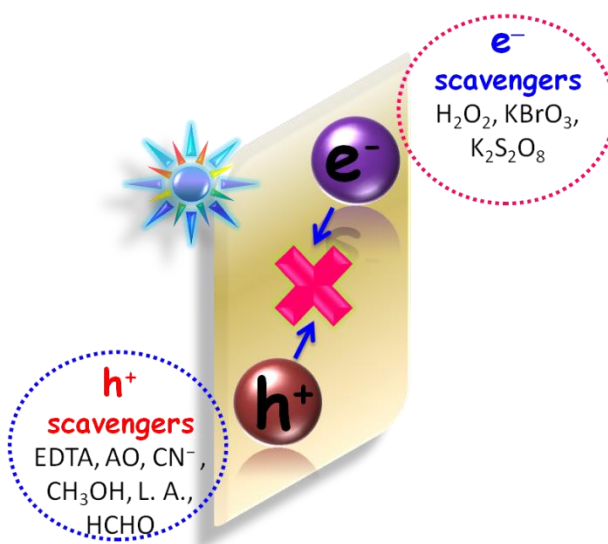
Figure 1.18 Photogenerated electron and holes trapped by e⁻ and h⁺ scavengers and restricted recombination and reduction of the formation of radical species

On the contrary, the addition of electron donors or hole scavengers in the photocatalytic process also affects the reactivity. These reagents react with the photogenerated holes at VB and inhibit the electron-hole recombination resulting in higher photocatalytic efficiency. It is necessary to opt an appropriate hole scavenger and the photogenerated electron can be captured on the surface of the semiconductor. The holes undergo a photocatalytic oxidation and reduction reaction with electrons. Some hole scavengers such as EDTA, ammonium oxalate, formaldehyde, lactic acid, cyanide ions, and solvents like ethanol and methanol have been reported and established to facilitate the photocatalytic activity [152-155]. In general, these species act as scavengers for holes and thus separates the charge carriers.

1.5.5.4 Charge Carrier Trapping

It is an alternative method to restrict the charge recombination by which lifetime of electrons and holes can be amplified more than a fraction of nanosecond for improved catalytic activity of a semiconductor [125-127]. Surface and bulk defects naturally happen during the synthesis of colloidal and polycrystalline photocatalysts. The deformities are connected with surface electron states and called as carrier-trapping surface defects and their energy state is different from the bulk semiconductor. These different energy states behave as charge carrier trap and assist to retard the electron-hole recombination [152].

1.5.6 Electrocatalysis

There are essentially two types of energy resources: natural or non-renewable, and renewable, used by a human being for the production of energy for our everyday life. Including oil, gas, coal and nuclear energy sources around ~90 % of the total energy resources covered by non-renewable energy sources (India) [156-159]. Only ~10% of natural resources are available as renewable energy sources shown in **Figure 1.19**. World's energy consumption patterns shifted from wood→coal→oil→gas based on greenhouse gas emission as well as hydrogen to carbon ratio (H/C ratio). Non-renewable sources release carbon dioxide, a major factor for the greenhouse effect which is a perennial problem for the environment. The environment pollution triggered energy crisis for future. Therefore, it is necessary to explore clean and renewable energy sources, which can replace the natural fuels effectively [157-158].
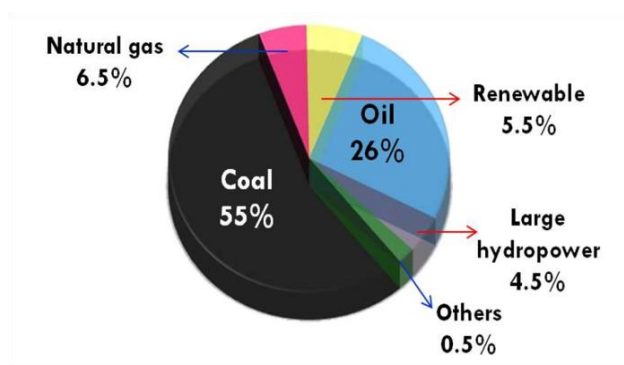
Figure 1.19 The distribution of energy resources (natural and non-renewable energy sources)

The energy requirement is highly dependent on renewable energy sources; hence it is needed to store this energy for the future [160-162]. Due to the increased percent consumption of coal and petroleum, the global climate is changing continuously and become a main concern. Hence, H_2 is considered as the environmentally benign fuel for both the electric power and transportation industries as it only produces the clean end products.

Owing to some advantage of hydrogen gas it catches the eyes of the civilized world to consider it as a substitute for renewable energy sources [163-168]:

1. The energy content per unit weight is 143 GJ/tonne in H_2 which is the highest of any known fuel and the only fuel which is chemically free from carbon content.

2. During combustion, hydrogen gives only water and energy. Also, its transportation and common use are safer than other gaseous fuels at normal temperature and pressure.

3. It is well known that the electrochemical process for hydrogen production, a safer avenue, is considered to be a promising route compared to other chemical or biological routes in order to supply the energy needs.

Hydrogen gas can be generated from a number of resources like water, fossil fuels, and biomass etc. It has been previously reported that water is transparent liquid so visible light will pass through directly and it cannot be split, but if the radiations with wavelengths shorter than 190 nm are used the splitting can happen [116,163]. The most fascinating route to produce H_2 is photocatalytic decomposition of water shown in equation (12) [159-160]. The hydrogen produced by the reaction in equation (12) can be stored and used in the fuel cells.

$$2H_2O + h\nu \rightarrow O_2 + 2H_2 \qquad (12)$$
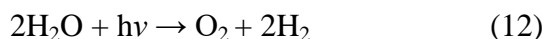
The reaction in equation (12) is performed in the absence of radiation which requires 286 kJmol^{-1} energy input in ambient conditions termed as electrochemical water splitting reaction or water electrolysis [159-164].

1.5.6.1 Hydrogen and Oxygen Evolution Reaction

At cathode, hydrogen evolution reaction (HER) and at anode oxygen evolution reaction (OER) are two crucial half-cell reactions of electrochemical water splitting.

$$\text{Cathode (HER): } 4H^+_{(aq)} + 4e^- \rightarrow 2H_{2(g)}, \ E^o_{red} = 0.00 \text{ V (vs. RHE)}$$
$$\text{Anode (OER): } 4H_2O_{(l)} \rightarrow O_2 + 4H^+_{(aq)} + 4e^-, \ E^o_{red} = -1.23 \text{ V (vs. RHE)}$$
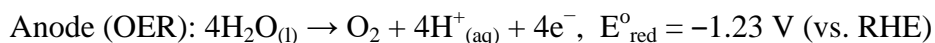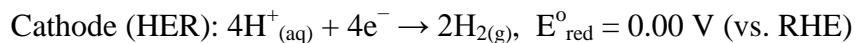
According to the thermodynamics, the breakdown of water into hydrogen and oxygen at standard temperature and pressure (25 ^{o}C, 1 atm) is not favorable, as depicted in the above equations. The standard reduction potential for HER is defined as 0 V *vs.* RHE (Reversible hydrogen electrode) whereas for OER is −1.23 V *vs.* RHE at standard temperature and pressure. It means for electrochemical decomposition of water the potential difference between the cathode and anodes must be more than 1.23 eV. In experimental water electrolysis complex charge transfer processes take place which leads to the reduced energy efficiency due to sluggish reaction kinetics and charge aggregation. The above mentioned higher potential, which is more than the thermodynamically determined reduction potential, required for the reaction called as overpotential (η) [165-166]. A much important concern is to design an appropriate catalyst for water splitting which can reduce the overpotential significantly and endorse the rate of the reaction and efficiency of the cell. Electrocatalysts in nanoscale could offer different intermediate states, reduction in activation energy and provide the energy required for the transition state to more number of surface adsorbed molecules. Hence, these facilitate the reaction rate and the reaction can carry out at a lower potential. Moreover, a catalyst having a porous and rational structure with increased reactive sites decreases the amount of catalyst and also contributes to alleviating the overpotential [166-168]. Amongst the various HER catalysts, platinum is a famous and largely used catalyst due to its zero overpotential and a very low Tafel slope. Afterward, more noble metals like palladium, gold, silver, and iridium also have been examined and proved excellent catalytic materials for HER but higher cost and scarcity of noble metals limits their applications on large scale. Therefore, it is essential to find an economical substitute with high efficiency. To do so, recently attention has been diverted toward OER catalysts based on non-noble metals such as Mn, Co, Ni, Fe and HER catalysts based on Mo and W [165-168].

1.5.6.2 Use of Semiconductor Nanomaterials in Electrochemical HER

In the 1970s, Honda and Fujishima utilized TiO_2 electrode for water splitting where TiO_2

irradiated with visible light for the generation of electrons and holes [70,63,116]. This perception, which appeared by using photoelectrochemical cells with semiconductor electrodes, has further been used to design a photocatalytic system using semiconductor nanomaterials as photocatalysts [164-168].

Recently, a range of nanomaterials with different morphologies have been developed and used as electrodes. Especially, catalysts are fabricated with the increased surface area, active sites, and conductivity. Their surface modifications with suitable light-harvesting materials have elevated their commercial use owing to higher efficiency [161,163].

A typical electrolysis cell connected to a potentiostat for water splitting reaction is shown in **Figure 1.20**. Here, an electric current is passed through water to split water into hydrogen, and oxygen. Hydrogen is generated at cathode, oxygen at anode and collected further. Hydrogen produced by this technique is tremendously clean, and results in no hazardous emissions and can be utilized as a replacement for renewable energy sources.
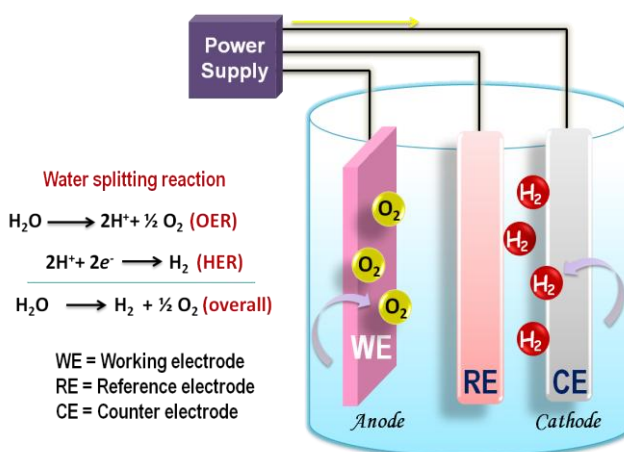
Figure 1.20 Electrolysis cell used for electrolytic hydrogen and oxygen production

There are two important aspects to be accomplished for the semiconductor materials used as efficient electrocatalysts for H_2 production [114,116]:

(i) The bandgap of the semiconductor should be higher than 1.23 eV and lower than the 3.26 eV.

(ii) The lowest edge of the CB should be more negative than the redox potential of H^+/H_2 which is 0 V *vs.* RHE while at the VB, higher edge should be more positive than the redox potential of O_2/H_2O which is -1.23 V *vs.* RHE.

The electrolysis of water consumes more energy in the form of electricity compared to that by other processes. For any mass-producible device, abundant, cheap and readily available materials are required to use as electrodes. In order to decrease the consumption of electrical energy, the researchers initiated the research on some alternative approaches. Moreover, the different aspects of hydrogen generation including the efficiency, ease of storage, and distribution are demanded its real-world applications. Therefore, in the future, it will be required to develop the materials which can work toward the aforementioned aspects. Evidently, there is a broad scope for significant advancements to develop both HER and OER electrocatalysts.

1.5.7 Scope and Incentive of the Thesis

- To construct different morphologies of semiconductor metal oxide and sulfide nanomaterials
- To design heterostructure by combining two different semiconducting metal oxide and sulfide nanomaterials with suitable energy levels to enhance the charge separation at the heterojunction interfaces.
- To synthesize environmental benign and reusable nanomaterials with good stability, availability, not toxicity, and low cost.
- To decorate the surface of metal oxide/sulfide nanomaterials with metal (Au, Ag, Pd, and Pt) nanoparticles
- To examine the photocatalytic reactivity of the as-synthesized nanomaterial for the degradation of textile dyes, phenolic compounds, nitro compounds and other organic pollutants under UV or visible light illumination by varying different reaction parameters including the nature and composition of the photocatalyst, reaction conditions, and time duration. The stability after the catalysis and recyclability of the as-synthesized catalyst will also be explored by its repetitive use.
- To investigate and enhance the efficiency of resultant nanomaterials for photocatalysis using several scavengers.
- Other prospective research directions can be predicted to extend the use of synthesized semiconductor in the field towards the production of sustainable and renewable energy sources such as hydrogen gas from splitting of water. The synthesized nanomaterials explored for the electrochemical hydrogen production reaction.

References

[1]   Jellinek, J. Nanoalloys: Tuning Properties and Characteristics through Size and Composition. *Faraday Discuss.* **2008**, *138*, 11-35.

[2]   Thompson, D. Michael Faraday's Recognition of Ruby Gold: The Birth of Modern Nanotechnology. *Gold Bull.* **2007**, *40*, 267-269.

[3]   Freestone, I.; Meeks, N.; Sax, M.; Higgitt, C. The Lycurgus Cup-A Roman Nanotechnology. *Gold Bull.* **2007**, *40*, 270-277.

[4]   Verhoeven, J. D.; Pendray, A. H.; Dauksch, W. E. The Key Role of Impurities in Ancient Damascus Steel Blades. *JOM* **1998**, *50*, 58-64.

[5]   Drexler, *E. Engines of Creation: The Coming Era of Nanotechnology and Nanosystems: Molecular Machinery, Manufacturing, and Computation*. Anchor Books, New York, **1986**.

[6]   Drexler, K. E. *Nanosystems: Molecular Machinery, Manucfacturing, and Computation*. Willey-VCH, Weinheim, **1992**.

[7]   Pradeep, T. A. *Text Book of Nanoscience and Nanotechnology*. McGraw-Hill Education (India) Private Limited, **2012**.

[8]   Rao, C. N. R.; Muller, A.; Cheetham, A. K. *Nanomaterials Chemistry: Recent Developments and New Directions*. Wiley-VCH, Weinheim, **2007**.

[9]   Vollath, D. *Nanomaterials: An Introduction to Synthesis, Properties and Applications*. Wiley-VCH, Weinheim, **2013**.

[10]   Taniguchi, N. *On the Basic Concept of 'Nano-Technology*. Proc. Intl. Conf. Prod. Eng. Tokyo, Part II, Japan Society of Precision Engineering, **1974**.

[11]   Capek, I. Nanocomposite Structures and Dispersions Science and Nanotechnology-Fundamental Principles and Colloidal Particles. *Studies in Interface Science* **2006**, *23,* 1-301.

[12]   Schmid, G. *Nanoparticles: From Theory to Application*. Wiley-VCH Weinheim, **2004**.

[13]   Giri, J.; Sriharsha, T.; Bahadur, D. Optimization of Parameters for the Synthesis of Nano-Sized $Co_{(1-x)}Zn_xFe_2O_4$, ($0 \leq x \leq 0.8$) by Microwave Refluxing. *J. Mater. Chem.* **2004**, *14*, 875-880.

[14]   Rodriguez, J. A.; Fernandez-Garcia, M. *Textbook of Synthesis, Properties and Applications of Oxide Nanomaterials*. Wiley Interscience, A John Wiley and Sons, Inc.,

Publication, **2007**.

[15]   Fageria, P.; Gangopadhyay, S.; Pande, S. Synthesis of ZnO/Au and ZnO/Ag Nanoparticles and Their Photocatalytic Application Using UV and Visible Light. *RSC Adv.* **2014**, *4*, 24962-24972.

[16]   Fageria, P.; Nazir, R.; Gangopadhyay, S.; Barshilia, H. C.; Pande, S. Graphitic-Carbon Nitride Support for the Synthesis of Shape-Dependent ZnO and their Application in Visible Light Photocatalysts. *RSC Adv.* **2015**, *5*, 80397-80409.

[17]   Guo, W.; Liu, T.; Huang, L.; Zhang, H.; Zhou, Q.; Zeng, W. HMT Assisted Hydrothermal Synthesis of Various ZnO Nanostructures: Structure, Growth and Gas Sensor Properties. *Physica E: Low-dimensional Systems and Nanostructures* **2011**, *44*, 680-685.

[18]   Hankare, P. P.; Vader, V. T.; Patil, N. M.; Jadhav, S. D.; Sankpal, U. B.; Kadam, M. R.; Chougule, B. K.; Gajbhiye, N. S. Synthesis, Characterization and Studies on Magnetic and Electrical Properties of Mg Ferrite with Cr Substitution. *Mater. Chem. Phys.* **2009**, *113*, 233-238.

[19]   Hankare, P. P.; Sankpal, U. B.; Patil, R. P.; Mulla, I. S.; Lokhande, P. D.; Gajbhiye, N. S. Synthesis and Characterization of $CoCr_xFe_2$- xO_4 Nanoparticles. *J. Alloys Compd.* **2009**, *485*, 798-801.

[20]   Zhang, S. C.; Messing, G. L.; Borden, M. Synthesis of Solid, Spherical Zirconia Particles by Spray Pyrolysis. *J. Am. Ceram. Soc.* **1990**, *73*, 61-67.

[21]   Pande, S.; Ghosh, S. K.; Praharaj, S.; Panigrahi, S.; Basu, S.; Jana, S.; Pal, A.; Tsukuda, T.; Pal, T. Synthesis of Normal and Inverted Gold-Silver Core-Shell Architectures in β-Cyclodextrin and Their Applications in SERS. *J. Phys. Chem. C* **2007**, *111*, 10806-10813.

[22]   Kundu, S.; Pal, A.; Ghosh, S. K.; Nath, S.; Panigrahi, S.; Praharaj, S.; Pal, T. A New Route to Obtain Shape-Controlled Gold Nanoparticles from Au(III)-β-diketonates. *Inorg. Chem.* **2004**, *43*, 5489-5491.

[23]   Panigrahi, S.; Kundu, S.; Ghosh, S.; Nath, S.; Pal, T. General Method of Synthesis for Metal Nanoparticles. *J. Nanopart. Res.* **2004**, *6*, 411-414.

[24]   Klabunde, K. J.; Richards, R. M. *Nanoscale Materials in Chemistry*. New York: Wiley Interscience, **2001**.

[25] Bonnemann, H.; Richards, R. M. Nanoscopic Metal Particles- Synthetic Methods and Potential Applications. *Eur. J. Inorg. Chem.* **2001**, *10*, 2455-2480.

[26] Hunter, R. J. *Foundations of Colloid Science*. Oxford; New York: Oxford University Press, **1987**.

[27] Evans, D. F.; Wennerstrom, H. In *The Colloidal Domain*, 2nd ed.; Wiley-VCH: New York, **1999**.

[28] Verwey, E. J.; Overbeek, J. T. G. *Theory of the Stability of Lyophobic Colloids*. Elsevier Publishing Company, INC. **1948**.

[29] Studart, A. R.; Amstad, E.; Gauckler, L. J. Colloidal Stabilization of Nanoparticles in Concentrated Suspensions. *Langmuir* **2007**, *23*, 1081-1090.

[30] Roucoux, A.; Schulz, J.; Patin, H. Reduced Transition Metal Colloids: A Novel Family of Reusable Catalysts? *Chem. Rev.* **2002**, *102*, 3757-3778.

[31] Alexandridis, P. Gold Nanoparticle Synthesis, Morphology Control, and Stabilization Facilitated by Functional Polymers. *Chem. Eng. Technol.* **2011**, *34*, 15-28.

[32] Ozkar, S.; Finke, R. G. Nanocluster Formation and Stabilization Fundamental Studies: Ranking Commonly Employed Anionic Stabilizers via the Development, Then Application, of Five Comparative Criteria. *J. Am. Chem. Soc.* **2002**, *124*, 5796-5810.

[33] Kalsin, A. M.; Fialkowski, M.; Paszewski, M.; Smoukov, S. K.; Bishop, K. J.; Grzybowski, B. A. Electrostatic Self-Assembly of Binary Nanoparticle Crystals with a Diamond-Like Lattice. *Science* **2006**, *312*, 420-424.

[34] Klajn, R.; Bishop, K. J.; Fialkowski, M.; Paszewski, M.; Campbell, C. J.; Gray, T. P.; Grzybowski, B. A. Plastic and Moldable Metals by Self-Assembly of Sticky Nanoparticle Aggregates. *Science* **2007**, *316*, 261-264

[35] Hierrezuelo, J.; Sadeghpour, A.; Szilagyi, I.; Vaccaro, A.; Borkovec, M. Electrostatic Stabilization of Charged Colloidal Particles with Adsorbed Polyelectrolytes of Opposite Charge. *Langmuir* **2010**, *26*, 15109-15111.

[36] Zecha, H. *Stabilization of Colloidal Dispersion by Polymer Adsorption*. Acta Polym. **1981**.

[37] Laible, R.; Hamann, K. Formation of Chemically Bound Polymer Layers on Oxide Surfaces and Their Role in Colloidal Stability. *Adv. Colloid Interface Sci.* **1980**, *13*, 65-99.

[38]   Temirov, R.; Soubatch, S.; Luican, A.; Tautz, F. S. Free-Electron-Like Dispersion in an Organic Monolayer Film on a Metal Substrate. *Nature* **2006**, *444*, 350-353

[39]   Romero-Cano, M. S.; Martin-Rodriguez, A.; De Las Nieves, F. J. Electrosteric Stabilization of Polymer Colloids with Different Functionality. *Langmuir* **2001**, *17*, 3505-3511.

[40]   Amiens, C.; De Caro, D.; Chaudret, B.; Bradley, J. S.; Mazel, R.; Roucau, C. Selective Synthesis, Characterization, and Spectroscopic Studies on a Novel Class of Reduced Platinum and Palladium Particles Stabilized by Carbonyl and Phosphine Ligands. *J. Am. Chem. Soc.* **1993**, *115*, 11638-11639.

[41]   Vidoni, O.; Philippot, K.; Amiens, C.; Chaudret, B.; Balmes, O.; Malm, J. O.; Bovin, J. O.; Senocq, F.; Casanove, M. J. Novel, Spongelike Ruthenium Particles of Controllable Size Stabilized Only by Organic Solvents. *Angew. Chem., Int. Ed.* **1999**, *38*, 3736-3738.

[42]   Jana, N. R.; Gearheart, L.; Murphy, C. J. Wet Chemical Synthesis of High Aspect Ratio Cylindrical Gold Nanorods. *J. Phys. Chem. B* **2001**, *105*, 4065-4067.

[43]   Murphy, C. J.; Jana, N. R. Controlling the Aspect Ratio of Inorganic Nanorods and Nanowires. *Adv. Mater.* **2002**, *14*, 80-82.

[44]   Murphy, C. J.; San, T. K.; Gole, A. M.; Orendorff, C. J.; Gao, J. X.; Gou, L.; Hunyadi, S. E.; Li, T. Anisotropic Metal Nanoparticles: Synthesis, Assembly, and Optical Applications. . *J. Phys. Chem. B* **2005**, *109*, 13857-13870.

[45]   Sau, T. K.; Rogach, A. L. Nonspherical Noble Metal Nanoparticles: Colloid-Chemical Synthesis and Morphology Control. *Adv. Mater.* **2010**, *22*, 1781-1804.

[46]   Sau, T. K.; Murphy, C. J. Room Temperature, High-Yield Synthesis of Multiple Shapes of Gold Nanoparticles in Aqueous Solution. *J. Am. Chem. Soc.* **2004**, *126*, 8648-8649.

[47]   Niu, W. X.; Li, Z. Y.; Shi, L. H.; Liu, X. Q.; Li, H. J.; Han, S.; Chen, J.; Xu, G. B. Seed-Mediated Growth of Nearly Monodisperse Palladium Nanocubes with Controllable Sizes. *Cryst. Growth Des.* **2008**, *8*, 4440-4444.

[48]   Liu, X.; Huang, R.; Zhu, J. Functional Faceted Silver Nano-Hexapods: Synthesis, Structure Characterizations, and Optical Properties. *Chem. Mater.* **2007**, *20*, 192-197.

[49]   Payne, E. K.; Shuford, K. L.; Park, S.; Schatz, G. C.; Mirkin, C. A. Multipole Plasmon Resonances in Gold Nanorods. *J. Phy. Chem. B* **2006**, *110*, 2150-2154.

[50]   Wirtz, M.; Martin, C. R. Template-Fabricated Gold Nanowires and Nanotubes. *Adv.*

Mater. **2003**, *15*, 455-458.

[51]   Yang, S. C.; Wang, Y. P.; Wang, Q. F.; Zhang, R. L.; Ding, B. J. UV Irradiation Induced Formation of Au Nanoparticles at Room Temperature: The Case of pH Values. *Colloids Surf A Physicochem Eng Asp.* **2007**, *301*, 174-183.

[52]   Hu, J.; Zhang, Y.; Liu, B.; Liu, J.; Zhou, H.; Xu, Y.; Jiang, Y.; Yang, Z.; Tian, Z. Q. Synthesis and Properties of Tadpole-Shaped Gold Nanoparticles. *J. Am. Chem. Soc.* **2004**, *126*, 9470-9471.

[53]   Murphy, C. J.; Sau, T. K.; Gole, A. M.; Orendorff, C. J.; Gao, J.; Gou, L.; Hunyadi, S. E.; Li, T. Anisotropic Metal Nanoparticles: Synthesis, Assembly, and Optical Applications. *J. Phys. Chem. B* **2005**, *109*, 13857-13870.

[54]   Skrabalak, S. E.; Au, L.; Li, X.; Xia, Y. Facile Synthesis of Ag Nanocubes and Au Nanocages. *Nat. Protoc.* **2007**, *2*, 2182-2190.

[55]   Link, S.; El-Sayed, M. A. Shape and Size Dependence of Radiative, Nonradiative and Photothermal Properties of Gold Nanocrystals. *Int. Reviews in Physical Chemistry* **2000**, *19*, 409-453.

[56]   Jana, N. R.; Sau, T. K.; Pal, T. Growing Small Silver Particle as Redox Catalyst. *J. Phys. Chem. B* **1999**, *103*, 115-121.

[57]   Jana, N. R.; Pal, T. Redox Catalytic Property of Still-Growing and Final Palladium Particles: A Comparative Study. *Langmuir* **1999**, *15*, 3458-3463.

[58]   Santos, C. S.; Gabriel, B.; Blanchy, M.; Menes, O.; Garcia, D.; Blanco, M.; Arconada, N.; Neto, V. Industrial Applications of Nanoparticles- A Prospective Overview. *Materials Today: Proceedings* **2015**, *2*, 456-465.

[59]   Dirix, Y.; Bastiaansen, C.; Caseri, W.; Smith, P. Hybrid Materials: Synthesis, Characterization, and Applications. *Adv. Mater.* **1999**, *11*, 223-7.

[60]   Narayanan, R.; El-Sayed, M. A. Shape-Dependent Catalytic Activity of Platinum Nanoparticles in Colloidal Solution. *Nano Lett.* **2004**, *4*, 1343-1348.

[61]   Omastova, M.; Trchova, M.; Kovarova, J.; Stejskal, J. Synthesis and Structural Study of Polypyrroles Prepared in the Presence of Surfactants. *Synth. Met.* **2003**, *138*, 447-455.

[62]   Kittel, C. *Introduction to Solid State Physics*, John Wiley & Sons, **2004**.

[63]   Hasegawa, H.; Ohno, H. Unified Disorder Induced Gap State Model for Insulator-Semiconductor and Metal-Semiconductor Interfaces. *J Vac. Sci.*

Technol. B *Nanotechnol. Microelectron.* **1986**, *4*, 1130-1138.

[64]   Suresh, S. Semiconductor Nanomaterials, Methods and Applications: A Review. *J. Nanosci. Nanotechnol.* **2013**, *3,* 62-74.

[65]   Sahu, S. N.; Nanda, K. K. Nanostructure Semiconductors: Physics and Applications. *Pinsa* **2001**, *67*, 103-130.

[66]   Rao, C. N. R.; Cheetham, A. K. Science and Technology of Nanomaterials: Current Status and Future Prospects. *J. Mater. Chem.* **2001**, *11,* 2887-2894.

[67]   Callister, J. W. D. Materials *Science and Engineering - An Introduction*. 4th Edition. John Wiley & Sons, Inc., New York, **1997**.

[68]   Hoffmann, M. R.; Martin, S. T.; Choi, W.; Bahnemann, D. W. Environmental Applications of Semiconductor Photocatalysis. *Chem. Rev.* **1995**, *95*, 69-96.

[69]   Teranishi, T.; Sakamoto, M. Charge Separation in Type-II Semiconductor Heterodimers. *J. Phys. Chem. Lett.* **2013**, *4*, 2867-2873.

[70]   Marschall, R. Semiconductor Composites: Strategies for Enhancing Charge Carrier Separation to Improve Photocatalytic Activity. *Adv. Funct. Mater.* **2014**, *24*, 2421-2440.

[71]   Kamat, P. V. Manipulation of Charge Transfer Across Semiconductor Interface. A Criterion That Cannot be Ignored in Photocatalyst Design. *J. Phys. Chem. Lett.* **2012**, *3*, 663-672.

[72]   Wang, Y.; Wang, Q.; Zhan, X.; Wang, F.; Safdar, M.; He, J. Visible Light Driven Type II Heterostructures and Their Enhanced Photocatalysis Properties: A Review. *Nanoscale* **2013**, *5*, 8326-8339.

[73]   Dalven, R. *Review of Semiconductor Physics*. Introduction to Applied Solid State Physics. Springer, Boston, MA, **1980**.

[74]   Sharma, A.; Sharma, A.; Sharma, R. Semiconductor Nanoparticles in Photocatalysis: Emerging Art and Perspectives. *Nanotechnology* **2012**, *2*, 73-76.

[75]   Zhou, Z. Y.; Tian, N.; Li, J. T.; Broadwell, I.; Sun, S. G. Nanomaterials of High Surface Energy with Exceptional Properties in Catalysis and Energy Storage. *Chem. Soc. Rev.* **2011**, *40*, 4167-4185.

[76]   Kamat, P. V. Meeting the Clean Energy Demand: Nanostructure Architectures for Solar Energy Conversion. *J. Phys. Chem. C* **2007**, *111*, 2834-2860.

[77]   Walkey, C.; Sykes, E. A.; Chan, W. C. W. Application of Semiconductor and Metal

Nanostructures in Biology and Medicine. *Hematology Am Soc Hematol Educ Program* **2009**, *1*, 701-707.

[78]   Alivisatos, A. P. Semiconductor Clusters, Nanocrystals, and Quantum Dots. *Science* **1996**, *271*, 933-937.

[79]   Burda, C.; Chen, X.; Narayanan, R.; El-Sayed, M. A. Chemistry and Properties of Nanocrystals of Different Shapes. *Chem. Rev.* **2005**, *105*, 1025-1102.

[80]   Smith, J. K. *Encyclopedia of Catalysis*. John Wiley & Sons, Inc., **2010**.

[81]   Lindstrom, B.; Pettersson, L. J. A Brief History of Catalysis. *Cattech* **2003**, *7*, 130-138.

[82]   Moulijn, J. A.; Leeuwen, P. W. N. M. van; Santen, R. A. van In Studies in Surface Science and Catalysis, History of Catalysis, *Elsevier*, **1993**, *79*, 3-21.

[83]   Farrauto, R. J.; Bartholomew, C. H. *Fundamentals of Industrial Catalytic Processes*. Blackie Academic & Professional, **1997**.

[84]   Meryem, S. S.; Nasreen, S.; Siddique, M.; Khan, R. An Overview of the Reaction Conditions for an Efficient Photoconversion of CO_2. *Rev Chem Eng* **2017**.

[85]   Thomas, J. M.; Thomas, W. J. *Principles and Practice of Heterogeneous Catalysis*. Weinheim, VCH, **1997**.

[86]   Teh, C. M.; Mohamed, A. R. Roles of Titanium Dioxide and Ion-Doped Titanium Dioxide on Photocatalytic Degradation of Organic Pollutants (Phenolic Compounds and Dyes) in Aqueous Solutions: A Review. *J. Alloys Compd.* **2011**, *509*, 1648-1660.

[87]   Zollinger, H. *Color Chemistry: Syntheses, Properties and Applications of Organic Dyes and Pigments*. Wiley-VCH: Weinheim, Germany, **1991**.

[88]   Kalogirou, S. A. Seawater Desalination Using Renewable Energy Sources. *Prog. Energy Combust. Sci.* **2005**, *31*, 242-281.

[89]   Mohan, D.; Pittman, C. U. Jr. Arsenic Removal From Water/Wastewater Using Adsorbents-A Critical Review. *J. Hazard. Mater.* **2007**, *142*, 1-53.

[90]   Wang, C.; Zhang, J.; Wang, P.; Wang, H.; Yan, H. Adsorption of Methylene Blue and Methyl Violet by Camellia Seed Powder: Kinetic and Thermodynamic Studies. *Desalin. Water Treat.* **2015**, *53*, 3681-3690.

[91]   Vrijheid, M.; Casas, M.; Gascon, M.; Valvi, D.; Nieuwenhuijsen, M. Environmental Pollutants and Child Health- A Review of Recent Concerns. *Int J Hyg Environ Health* **2016**, *219*, 331-342.

[92] Wang, C. C.; Li, J. R.; Lv, X. L.; Zhang, Y. Q.; Guo, G. Photocatalytic Organic Pollutants Degradation in Metal-Organic Frameworks. *Energy Environ. Sci.* **2014**, *7*, 2831-2867.

[93] Litter, M. I. Heterogeneous Photocatalysis: Transition Metal Ions in Photocatalytic Systems. *Appl. Catal. B-Environ.* **1999**, *23*, 89-114.

[94] Li, G. Z.; Yu, M.; Wang, Z. L.; Lin, J.; Wang, R. S.; Fang, J. Sol-Gel Fabrication and Photoluminescence Properties of SiO_2@ Gd_2O_3: Eu^{3+} Core-Shell Particles. *J. Nanosci. Nanotechno.* **2006**, *6*, 1416-1422.

[95] Miyauchi, M.; Nukui, Y.; Atarashi, D.; Sakai, E. Selective Growth of *n*-Type Nanoparticles on *p*-Type Semiconductors for Z-Scheme Photocatalysis. *ACS Appl. Mater. Interfaces* **2013**, *5*, 9770-9776.

[96] Chong, M. N.; Jin, B.; Chow, C. W.; Saint, C. Recent Developments in Photocatalytic Water Treatment Technology: A Review. *Water Res.* **2010**, *44*, 2997-3027.

[97] Nakata, K.; Fujishima, A. TiO_2 Photocatalysis: Design and Applications. *J. Photoch. Photobio. C.* **2012**, *13*, 169-189.

[98] Thompson, T. L.; Yates, J. T. Surface Science Studies of the Photoactivation of TiO_2 New Photochemical Processes. *Chem. Rev.* **2006**, *106*, 4428-4453.

[99] Mills, A.; Le Hunte, S. An Overview of Semiconductor Photocatalysis. *J. Photoch. Photobio. A* **1997**, *108*, 1-35.

[100] Ayoub, K.; Van Hullebusch, E. D.; Cassir, M.; Bermond, A. Application of Advanced Oxidation Processes for TNT Removal: A Review *J. Hazard. Mater.* **2010**, *178*, 10-28.

[101] Akpan, U. G.; Hameed, B. H. Parameters Affecting the Photocatalytic Degradation of Dyes Using TiO_2-Based Photocatalysts: A Review. *J. Hazard. Mater.* **2009**, *170*, 520-529.

[102] Opoku, F.; Govender, K. K.; Sittert, C. G. C. E. V.; Govender. P. P. Recent Progress in the Development of Semiconductor Based Photocatalyst Materials for Applications in Photocatalytic Water Splitting and Degradation of Pollutants. *Adv. Sustainable Syst.* **2017**, 1700006.

[103] Rajeshwara, K.; Osugi, M. E.; Chanmanee, W.; Chenthamarakshan, C. R.; Zanoni, M. V. B.; Kajitvichyanukul, P.; Ayer, R. K. Heterogeneous Photocatalytic Treatment of Organic Dyes in Air and Aqueous Media. *J. Photochem. Photobiol. C* **2008**, *9*, 171-192.

[104] Houas, A.; Lachheb, H.; Ksibi, M.; Elaloui, E.; Guillard, C.; Herrmann, J. M. Photocatalytic Degradation Pathway of Methylene Blue in Water. *Appl. Catal. B* **2001**, *31*, 145-157.

[105] Robinson, T.; McMullan, G.; Marchant, R. P. N., Remediation of Dyes in Textile Effluent: A Critical Review on Current Treatment Technologies with A Proposed Alternative. *Bioresour. Technol.* **2001**, *77*, 247-255.

[106] Prevot, A. B.; Baiocchi, C.; Brussino, M. C.; Pramauro, E.; Savarino, P.; Augugliaro, V.; Marci, G.; Palmisano, L. Photocatalytic Degradation of Acid Blue 80 in Aqueous Solutions Containing TiO_2 Suspensions. *Environ. Sci. Technol.* **2001**, 35, 971-976.

[107] Tran, P. D., Wong, L. H., Barber, J.; Loo, J. S. Recent Advances in Hybrid Photocatalysts for Solar Fuel Production *Energy Environ. Sci.* **2012**, *5*, 5902-5918.

[108] Beydoun, D.; Amal, R.; Low, G.; McEvoy, S. Role of Nanoparticles in Photocatalysis. *J. Nanopart. Res* **1999**, *1*, 439-458.

[109] Markham, M. C. Photocatalytic Properties of Oxides *J. Chem. Educ.***1955**, *32*, 540-543.

[110] Reiss, P.; Protiere, M.; Li, L. Core/Shell Semiconductor Nanocrystals. *Small* **2009**, *5*, 154-168.

[111] Xu, F.; Zhang, P., Navrotsky, A. Hierarchically Assembled Porous ZnO Nanoparticles: Synthesis, Surface Energy, and Photocatalytic Activity. *Chem. Mater.* **2007**, *19*, 5680-5686.

[112] Serpone, N.; Emeline, A. V. Semiconductor Photocatalysis-Past, Present, and Future Outlook. *J. Phys. Chem. Lett.* **2012**, *3*, 673-677.

[113] Kubacka, A.; Fernandez-Garcia, M.; Colon, G. Advanced Anoarchitectures for Solar Photocatalytic Applications. *Chem. Rev.* **2012**, *112*, 1555-1614.

[114] Batzill, M. Fundamental Aspects of Surface Engineering of Transition Metal Oxide Photocatalysts. *Energy Environ. Sci.* **2011**, *4*, 3275-3286.

[115] Ajmal, A.; Majeed, I.; Malik, R. N.; Idriss, H.; Nadeem, M. A. Principles and Mechanisms of Photocatalytic Dye Degradation on TiO_2 based Photocatalysts: A Comparative Overview. *RSC Adv.* **2014**, *4*, 37003-37026.

[116] Natarajan, K.; Natarajan, T. S.; Kureshy, R. I.; Bajaj, H. C.; Jo, W. K.; Tayade, R. J. Photocatalytic H_2 Production using Semiconductor Nanomaterials via Water Splitting-An Overview. *Adv. Mater. Res.* **2015**, *1116*, 130-156.

[117] Fresno, F.; Portela, R.; Suarez, S.; Coronado, J. M. Photocatalytic Materials: Recent Achievements and Near Future Trends. *J. Mater. Chem. A* **2014**, *2*, 2863-2884.

[118] Zhang, X.; Qin, J.; Xue, Y.; Yu, P.; Zhang, B.; Wang, L.; Liu, R. Effect of Aspect Ratio and Surface Defects on the Photocatalytic Activity of ZnO Nanorods. *Sci. Rep.* **2014**, *4*, 4596.

[119] Jassby, D.; Budarz, J. F.; Wiesner, M. Impact of Aggregate Size and Structure on the Photocatalytic Properties of TiO$_2$ and ZnO Nanoparticles. *Environ. Sci. Technol.* **2012**, *46*, 6934-6941.

[120] Kong, M.; Li, Y.; Chen, X.; Tian, T.; Fang, P.; Zheng, F.; Zhao, X. Tuning the Relative Concentration Ratio of Bulk Defects to Surface Defects in TiO$_2$ Nanocrystals Leads to High Photocatalytic Efficiency. *J. Am. Chem. Soc.* **2011**, *133*, 16414-16417.

[121] Zhao, D.; Chen, C.; Wang, Y.; Ji, H.; Ma, W.; Zang, L.; Zhao, J. Surface Modification of TiO$_2$ by Phosphate: Effect on Photocatalytic Activity and Mechanism Implication. *J. Phys. Chem. C* **2008**, *112*, 5993-6001.

[122] Prasanna V. L.; Rajagopalan, V. A New Synergetic Nanocomposite for Dye Degradation in Dark and Light. *Sci. Rep.* **2016**, *6*, 38606-10.

[123] Rochkind, M.; Pasternak, S.; Paz, Y. Using Dyes for Evaluating Photocatalytic Properties: A Critical Review. *Molecules* **2015**, *20*, 88-110.

[124] Vinodgopal, K.; Bedja, I.; Hotchandani, S.; Kamat, P. V. A Photocatalytic Approach for the Reductive Decolorization of Textile Azo Dyes in Colloidal Semiconductor Suspensions. *Langmuir* **1994**, *10*, 1767-1771.

[125] Wang, P.; Huang, B.; Daia, Y.; Whangbo, M. Plasmonic Photocatalysts: Harvesting Visible Light with Noble Metal Nanoparticles. *Phys. Chem. Chem. Phys.* **2012**, *14*, 9813-9825.

[126] Teoh, W. Y.; Scott, J. A.; Amal, R. Progress in Heterogeneous Photocatalysis: From Classical Radical Chemistry to Engineering Nanomaterials and Solar Reactors. *J. Phys. Chem. Lett.* **2012**, *3*, 629-639.

[127] Takai, A.; Kamat, P. V. Capture, Store, and Discharge, Shuttling Photogenerated Electrons across TiO$_2$-Silver Interface. *ACS Nano* **2011**, *5*, 7369-7376.

[128] Chen, Y.; Zhang, C.; Zhang, X.; Ou, X.; Zhang, X. One-step Growth of Organic Single-Crystal p-n Nano-heterojunctions with Enhanced Visible-light Photocatalytic Activity.

Chem. Commum. **2013**, *49*, 9200-9202.

[129] Liu, H. R.; Shao, G. X.; Zhao, J. F.; Zhang, Z. X.; Zhang, Y.; Liang, J.; Liu, X. G.; Jia, H. S.; Xu, B. S. Worm-Like Ag/ZnO Core-Shell Heterostructural Composites: Fabrication, Characterization, and Photocatalysis. *J. Phys. Chem. C* **2012**, *116*, 16182-16190.

[130] Chiou, J. W.; Ray, S. C.; Tsai, H. M.; Pao, C. W.; Chien, F. Z.; Pong, W. F.; Tseng, C. H.; Wu, J. J.; Tsai, M. H.; Chen, C. H.; Lin, H. J.; Lee, J. F.; Guo, J. H. Correlation between Electronic Structures and Photocatalytic Activities of Nanocrystalline- (Au, Ag, and Pt) Particles on the Surface of ZnO Nanorods. *J. Phys. Chem. C* **2011**, *115*, 2650-2655.

[131] Xue, X.; Chen, Z.; Xing, L.; Ma, C.; Chen, Y.; Wang, T. Enhanced Optical and Sensing Properties of One-Step Synthesized Pt-ZnO Nanoflowers. *J. Phys. Chem. C* **2010**, *114*, 18607-18611.

[132] Zheng, Y.; Zheng, L.; Zhan, Y.; Lin, X.; Zheng, Q.; Wei, K. Ag/ZnO Heterostructure Nanocrystals: Synthesis, Characterization, and Photocatalysis. *Inorg. Chem.* **2007**, *46*, 6980-6986.

[133] Zheng, Y.; Chen, C.; Zhan, Y.; Lin, X.; Zheng, Q.; Wei, K.; Zhu, J. Photocatalytic Activity of Ag/ZnO Heterostructure Nanocatalyst: Correlation between Structure and Property. *J. Phys. Chem. C* **2008**, *11*, 10773-10777.

[134] Lin, D.; Wu, H.; Zhang, R.; Pan, W. Enhanced Photocatalysis of Electrospun Ag-ZnO Heterostructured Nanofibers. *Chem. Mater.* **2009**, *21*, 3479-3484.

[135] Chang, Y.; Xu, J.; Zhang, Y.; Ma, S.; Xin, L.; Zhu, L.; Xu, C. Optical Properties and Photocatalytic Performances of Pd Modified ZnO Samples. *J. Phys. Chem. C* **2009**, *113*, 18761-18767.

[136] Geng, J.; Song, G. H.; Jia, X. D.; Cheng, F.; Zhu, J. Fast One-Step Synthesis of Biocompatible ZnO/Au Nanocomposites with Hollow Doughnut-Like and Other Controlled Morphologies. *J. Phys. Chem. C* **2012**, *116*, 4517-4525.

[137] Vinodgopal, K.; Kamat, P. V. Enhanced Rates of Photocatalytic Degradation of an Azo Dye Using SnO_2/TiO_2 Coupled Semiconductor Thin Films. *Environ. Sci. Technol.* **1995**, *29*, 841-845.

[138] Lin, C.-F.; Wu, C.-H.; Onn, Z.-N. Degradation of 4-chlorophenol in TiO_2, WO_3, SnO_2, TiO_2/WO_3 and TiO_2/SnO_2 Systems. *J. Hazard. Mater.* **2008**, *154*, 1033-1039.

[139] Ge, M.; Guo, C.; Zhu, X.; Ma, L.; Han, Z.; Hu, W.; Wang, Y. Photocatalytic Degradation

of Methyl Orange Using ZnO/TiO$_2$ Composites. *Front. Environ. Sci. En.* **2009**, *3*, 271-280.

[140] Daskalaki, V. M.; Antoniadou, M.; Puma, G. L.; Kondarides, D. I.; Lianos, P. Solar Light-Responsive Pt/CdS/TiO$_2$ Photocatalysts for Hydrogen Production and Simultaneous Degradation of Inorganic or Organic Sacrificial Agents in Wastewater. *Environ. Sci. Technol.* **2010**, *44*, 7200-7205.

[141] Shuai, X. M.; Shen, W. Z. A Facile Chemical Conversion Synthesis of ZnO/ZnS Core/Shell Nanorods and Diverse Metal Sulfide Nanotubes. *J. Phys. Chem. C* **2011**, *115*, 6415-6422.

[142] Lin, D.; Wu, H.; Zhang, R.; Zhang, W.; Pan, W. Facile Synthesis of Heterostructured ZnO-ZnS Nanocables and Enhanced Photocatalytic Activity. *J. Am. Ceram. Soc.* **2010**, *93*, 3384-3389.

[143] Dapeng, W.; Yi, J.; Yafei, Y.; Junshu, W.; Kai J. ZnO-ZnS Heterostructures with Enhanced Optical and Photocatalytic Properties. *J. Nanopart. Res* **2011**, *13*, 2875-2886.

[144] Chen, W.; Ruan, H.; Hu, Y.; Li, D.; Chen, Z.; Xian, J.; Chen, J.; Fu, X.; Shao, Y.; Zheng, Y. One-step preparation of Hollow ZnO$_{core}$/ZnS$_{shell}$ Structures with Enhanced Photocatalytic Properties. *CrystEngComm* **2012**, *14*, 6295-6305.

[145] Lee, M.; Yong, K. Highly Efficient Visible Light Photocatalysis of Novel CuS/ZnO Heterostructure Nanowire Arrays. *Nanotechnology* **2012**, *23*, 194014-194020.

[146] Zhang, J.; Yu, J.; Zhang, Y.; Li, Q.; Gong, J. R. Visible Light Photocatalytic H$_2$-Production Activity of CuS/ZnS Porous Nanosheets Based on Photo Induced Interfacial Charge Transfer. *Nano Letters.* **2011**, *11*, 4774-4779.

[147] Serpone, N. Maruthamuthu, P.; Pichat, P.; Pelizzetti, E.; Hidaka, H. Exploiting the Interparticle Electron Transfer Process in the Photocatalysed Oxidation of Phenol, 2-Chlorophenol and Pentachlorophenol: Chemical Evidence for Electron and Hole Transfer between Coupled Semiconductors. *J. Photochem. Photobiol. A* **1995**, *85*, 247-255.

[148] Serpone, N.; Emeline, A. V.; Horikoshi, S.; Kuznetsovb, V. N.; Ryabchuk, V. K. On the Genesis of Heterogeneous Photocatalysis: A Brief Historical Perspective in the Period 1910 to the mid-1980s. *Photochem. Photobiol. Sci* **2012**, *11*, 1121-1150.

[149] Benxia, L.; Yenfen, W. Synthesis, Microstructure, and Photocatalysis of ZnO/CdS Nano-Heterostructure. *J. Phys. Chem. Solids* **2011**, *72*, 1165-1169.

[150] Yu, J.; Zhang J.; Liu, S. Ion-Exchange Synthesis and Enhanced Visible-Light Photoactivity of CuS/ZnS Nanocomposite Hollow Spheres. *J. Phys. Chem. C* **2010**, *114*, 13642-13649.

[151] Basu, M.; Garg, N.; Ganguli, A. K. A Type-II Semiconductor (ZnO/CuS Heterostructure) for Visible Light Photocatalysis. *J. Mater. Chem. A* **2014**, 2, 7517-7525.

[152] Shkrob, I. A.; Sauer, M. C. Hole Scavenging and Photo-Stimulated Recombination of Electron-Hole Pairs in Aqueous TiO_2 Nanoparticles. *J. Phys. Chem. B* **2004**, *108*, 12497-12511.

[153] Macdonald, I. R.; Rhydderch, S.; Holt, E.; Grant, N.; Storey, John. M. D.; Howe, R. F. EPR Studies of Electron and Hole Trapping in Titania Photocatalysts. *Catal. Today* **2012**, *182*, 39-45.

[154] Djellabi, R.; Ghorab, M. F. Photoreduction of Toxic Chromium using TiO_2-Immobilized Under Natural Sunlight: Effects of Some Hole Scavengers and Process Parameters. *Desalin Water Treat* **2014**, *55*, 1-8.

[155] Liu, T.; Wang, L.; Lu, X.; Fan, Cai, J. X.; Gao, B.; Miao, R.; Wang, J.; Lv, Y. Comparative Study of the Photocatalytic Performance for the Degradation of Different Dyes by $ZnIn_2S_4$: Adsorption, Active Species, and Pathways. *RSC Adv.* **2017**, *7*, 12292-12300.

[156] Moriartya, P.; Honnery, D. Intermittent Renewable Energy: The Only Future Source of Hydrogen? *Int. J. Hydrog. Energy.* **2007**, 32, 1616-1624.

[157] Marban, G.; Valdes-Solis, T. Towards the Hydrogen Economy? *Int. J. Hydrog. Energy.* **2007**, *32*, 1625-1637.

[158] Chu, S.; Majumdar, A. Opportunities and Challenges for A Sustainable Energy Future. *Nature* **2012**, *488*, 294-303.

[159] Lubitz, W. Hydrogen: An Overview. *Chem. Rev.* **2007**, *107*, 3900-3903.

[160] Yang, Z.; Zhang, J.; Kintner-Meyer, M. C. W.; Lu, X; Choi, D.; Lemmon, J. P.; Liu, J. Electrochemical Energy Storage for Green Grid. *Chem. Rev.* **2011**, *111*, 3577-3613.

[161] Roger, I.; Shipman, M. A.; Symes, M. D. Earth-Abundant Catalysts for Electrochemical and Photoelectrochemical Water Splitting. *Nat. Rev. Chem.* **2017**, *1*, 0003.

[162] Li, X.; Hao, X.; Abudula A.; Guan G. Nanostructured Catalysts for Electrochemical Water Splitting: Current State and Prospects. *J. Mater. Chem. A* **2016**, *4*, 11973-12000.

[163] Fujishima, A; Honda, K. Electrochemical Photolysis of Water at A Semiconductor Electrode. *Nature* **1972**, *238*, 37-8.

[164] Bard, A. J. Design of Semiconductor Photoelectrochemical Systems for Solar Energy Conversion. *J. Phys. Chem.* **1982**, *86*, 172-177.

[165] Anantharaj, S.; Ede, S. R.; Sakthikumar, K.; Karthick, K.; Mishra, S.; Kundu, S. Recent Trends and Perspectives in Electrochemical Water Splitting with an Emphasis on Sulfide, Selenide, and Phosphide Catalysts of Fe, Co, and Ni: A Review. *ACS Catal.* **2016**, *6*, 8069-8097.

[166] Chen, C.-J.; Chen, P.-T.; Basu, M.; Yang, K.-C.; Lu, Y.-R.; Dong, C.-L.; Ma, C.-G.; Shen, C.-C.; Hu, S.-F.; Liu, R.-S. An Integrated Cobalt Disulfide (CoS_2) Co-Catalyst Passivation Layer on Silicon Microwires for Photoelectrochemical Hydrogen Evolution. *J. Mater. Chem. A* **2015**, *3*, 23466-23476.

[167] McEnaney, J. M.; Soucy, T. L.; Hodges, J. M.; Callejas, J. F.; Mondschein, J. S.; Schaak, R. E. Colloidally-Synthesized Cobalt Molybdenum Nanoparticles as Active and Stable Electrocatalysts for the Hydrogen Evolution Reaction Under Alkaline Conditions. *J. Mater. Chem. A* **2016**, *4*, 3077-3081.

[168] Jin, Z.; Li, P.; Huang, X.; Zeng, G.; Jin, Y.; Zheng, B.; Xiao, D. Three-Dimensional Amorphous Tungsten-Doped Nickel Phosphide Microsphere as an Efficient Electrocatalyst for Hydrogen Evolution. *J. Mater. Chem. A* **2014**, *2*, 18593-18599.

Chapter 2

Materials, Methods and Instrumentation

✿ *It contains the details of chemical used for the synthesis, calculation methods and instruments used for all the experiments included in thesis.*

This chapter deals with the materials, methodologies used for the synthesis of all the semiconducting metal oxide, metal sulfide and other nanomaterials in pure and modified state and their characterization techniques. The various techniques employed for the characterization of nanomaterials including UV-visible spectroscopy (UV-vis), Powder X-ray diffraction (PXRD), X-ray photoelectron spectroscopy (XPS), Scanning electron microscopy (SEM), transmission electron microscopy (TEM), Photoluminescence spectroscopy (PL), Fourier transform infrared (FTIR) spectroscopy, and catalytic studies performed with the help of UV-vis and CH potentiostat.

2.1 Used Reagents

Table 2.1 List of the chemicals used in this study along with the name of their suppliers

S. No.	Chemicals	Name of Supplier
1	Hydrogen tetrachloroaurate trihydrate ($HAuCl_4 \cdot 3H_2O$)	Sigma-Aldrich, India
2	Silver nitrate ($AgNO_3 \geq 99.9\%$)	Sigma-Aldrich, India
3	Potassium tetrachloropalladate (II) (K_2PdCl_4)	Sigma-Aldrich, India
4	4-aminophenol ($H_2NC_6H_4OH$)	Sigma-Aldrich, India
5	Ammonium molybdate tetrahydrate [$(NH_4)_6Mo_7O_{24} \cdot 4H_2O$]	Sigma-Aldrich, India
6	Nafion	Sigma-Aldrich, India
7	Isopropanol (C_3H_8O)	Sigma-Aldrich, India
8	Mesoporous carbon powder	Sigma-Aldrich, India
9	Zinc sulphate ($ZnSO_4 \cdot 7H_2O$)	SD fine, India
10	Urea Extrapure (NH_2CONH_2)	SD fine, India
11	Hydrazine hydrate ($NH_2 \cdot NH_2 \cdot H_2O$)	SD fine, India
12	Zinc nitrate hexahydrate [$Zn(NO_3)_2 \cdot 6H_2O$]	SD fine, India
13	4-Nitrophenol ($C_6H_5NO_3$)	SD fine, India
14	Sodium borohydride ($NaBH_4$)	SD fine, India
15	Barium sulphate ($BaSO_4$)	SD fine, India
16	Potassium Bromide (KBr)	SD fine, India

17	Sulphuric acid (H_2SO_4)	SD fine, India
18	Ammonia solution with sp. gr. 0.91	SD fine, India
19	Phenol	SD fine, India
20	Ammonium oxalate ($C_2H_8N_2O_4$)	SD fine, India
21	Tertiary butyl alcohol ($C_4H_{10}O$)	SD fine, India
22	Cetyltrimethylammoniumbromide (CTAB, $C_{19}H_{42}BrN$)	Spectrochem
23	Nitric acid (HNO_3)	Spectrochem
24	Ethanol	Spectrochem
25	Trisodium citrate ($Na_3C_6H_5O_7$)	SRL, India
26	Ascorbic acid ($C_6H_8O_6$)	SRL, India
27	Thiourea (NH_2CSNH_2)	Merck, India
28	Hexamethylenetetramine (HMT, $C_6H_{12}N_4$)	Alfa aesar, USA
29	Fullerene carbon nanotube multiwalled	Alfa aesar, USA
30	Sodium sulfide (Na_2S)	Alfa aesar, USA
31	Methylene blue	Alfa aesar, USA
32	Malachite green	Alfa aesar, USA
33	Rhodamine B	Alfa aesar, USA

2.2 Methods

2.2.1 Calculation of Band Gap

The band gap generally refers to the energy difference (in electron volts) between the top of the valence band and the bottom of the conduction band in semiconductors. To calculate the band gap of the sample, UV-vis absorption spectra have been recorded first. In crystalline semiconductors, the following equation has been used to relate the absorption coefficient to incident photon energy [1-3].

$$\alpha(v)hv = B(hv - E_g)^{1/2}$$

where α = absorption coefficient, E_g = optical gap, B = constant that depends on the transition probability, h is the Plank constant and v is the frequency.

Known function:

$$hv = h\frac{c}{\lambda} = \frac{1240}{\lambda}$$

$$(\alpha\frac{1240}{\lambda})^2 = B(\frac{1240}{\lambda} - E_g)$$

$$\alpha E_p = B(E_p - E_g)^{1/2}$$

A classical Tauc approach is further employed to estimate the E_g value of semiconductor using a plot of $(\alpha E_p)^2$ vs. E_p [1-2]. The extrapolated straight line of this plot meets the E_p axis at $\alpha = 0$ which represents the absorption edge energy corresponds to the band gap (E_g) of the material. It should already be noted that the Tauc plot is not characterized by a unique slope and hence the determined value of optical band gap E_g strongly depends on the choice of the linear region.

2.2.2 Photocatalysis Methods and Calculations

To assess the photocatalytic performance of the as-prepared catalysts, various pollutants were degraded under irradiation of visible and UV-light. The certain concentration of dye and catalyst were added in a fixed volume of water and dispersed. Prior to photo-irradiation to establish the adsorption-desorption equilibrium between dye and catalyst, the reaction mixture was kept in dark for 30 min. Afterward, the light was illuminated to perform the photocatalysis. The reaction mixture was magnetically stirred throughout the experiment. At the given irradiation time, 3.0 mL sample was collected and centrifuged to remove the catalyst. The degradation efficiency of dye was recorded on a UV-visible spectrophotometer.

% Dye degradation was calculated from the equation given below:

$$X\% = (A_0\text{-}A_t)/A_0 \times 100$$

Where A_0 = Peak intensity at '0' time and A_t = peak intensity at time 't'.

The value of rate constant has been calculated from the slopes of the exponential plot (A_0/A_t) vs. t and linear curve ln (A_0/A_t) vs. t. The order of the reaction was pseudo first order in all the cases.

2.3 Sample Preparations for Analysis

2.3.1 Sample Preparation for TEM

The samples were prepared onto 400-mesh carbon-coated copper grids by placing 3-4 drops of a freshly prepared aqueous dilute solution of the sample and the grids were dried for overnight. Solid powder samples were dispersed in water and liquid samples were used directly on the grid.

2.3.2 Sample Preparation for XPS

XPS samples were prepared by dropping 10.0 µL of the aqueous solution sample onto a small piece of Si wafer and carbon tape and dried under dry nitrogen line. To compensate for any kind of charging effect, the binding energy of C 1s peak at 284.5 eV has been used as a reference.

2.3.3 Preparation of Working Electrode for Electrocatalysis

Three electrode system, Glassy carbon electrode (GCE), Pt-wire and Ag/AgCl as a working electrode, counter electrode, and reference electrode, respectively, were used. In order to prepare a working electrode, the as-synthesized materials were coated with an ink which was drop-casted onto the electrode. Typically, the ink was prepared as follows. 5 mg sample was dispersed in 300 µL of iso-propyl alcohol and 30 µL of Nafion (adhesive). Then, the mixture was sonicated for 10 min in order to obtain a homogeneous suspension. Finally, 5.0 µL of the homogeneous mixture of ink was dropped onto GCE and allowed to dry.

2.4 Electrochemical Analysis and Calculations

2.4.1 Voltammetry

Voltammetry is an electroanalytical technique in which the current through a cell is measured while varying the potential supply. It is usually done in a 3-electrode system comprising of a working electrode, a counter electrode, and a reference electrode. The working electrode is the one on which the reaction occurs. The counter or auxiliary electrode simply serves to complete the analogous circuit, i.e., should the working electrode behave as a cathode, the counter behaves as an anode and vice versa. The reference electrode, on the other hand, is an

electrode which has a known stable electrical potential. The potential of the working electrode is measured against the potential of the reference electrode. The voltammetry technique used in this study is Linear Sweep Voltammetry (LSV). In LSV, the voltage is varied linearly across the range we desire. Once the voltage reaches the end point, the voltage supply is cut. The results of interest from this study are the response and the onset potential.

2.4.2 Tafel Slope

The Tafel plot of an electrocatalytic process is obtained by the polarization curve as a plot of log (j) vs. η. The slope of the linear portion of the Tafel plot is defined as the dependence between the *iR*-compensated overpotential and the current density, which is expressed as below [4,5]:

$$\frac{d \log(j)}{d\eta} = 2.303RT/\alpha nF$$

α = charge transfer coefficient, η = Overpotential R = ideal gas constant, T = temperature, F = Faraday constant, n = number of electrons transferred, which is equal to 4 for the OER and 2 for the HER.

2.4.3 Mass and Specific Activities

The mass and specific activities of an electrocatalyst are two other quantitative parameters used to define the catalytic activity of an electrocatalyst. The current normalized by the catalyst loading is the mass activity, which is expressed in amperes per gram (A/g). On the other hand, the current normalized by the electrochemical active surface area (ECSA) or the Brunauer-Emmett-Teller (BET) surface area is the specific activity [4, 5].

$$\text{Mass Activity} = \frac{\text{observed current density at fixed potential}}{\text{catalyst loading}}$$

$$\text{Specific Activity} = \frac{\text{observed current at fixed potential}}{\text{electrochemically active surface area}}$$

2.5 Instrumentation

2.5.1 List of Instruments

1. 1 cm quartz cuvettes (ERMA, 1 cm light path, capacity of 3.5 ml, Model: MCQ-4/104).

2. Magnetic stirrer: IKA RCT basic

3. Balance: Denver Instrument, Japan.

4. Water bath, S. N. Scientific company.

5. Teflon lined autoclave, Aamer equipment.

6. UV-visible Spectrophotometer: UV-vis absorption spectra for liquid samples were obtained using a Shimadzu (UV-1800) and Jasco V-650 spectrophotometer (model no. UV-1800).

7. Ultra violate-visible diffuse reflection spectra for solid samples were recorded on a Shimadzu Spectrophotometer (model no. UV-2450).

8. Powder X-ray diffraction (PXRD) using a Rigaku Mini Flex II diffractometer and X'Pert PRO diffractometer with Cu-Kα radiation at 25 °C.

9. For XPS measurements a commercial Omicron EA 125 spectrometer equipped with a seven-channel detection system was used. As an X-ray source, a monochromatic light of Al-Kα radiation of energy 1486.7 eV has been used. All high-resolution spectra were collected with an energy step of 0.1 eV, pass energy of 20 eV and a dwell time of 1sec per step. The emission current was set to 15 mA for all measurements. The XPS chamber base pressure was maintained below $< 3 \times 10^{-10}$ mbar during the measurement.

10. FESEM analysis was also carried out using Nova NanoSem 450 operated from 0.5 kV to 30 kV. EDS measurements were performed using Bruker XFlash 6130, attached with FESEM instrument. All the as-synthesized samples were analyzed after coating with platinum metal.

11. TEM micrographs were obtained using a JEOL-2010F TEM instrument operating with an electron beam of energy of 200 kV. EDS measurement was carried out with the same instrument and in a particular area of the samples. Transmission electron microscopy imaging was also carried out on a Bruker microscope operated at 200 kV.

12. Room temperature Fourier transform infrared spectra of the powder samples (pellets in KBr, without moisture) were measured by using a Perkin Elmer 2000 infrared spectrometer in the range of 500-4000 cm^{-1}.

13. Raman analysis was carried out using an Airix (STR 500) instrument.

14. Room temperature Photoluminescence measurements were performed using a Horiba Jobin Yvon Fluoromax-4 spectrofluorimeter.

15. To determine the surface area of solid nanomaterials, N_2 adsorption-desorption isotherms were measured with Autosorb iQ Station 1 (Quantachrome Instruments, version 3.01) at a bath temperature of 77.35 K.

16. Zeta potential analysis was performed using a Zeta Sizer model Nano ZS (ZEN 3600, 102 Malvern Instruments, UK).

17. The mass spectroscopy analysis was recorded using mass tynx 4.0 software with Acuity UPLC class instrument purchased from Waters Company.

18. All the electrochemical data was recorded in CH Instrument (CHI 604E) at 25°C.

The details of the characterization techniques are as follows:

2.5.2 UV-visible Spectrophotometer

Absorption spectroscopy is the most widely used spectroscopic tools which provide useful information about the sample under studied. It measures the absorption of radiation, as a function of frequency or wavelength, due to its interaction with a sample. The environmental effects alter the relative energy of ground and excited states, and this alteration causes spectral shifts. The absorbance (A) of an absorber (concentration, C) having a molar extinction coefficient ε_λ at wavelength λ is given by the equation.

$$A = \log (I_o/I_t) = \varepsilon_\lambda\, Cl$$

where A is absorbance (optical density), I_0 and I_t represent the intensity of the incident and transmitted light, respectively, C is the concentration of the light absorbing species and '*l*' is the path length of the light absorbing medium [6,7].

2.5.3 Powder X-ray Diffraction

Powder XRD is a scientific technique which uses X-ray on powder or microcrystalline samples for crystallinity and particle size elucidation of the nanomaterials. Crystals contain atoms arranged in specific patterns and planes all while separated by specific distances. These distances are so small that they are capable of scattering electromagnetic radiations. Cathode ray tube acts as the source of the X-ray, and before directed towards the sample, these rays are filtered to produce monochromatic radiation, collimated to concentrate.

The atomic planes of a crystal cause an incident beam of X-rays to interfere with one another as they leave the crystal. If an incident X-ray beam encounters a crystal lattice, general scattering occurs. Although most scattering interferes with itself and is eliminated, diffraction occurs when scattering in a certain direction is in phase with scattered rays from other atomic planes. Under this condition the reflections combine to form newly enhanced wavefronts that mutually reinforce each other. Crystal diffracts X-rays in a unique characteristic pattern because each crystalline material has a characteristic atomic structure. For a given set of lattice planes with an inter-plane distance of d, the condition for a diffraction to occur can be simply written as Bragg's equation [8]:

$$2d_{hkl} \sin \theta = n\lambda$$

where λ is the wavelength of the X-ray, θ is the scattering angle where d is the interplanar spacing for a given set of *hkl* and θ the Bragg angle and n is an integer. These energetic X-rays can penetrate deep into the material and provide information about the structural arrangement of atoms and molecules.

The particle size can be calculated from the Scherrer formula [8]:

$$t = 0.9 \, \lambda \, / \, B \cos \theta$$

where, B is the intensity at FWHM in terms of 2θ and t is the thickness (particle size).

2.5.4 X-ray Photoelectron Spectroscopy

The photoelectron spectroscopy experiment involves measuring the intensity of photo-emitted electrons from the core levels and valence band of a material, as a function of kinetic energy of the emitted electrons. XPS is a surface-sensitive quantitative spectroscopic technique that deals with the elemental composition at the parts per thousand range, empirical formula, chemical state and electronic state of the elements that exist within a material. It is based on the photoelectric effect, whereby absorption of light by an atom, molecule, or solid/surface results in the ejection of electrons, provided that the photon energy is sufficient to overcome the binding energy of the electron. For XPS, Al Kα (1486.6 eV) or Mg Kα (1253.6 eV) photons are generally used [3,6]. Both valence and core electrons can be ejected by X-ray radiation. The core electron binding energies are characteristic of each element, and the peak areas can be used to determine the composition. As the peak shape and binding energy are sensitive to the oxidation and

chemical state of the emitting atom, XPS can also provide chemical bonding information. The XPS technique is highly surface specific due to the short range of the ejected photoelectrons.

2.5.5 Electron Microscopy

Microscope is the instrument with which we form enlarged images. The word "microscope" came from two Greek words, micros mean small and skopos means to look out. Ever since the introduction of the concepts of molecular biology and material chemistry at sub-micro levels the requirement for a device with the capabilities of extremely high resolution arose. Light microscopes which use lenses to magnify objects, a projector lens to project the image onto an image plane which can be photographed or stored. The acquired images are substantially lower than that required to visualize molecules at the nano-scale. This led to the development of the concept of electron microscopy [3, 9-13].

2.5.5.1 Scanning Electron Microscopy

A scanning electron microscopy (SEM) is largely used electron microscopic technique due to its versatility, different modes of imaging, simple sample preparation, the possibility of spectroscopy and diffraction including easy interpretation of images [9]. In the SEM, the electron beam is sourced from a cathode. An energy greater than the work function of the material (to drive the electrons out of its orbits) is supplied in the form of potential or heat (these sources are categorized as field emission or thermionic respectively). Since electrons that produced from the cathode appear non-uniformly, they are passed through an anode which diverges the non-uniform beam. These beams are re-focused by the use of magnetic lenses. These re-focused beams are allowed to fall on the stage where they interact with the substrate and undergo scattering. Devices such as secondary electron detectors and backscattered electron detectors (placed in the sample chamber) gather information regarding the electron interactions with the substrate. This data is sent to the processor as signals which are interpreted to obtain sample images [9,11].

2.5.5.2 Energy-Disperse X-ray Microanalysis

This analytical technique is often used in conjunction with SEM. An electron beam (typically 10-20 keV) strikes the surface of a conducting sample, causing X-rays to be emitted, whose energies depend on the material under examination. The X-rays are generated in a region about 2 μM in depth. By scanning the electron beam across the material, an image of each element in the sample can be obtained which shows the chemical composition of individual nanoparticles. In EDS, all photons emitted by the samples are collected and measured simultaneously by a solid state X-ray detector.

2.5.5.3 Transmission Electron Microscopy

The transmission electron microscope (TEM) uses transmitted electrons to create an image of the sample. In TEM, the electron beam is passed through a thin layer of the sample. The beam interacts with this layer and the transmitted beam is then focused onto an imaging device. Such devices include fluorescent screens and photographic films [12,13]. Since SEM works on the principle of beam scattering it only provides information on the morphology of the sample. In the case of TEM however, since imaging is done from the transmitted electrons, it can also provide information on magnetic domains, stresses, and crystal structure. It also has higher resolution than SEMs, called high-resolution transmission electron microscopy (HRTEM). From HRTEM images fringe spacing (d) can be calculated, which corresponds to a particular crystal plane (h,k,l).

2.5.6 Fourier Transform Infrared Spectroscopy

Infrared spectroscopy deals with the interaction of an infrared region of the electromagnetic spectrum with the matter. In this region associated photon energies (1 to 15 kcal/mole) are not adequate enough to excite the electrons; however, they may induce vibrational excitation in covalently bonded atoms and groups [14]. According to the gross selection rule of IR spectroscopy, an 'IR active' vibrational mode must be associated with changes in the electric dipole moment. The molecule need not have permanent dipole, however, requires only a change in dipole moment during the vibration.

References

[1]   Ghobadi, N. Band Gap Determination Using Absorption Spectrum Fitting Procedure. *Int Nano Lett* **2013,** *3*, 2-6.

[2]   Liu, P.; Longo, P.; Zaslavsky, A.; Pacifici, D. Optical Bandgap of Single- and Multi-layered Amorphous Germanium Ultra-thin Films. *J Appl. Phys.* **2016,** *119*, 014304-9.

[3]   Pradeep, T. A. *Text Book of Nanoscience and Nanotechnology*. McGraw-Hill Education (India) Private Limited, **2012**.

[4]   Anantharaj, S.; Ede, S. R.; Sakthikumar, K.; Karthick, K.; Mishra, S.; Kundu, S. Recent Trends and Perspectives in Electrochemical Water Splitting with an Emphasis on Sulfide, Selenide, and Phosphide Catalysts of Fe, Co, and Ni: A Review. *ACS Catal.* **2016**, *6*, 8069-8097.

[5]   Shi, H.; Zhao, G. Water Oxidation on Spinel $NiCo_2O_4$ Nanoneedles Anode: Microstructures, Specific Surface Character, and The Enhanced Electrocatalytic Performance. *J. Phys. Chem. C* **2014**, *118*, 25939-25946.

[6]   Kelsall, R.; Hamley, I.; Geoghegan M. *Nanoscale Science and Technology*. John Wiley and Sons. Ltd., **2005**.

[7]   Perkampus, H. H. *UV-Vis Spectroscopy and its Applications*, Springer-Verlag, Berlin, Germany, **1992**.

[8]   Lonsdale, K. X-ray Study of Crystal Dynamics: An Historical and Critical Survey of Experiment and Theory. *Proc. Phys. Soc.* **1942,** *54*, 314-353.

[9]   Wells, O. C. *Scanning Electron Microscopy*. McGraw-Hill, **1974**.

[10]   Joshi, M.; Battacharyya, A.; Ali, S. W. Characterization Techniques for Nanotechnology Applications in Textiles. *Indian Journal of Fiber and Textile Research* **2008**, *33*, 304-317.

[11]   Li, D. *Fabrication and Characterization of Metal Oxide Nanostructures*. Open Dissertation Press, **2007**.

[12]   Fultz, B.; Howe, J. M. *Transmission Electron Microscopy and Diffractometry of Materials*. Springer, **2008**.

[13]   Amelinckx, S. *Electron microscopy: Principles and Fundamentals*. VCH, **1997**.

[14]   Kendall, D. N. *Applied Infrared Spectroscopy*. Reinhold Pub. Corp. New York, **1966**.

Synthesis of Au and Ag Nanoparticles on ZnO Nanoflower and their Photocatalytic Application using UV and Visible Light

✿ *Synthesis of ZnO nanoflower and deposition of gold and silver nanoparticles on its surface followed by their use in photocatalysis under UV and visible light irradiation has been reported.*
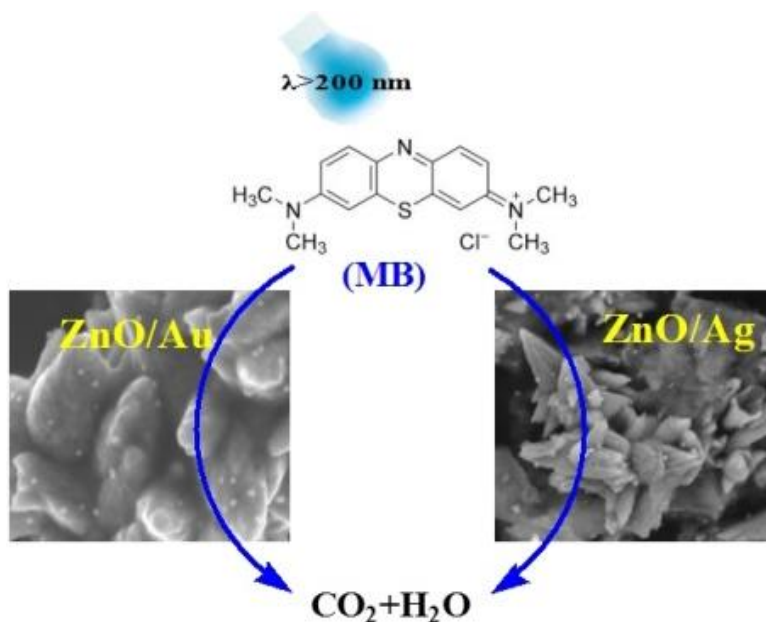
Abstract

We report a simple and convenient method for the synthesis of ZnO/Au and ZnO/Ag heterostructure nanoflower applying a surfactant mediated route. Initially, pure ZnO nanoflower have been synthesized followed by Au and Ag deposition on ZnO surface using hydrazine hydrate as a reducing agent. Structure, crystallinity, and morphology have been assessed by X-ray diffraction, X-ray photoelectron spectroscopy, and electron microscopy techniques. The influences of the deposited metal nanoparticles (Au and Ag) on the surface of ZnO have been emphasized by applying the as-synthesized nanostructure in dye degradation under illumination of UV and visible light. The basic motivation behind this work is to find a superior photocatalyst, which can work under UV as well as visible light i.e., to cover the whole range of the solar spectrum. Photocatalytic performances of bare ZnO, ZnO/Au, and ZnO/Ag have been studied thoroughly. Photodegradation results in UV and visible light demonstrated that the incorporation of noble metal nanoparticles significantly (or drastically) increase the catalytic efficiency by promoting the photogenerated charge carrier separation. The main advantage of the proposed ZnO/Au and ZnO/Ag semiconductor is that it delays the recombination process of the electron-hole pairs generated by the photon absorption, which in lieu increases the photocatalytic efficiency. It is a challenging issue to fabricate stable photocatalysts which can work under the visible light as it covers 43% of the sunlight. To investigate the role of photogenerated electron and hole in dye degradation, scavenging experiment using different scavengers have also been performed.

3.1 Introduction

In recent years, scientists are investigating many semiconductor-assisted photocatalysts due to their ability to degrade a large number of recalcitrant chemicals in aqueous systems with large efficiency. Among those semiconductors assisted photocatalysts, ZnO nanomaterials have extensively been studied due to their high surface area and high photosensitivity [1-4]. However, owing to its high band gap (3.37 eV) and large exciton binding energy (60 MeV), [1] the use of ZnO in photocatalysis is limited mainly under UV light of wavelength below 385 nm. As the sunlight reaching to the earth's surface contains even less than 5% of it in the form of UV light, the practical application of ZnO photocatalysts is largely restricted. However, modified ZnO with noble metals, such as Pt, [5,6] Au, [7,8] and Ag [9] possess many unique properties such as easy reduction, high chemical stability, and bio-affinity. In addition, noble metals also act as an electron sink, which can significantly enhance the photocatalytic activity in both UV and visible light [10-13]. Therefore, it is of high practical importance to show how the plasmonic energy can be converted to chemical energy when ZnO nanoflower surface has been functionalized with gold and silver nanoparticles.

Synthesis of zinc oxide nanoparticles has been reported by different groups using various methods such as hydrothermal synthesis, [14,15] alkali precipitation, [16,17] thermal decomposition, [18] organo-zinc hydrolysis, [19] etc. Yang and co-workers reported cetyltrimethylammonium bromide (CTAB) assisted hydrothermal synthesis of ZnO nanoflower using an autoclave at 120 °C [14]. Synthesis of ZnO nanorod and prism using zinc foil, NaOH, and CTAB at a temperature ~ 160 °C has been reported by Wang and co-workers [20]. Low-temperature synthesis of various superstructures (ring, sheet, and platelet) of ZnO using CTAB has also been reported by Lee and co-workers [21]. Room temperature synthesis of flower-like ZnO nanostructures without using any external capping agent at alkaline pH has been reported by Kumbhakar and co-workers [22]. Flower-like morphology of ZnO has been found by Miao and co-workers using lignin amine for 5 h in the 80 °C water bath [23].

Hence, from all the reported literature it has been quite clear that autoclave at elevated temperature as well as room temperature can be a useful method for the synthesis of ZnO particles [24-27]. Whereas, within this study, we report a simple approach for the synthesis of ZnO nanoflower at low temperature using CTAB as a growth controlling agent and their surface

modification with noble metal nanoparticles, which can work as an active and efficient photocatalyst covering the whole solar spectrum.

Surface modification/decoration of ZnO with noble metal nanoparticles (Au and Ag) offer many potential challenges. Lee and co-workers reported the synthesis of glutathione protected gold nanoparticles on the surface of ZnO and their successful application in photocatalysis [28]. Moreover, they also reported that the size-dependent gold nanoparticles synthesis on the ZnO surface and their photocatalytic activity can be controlled by a size-dependent gold capacitor [29]. Kamat and co-workers reported the synthesis of ZnO-Au nanoparticles and the Fermi level equilibration during the interaction between the semiconductor and noble metal [30]. This phenomenon is very much important to detect the role of noble metal in photocatalysis. They have reported the Fermi level shift towards the conduction band in a semiconductor in case of ZnO-Au [30]. Synthesis of Ag/ZnO heterostructures with different silver content using the solvothermal method and their application in photocatalysis has been reported by Zheng and co-workers [31]. Worm-like core-shell composites of Ag/ZnO with different silver content under ultrasonic irradiation have been synthesized by Jia and co-workers [32]. Zhou *et al.* reported the synthesis of the flower-like ternary heterostructure of Ag/ZnO encapsulating carbon spheres and photocatalytic ability has been explored by the photodegradation of reactive black GR and metronidazole under sunlight and visible light irradiation. They have compared the photoactivity of ZnO@C, Ag/ZnO, and Ag/ZnO@C and explained the surface plasmon effect of metal and surface photosensitizing effect of C spheres which improved the catalytic activity of ZnO [33]. One-pot hydrothermal synthesis of ZnO/Pd and ZnO/Pt have been performed by Sun *et al.* and proved that on a metal oxide support, noble metal deposition is a good approach to improve the stability of the catalyst during chemical reactions and also reduce the cost of noble metals [34]. Wang *et al.* reported the synthesis of flower-like ZnO/Ag nanocomposites via a simple, green and cost-efficient method and showed its more efficient photocatalytic activity in the degradation of MB than pure ZnO under visible light irradiation [35].

In general, pure ZnO shows less reactivity as photocatalyst due to the lack of electron and hole trapping agents at conduction and valence band, respectively. Upon modification with noble metals (Au and Ag), the photocatalytic activity of ZnO significantly increases, as the metal centers act as an electron sink/trap on the semiconductor surface [10-13]. Moreover, due to the

difference in work function values of different metals, metal semiconductor heterostructure exhibits variable catalytic efficiency in photocatalysis upon irradiation of visible and UV light [9]. Therefore, for a better understanding of the effect of noble metals on ZnO nanoparticles and their Fermi level shift, we explore a simple and facile approach for the decoration of Au and Ag nanoparticles on ZnO surface and investigate their application in organic pollutant degradation [34,35]. However, a comparative study of the decoration of both Au and Ag nanoparticles on ZnO surface and their photocatalytic effect using UV and visible light is still missing which has been reported within this chapter.

In this chapter, we report a solution based one-step synthesis of ZnO nanoflower at a relatively lower temperature (~ 80 °C), using cetyltrimethylammoniumbromide (CTAB) as a growth controlling agent. Afterward, the noble metals (Au and Ag) were deposited on the surface of ZnO nanoflower using hydrazine hydrate as a reducing agent. The as-synthesized ZnO/Au and ZnO/Ag heterostructure nanoparticles are characterized using UV-vis, PL, XRD, XPS, FESEM, TEM, and EDS techniques. The detailed mechanism for the growth of ZnO nanoflower, ZnO/Au, and ZnO/Ag is thoroughly discussed. Photocatalytic performance of the as-prepared catalysts was evaluated by using a cationic dye, methylene blue (MB) and phenol in water, under illumination of UV and visible light. The main importance of this work is to modify ZnO flower surface with gold and silver nanoparticles and to find out their Fermi level shift towards the conduction band of the semiconductor, which can influence the photoactivity of ZnO. The key role of the noble metal (Au and Ag) on ZnO surface is also examined in dye degradation reaction. Finally, scavenging experiment using some scavengers is executed to know the degradation mechanism.

3.2 Experimental Section

3.2.1 Synthesis of ZnO Nanoparticles

ZnO nanoparticles were synthesized using the following procedure. Firstly, in a 500 mL beaker, an equal volume of (4 ml) of zinc sulphate (1 M) and CTAB (1 M) solutions were dissolved in 400 mL water so that the final concentration of both was 0.01 M and stirred well. Afterward, the whole solution was kept on a water bath at ~ 80 °C for ~ 5 h and without stirring.

Secondly, 2 mL of concentrated ammonia solution (directly from the bottle) was added to the above solution and the pH was maintained ~ 10. Immediately, the whole solution was cloudy, which was due to the formation of zinc hydroxide. Finally, white powder of ZnO was formed and precipitated. The white precipitate was collected and washed two times with water and dried well in air.

3.2.2 Synthesis of ZnO/Au and ZnO/Ag Nanoparticles

Deposition of Au and Ag on ZnO surface was done by the following procedure. At first, in a 100 mL beaker, 100 mg of the as-synthesized white ZnO powder was dispersed well in 10 mL water by sonication for ~ 30 min. Secondly, 10 mL of 1×10^{-2} M HAuCl$_4$ was added to the above-dispersed ZnO solution, so that the final concentration of HAuCl$_4$ was maintained at 0.5×10^{-2} M with continuous stirring but without the addition of any extra growth controlling agent. As a result, in the above solution the weight ratio of ZnO:AuCl$_4^-$ was 2.5:1. The whole solution was stirred well for ~ 2 h so that the HAuCl$_4$ was adsorbed well on ZnO surface. Afterward, the HAuCl$_4$ adsorbed ZnO precipitate was collected and washed several times with water to drain out the excess HAuCl$_4$ from the solution. In the third step, the precipitate was re-dispersed again in 20 mL water followed by addition of 0.2 mL of 1 M hydrazine hydrate within the solution with continuous stirring. Au nanoparticles were deposited on to the surface of ZnO particles which results in a purple colored precipitate formation. Finally, this purple color powder was collected and washed with deionized water twice and dried well for further characterization and application.

ZnO/Ag nanoparticles were synthesized using the same protocol described for ZnO/Au nanoparticles, except AgNO$_3$ was used instead of HAuCl$_4$ where a yellow color precipitate was obtained.

3.3 Results and Discussion

3.3.1 Characterization

All as-synthesized nanoparticles are very stable and used for other characterizations which have been discussed in the following.

3.3.1.1 Optical Characterization

Figure 3.1 shows the absorption spectra of the ZnO, ZnO/Au, and ZnO/Ag nanoparticles in the ultraviolet-visible spectral region. ZnO exhibits a sharp band at 369 nm, which corresponds to the formation of ZnO particles. From the absorption spectrum of ZnO an estimated optical band gap can be derived using the following equation:

$$\alpha E_p = K(E_p - E_g)^{1/2}$$

where α stands for the absorption coefficient, K is a constant, E_p is the discrete photo energy, and E_g is the band gap energy. A classical Tauc approach is further employed to estimate the E_g value of ZnO nanoparticles [36-38]. A plot of $(\alpha E_p)^2$ vs. E_p is shown within the inset of **Figure 3.1**. The extrapolated straight line of this plot meets the E_p axis at $\alpha = 0$ which represents the absorption edge energy corresponds to the band gap (E_g) of the material. The band gap value of ZnO from the experimental data was calculated to be 3.12 eV, which is in good agreement with the value reported in the literature [39].
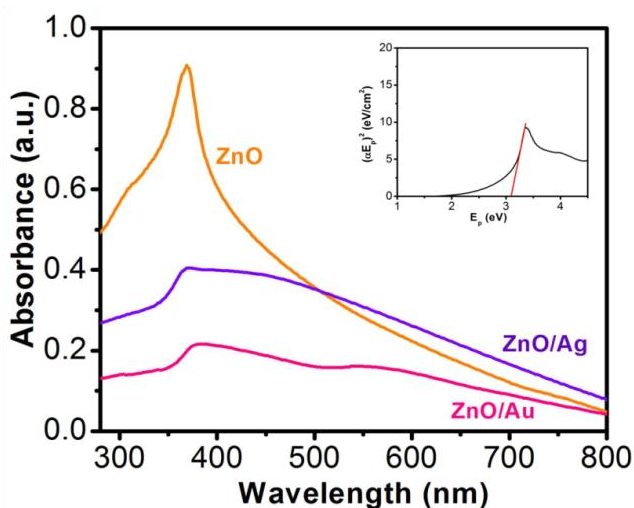
Figure 3.1 UV-vis absorption spectra for ZnO, ZnO/Au, and ZnO/Ag nanoparticles, where all the powder samples were dispersed in water and sonicated for ~20 min. Aqueous solution was used for background subtraction whereas. 1.0 cm cuvette was used for UV-Vis measurement. Here, all absorbance values are in arbitrary unit and each spectrum corresponds to different absorbance (not in relative scale). From the UV-vis spectrum of ZnO, inset shows $(\alpha E_p)^2$ vs. E_p plot for band gap (E_g) calculation of ZnO nanoparticles

In case of ZnO/Au, spectroscopy shows two bands at 378 nm and 560 nm, respectively. The band position at 378 nm corresponds to the presence of ZnO whereas the other band represents the formation of Au nanoparticles. For ZnO/Ag samples a broad band at 450 nm, representative of the Ag nanoparticles appears along with the unshifted band at 369 nm for ZnO particles. The shift in ZnO band position in the case of ZnO/Au nanoparticles can be attributed to the higher electronegativity of gold compared to that of silver. As a result, gold withdraws electron density more towards itself, which finally affect the movement of the band position of ZnO. In addition, a significant decrease in absorbance intensity of ZnO peak at 369 nm for ZnO/Au and ZnO/Ag have also been observed, which indicates the presence of gold and silver on ZnO surface. Therefore, the presence of UV and visible absorbance maxima both for ZnO/Au and ZnO/Ag clearly demonstrates that the material becomes photoactive in both UV and visible light region.
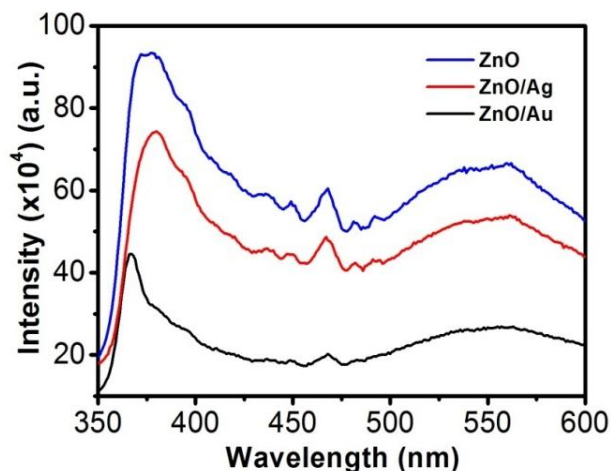
Figure 3.2 Room temperature photoluminescence spectra of ZnO, ZnO/Au, and ZnO/Ag nanoparticles. All the powder samples were well dispersed in water using a sonicator for PL measurements using an excitation wavelength (λ_{ex}) of 325 nm

Room-temperature PL spectra of the ZnO, ZnO/Au, and ZnO/Ag are shown in **Figure 3.2**, which was obtained with an excitation wavelength of 325 nm. For all the nanoparticles three bands are observed in PL spectrum: (a) UV near-band-edge emission peak at 378 nm, (b) small band at 467 nm, and (c) a broad green light emission at 560 nm. The green emission peak is

commonly referred to a deep level of trap-state emission [40]. More precisely, the green transition has been attributed to the singly ionized oxygen vacancy in ZnO and the emission results from the radiative recombination of a photogenerated hole with an electron occupying the oxygen vacancy [40,41]. The stronger intensity suggests the presence of higher singly ionized oxygen vacancies in ZnO [29]. When ZnO is modified with metal nanoparticles, the intensity of all the three bands decreases, which states that the electrons and holes are more separated and recombination process is inhibited. The relatively lower intensity bands for the case of ZnO/Au prove the inhibited electron-hole pair recombination is maximum for the ZnO/Au nanoparticles. However, the shifting of UV near-band-edge emission peak at 367 nm for ZnO/Au is still not well understood.

3.3.1.2 XRD Analysis of ZnO, ZnO/Au, and ZnO/Ag Nanoparticles

The crystallinity, phase, and purity of the as-prepared samples were determined by powder x-ray diffraction (PXRD). Typical PXRD patterns of the as-synthesized ZnO, ZnO/Au, and ZnO/Ag particles are shown in **Figure 3.3**.
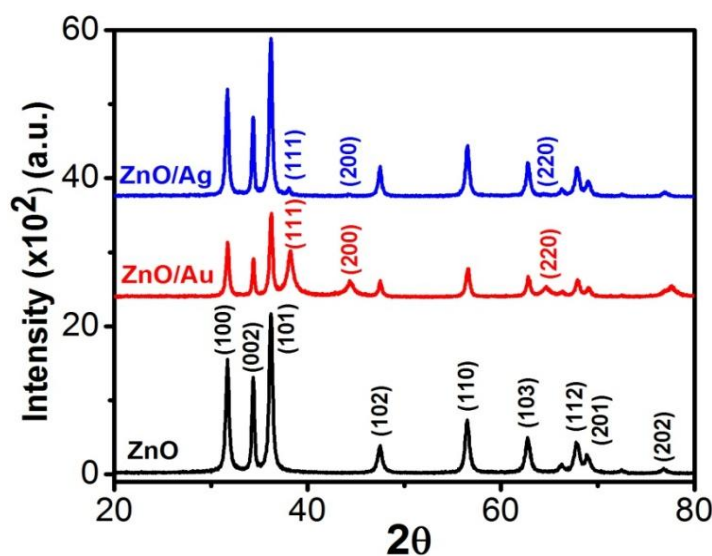
Figure 3.3 Powder X-ray diffraction patterns of ZnO, ZnO/Au, and ZnO/Ag nanoparticles. During scan 2θ values varies from 20-80° and the scanning rate was fixed at 2° per min

Nine major reflection peaks appear at 2θ values of 31.80°, 34.41°, 36.21°, 47.52°, 56.53°, 62.74°, 67.80°, 69.11°, and 77.46° which corresponds to the (100), (002), (101), (102), (110), (103), (112), (201), and (202) crystal planes of the hexagonal ZnO structure, respectively. All these peaks of the ZnO nanoparticles can be indexed to wurtzite (hexagonal) structure of ZnO (JCPDS card No. 36-1451) [14]. The absence of characteristic impurity peaks such as $Zn(OH)_2$ and unhydrolyzed Zn(II)-sulphate indicate a high-quality ZnO nanoparticles.

The PXRD patterns of ZnO/Au exhibits three additional peaks at 2θ values of 38.23°, 44.38°, and 64.7° corresponds to the (111), (200), and (220) crystal planes of Au, respectively, which confirm the formation of gold nanoparticles on ZnO surface [42]. PXRD pattern of ZnO/Ag shows a clear peak at 38.05°, which is due to the presence of (111) crystal plane of silver particle on ZnO surface. The other two peaks at 44.38° and 64.7° for (200) and (220) crystal planes of Ag are not clear [31]. All these PXRD findings clearly indicate the formation of metal nanoparticles. Au and Ag particle sizes were calculated using Debye Scherrer formula, which represents 20 nm and 32 nm for Au and Ag nanoparticles, respectively.

3.3.1.3 Surface Characterizations

The morphological analysis of the as-synthesized samples was carried out using an FESEM, which is depicted in **Figure 3.4**. ZnO particles show flower shaped structures having diameter of 600 nm (length) of the petal. **Figure 3.4.a** and **b** show a surface overview and closer look FESEM images of ZnO particles, respectively, which contain a sharp petal with breadth of 220 nm for only one petal in ZnO nanoflower. High resolution SEM image clearly shows a little surface roughening of the ZnO flower petals. A similar kind of flower-like structure has also been reported by Yang and co-workers, where they used a saturated CTAB aqueous solution at ~120 °C for 20 h and a teflon-lined stainless steel autoclave [14]. Whereas, in this study, ZnO particles were synthesized in a much simpler way, using water bath at ~ 80 °C for 5 h.

FESEM images of gold and silver nanoparticles, deposited on ZnO surfaces are shown in **Figure 3.4.c** and **d**, respectively. Randomly scattered spherical particles with uniform size-distribution of gold and silver were nicely resolved on ZnO surface. From the FESEM images, it has been observed that the average particle diameter for gold is about 30 nm, whereas for silver it rises to 40 nm. Hence, from the above findings we can conclude that the synthesis of ZnO/Au

and ZnO/Ag nanoparticles by a simple wet-chemical method, using hydrazine hydrate as reducing agent, is very much useful.
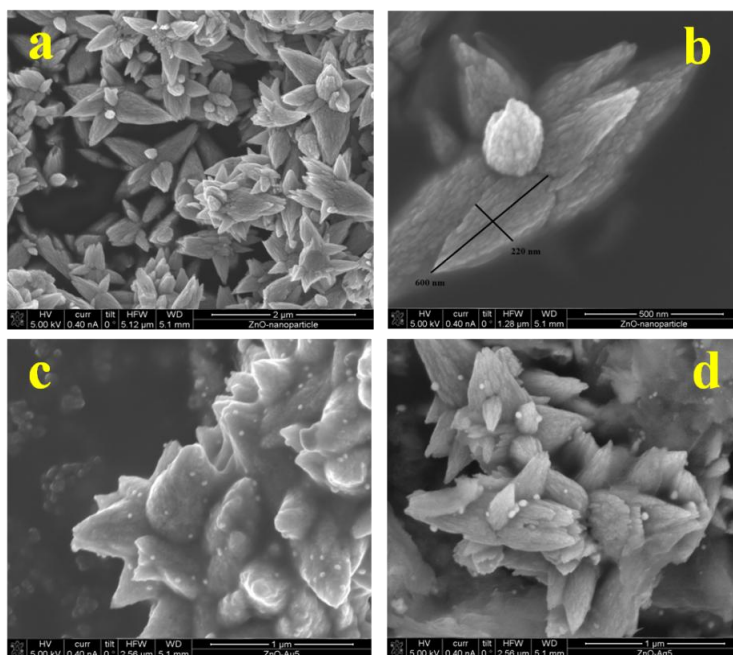
Figure 3.4 FESEM images of ZnO nanoparticles: (a) large scale overview and (b) closer look of bare ZnO nanoflowers. High-resolution FESEM images of (c) ZnO/Au and (d) ZnO/Ag. Particle sizes for Au and Ag were measured using randomly chosen ~ 30 particles
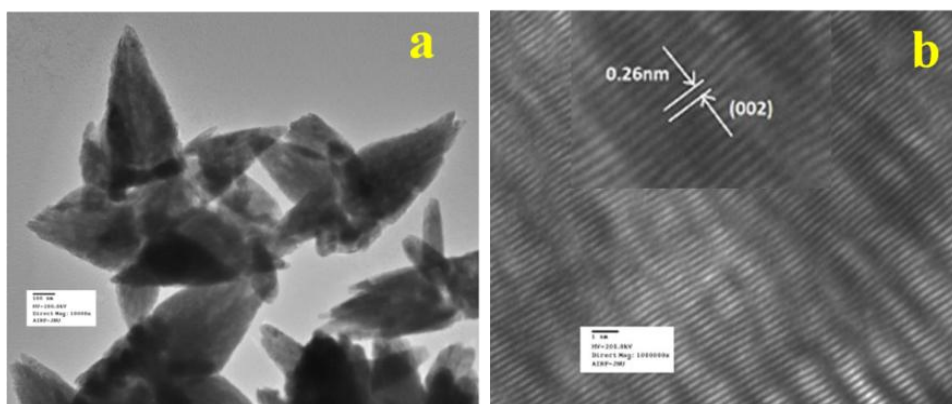
Figure 3.5 (a) TEM and (b) HRTEM images of ZnO nanoparticles. HRTEM image was used to calculate the fringe spacing

Figure 3.5.a shows the TEM image of flower shape structure of the ZnO nanoparticles. TEM result also confirms the presence of sharp petal with an average size of 600 nm long (length) and 230 nm (breadth) diameter as well as little surface roughening of the petal structure. High resolution TEM image of ZnO particle is shown in **Figure 3.5.b**, which clearly depicts lattice fringes of ZnO with an interplaner spacing of 'd' = 0.26 nm, which matches well with the spacing between (002) crystal planes of ZnO. This finding of (002) plane oriented growth of ZnO corroborates well with the earlier PXRD results.

Figure 3.6.a represents the TEM image of ZnO/Au nanoparticles, which strongly suggests that the formation of spherical gold nanoparticles randomly distributed on the surface of ZnO. An HRTEM image of ZnO/Au is shown in **Figure 3.6.b**, which further confirms the presence of both ZnO and gold nanoparticles. The interplaner spacing 'd' of 0.24 nm and 0.26 nm exhibits the presence of (111) plane of gold nanoparticles on (002) plane of ZnO surface, respectively.
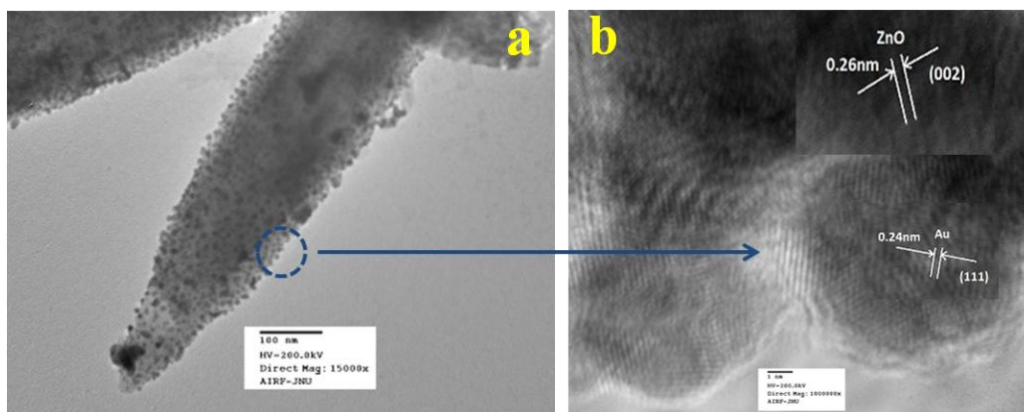
Figure 3.6 (a) TEM and (b) HRTEM images of ZnO/Au nanoparticles. Fringe spacing for ZnO and Au were separately calculated using HRTEM image

A similar kind of TEM and HRTEM images of ZnO/Ag are presented in **Figure 3.7.a** and **3.7.b**. It is observed that, the spherical silver particles are well distributed on ZnO surface. A clear contrast of fringe spacing was observed between the ZnO and silver particles. Separate lattice fringes were observed for ZnO and silver with the value of 'd' of 0.26 nm and 0.23 nm, which can be assigned to the presence (111) planes of silver on (002) ZnO surface. All TEM

images for the as-synthesized particles are in good agreement with FESEM findings. Both FESEM and TEM images clearly indicate a higher density of metal nanoparticles for of ZnO/Au compare to the ZnO/Ag.
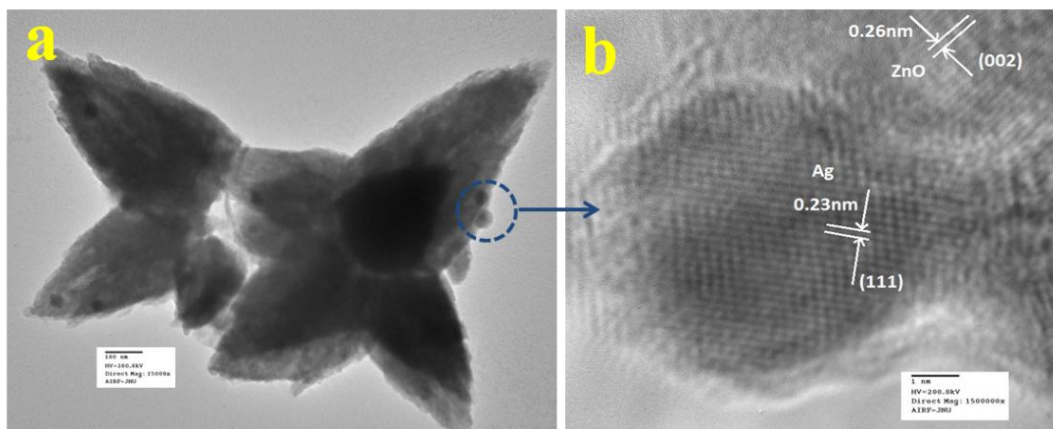
Figure 3.7 (a) TEM and (b) HRTEM images of ZnO/Ag nanoparticles. Fringe spacing for ZnO and Ag were separately calculated using HRTEM image
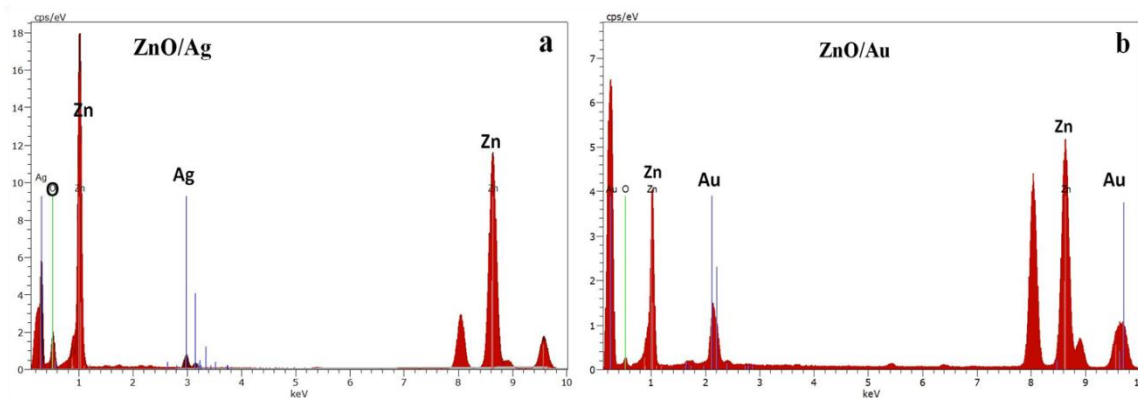
Figure 3.8 EDS Spectrum of (a) ZnO/Au and (b) ZnO/Ag nanoparticles

Finally, EDS analysis of ZnO/Au and ZnO/Ag for selected area also confirms the presence of Zn, O, Au, and Ag, which is shown in **Figure 3.8**. The EDS signal of Au and Ag are very uniform in the observed area, indicating the completely random distribution of gold and silver nanoparticle on ZnO surface.

3.3.1.4 X-ray Photoelectron Spectroscopy

As a surface monitoring technique, XPS was employed to further support the formation of ZnO, ZnO/Au, and ZnO/Ag nanoparticles. The high-resolution XPS spectra of Zn^{2+} and O^{2-} regions of ZnO particles, synthesized by wet chemical technique are shown in **Figure 3.9.a** and **b**. The binding energy positions for $Zn^2P_{3/2}$ and $Zn^2P_{1/2}$ are obtained at 1022.1 eV and 1045.1 eV, respectively. The difference in binding energy between two Zn peaks is about 23.0 eV, which matches well with the earlier reported value [42]. The O_{1s} peak shows the binding energy position at 530.6 eV. All these findings clearly suggest the formation of ZnO [42,43].
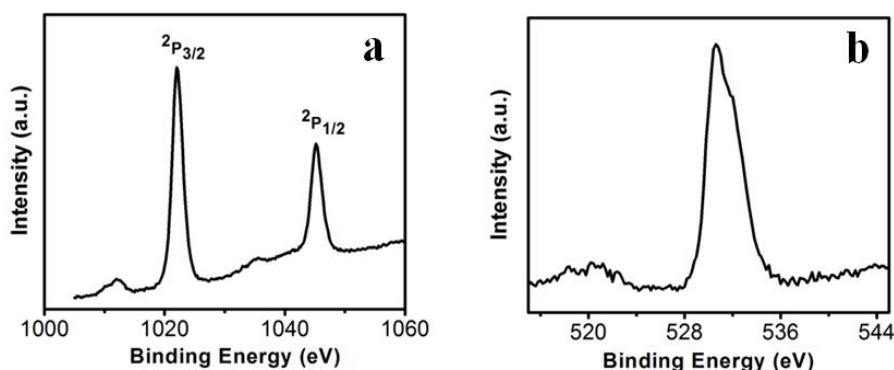
Figure 3.9 (a) High-resolution X-ray Photoelectron spectrum of Zn and (b) High-resolution X-ray Photoelectron spectrum of O
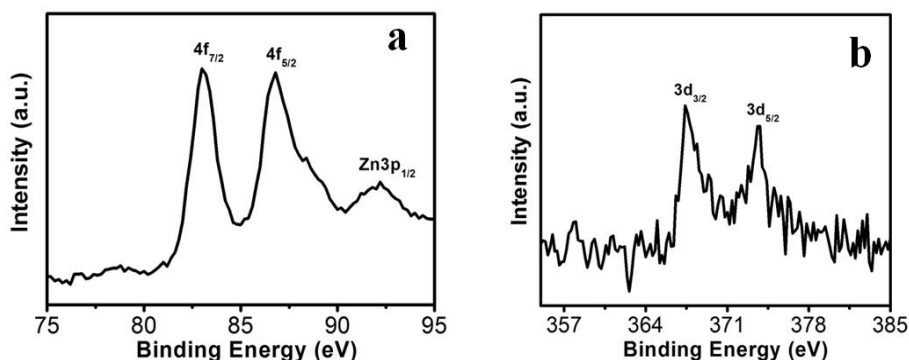
Figure 3.10 High-resolution XP spectra of (a) ZnO/Au and (b) ZnO/Ag samples deposited on conducting carbon tapes. XPS peak positions were referenced to the C1s peak at 284.5 eV

The high-resolution XP spectra of ZnO/Au and ZnO/Ag are shown in **Figure 3.10.a** and **b**. The Au $4f_{7/2}$ and $4f_{5/2}$ binding energy peaks are centered around 83.04 eV and 87.14 eV, respectively, which are consistent with those for bulk Au at 83.95 eV and 87.68 eV, indicating the formation of Au(0) nanoparticle on the surface of ZnO using hydrazine hydrate as reducing agent [44,45].

Similarly, for ZnO/Ag, the binding energy peaks are located at 373.71 eV ($3d_{3/2}$) and 368.33 eV ($3d_{5/2}$), favouring the formation of Ag(0) nanoparticles. The binding energies for Ag(0) are matches well with the reported literature values for bulk Ag at 373.4 eV and 368.22 eV, respectively [44,46]. From these binding energy values of gold and silver it has been observed that, there is negligible shift of binding energies (gold and silver) on ZnO surface as compared to their bulk.

3.3.2 Mechanism of Formation of ZnO, ZnO/Au, and ZnO/Ag Nanoparticles

The mechanism of the formation of ZnO particles in alkaline medium is given below.

At alkaline pH, available OH^- ion in the aqueous solution initially reacts with Zn^{2+} ion and introduces the formation of $Zn(OH)_2$. At pH 10, $Zn(OH)_2$ is the main colloid species in the solution. During hydrolysis at ~ 80 °C, part of $Zn(OH)_2$ colloid dissolves into Zn^{2+} and OH^- within the solution, which creates the formation of ZnO nuclei. Furthermore, at alkaline pH, $Zn(OH)_2$ further reacts with OH^- ion and therefore $[Zn(OH)_4]^{2-}$ is formed. Finally, at elevated reaction temperature (~ 80 °C), the growth of ZnO nanoflower initiates in presence of CTAB due to the coulomb attraction between the cationic charge CTAB and anionic $[Zn(OH)_4]^{2-}$ species [14]. The overall reaction for the formation of ZnO is shown below:

$$Zn^{+2} + 2OH^- \rightarrow Zn(OH)_2$$
$$Zn(OH)_2 + 2OH^- \rightarrow [Zn(OH)_4]^{2-}$$
$$[Zn(OH)_4]^{2-} \rightarrow ZnO + OH^- + H_2O$$
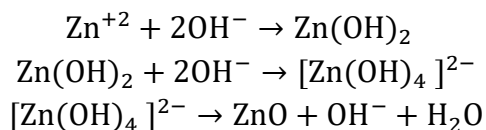
To understand the effect of alkaline medium on formation of ZnO particle, a similar kind of reaction was also carried out in absence of ammonia solution. Surprisingly, no ZnO particle was found (**Scheme 3.1**). In case of surfactant assisted synthesis of ZnO, surfactant plays a crucial role and acts as a driving force for the formation of ZnO nanoflower [14]. Therefore, to

know the role of CTAB in nanoflower formation, hydrothermal experiment was conducted without CTAB, which results in the formation of largely agglomerated ZnO particles instead of a flower-like morphology. The FESEM image of the agglomerated form of ZnO is shown in **Figure 3.11**.
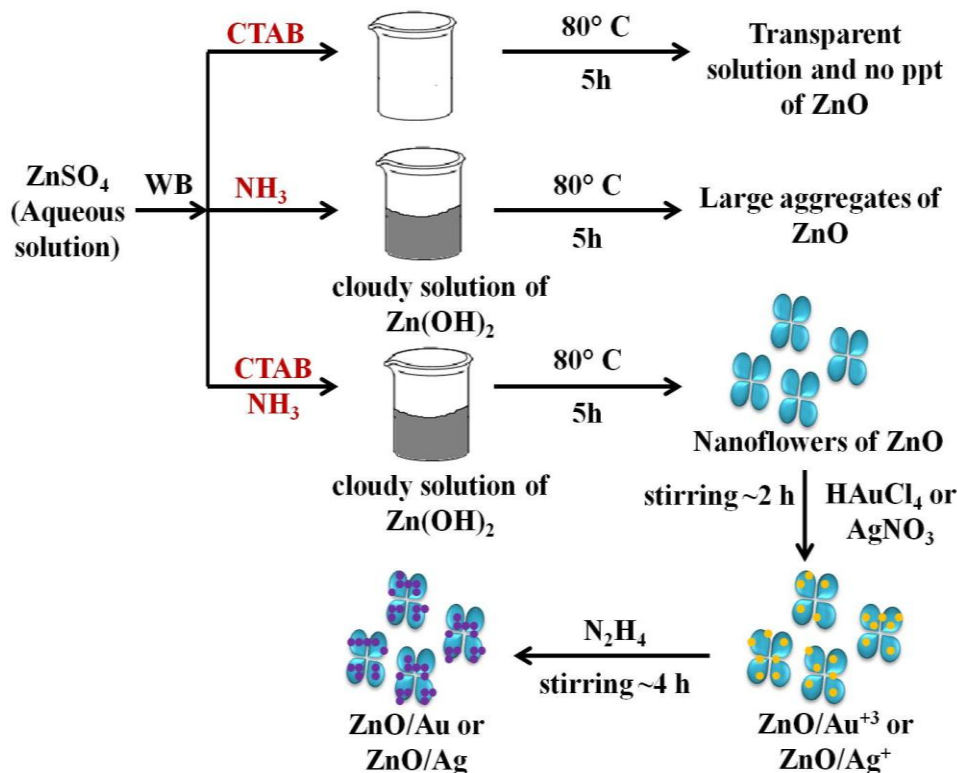
Scheme 3.1 The overall mechanism of ZnO/Au and ZnO/Ag nanoparticle formation on ZnO nanoflower surface. Here, WB represents water bath

Without the CTAB, there was no growth directing agent. As a result, larger particles are randomly deposited. From **Figure 3.11**, it is well understood that the role of CTAB is very important for the formation of ZnO flower. Therefore, CTAB is very much essential to generate the flower like morphology of ZnO. Yang and co-workers also reported the formation of pointed sword-like ZnO nanoparticle (~100 nm) instead of a flower-like morphology, without using the CTAB [14]. The same group also reported at lower growth temperature (120 °C), there was not enough driving force for the growth of similar sword-like ZnO nanorods [14].
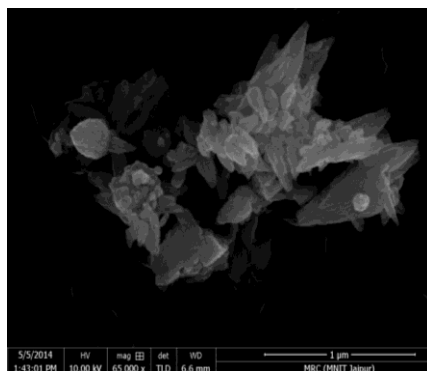
Figure 3.11 FESEM image of ZnO nanoparticles synthesized without CTAB, agglomerated particles of ZnO

In order to comprehend the complete growth mechanism of ZnO nanostructures in presence of CTAB, a time-dependent analysis of growth features was conducted using FESEM analysis as can be seen in **Figure 3.12**. During synthesis, ZnO powder samples were collected at intervals of 1 h, 3 h, and 5 h, respectively, from the reaction container. Figure 9a represents the FESEM image of ZnO after 1 h of synthesis, which shows the formation of spherical particles and initiates the formation of ZnO flower. After 3 h of synthesis, ZnO nanoflower formation was started but the growth uniformity was not observed (**Figure 3.12**). Finally, the complete growth/formation of ZnO flower was ended after 5 h of synthesis, as shown in **Figure 3.12**. Even longer synthesis does not make any significant changes of the ZnO flower morphology. Therefore, the optimization of reaction time and the role of CTAB during the formation of ZnO were confirmed by growth study.

1 hour *3 hour* *5 hour*
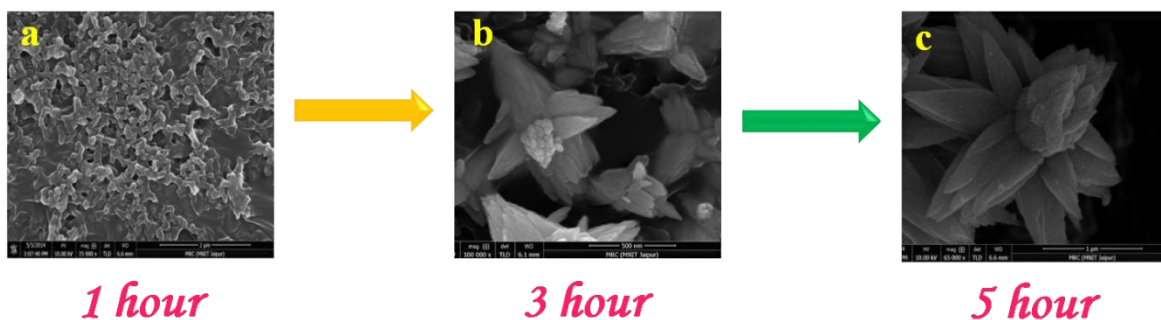
Figure 3.12 FESEM images of ZnO nanostructure synthesis after (a) 1 h, (b) 3 h, and (c) 5 h

For the formation of ZnO/Au and ZnO/Ag particles, the as-synthesized ZnO nanoparticles were well dispersed in aqueous medium and as source materials of Au and Ag nanoparticle, $HAuCl_4$ and $AgNO_3$ were used. Weak van der Waals force or electrostatic interaction may act as a driving force behind the absorption of metal ions on the surface of ZnO. Finally, the adsorbed $AuCl_4^-$ and Ag^+ ions were reduced and deposited randomly on the surface of ZnO using hydrazine hydrate as a reducing agent. Though similar synthetic approaches were used for Au and Ag, the density of deposited Au nanoparticles was higher than that of Ag, which presumably due to higher affinity of $AuCl_4^-$ than Ag^+ towards ZnO surface.

This higher affinity of $AuCl_4^-$ ion could be explained from zeta-potential analysis of ZnO particles. The zeta-potential value of ZnO is (+)25.4±0.63 mV, which confirms a positively charged ZnO surface which is stabilized in the ambient of cationic charge CTAB [14]. Hence, a strong electrostatic interaction between the positively charged ZnO and negatively charged $AuCl_4^-$ is expected which results in a high density of Au nanoparticle on ZnO surface. Whereas, on the other hand, Coulomb repulsion between Ag^+ ion and ZnO significantly exists. However, the diffusion energy successfully overcomes the electrostatic repulsion and finally Ag nanoparticles can deposit on ZnO surface. It is quite clear that the driving force for Ag deposition is much weaker compare to the Au, and hence a lower particle density for Ag is observed. Zhu and co-workers also reported a high density of Au nanoparticles on ZnO using electrochemical deposition [42]. The overall mechanism behind the formation of ZnO/Au and ZnO/Ag nanoparticle on ZnO nanoflower are explained as can be find in **Scheme 3.1**.
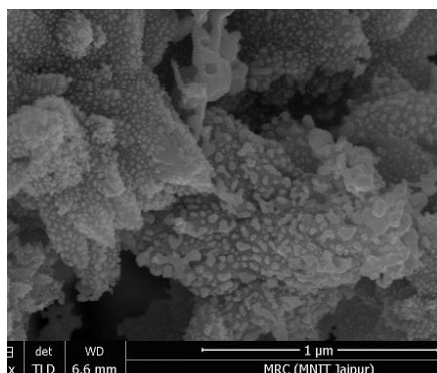
Figure 3.13 FESEM image of ZnO/Au using sodium borohydride (non-uniform deposition of Au nanoparticles)

To substantially understand the role of hydrazine hydrate, a similar kind of experiment was carried with sodium borohydride as reducing agent. A large and agglomerated particles of Au and Ag were observed on the surface of ZnO nanoflower. **Figure 3.13** shows the FESEM image of ZnO/Au using sodium borohydride where the Au nanoparticle appear in large, non-uniform, and aggregated nature. Trisodium citrate and ascorbic acid were also used as reducing agent but there were no desirable nanoparticle formation in the followed reaction condition.

Therefore, it is well understood from our findings that hydrazine hydrate can be used as a reducing agent to deposit uniform Au and Ag nanoparticles on ZnO surface.

3.3.3 Photocatalysis Study

To examine the photocatalytic activity, MB was chosen as a probe molecule. To study the photocatalytic effect, 4.0 mL of 5×10^{-5} M MB and 50 mg catalyst were collected in 16 mL water. Prior to any irradiation, the aqueous solution of MB and catalyst were agitated continuously at room temperature for ~ 40 min using a sonicator, so that MB was adsorbed well on the catalytic surface. After agitation, the reaction mixture was kept under a UV/visible light to initiate the reaction with continuous stirring and the distance between the light source and reaction mixture was fixed at ~ 20 cm. The UV light was provided by a UV lamp with major emission at $\lambda = 365$ nm whereas visible light was supplied using a tungsten lamp of 60 W, which emits a continuous spectrum of light in between 300-1400 nm. During the photocatalysis investigation, reaction mixture was stirred continuously. Finally, at a regular irradiation time interval, the dye containing solution was quantified by measuring the absorbance using the UV-vis spectroscopy. The as-synthesized nanoparticles were very stable and the morphology was unchanged even after prolonged photodecomposition. To check the reusability, the catalyst particles were collected and washed 3-4 times with deionized water.

Similar photocatalysis study was also performed with phenol using ZnO/Au and ZnO/Ag nanocatalysts. For this study, 0.8 mL of 5×10^{-3} M phenol and 50 mg catalyst were mixed in 20 mL water. After ~ 40 min sonication of the reaction mixture, a tungsten lamp of 60 W was used as a vissible light source to degrade the phenol.

The efficiency of dye degradation was calculated using the following equation:

$$\text{\% Degradation} = (A_0 - A_t)/A_0 \times 100$$

where, A_0 = initial absorbance and A_t = absorbance at time 't'.

Figure 3.14.a, b, and **c** shows the visible light active dye degradation results using 50 mg ZnO/Au as a catalyst where tungsten lamp (60 W) was used as a visible light source. Under the experimental condition, ZnO/Au exhibits 99% dye decomposition within 30 min, with a rate constant of 0.8×10^{-1} min^{-1}. It is known that the concentration of the dye at different time is proportional to the absorbance of the dye solution and therefore, exponential nature of absorbance vs. time (A_t/A_0 vs. t) plot confirms the pseudo first order kinetics of the reaction, as shown in **Figure 3.14.b**. From the logarithmic plot of absorbance vs. time (ln A_t/A_0 vs. t) the degradation rate constant 'k' was calculated, which is found to be 0.8×10^{-1} min^{-1}, significantly higher than the earlier reported values for MB dye decomposition (**Figure 3.14.c**).

It can be noticed that negligible amount of dye degradation occurs in visible light using bare ZnO particle. Even, without any catalyst MB itself has less absorption (~ 9% only) in visible light. Whereas, using ZnO/Ag catalyst, 40% of dye degradation can be achieved within 2 h under same visible light, with a rate constant of 0.04×10^{-1} min^{-1} (**Figure 3.15.a** and **b**).
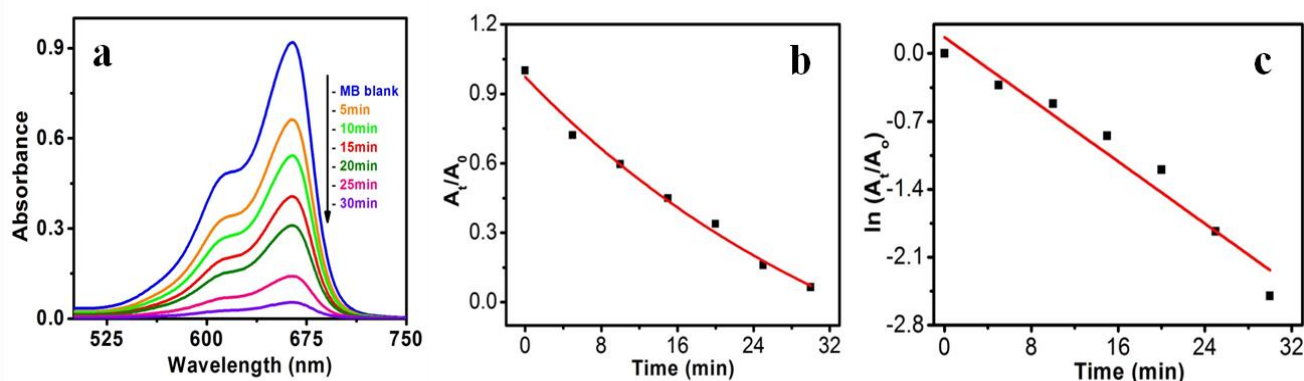
Figure 3.14 UV-vis absorption spectra of (a) degradation of MB dye in presence of ZnO/Au under visible light (b) A$_t$/A$_0$ vs. time (min) plot and (c) ln A$_t$/A$_0$ vs. time (min) plot. During the photocatalysis measurements, reaction mixture was stirred continuously. Conditions: [MB] = 10^{-5} M and amount of catalyst = 50 mg
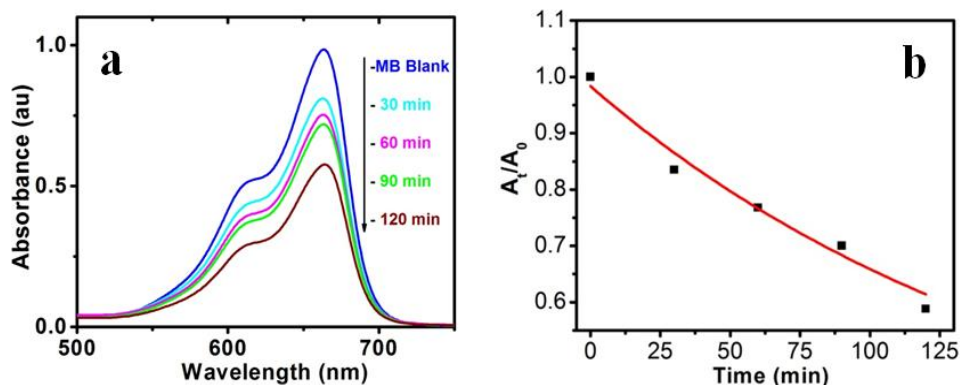
Figure 3.15 (a) Degradation of MB dye in presence of ZnO/Ag nanoparticles under visible light and (b) A_t/A_o vs. time (min) plot

Afterward, there is no change in dye degradation using ZnO/Ag and in visible light-medium. Similar dye degradation reaction was also carried out in presence of ZnO, ZnO/Au, and ZnO/Ag catalysts in dark condition, which shows there is no change in the intensity of MB even after 3 h (**Figure 3.16**). This experiment confirms that the dye is not getting adsorbed on the surface of the catalyst. Therefore, we can conclude that the incorporation of Au nanoparticles on ZnO surface can drastically enhance the dye degradation rate up to 20 times as compared to Ag nanoparticle incorporation using visible light.
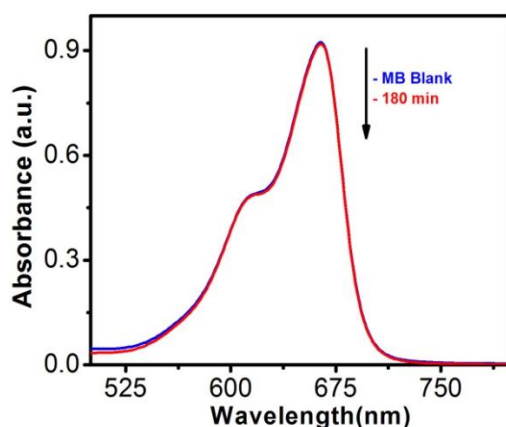
Figure 3.16 Degradation of MB dye in presence of ZnO, ZnO/Au, and ZnO/Ag nanoparticles under dark condition

The higher degradation rate for metal-induced ZnO can be explained in terms of better separation of the electrons and holes and higher inhibition towards their recombination. This phenomenon of ZnO/Au is in accordance with the PL result, which proves the higher inhibition of electron hole pair recombination for ZnO/Au nanoparticles. From all these results it is well understood that the modified ZnO with Au and Ag metal nanoparticles shows significantly higher photocatalytic efficiency in visible light region.

Photocatalytic activity of ZnO/Au and ZnO/Ag was also performed using another organic pollutant, phenol, under a visible light irradiation. Phenol, a colourless pollutant, was chosen as it has no absorption in the visible light range. Higher concentration of phenol, 2×10^{-4} M and 50 mg catalyst were used for this degradation study. **Figure 3.17.a** and **b** exhibits the decomposition of phenol with time, using ZnO/Au and ZnO/Ag catalyst, respectively.

As shown in **Figure 3.17.a**, ~ 96% degradation of phenol can be achieved after 6 h using ZnO/Au with a rate constant of 0.51 min^{-1}. Whereas, ~ 72% of degradation under visible light is found with ZnO/Ag as shown in **Figure 3.17.b**. Using ZnO/Ag, the rate constant value was 0.20 min^{-1}. Therefore, a significantly faster photocatalytic performance was observed with ZnO/Au, 2.5 times higher than ZnO/Ag. The above result proves that under visible light ZnO/Au can be a better catalyst than ZnO/Ag, which is matching well with the earlier MB degradation result.
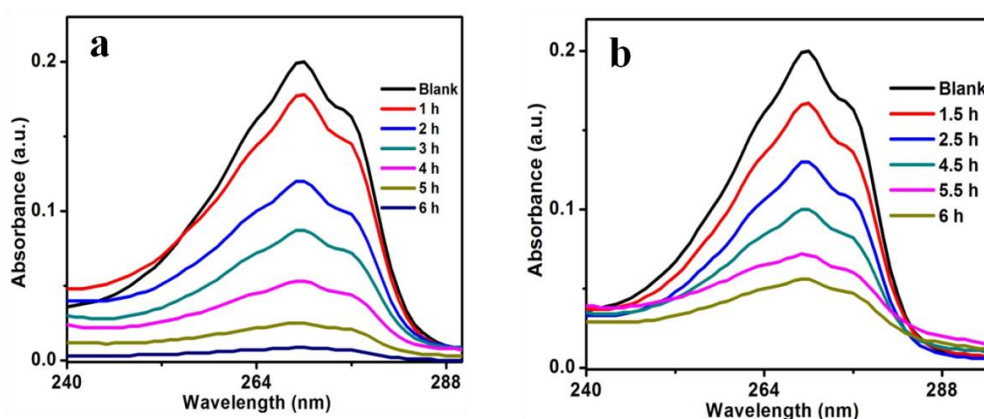
Figure 3.17 (a) UV-vis absorption spectra to show (a) decomposition of phenol using ZnO/Au catalyst, under irradiation of visible light (b) decomposition of phenol using ZnO/Ag under irradiation with visible light. Conditions: [phenol] = 2×10^{-4} M and amount of catalyst = 50 mg

In case of dye degradation using pure ZnO nanoparticles, a relatively higher photon energy (UV-light of wavelength 365 nm) as well as much longer exposure time is required for ~ 50% of decomposition. Whereas, under illumination of UV-light for 30 min, ZnO/Au can successfully degrade up to 99% of the dye. In the case of ZnO/Ag nanoparticles, 95% degradation can be achieved for exposure duration of 3 h. UV-vis spectra of MB dye degradation with ZnO, ZnO/Au, and ZnO/Ag using UV light are compared within the **Figure 3.18**, **3.19**, and **3.20**. From the kinetic plots of dye degradation with ZnO particles (A_t/A_0 vs. t and ln A_t/A_0 vs. t) it is quite clear that the reaction follows pseudo first order and the rate constant value is found to be 0.04×10^{-1} min^{-1}.
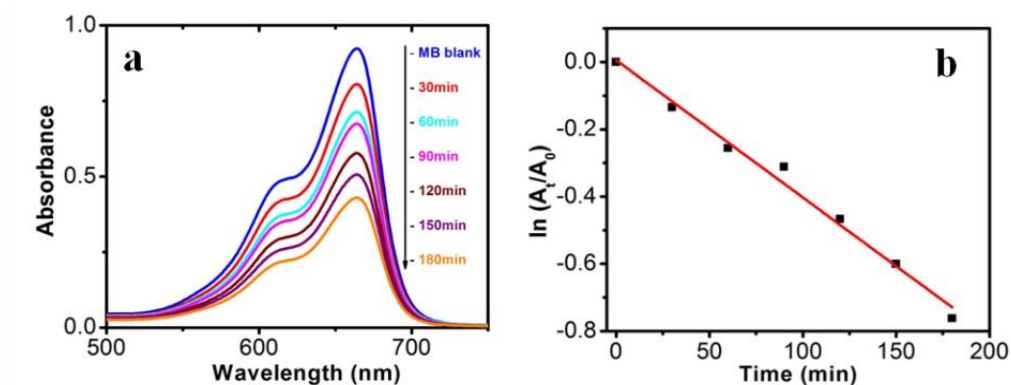
Figure 3.18 (a) Degradation of MB dye in presence of ZnO nanoparticles under UV light and (b) ln A_t/A_o vs. time (min) plot
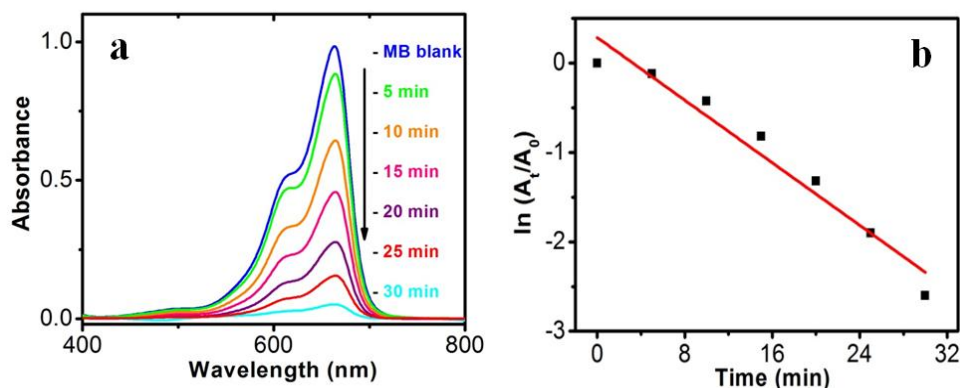
Figure 3.19 (a) Degradation of MB dye in presence of ZnO/Au nanoparticles under UV light and (b) ln A_t/A_o vs. time (min) plot
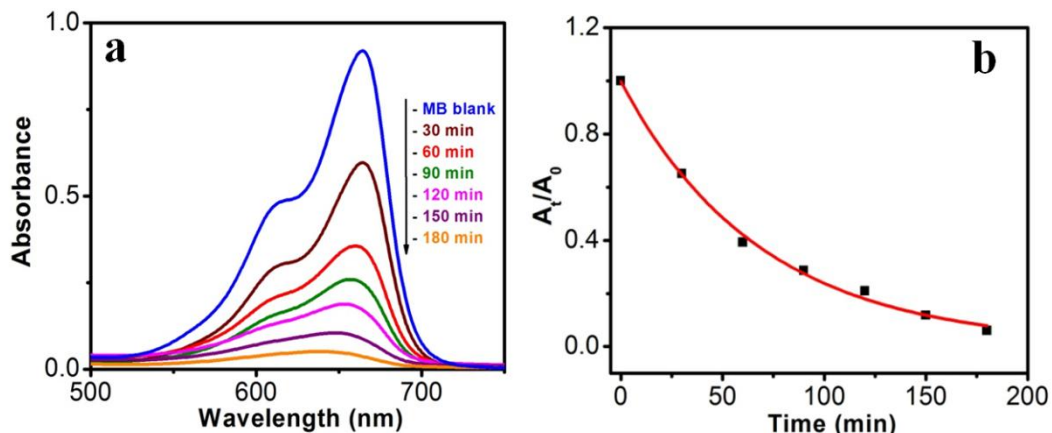
Figure 3.20 (a) Degradation of MB dye in presence of ZnO/Ag nanoparticles under UV light and (b) A_t/A_o vs. time (min) plot

Using ZnO/Au, the dye degradation rate constant value is drastically improved to 0.9×10^{-1} min^{-1} while following the similar pseudo first order kinetics.

A similar kinetics and rate constant value (0.15×10^{-1} min^{-1}) is also observed with ZnO/Ag particles, which can be seen in **Figure 3.20.a** and **b**.

A comparative study of ln A_t/A_0 vs. time plot for the as-synthesized particles for MB dye decomposition using UV light is shown in **Figure 3.21.a** and **b**.

This result shows that Au decorated ZnO provide maximum rate constants compare to that of ZnO/Ag and bare ZnO, which is in good agreement with the reported literature [10,42].
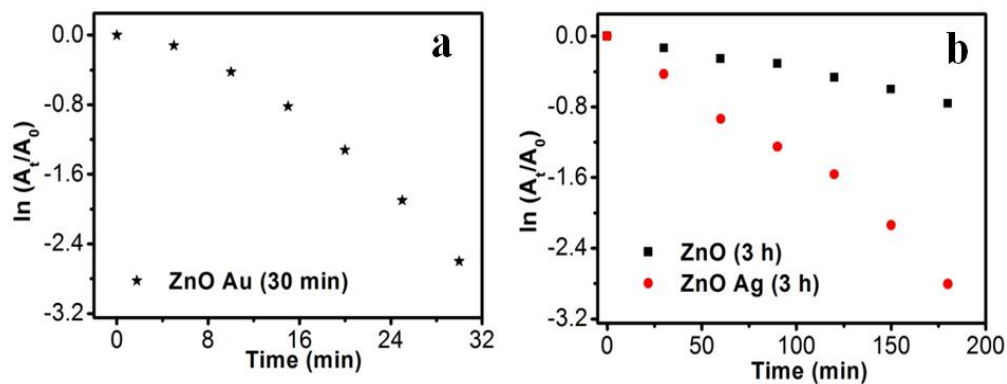
Figure 3.21 Comparative study using (a) ZnO/Au, (b) ZnO and ZnO/Ag under UV light

3.3.4 Photocatalytic Mechanism

Scheme 3.2.a represents the overall photocatalytic degradation mechanism under irradiation with visible light. The as-obtained visible light photocatalysis result confirms that ZnO/Au is a better photocatalyst than ZnO/Ag and ZnO particles, which can be explained on the basis of work function. The work function values of ZnO, Au, and Ag are reported as 5.2 eV, 5.0 eV, and 4.26 eV, respectively [28,47-50]. Normally, a Schottky barrier will form, when two materials with different work functions are combined. Therefore, electrons will transfer from the lower work function material to the higher work function material [30,47-50]. In case of Au and Ag the Fermi level (F_M) is higher than ZnO Fermi level (F_{MO}) because of its higher work function. This directs the transfer of electron from the Au and Ag Fermi level to the ZnO Fermi level, till it reaches the equilibrium and form a new equilibrium Fermi level (F_{Eq}).

Upon irradiation with visible light, the electrons in F_{Eq} were injected quickly to the conduction band (CB) of ZnO via a surface phonon resonance (SPR) mechanism, leaving behind holes on the metal surface. Now, the injected electrons in CB reacts with dissolve oxygen to produce superoxide radical anion ($O_2^{-\bullet}$), which can subsequently react with H_2O to give hydroxyl radicals ($OH^\bullet$) in a consecutive reaction pathway [31,49]. These superoxide radical anion and hydroxyl radicals are responsible for the decomposition of MB dye and phenol pollutant under visible light irradiation [28]. Therefore, due to higher work function of Au as compared to Ag, ZnO/Au can act as a better photocatalyst than ZnO/Ag [47-49]. As the formation of reactive radical species is much faster in ZnO/Au compared to the ZnO/Ag, which is also directly correlated with photocatalytic activity, the ZnO/Au particle shows a superior activity. This result is well corroborated with the lower intensity of ZnO/Au than ZnO/Ag in PL study (**Figure 3.2**).

Scheme 3.2.b demonstrates the degradation mechanism upon irradiation with UV light using ZnO, ZnO/Au, and ZnO/Ag catalysts. In case of ZnO, during illumination with UV light valence band (VB) electrons get excited and move to the CB, leaving behind holes (h^+) in the VB of the semiconductor particles. Then the excited electrons in CB react with dissolve oxygen to produce superoxide radical anions ($O_2^{-\bullet}$), which can subsequently react with H_2O to provide $OH^\bullet$ radicals in a consecutive reaction pathway [31]. At the same time, the holes in VB react with surface OH^- ion or adsorbed H_2O molecule to produce the reactive $OH^\bullet$ radicals. These $O_2^{-\bullet}$ and

OH$^{\bullet}$ radicals are also responsible for the further degradation of dye molecules [9,51]. As a result, the dye molecules finally degrade to CO_2 and H_2O. On the other hand, with ZnO/Au and ZnO/Ag, the presence of Au and Ag nanoparticles effectively adsorb electrons from CB and hence prevent the immediate recombination process [52]. Here, Au and Ag nanoparticles are used as surface traps, which usually capture the electrons from the ZnO surface and utilizes for dye degradation [10-13]. Successive electron transfer will be favorable with the suitable junction formation between ZnO and metal nanoparticle (**Figure 3.6.b, 3.7.b**).
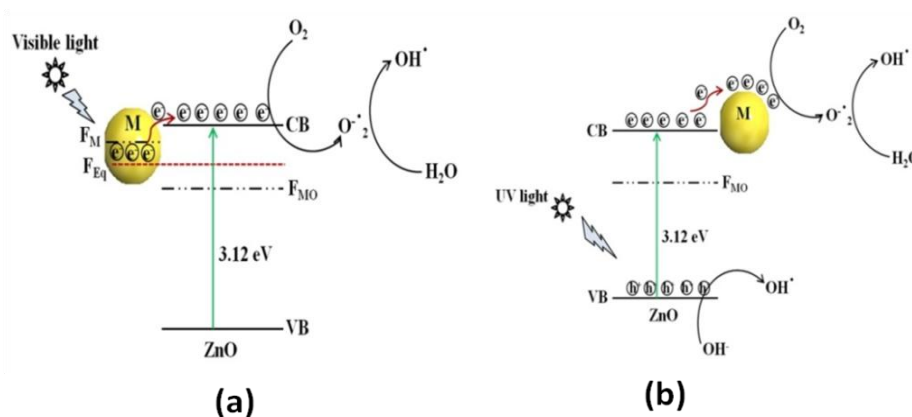
Scheme 3.2 The overall dye degradation mechanism under irradiation of (a) visible light and (b) UV light, with ZnO/Au and ZnO/Ag nanoparticles. Here, VB = valence band, CB = conduction band, F_{MO} = Fermi level of metal oxide, F_M = Fermi level of metal, F_{Eq} = Fermi level of equilibrium, and M = Au and Ag

Therefore, the deposited metal nanoparticles (Au and Ag) can act as an electron sink or trap on the surface of ZnO particles [30]. Under the same conditions, the higher work function value of Au as compared to Ag make ZnO/Au more-effective for electron acceptor [47-49]. As a result, ZnO/Au exhibits better photocatalytic efficiency in comparison with ZnO/Ag and ZnO. This result is also in line with PL study of ZnO/Au and ZnO/Ag particles (**Figure 3.2**). The overall reaction during photocatalysis with visible and UV light are shown below.

$$ZnO + h\nu \text{ (UV)} \rightarrow ZnO \ (e_{CB}^- + \ h_{VB}^+)$$
$$ZnO \ /M + h\nu \text{ (Visible)} \rightarrow ZnO \ /M^*(e^-)$$

$$ZnO\ /M^*(e^-\ ) \rightarrow\ ZnO\ (e^-_{CB}) + M$$
$$e^-_{CB} +\ O_2 \rightarrow\ O^-_2{}^{\cdot}$$
$$h^+_{VB} +\ OH^- \rightarrow\ OH^{\cdot}$$
$$O^-_2{}^{\cdot} +\ 2H^+ \ \rightarrow 2OH^{\cdot}$$
$$OH^{\cdot} + MB/\ Phenol\ \rightarrow Decomposed\ Products$$
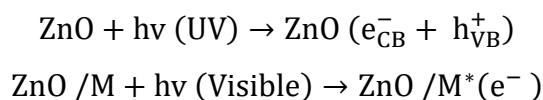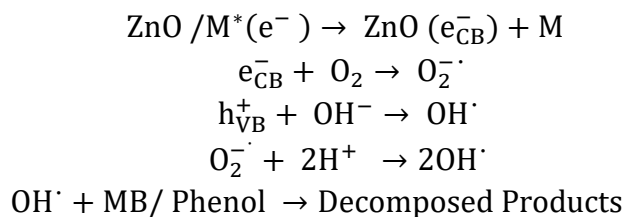
To further investigate the photocatalytic mechanism with better clarity or to understand the actual involvement of the species (e^- or h^+) for the dye degradation, several scavenging experiments were systematically performed. Ammonium oxalate (AO) and tertiary butyl alcohol (TBA) were used for hole and OH^-/e^- scavenger, respectively. While doing the photocatalysis reaction, 0.1 g of AO and 2 mL of TBA were added to the solution, prior to any addition of catalyst while keeping the other parameters unaltered. It can be noted that the photocatalytic activity of ZnO/Au decreases significantly with the addition of both AO and TBA under a visible light source. A significant decrease is also noticed when AO was added, which behave as hole scavenger. For ZnO/Au, all photocatalytic studies were performed for 30 min. In presence of AO, ZnO/Au catalyst shows 36.67% dye degradation when illuminated with visible light, whereas, with TBA 86.82% dye degradation was observed. Therefore, from this finding, it can be concluded that the holes play an important role towards dye degradation under visible light. On the other hand, in presence of UV-light, photodegradation rate is significantly decreased for both ZnO/Au and ZnO/Ag when AO and TBA were added. In presence of AO and TBA degradation of only 39.41% and 36.87% dye are observed with ZnO/Au in presence of UV light. Whereas, for ZnO/Ag catalyst, the amount of dye degradation increased to 68.18% and 42.45%, respectively. This photodegradation result confirms that the photogenerated holes and electrons both can play a major role when catalysis experiments are performed under UV light. The overall scavenging results match well with the earlier literature for both UV and visible light [32,53].

3.3.5 Reusability of the Catalyst Particles

The reusability of ZnO/Au nanoparticles as a photocatalyst in dye decomposition process, have also been tested using a visible light source. The catalyst particles were centrifuged and washed thoroughly before using for each cycle. The photodegradation experiments were repeated for three times with visible light and the corresponding degradation results show 94.7%, 86.2%,

and 76.4% of dye degradation for first, second, and third cycle, respectively. **Figure 3.22.a** represents the percentage of degradation after 30 min as a function of cycle number, which confirms that the catalysts remain stable even after third cycle.

After photocatalysis, the crystal structure of the ZnO, ZnO/Au, and ZnO/Ag catalyst particles was confirmed with the help of PXRD and the result is shown in **Figure 3.22.b**. The reusability of ZnO/Au and ZnO/Ag catalysts using UV light has also been examined and the results confirm its activeness even after third cycle, as can be seen in the, **Figure 3.23**.
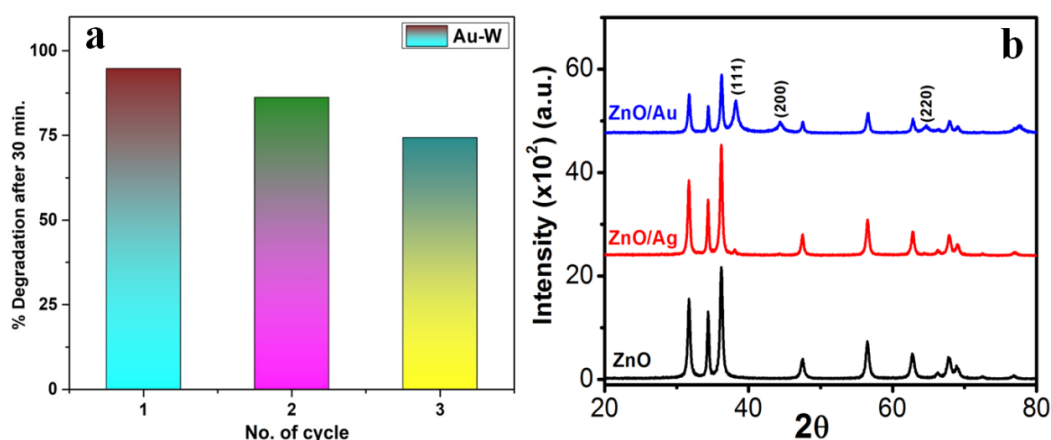
Figure 3.22 (a) Percentage of degradation vs. number of cycle plot for ZnO/Au nanoparticles after 30 min exposure under a visible light source. The catalyst particles were centrifuged and washed well before each cycle of use and (b) powder X-ray diffraction patterns of ZnO, ZnO/Au, and ZnO/Ag nanoparticles after reusability of catalyst
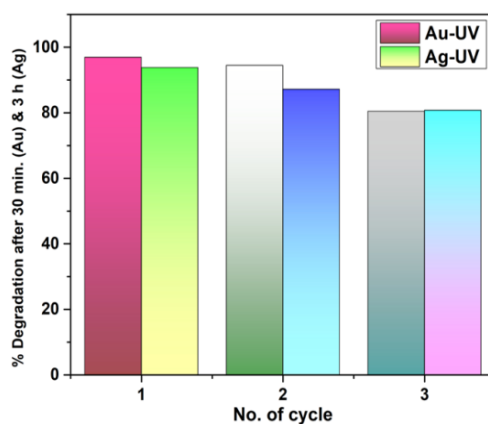
Figure 3.23 Reusability test with ZnO/Au and ZnO/Ag nanoparticles using UV light

3.4 Conclusion

In summary, a surfactant assisted simple and convenient method is developed for the preparation of ZnO nanoflower. This ZnO nanoflower surface is further modified with Au and Ag metal nanoparticle which significantly improves the catalytic behaviour of the material. Characterizations accomplish using UV, PL, PXRD, FESEM, TEM, EDS, and XPS techniques very much confirms the formation of nanometer scale Au/Ag dots of homogeneous size and density on top of the flower-like ZnO surfaces. Photodegradation tests using MB dye in presence of UV and visible light ensures a drastic improvement of the catalytic efficiency and photoreactivity of the material after introducing the metal nanoparticles. Scavenging experiments with different scavengers significantly help to understand the underlying mechanism of the reactive species (holes and electrons) involved in photodegradation reaction. Finally, the entire study has a large scale impact and remarkable application on treatment of dye effluents from the textile industries. Therefore, it can be concluded that our investigations can provide a new avenue for the controlled synthesis of size and shape dependent Au and Ag nanoparticles on a semiconductor surface, which can widely be used in electrocatalysis, water splitting etc.

References

[1]   Das, J.; Khushalani, D. Nonhydrolytic Route for Synthesis of ZnO and its use as a Recyclable Photocatalyst. *J. Phys. Chem. C* **2010**, *114*, 2544-2550.

[2]   Becker, J.; Raghupathi, K. R.; Pierre, J. S.; Zhao, D; Koodal, R. T. Tuning of the Crystallite and Particle Sizes of ZnO Nanocrystalline Materials in Solvothermal Synthesis and their Photocatalytic Activity for Dye Degradation. *J. Phys. Chem. C* **2011**, *115*, 13844-13850.

[3]   Zeng, H.; Cai, W.; Liu, P.; Xu, X.; Zhou, H.; Klingshirn, C.; Kalt, H. ZnO-Based Hollow Nanoparticles by Selective Etching: Elimination and Reconstruction of Metal−Semiconductor Interface, Improvement of Blue Emission and Photocatalysis. *ACS Nano* **2008**, *8*, 1661-1670.

[4]   Zeng, H.; Liu, P.; Cai, W.; Yang, S.; Xu, X. Controllable Pt/ZnO Porous Nanocages with Improved Photocatalytic Activity. *J. Phys. Chem. C* **2008**, *112*, 19620-19624.

[5]   Yuan, J.; Choo, E. S.; Tang, X.; Sheng, Y.; Ding J.; Xue, J. Synthesis of ZnO-Pt Nanoflowers and their Photocatalytic Applications. *Nanotechnology* **2010**, *21*, 185606.

[6]   Zhang, Y.; Xu, J.; Xu, P.; Zhu, Y.; Chen, X.; Yu, W. Decoration of ZnO Nanowires with Pt Nanoparticles and their Improved Gas Sensing and Photocatalytic Performance. *Nanotechnology* **2010**, *21*, 285501.

[7]   Li, P.; Wei, Z.; Wu, T.; Peng, Q.; Li, Y. Au-ZnO Hybrid Nanopyramids and their Photocatalytic Properties. *J. Am. Chem. Soc.* **2011**, *133*, 5660-5663.

[8]   Wang, Q.; Geng, B.; Wang, S. ZnO/Au Hybrid Nanoarchitectures: Wet-Chemical Synthesis and Structurally Enhanced Photocatalytic Performance. *Environ. Sci. Technol.* **2009**, *43*, 8968-8973.

[9]   Zheng, Y.; Chen, C.; Zhan, Y.; Lin, X.; Zheng, Q.; Wei, K.; Zhu, J. Photocatalytic Activity of Ag/ZnO Heterostructure Nanocatalyst: Correlation Between Structure and Property. *J. Phys. Chem. C* **2008**, *112*, 10773-10777.

[10]   Deng, Q.; Duan, X.; Ng, D. H.; Tang, H.; Yang, Y.; Kong, M.; Wu, Z.; Cai, W.; Wang, G. Ag Nanoparticle Decorated Nanoporous ZnO Microrods and their Enhanced Photocatalytic Activities. *ACS Appl. Mater. Interfaces* **2012**, *4*, 6030-6037.

[11]   Kowalska, E.; Remita, H.; Colbeau-justin, C.; Hupka, J.; Belloni, J. Modification of

Titanium Dioxide with Platinum Ions and Clusters: Application in Photocatalysis. *J. Phys. Chem C* **2008**, *112*, 1124-1131.

[12]   Wang, P.; Huang, B.; Dai, Y; Whangbo, M.H. Plasmonic Photocatalysts: Harvesting Visible Light with Noble Metal Nanoparticles. *Phys. Chem. Chem. Phys.* **2012**, *4*, 9813-9825.

[13]   Chan, S.C.; Barteau, M.A. Preparation of Highly Uniform Ag/TiO$_2$ and Au/TiO$_2$ Supported Nanoparticle Catalysts by Photodeposition. *Langmuir* **2005**, *21*, 5588-5595.

[14]   Zhang, H.; Yang, D.; Ji, Y.; Ma, X.; Xu, J.; Que, D. Low Temperature Synthesis of Flowerlike ZnO Nanostructures by Cetyltrimethylammonium Bromide-Assisted Hydrothermal Process. *J. Phys. Chem. B* **2004**, *108*, 3955-3958.

[15]   Komarneni, S.; Bruno, M.; Mariani, E. Synthesis of ZnO with and without Microwaves. *Mater. Res. Bull.* **2000**, *35*, 1843-1847.

[16]   Cheng, Y.; Jiao, W.; Li, Q.; Zhang, Y.; Li, S.; Li, D.; Che R. Two hybrid Au-ZnO aggregates with different hierarchical structures: A comparable study in photocatalysis. *J. Colloid Interface Sci.* **2018**, *509*, 58-67.

[17]   Zhang, X. H.; Xie, S. Y.; Jiang, Z. Y.; Zhang, X.; Tian, Z. Q.; Xie, Z.X.; Huang, R. B.; Zheng, L. S. Rational Design and Fabrication of ZnO Nanotubes from Nanowire Templates in a Microwave Plasma System. *J. Phys. Chem. B* **2003**, *107*, 10114-10118.

[18]   Shao, Z. B.; Wang, C. Y.; Geng, S. D.; Sun, X. D.; Geng, S. J. Fabrication of Nanometer-Sized Zinc Oxide at Low Decomposing Temperature. *J. Mater. Process. Technol.* **2006**, *178*, 247-250.

[19]   Perez-Lopez, O. W.; Farias, A. C.; Marcilio, N. R.; Bueno, J. M. C. The Catalytic Behavior of Zinc Oxide Prepared from Various Precursors and by Different Methods. *Mater. Res. Bull.* **2005**, *40*, 2089-2099.

[20]   Wang, D.; Song, C. Controllable Synthesis of ZnO Nanorod and Prism Arrays in a Large Area. *J. Phys. Chem. B* **2005**, *109*, 12697-12700.

[21]   Tang, H.; Chang, J. C.; Shan, Y.; Lee, S. T. Surfactant-Assisted Alignment of ZnO Nanocrystals to Superstructures. *J. Phys. Chem. B* **2008**, *112,* 4016-4021.

[22]   Chakraborty, S.; Kole, A. K.; Kumbhakar, P. Room Temperature Chemical Synthesis of Flower-Like ZnO Nanostructures. *Mater. Lett.* **2012**, *67*, 362-364.

[23]   Miao, T. T.; Sun, D. X.; Guo, Y. R.; Li, C.; Ma, Y. L.; Fang, G. Z.; Pan, Q. J. Low-

Temperature Precipitation Synthesis of Flower-Like ZnO with Lignin Amine and its Optical Properties. *Nanoscale Res. Lett.* **2013**, *8*, 431.

[24] Kaviyarasu, K.; Devarajan, P. A. A Convenient Route to Synthesize Hexagonal Pillar Shaped ZnO Nanoneedles via CTAB Surfactant. *Adv. Mat. Lett.* **2013**, *4*, 582-585.

[25] Song, L.; Zhang, S.; Wu, X.; Wei, Q. Controllable Synthesis of Hexagonal, Bullet-Like ZnO Microstructures and Nanorod Arrays and their Photocatalytic Property. *Ind. Eng. Chem. Res.* **2012**, *51*, 4922-4926.

[26] Wen, B.; Huang, Y.; Boland, J. J. Controllable Growth of ZnO Nanostructures by a Simple Solvothermal Process. *J. Phys. Chem.* **2008**, *112*, 106-111.

[27] Shen, L.; Bao, N.; Yanagisawa, K.; Domen, K.; Grimes, C. A.; Gupta, A. Organic Molecule-Assisted Hydrothermal Self-Assembly of Size-Controlled Tubular ZnO Nanostructures. *J. Phys. Chem. C* **2007**, *111*, 7280-7287.

[28] Udawatte, N.; Lee, M.; Kim, J.; Lee, D. Well-Defined Au/ZnO Nanoparticle Composites Exhibiting Enhanced Photocatalytic Activities. *ACS Appl. Mater. Interfaces* **2011**, *3*, 4531-4538.

[29] Lee, J.; Shim, H. S.; Lee, M.; Song, J. K.; Lee, D. Size-Controlled Electron Transfer and Photocatalytic Activity of ZnO-Au Nanoparticle Composites. *J. Phys. Chem. Lett*. **2011**, *2*, 2840-2845.

[30] Subramanian, V.; Wolf, E. E.; Kamat, P. V. Green Emission to Probe Photoinduced Charging Events in ZnO-Au Nanoparticles. Charge Distribution and Fermi-Level Equilibration. *J. Phys. Chem. B* **2003**, *107*, 7479-7485.

[31] Zheng, Y.; Zheng, L.; Zhan, Y.; Lin, X.; Zheng, Q.; Wei, K. Ag/ZnO Heterostructure Nanocrystals: Synthesis, Characterization, and Photocatalysis. *Inorg. Chem.* **2007**, *46*, 6980-6986.

[32] Liu, H. R.; Shao, G. X.; Zhao, J. F.; Zhang, Z. X.; Zhang, Y.; Liang, J.; Liu, X. G.; Jia, H. S.; Xu, B. S. Worm-Like Ag/ZnO Core-Shell Heterostructural Composites: Fabrication, Characterization, and Photocatalysis. *J. Phys. Chem. C* **2012**, *116*, 16182-16190.

[33] Zhao, X.; Su, S.; Wu, G.; Li, C.; Qin, Z.; Lou, X.; Zhou, J. Facile Synthesis of the Flower-like Ternary Heterostructure of Ag/ZnO Encapsulating Carbon Spheres with Enhanced Photocatalytic Performance. *Appl. Surf. Sci.* **2017**, *406*, 254-264.

[34] Bao, Z.; Yuan, Y.; Leng, C.; Li, L.; Zhao, K.; Sun Z. One-Pot Synthesis of Noble

Metal/Zinc Oxide Composites with Controllable Morphology and High Catalytic Performance. *ACS Appl. Mater. Interfaces* **2017,** *9*, 16417-16425.

[35] Yang, Y.; Li, H.; Hou, F.; Hu, J.; Zhang, X.; Wang, Y. Facile Synthesis of ZnO/Ag Nanocomposites with Enhanced Photocatalytic Properties under Visible Light. *Mater. Lett.* **2016**, *180*, 97-100.

[36] Pande, S.; Ghosh, S. K.; Nath, S.; Praharaj, S.; Jana, S.; Panigrahi, S.; Basu, S.; Pal, T. Reduction of Methylene Blue by Thiocyanate: Kinetic and Thermodynamic Aspects. *J Colloid Interface Sci.* **2006**, *299*, 421-427.

[37] Brus, L. Electronic Wave Functions in Semiconductor Clusters: Experiment and Theory. *J. Phys. Chem.* **1986**, *90,* 2555-2560.

[38] Ghobadi, N. Band Gap Determination Using Absorption Spectrum Fitting Procedure. *Int. Nano Lett.* **2013**, *3*, 2.

[39] Chandrappa, K. G.; Venkatesha, T. V. Electrochemical Synthesis and Photocatalytic Property of Zinc Oxide Nanoparticles. *Nanomicrolett* **2012**, *4*, 14-24.

[40] Sarkar, S.; Makhal, A.; Bora, T.; Baruah, S.; Dutta, J.; Pal, S. K. Photoselective Excited State Dynamics in ZnO-Au Nanocomposites and their Implications in Photocatalysis and Dye-Sensitized Solar Cells. *Phys. Chem. Chem. Phys.* **2011**, *13*, 12488-12496.

[41] Van Dijken, A.; Meulenkamp, E. A.; Vanmaekelbergh, D.; Meijerink, A. The Kinetics of the Radiative and Nonradiative Processes in Nanocrystalline ZnO Particles upon Photoexcitation. *J. Phys. Chem. B* **2000**, *104*, 1715-1723.

[42] Ahmad, M.; Yingying, S.; Nisar, A.; Sun, H.; Shen, W.; Wei, M.; Zhu, J. Synthesis of Hierarchical Flower-like ZnO Nanostructures and their Functionalization by Au Nanoparticles for Improved Photocatalytic and High Performance Li-ion Battery Anodes. *J. Mater. Chem.* **2011**, *21*, 7723-7729.

[43] Dake, L. S.; Baer, D. R.; Zachara, J. M. Auger Parameter Measurements of Zinc Compounds Relevant to Zinc Transport in the Environment. *Surf. Interface Anal.* **1989**, *14*, 71-75.

[44] Pande, S.; Ghosh, S. K.; Praharaj, S.; Panigrahi, S.; Basu, S.; Jana, S.; Pal, A.; Tsukuda, T.; Pal, T. Synthesis of Normal and Inverted Gold-Silver Core-Shell Architectures in β-cyclodextrin and their Applications in SERS. *J. Phys. Chem. C* **2007**, *111*, 10806-10813.

[45] Mansour, A. N. Gold Mg K$_\alpha$ XPS Spectra from the Physical Electronics Model 5400 Spectrometer. *Surf. Sci. Spectra* **1994**, *3*, 197-201.

[46] Seah, M. P.; Gilmore, I. S.; Beamson, G. XPS: Binding Energy Calibration of Electron Spectrometers 5-Re-evaluation of the Reference Energies. *Surf. Interface Anal.* **1998**, *26*, 642-649.

[47] Ansari, S. A.; Khan, M. M.; Ansari, M. O.; Lee, J.; Cho, M. H. Biogenic Synthesis, Photocatalytic, and Photoelectrochemical Performance of Ag-ZnO Nanocomposite. *J. Phys. Chem. C* **2013**, *117*, 27023-27030.

[48] Saravanan, R.; Karthikeyan, N.; Gupta, V. K.; Thirumal, E.; Thangadurai, P.; Narayanan, V.; Stephen, A. ZnO/Ag Nanocomposite: An Efficient Catalyst for Degradation Studies of Textile Effluents Under Visible Light. *Mater. Sci. Eng. C* **2013**, *33*, 2235-2244.

[49] Sangpour, P.; Hashemi, F.; Moshfegh, A. Z. Photoenhanced Degradation of Methylene Blue on Cosputtered M: TiO$_2$ (M= Au, Ag, Cu) Nanocomposite Systems: A Comparative Study. *J. Phys. Chem. C* **2010**, *114*, 13955-13961.

[50] Jing, L.; Zhou, W.; Tian, G.; Fu, H. Surface Tuning for Oxide-Based Nanomaterials as Efficient Photocatalysts. *Chem. Soc. Rev.* **2013**, *42*, 9509-9549.

[51] Height, M. J.; Pratsinis, S. E.; Mekasuwandumrong, O.; Praserthdam, P. Ag-ZnO Catalysts for UV-Photodegradation of Methylene Blue. *Appl. Catal. B: Environ.* **2006**, *63*, 305.

[52] Furube, A.; Du, L.; Hara, K.; Katoh, R.; Tachiya, M. Ultrafast Plasmon-Induced Electron Transfer from Gold Nanodots into TiO$_2$ Nanoparticles. *J. Am. Chem. Soc.* **2007**, *129*, 14852-14853.

[53] Zhang, N.; Liu, S.; Fu, X.; Xu, Y. J. Synthesis of M@TiO$_2$ (M= Au, Pd, Pt) Core-Shell Nanocomposites with Tunable Photoreactivity. *J. Phys. Chem. C* **2011**, *115*, 9136-9145.

Shape-dependent Synthesis of ZnO on Graphitic-Carbon Nitride Support for Photocatalytic Activity under Visible Light

✿ *A simple wet-chemical approach for the synthesis of morphology-dependent (dumbbell and cone) ZnO nanostructure on g-C₃N₄ surface using different hydrolyzing agents has been reported successfully.*

✿ *The heterostructure g-C₃N₄/ZnO used as a visible light driven photocatalyst to degrade MB and phenol.*
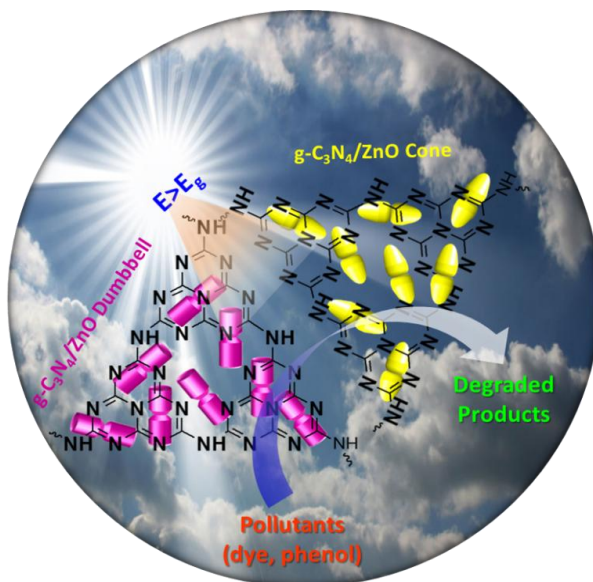
Abstract

Shape-dependent synthesis of ZnO has been developed on the surface of g-C$_3$N$_4$ following a simple and reproducible strategy. Initially, graphitic-carbon nitride (g-C$_3$N$_4$) was synthesized by pyrolysis of urea which was further used to grow ZnO nanostructures via refluxing condition. Different hydrolyzing agents, such as hexamethylenetetramine (HMT) and ammonia were used to synthesize dumbbell and cone structures, respectively. Apart from hydrolyzing agents, cetyltrimethylammoniumbromide (CTAB) was also used as a growth controlling agent. Structural, morphological and optical characterizations of the as-synthesized materials were performed by using FESEM, TEM, XRD, XPS, UV-vis etc. techniques. After successful synthesis, the as-synthesized heterostructures were explored as visible light driven photocatalysts towards the organic pollutant (methylene blue and phenol) degradation. Photocatalytic performance of bare ZnO, dumbbell and cone structures of g-C$_3$N$_4$/ZnO as well as g-C$_3$N$_4$, have been examined thoroughly. Photocatalytic results revealed that g-C$_3$N$_4$/ZnO heterostructures exhibit a higher efficiency under the illumination of visible light as compared to pure g-C$_3$N$_4$. Superior photodegradation activity of g-C$_3$N$_4$/ZnO heterostructure originated from the synergistic effect and high charge separation at the interface of g-C$_3$N$_4$ and ZnO has also been discussed.

4.1 Introduction

Carbon nitride has attracted enormous attention in the field of material science, since Liu and Cohen guess that carbon and nitride are good applicants for the intense rigidity of materials [1]. Unique layered structure and a characteristic electronic band structure of carbon nitride (C_3N_4) make it stable at ambient condition. Owing to their exclusive physicochemical properties, such as rigidity, light weight, chemical inertness, water resistivity, and biocompatibility, C_3N_4 has been regarded as one of the promising materials for surface functionalization, light emitting devices, and metal free electrocatalysis and photocatalysis [2-7]. Among the various allotropes of polymeric C_3N_4, graphite like carbon nitride (g-C_3N_4) is a promising and most stable allotrope. Graphitic (g)-C_3N_4 as an analogue of graphite has attracted considerable interests because of its suitable band alignment for water splitting, selective oxidation reactions, and environment pollutant degradation [2,8-10]. Interestingly, the matrix of g-C_3N_4 can offer active sites for binding with many organic/inorganic compounds or metals, which supply a convenient route to functionalize g-C_3N_4 surface with high reactivity [8,11-13].

g-C_3N_4 represents an important class of conjugated polymeric semiconductors [14]. Similar to graphene, g-C_3N_4 possesses π-conjugated electronic structure with a band gap of 2.7 eV [2-5,8,9,15]. g-C_3N_4 is a layered metal-free semiconductor with an interlayer distance of about 0.33 nm (single layer of g-C_3N_4) [6]. Bulk g-C_3N_4 can easily be prepared by polycondensation reaction of organic precursors, e.g., urea, cyanamide, dicyandiamide, and melamine. Liu and co-workers demonstrated a large-scale production of g-C_3N_4 by pyrolysis of urea using different reaction temperatures and times. They have also reported the photocatalytic activity of g-C_3N_4 in dye degradation using visible light [13]. Another simpler approach for the synthesis of polymeric g-C_3N_4 using urea as precursors and their application in rhodamine B (RhB) dye degradation using visible light has been reported by Dong and co-workers [12]. Surfactant (Pluronic P123) assisted synthesis of porous g-C_3N_4 using melamine has been reported by Yan and co-workers, where they found a significant improvement in the photocatalytic H_2 evolution from water using visible light [16]. Wang and co-workers [9] reported chemically and thermally stable polymeric carbon nitride, a metal free photocatalyst with high capability, to generate hydrogen from water. Additionally, they have modified the carbon nitride with small amount of Pt metal to vary the hydrogen production with better activity

and minimized experimental error. However, low quantum efficiency for Pt modified C_3N_4 surface has also been observed [9].

The photocatalytic performance of bare g-C_3N_4 is limited due to the high recombination rate of the photogenerated electron-hole pairs [17-21]. This restricted photocatalytic performance of g-C_3N_4 can be enhanced by synthesizing porous structures, [20-23] doping and/or coupling of g-C_3N_4 with transition metals, metal oxides and sulphides, and active protonation [19,24-28]. To increase the separation between photogenerated electron-hole pairs and to promote the photocatalytic activity, researchers have coupled g-C_3N_4 with ZnO, TiO_2, CdS, $ZnWO_4$, $BiPO_4$, Bi_2WO_6, and Ag_2O semiconductors [20-29]. Hence, efforts have been given to suppress the rate of recombination of charge carriers and improving the consumption of solar light, by combining two semiconductors. ZnO is an UV-light active and large exciton binding energy (60 MeV) material with $E_g = 3.37$ eV that also limits the practical application in visible light photocatalysis [30]. Sun and co-workers [20] reported a calcination process for the synthesis of a composite g-C_3N_4-ZnO as visible light photocatalysts with variable amount of ZnO, which they have utilized for methyl orange and p-nitrophenol photodegradation using visible light with 3-6 times better activity as compared to bare g-C_3N_4 [20]. The improved photocatalytic activity and optimum synergistic effect of ZnO hybridized g-C_3N_4 has also been reported by Wang and co-workers [21]. Synthesis of core-shell nanoplates of N-doped ZnO/g-C_3N_4 via ultrasonic dispersion process and their excellent visible light photocatalytic activity has been reported by Kumar and co-workers, [30] which was due to the less electron-hole pair recombination at the interface of N-doped ZnO/g-C_3N_4. Liu and co-workers [31] reported the synthesis of g-C_3N_4/ZnO composite by deposition-precipitation technique, which has been used as a visible light active photocatalyst with a first-order kinetics for both photooxidation and photoreduction reaction. Synthesis of g-C_3N_4/ZnO nanotube by electrochemical methods and their improved photoelectrochemical properties due to synergistic effect between g-C_3N_4 and ZnO has been reported by Wang and co-workers [32]. All these reports demonstrate a heterostructure semiconductor, combination of ZnO and g-C_3N_4, having eminent photocatalytic performance under the illumination of visible light.

Being inspired from the above studies we have synthesized morphology-dependent ZnO structures on g-C_3N_4 surface. Best of our knowledge, here we are reporting for the first time the shape-dependent synthesis of ZnO on g-C_3N_4 surface and their application in photocatalysis.

Within this chapter, we report a simple and facile approach to synthesize visible light active heterostructures of g-C_3N_4 and ZnO, via chemisorption of zinc precursors followed by hydrolysis and dehydration. Firstly, bulk g-C_3N_4 was synthesized followed by the formation of dumbbell and cone shaped ZnO on its surface using CTAB and different hydrolyzing medium. The analytical techniques like UV-vis, PXRD, FTIR, SEM, TEM, EDS, and XPS were used as characterizing tools to corroborate the synthesis of bulk g-C_3N_4 and g-C_3N_4/ZnO composite. Methylene blue dye and phenol were chosen as model compounds to evaluate the photo-activity of the as-synthesized catalysts under the illumination of visible light. g-C_3N_4/ZnO heterostructures show superior activity as compared to bare g-C_3N_4 as well as pure ZnO nanoparticles. Due to type-II band alignment (**Figure 1.10**) of ZnO and g-C_3N_4, interface between g-C_3N_4 and ZnO helps for faster transportation of photogenerated charge, which results g-C_3N_4/ZnO to be an efficient photocatalyst. Finally, the reusability of g-C_3N_4/ZnO has also been executed to prove the stability of catalyst.

4.2 Experimental section

4.2.1 Synthesis of Bulk g-C_3N_4

Synthesis of bulk g-C_3N_4 was reported elsewhere [13-15]. Briefly, bulk g-C_3N_4 was synthesized by thermal treatment of 10.0 g urea in a covered silica crucible under ambient air pressure. Initially, urea powder was dried at 80 °C for an hour on water bath and then the crucible with urea was placed in the muffle furnace at 550 °C for 2.5 hour keeping the heating rate of 10° min^{-1}. Finally, the yellow colour product was collected at room temperature and washed with nitric acid (0.1 M) four times to remove the extra impurities (e.g., NH_3 etc.), which was formed during the reaction and dried at 80 °C.

4.2.2 Synthesis of Dumbbell and Cone Structure of ZnO on g-C_3N_4 Surface

The as-prepared bulk g-C_3N_4 powder was used as a support for the synthesis of ZnO dumbbell. Initially, 50 mg of bulk g-C_3N_4 powder was sonicated for 30 min in 50 mL of water for complete dispersion. Now, to the aqueous dispersion of g-C_3N_4, 2.5 mL of 10^{-1} M $ZnSO_4 \cdot 7H_2O$ and 2.5 mL of 10^{-1} M CTAB were added in 1:1 ratio with manual stirring. The pH

of the above solution was set up to alkaline (pH ~ 7.5) using hexamethylenetetramine (HMT) (5 mL of 10^{-1} M was added) solution with continuous stirring. Subsequently, the reaction mixture was kept at 90-95 °C for 6 h in reflux condition to complete the formation of ZnO dumbbell on the surface of g-C_3N_4. The white powder was collected and washed five times using methanol and dried in air.

g-C_3N_4/ZnO cone heterostructure was synthesized using the same procedure described for g-C_3N_4/ZnO dumbbell, except ammonia solution was used to maintain the alkaline (pH ~ 9-10) instead of HMT solution.

4.3 Results and Discussion

4.3.1 Characterization

The characterization, photocatalysis results and possible photodegradation mechanism of g-C_3N_4 and coupled g-C_3N_4/ZnO heterostructures are discussed in the following section.

4.3.1.1 UV-vis and Photoluminescence Study

Figure 4.1 shows UV-vis spectra of g-C_3N_4 and g-C_3N_4/ZnO heterostructures. g-C_3N_4 and g-C_3N_4/ZnO show strong absorption in visible light with absorption edge at ~440 nm. The position of absorption edge remains unchanged for all the samples whereas g-C_3N_4/ZnO heterostructure shows an increased absorption as compared to the bare g-C_3N_4, which is due to the presence of ZnO nanostructure [23,31]. The absorption intensity for both g-C_3N_4/ZnO heterostructure shapes are similar, which can be attributed to the UV-light absorption of ZnO. Hence, the morphological shape of various ZnO structures on g-C_3N_4 surface doesn't affect the absorption intensity within the visible region. Although, a sharp band at 369 nm for ZnO has been reported in the literature, [33] g-C_3N_4/ZnO heterostructures do not show any distinct peak for ZnO within the UV-vis spectrum.

The band gap (E_g) of g-C_3N_4 can be estimated from the plot of $(\alpha E_p)^2$ vs. photon energy (E_p) using the extrapolated value of E_p at $\alpha = 0$, following equation: $\alpha E_p = k(E_p - E_g)^{1/2}$, where, α = absorption coefficient, E_p = discrete photon energy, E_g = band gap energy, and k = constant. The calculated E_g value for g-C_3N_4 is found to be ~ 2.88 eV (**Figure 4.1 (inset)**), which is

consistent with previous reports [20].
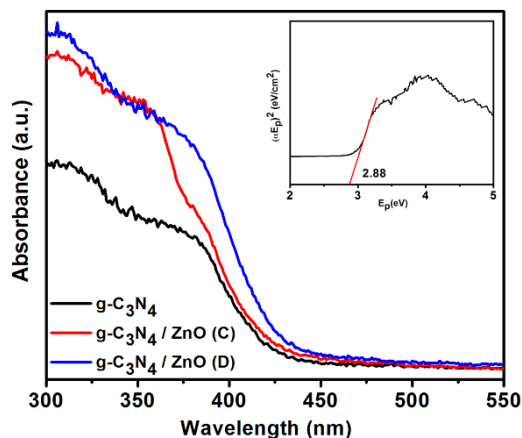
Figure 4.1 UV-vis DRS for bulk g-C$_3$N$_4$, g-C$_3$N$_4$/ZnO (dumbbells), and g-C$_3$N$_4$/ZnO (cones), where all the powder samples were mixed with BaSO$_4$ as reference. Here, all absorbance values are in arbitrary unit and each spectrum corresponds to different absorbance (not in relative scale). From the UV-vis spectrum of g-C$_3$N$_4$, inset shows (αE$_p$)^2 vs. E$_p$ plot for band gap (E$_g$) calculation
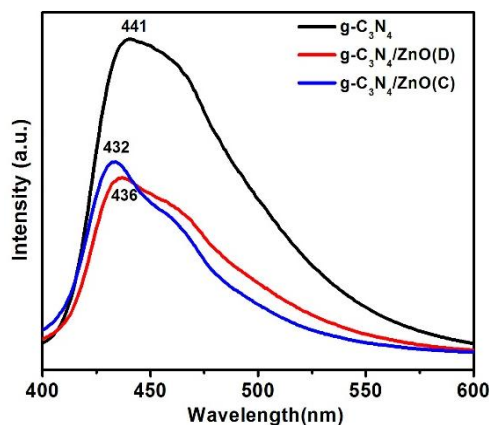
Figure 4.2 Room temperature photoluminescence spectra of bulk-g-C$_3$N$_4$, g-C$_3$N$_4$/ZnO (dumbbells), and g-C$_3$N$_4$/ZnO (cones). For PL measurements all the powder samples were dispersed well in water using a sonicator with an excitation wavelength, λ_{ex} = 315 nm

In order to analyze the effect of ZnO and the fate of photogenerated electron-hole pairs

on g-C$_3$N$_4$ surface, photoluminescence (PL) spectral analysis has been carried out. **Figure 4.2** shows the PL spectra of g-C$_3$N$_4$ and g-C$_3$N$_4$/ZnO heterostructures with an excitation wavelength of 315 nm.

The intense emission peak is centred at around 441 nm for pure bulk g-C$_3$N$_4$, which could be assigned to the higher recombination rate of the photogenerated electrons and holes [12,32]. In case of g-C$_3$N$_4$/ZnO heterostructures, blue shifted emission peaks appear at 436 nm and 432 nm for dumbbell and cone structure, respectively. The decrease in emission peak intensity for g-C$_3$N$_4$/ZnO heterostructures is due to inhibited recombination of photogenerated electron-hole pairs in g-C$_3$N$_4$ and ZnO heterojunction, which further indicates a successful charge separation. However, PL study confirms about the increased lifetime of the photogenerated carrier in g-C$_3$N$_4$/ZnO heterostructures compared to bare g-C$_3$N$_4$, which is due to the type-II band alignment of ZnO and C$_3$N$_4$.

4.3.1.2 Structure and Morphological Characterization

The FTIR spectra for pure g-C$_3$N$_4$, ZnO, and composite g-C$_3$N$_4$/ZnO heterostructures are shown in **Figure 4.3**. In case of pure g-C$_3$N$_4$, the peak centred at 1636 cm^{-1} is attributed to the C=N stretching vibration, while the peaks at 1240, 1318, and 1406 cm^{-1} represent the aromatic C–N stretching vibration modes of C$_3$N$_4$ ring. The out-of-plane bending modes of C–N heterocycles are represented by a band at ~811 cm^{-1}[20,21,30]. From **Figure 4.3**, it is quite clear that the main characteristic peaks of g-C$_3$N$_4$ and ZnO appears in g-C$_3$N$_4$/ZnO heterostructures with a red shift, which indicates weaker bond strengths of C–N and C=N within the g-C$_3$N$_4$/ZnO heterostructures. This phenomenon suggests that the conjugated system of g-C$_3$N$_4$ is stretched and appears in a more widely conjugated system in g-C$_3$N$_4$/ZnO heterostructures [21]. Therefore, FTIR spectra reveal the existence of g-C$_3$N$_4$, ZnO, and g-C$_3$N$_4$/ZnO, which are well matched with the reported stretching frequency values and further indicates an intense interaction between g-C$_3$N$_4$ and ZnO [20,21,24,30].

In order to check the phase purity and structural property of the as-synthesized g-C$_3$N$_4$ and g-C$_3$N$_4$/ZnO composites, powder X-ray diffraction (PXRD) analysis has been performed, as shown in **Figure 4.4**. The XRD pattern (**inset** of **Figure 4.4**) of pure g-C$_3$N$_4$ reveals two distinct peaks at 2θ = 13.3° and 27.6°. The weaker peak at 13.3° corresponds to the presence of (100)

crystalline plane, which is due to in-plane ordering of tri-s-triazine units. The relatively stronger peak at 27.6° is recognized as the reflection from (002) lattice plane which also resembles an interlayer spacing of d = 0.32 nm, the long-range interlayer stacking of the aromatic system of g-C_3N_4 [12,13].
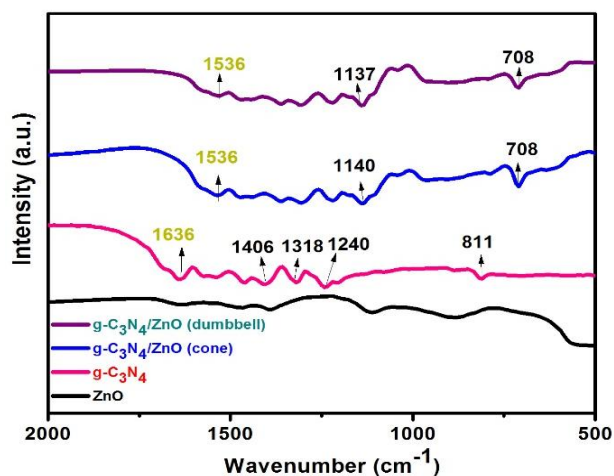
Figure 4.3 FTIR spectra of bare g-C$_3$N$_4$, ZnO, g-C$_3$N$_4$/ZnO (dumbbells), and g-C$_3$N$_4$/ZnO (cones). All the powder samples were mixed with KBr reference to form a pellet
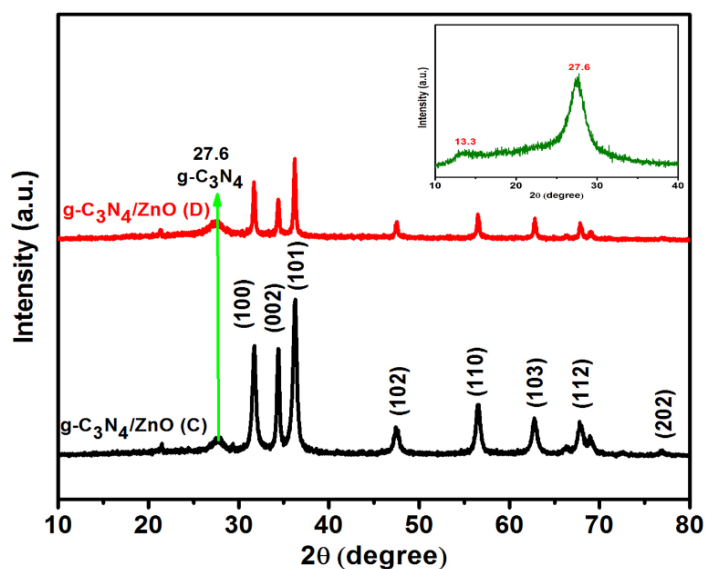
Figure 4.4 Powder X-ray diffraction patterns of bulk g-C$_3$N$_4$ (inset), g-C$_3$N$_4$/ZnO (dumbbells), and g-C$_3$N$_4$/ZnO (cones). During PXRD measurement, 2θ varies from 10-80° and the scanning rate was fixed at 2° per min.

In case of g-C$_3$N$_4$/ZnO heterostructures, eight major reflection peaks for ZnO are observed at 2θ = 31.78°, 34.42°, 36.19°, 47.40°, 56.47°, 62.63°, 68.85°, and 76.71°, correspond to the (100), (002), (101), (102), (110), (103), (112), and (202) crystal planes of ZnO (**Figure 4.4**). According to JCPDS card no. 89-1397, all the observed diffraction peaks match well with the wurtzite (HCP) structure of ZnO for both the cone and dumbbell shape morphologies [33]. Apart from the eight major peaks for ZnO, another diffraction peak at 2θ = 27.6°, representing the (002) lattice plane of g-C$_3$N$_4$, also appears which confirms the existence of ZnO on g-C$_3$N$_4$ surface (**Figure 4.4**). Absence of any impurity peak, originated from unreacted urea, non-hydrolyzed Zn^{2+} precursor salt, and Zn(OH)$_2$, within the XRD pattern of g-C$_3$N$_4$ and g-C$_3$N$_4$/ZnO heterostructures also confirms the material's phase purity.

The morphological analysis of the as-synthesized ZnO has been done using a field emission scanning electron microscopy (FESEM). **Figure 4.5.a** and **b** represent the low and high resolution FESEM images of ZnO structures, synthesized using HMT hydrolyzing agent.
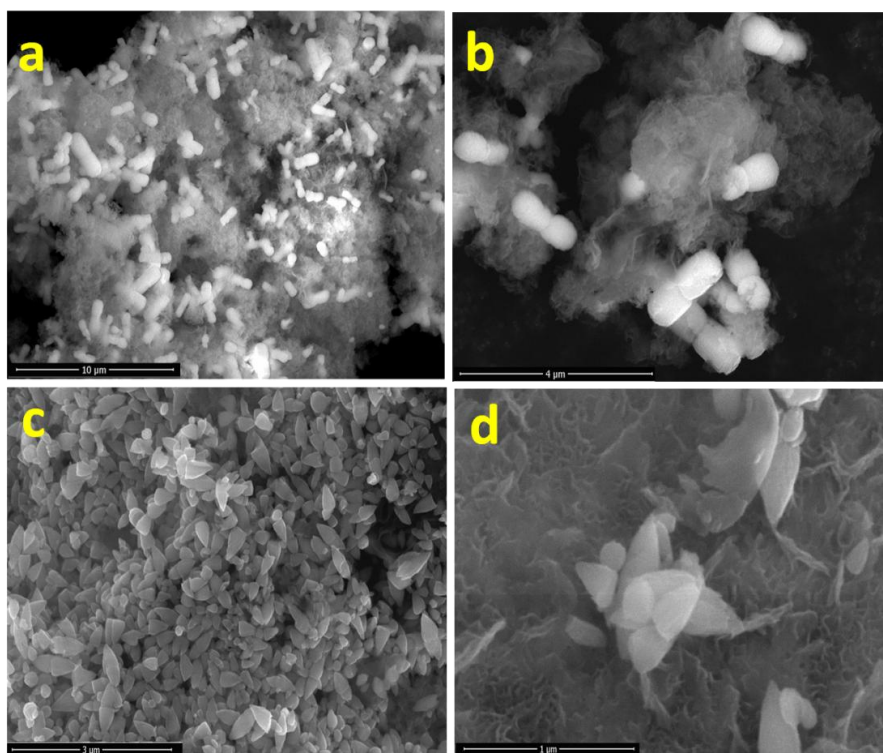
Figure 4.5 FESEM images of g-C$_3$N$_4$/ZnO dumbbells (a) at low resolution and (b) at high-resolution. FESEM images of g-C$_3$N$_4$/ZnO cones (c) at low resolution and (d) at high-resolution

Figure 4.5.a shows an SEM image of randomly distributed dumbbell shaped ZnO structure on g-C₃N₄ surface maintaining the shape uniformity. The average length and breadth of ZnO dumbbells on g-C₃N₄ surface is about 1.76 μm and 0.76 μm, respectively, as can be seen in **Figure 4.5.b**. **Figure 4.5.c** and **d** exhibit FESEM images of cone shaped ZnO structures, where ammonia was utilized as hydrolyzing agent. The average length of the side of a cone is found to be about 0.51 μm (**Figure 4.5.d**), which is significantly shorter than the dumbbell shape. The presence of ZnO cone on g-C₃N₄ surface is aggregated even with an uniform shape. Pure bulk g-C₃N₄ also appears in aggregated morphology with many C₃N₄ sheets and layered structure (**Figure 4.6**). All these findings clearly suggest a random growth of ZnO on g-C₃N₄ surface, for both dumbbells and cones and results in different growth morphologies for HMT (dumbbell shape) and ammonia (cone shape) hydrolyzing agent.
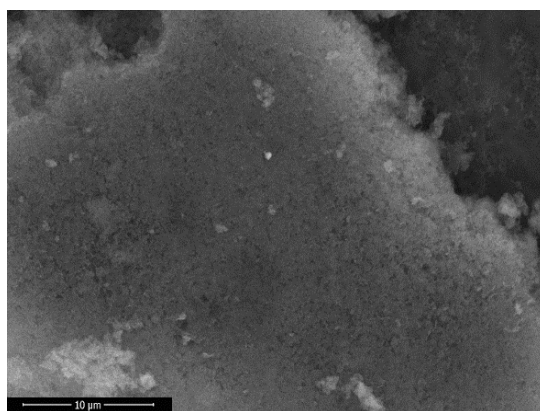
Figure 4.6 FESEM image of bare g-C₃N₄ surface

The structures and shapes of ZnO dumbbells and cones on g-C₃N₄ surface have also been investigated with the help of TEM. TEM images of morphology dependent ZnO are shown in **Figure 4.7**. **Figure 4.7.a** exhibits a TEM image of ZnO dumbbell on g-C₃N₄ surface, which was synthesized using the HMT. The length and breadth of a single dumbbell is found to be 1.73 μm and 0.78 μm (**inset** of **Figure 4.7.a**), respectively, which are complementary to our FESEM findings. It can also be noted that the size and shape of the ZnO dumbbells are quite uniform. High-resolution TEM image (**Figure 4.7.b**) of C₃N₄/ZnO heterostructure shows a fringe spacing value of 0.26 nm, which corresponds to the (002) crystal planes of ZnO. Hence, we can conclude that the growth of ZnO dumbbell on g-C₃N₄ surface occurred along (002) plane. TEM and

HRTEM images of ZnO cones on g-C$_3$N$_4$ surface (synthesized by using ammonia) are shown in **Figure 4.7.c** and **d**. From the inset of **Figure 4.7.c**, the length of a cone can be estimated to 0.51 μm, well in line with earlier FESEM analysis. **Figure 4.7.d** shows clear lattice fringes of ZnO on g-C$_3$N$_4$ surface with fringe spacing of d = 0.26 nm, which can be attributed to the (002) lattice planes of the wurtzite ZnO crystal, and also complementary with our XRD results. Finally, TEM and HRTEM analysis also confirm the morphology dependent synthesis of ZnO using various hydrolyzing agents and their random distribution on g-C$_3$N$_4$ surface.
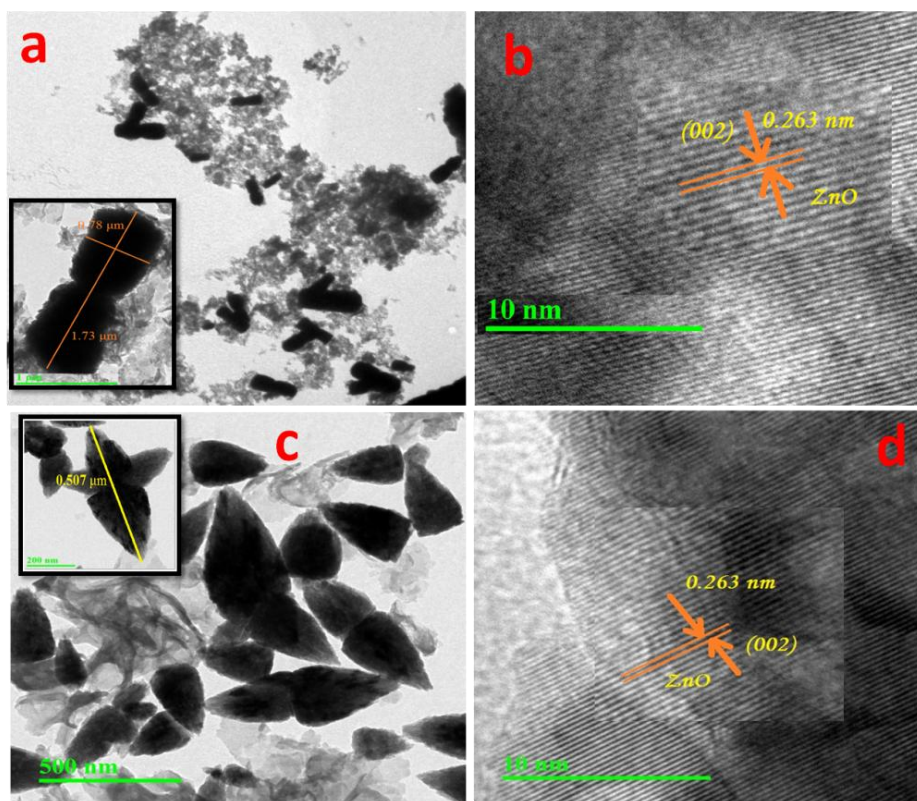
Figure 4.7 (a) TEM and (b) HRTEM images of g-C$_3$N$_4$/ZnO dumbbell. (c) TEM and (d) HRTEM images of g-C$_3$N$_4$/ZnO cones. Insets of Figure (a) and (c) show a single dumbbell and cone at high-resolution

Selected area elemental mapping of g-C$_3$N$_4$/ZnO cone shaped heterostructures (**Figure 4.8 b-f**), has been performed by EDS technique which confirms the presence of C, N, Zn, and O elements. The line mapping of g-C$_3$N$_4$/ZnO heterostructure shows different lines for Zn, O, C,

and N (**Figure 4.8.a**) which clearly proves the random distribution of ZnO over the g-C$_3$N$_4$ surface.
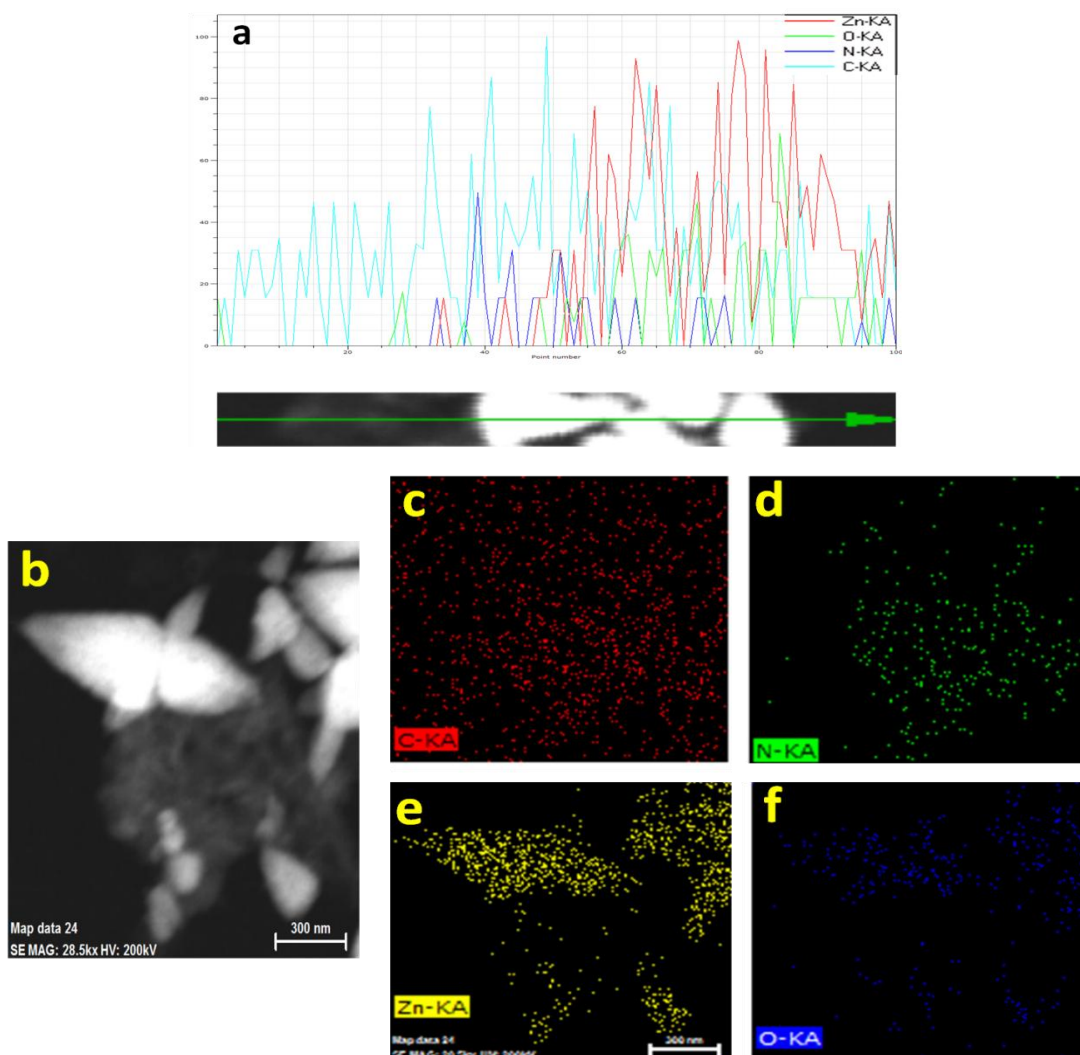
Figure 4.8 (a) EDS line spectrum of g-C$_3$N$_4$/ZnO (cone), (b) FESEM image from where line spectrum and point mapping were performed, and (c, d, e, f) point mapping of C, N, Zn, and O respectively in g-C$_3$N$_4$/ZnO cone heterostructures

N$_2$ adsorption-desorption isotherms of the as-decorated dumbbell and cone shaped ZnO catalyst samples have been used to determine the surface areas of the catalysts, which further helps to quantify the adsorption property. The BET surface area values of 45.35 and 23.67 m^2/g have been observed for g-C$_3$N$_4$/ZnO dumbbells and cones, respectively. The larger surface area value of ZnO dumbbells confirms better adsorption property over the ZnO cones. The N$_2$

adsorption-desorption isotherms of ZnO dumbbell and cone structures are presented in **Figure 4.9**.
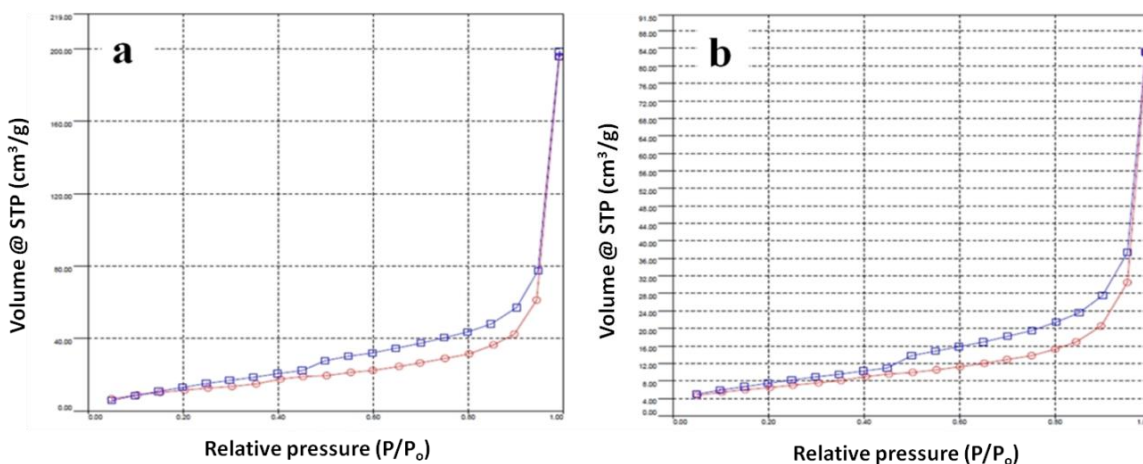
Figure 4.9 N$_2$ adsorption-desorption isotherm using g-C$_3$N$_4$/ZnO dumbbell (a) and cone (b) structures

4.3.1.3 Surface Chemical Analysis of ZnO on g-C$_3$N$_4$ Surface

To investigate the surface chemical properties, relative surface coverages and the oxidation states of the dumbbell and the cone shaped ZnO structures synthesized on g-C$_3$N$_4$ surface, XPS technique has been employed as a characterizing tool. Successful formation of both types of ZnO shapes on g-C$_3$N$_4$ surface and relative comparison of their surface coverage as well as oxidation states are depicted in **Figure 4.10**.

Survey spectra for cone (ZnO-C) and dumbbell (ZnO-D) shaped structures on graphitic carbon nitride layers are shown in **Figure 4.10.a**. Both scans appear with strong existence of Zn, N, C, and O core level binding energy as well as Auger peaks, which further confirm the successful formation of ZnO on g-C$_3$N$_4$ surface. High resolution scans of Zn 2p core level spectra are shown in **Figure 4.10.b**. The binding energy positions for Zn 2P$_{3/2}$ and Zn 2P$_{1/2}$ are observed at around 1021.6 eV and 1044.7 eV, respectively, which are in good agreement with the earlier reported values for Zn(+2) oxidation state of ZnO material [24,28,30]. However, stronger peak intensity in ZnO-C spectrum clearly suggests a significantly higher surface coverage for the cone-shaped structures on g-C$_3$N$_4$ as compared to that of the dumbbell shaped ZnO.

Another comparison of the binding energy peak intensities for N1s line is also presented in **Figure 4.10.c**. In contrast to earlier Zn 2p lines, here, the N1s line appears stronger for ZnO-D materials which can be explained in terms of attenuation of the N1s photoelectrons emitted from the g-C$_3$N$_4$ surface, within the ZnO over layers for ZnO-C sample. This finding is very much complementary with our SEM results. In addition, it can be noted that there is a little relative shift in N1s binding energy peak position towards the higher energy for ZnO-C sample. This might be attributed to a relatively lower electron density of the N atoms within the ZnO-C.
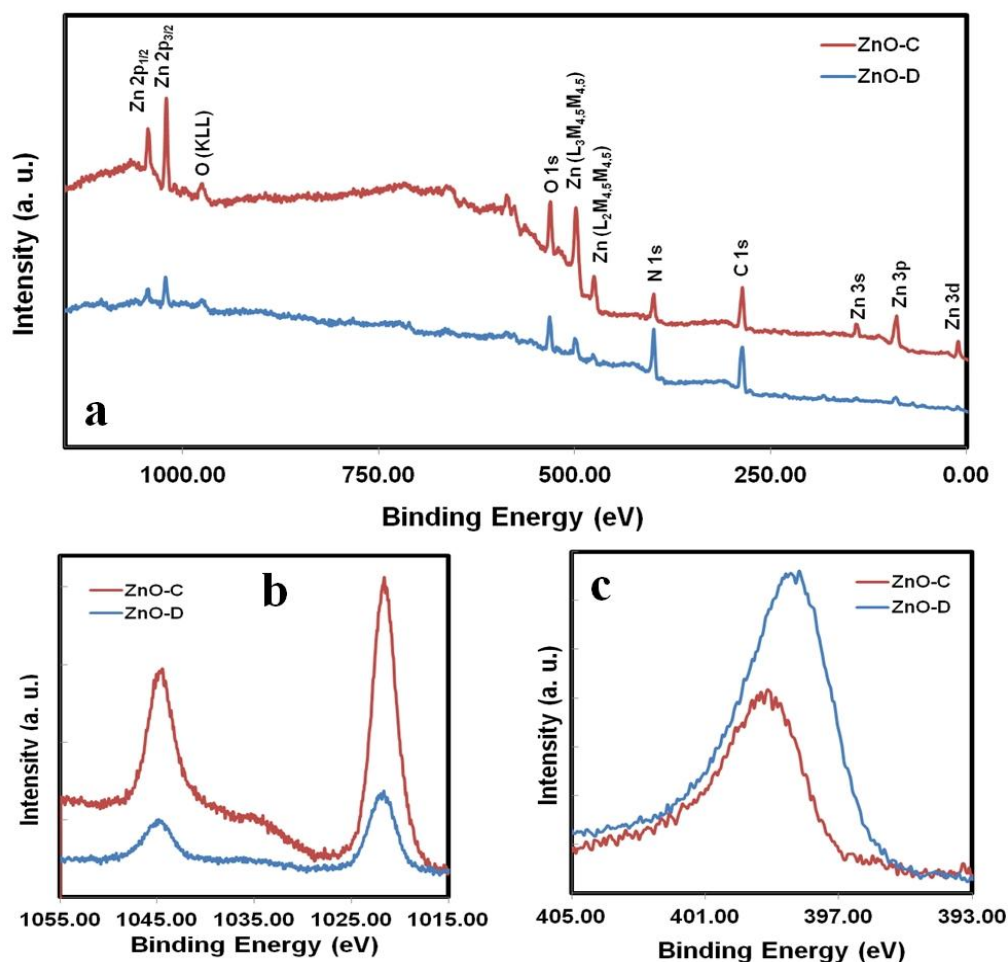
Figure 4.10 XP spectra of (a) wide scan survey of cone (ZnO-C) and dumbbell (ZnO-D) shaped g-C$_3$N$_4$/ZnO structures. High resolution scans of (b) Zn 2p and (c) N 1s core level photoelectrons
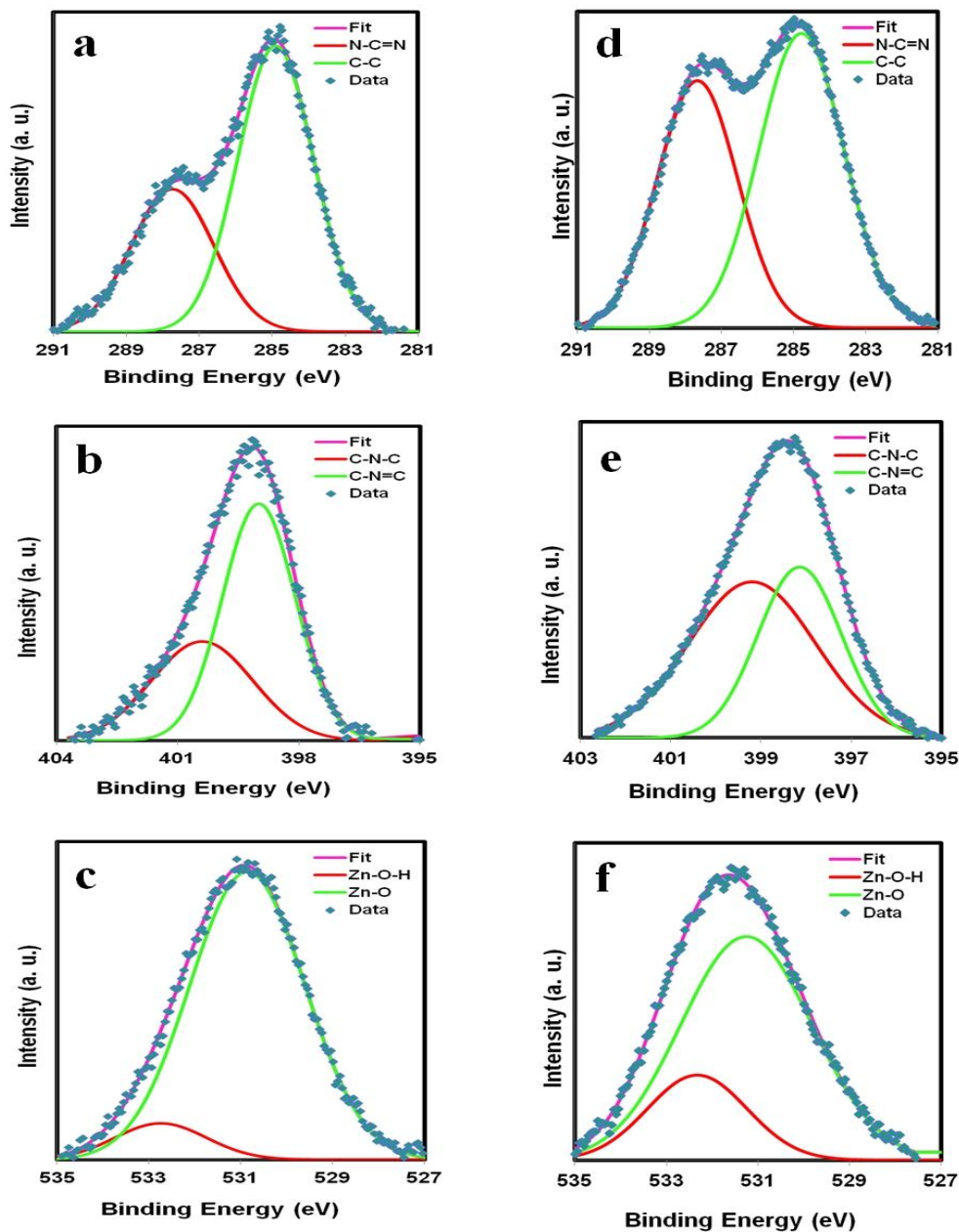
Figure 4.11 High-resolution XP spectra of g-C₃N₄/ZnO samples with various deconvolution components of C 1s, N 1s, and O 1s photoelectrons. (a-c) cone morphology (ZnO-C) and (d-f) dumbbell morphology (ZnO-D)

A similar kind of peak shift for O1s line in the opposite direction is also observed (**Figure 4.11**), which can be correlated to a relatively higher electron density of the O atoms within the ZnO-C sample. Both these relative peak shifts (N1s and O1s) suggest that there are

some possibilities for partial transfer of electrons from the N atom of g-C_3N_4 to the O atoms of ZnO. This assumption is also complementary with the higher electro-negativity of O compared to that of N. Therefore, we can conclude that a composite of g-C_3N_4/ZnO is obtained rather than a physical mixture of ZnO and g-C_3N_4 is formed within the samples [32].

High-resolution XP spectra of C1s, N1s and O1s binding energy peaks for both g-C_3N_4/ZnO samples are presented in **Figure 4.11**. All spectral analysis with various de-convolution processes is performed using a linear background subtraction and a mixture of Lorentzian and gauss fitting. **Figure 4.11.a-c** represent the corresponding spectra of ZnO-C sample whereas, **Figure 4.11.d-f** depict the spectral analysis for ZnO-D sample, respectively. C1s binding energy spectra of the ZnO-C and ZnO-D samples are shown in **Figure 4.11.a** and **d**, respectively. The deconvoluted components of C1s line appear in two main binding energy peaks positioned at about 287.7 and 284.6 eV. The peak centered at 287.7 eV is identified as sp^2 bonded carbon (N-C=N), whereas the peak positioned at 284.6 eV corresponds to the graphitic carbon (C-C) of the materials and adventitious hydrocarbon from the instrument.

Similar to an earlier observation, **Figure 4.11.b** and **e** show the deconvoluted spectra of N1s for ZnO-C and ZnO-D samples, respectively. The asymmetrical shape of the observed N1s lines indicates chemically different N species within the g-C_3N_4. Two major components appear within the deconvoluted spectra are assigned to the sp^2 hybridized nitrogen (C-N=C) at lower binding energy and the sp^3 hybridized tertiary nitrogen (C-N-C) at relatively higher binding energy. Additionally, a relative peak shift for ZnO-D samples toward the lower energy side can also be observed, which has already been discussed earlier. The deconvolution of O1s spectra for both ZnO-C and ZnO-D samples can be seen in **Figure 4.11.c** and **f**, respectively. The oxygen species mainly appear in (−2) oxidation state within the crystalline ZnO matrix, with a minor fraction of surface hydroxides. Similar to N1s, a relative peak shift for O1s spectra in opposite direction originated from partial charge transfer between g-C_3N_4 and ZnO can also be noted. For better understanding and clarity, every detail of all the deconvoluted spectra is summarized in **Table 4.1**.

Table 4.1 Binding energy positions and relative intensities of deconvoluted C 1s, N 1s, and O 1s spectra for cone (ZnO-C) and dumbbell (ZnO-D) shaped g-C$_3$N$_4$/ZnO samples

Sample		ZnO-C		ZnO-D	
B.E. Peaks	Sub-peaks	Peak position	Relative intensity	Peak position	Relative intensity
C1s	N-C=N	287.7	55585	287.7	86873
	C-C	284.9	102606	284.8	109997
N1$_S$	C-N=C	398.9	59580	398.1	103713
	C-N-C	400.4	34681	399.2	75326
O1s	Zn-O	530.9	199188	531.3	100847
	Zn-O-H	532.7	19771	532.3	29034

4.3.2 Mechanism of Formation of g-C$_3$N$_4$/ZnO Heterostructures

The mechanism of the formation of bulk g-C$_3$N$_4$ is reported elsewhere [8-13]. In brief, pyrolysis of urea takes place which afterward results in a polymerized product. After successfully synthesizing the g-C$_3$N$_4$, it was washed with 0.1 M HNO$_3$ to remove any kind of impurities. Dumbbell and cone structures of ZnO were formed on the surface of g-C$_3$N$_4$ by refluxing technique, using a different hydrolyzing agent. At first, g-C$_3$N$_4$ powder was sonicated in water to obtain a well disperse layered structure of g-C$_3$N$_4$. Secondly, Zn^{2+} precursor salt and CTAB were added for the synthesis of g-C$_3$N$_4$/ZnO heterostructures. Finally, HMT and ammonia were used as hydrolyzing agents for the synthesis of dumbbell and cone-shaped structures of ZnO, respectively.

During the synthesis, CTAB was used as a stabilizer and growth controlling agent for the growth of ZnO nanostructure on g-C$_3$N$_4$ surface. It is predicted that the surface of g-C$_3$N$_4$ is negatively charged (-24.6±2.4 mV), which has also been confirmed from zeta-potential analysis. Therefore, Zn^{2+} precursor salt (ZnSO$_4$.7H$_2$O) can easily be adsorbed on the negatively charged g-C$_3$N$_4$ surface and cationic surfactant (CTAB) can readily interact with adsorbed Zn^{2+} ions on the same surface. In addition, various hydrolyzing agents, such as HMT and ammonia were used to supply OH$^-$ ions in the solution, which is essential for the ZnO formation. Dumbbell shape

(**Figure 4.6 and 4.7**) of ZnO was obtained for a pH ~7.5 of HMT, which acts as a rich source of OH^- ions upon thermal degradation. Railey and co-workers reported that HMT acts as a source of OH^- ion and its thermal decomposition produces ammonia and formaldehyde [34]. Dutta and co-workers also reported the release of OH^- ions upon thermal degradation of HMT [35]. Whereas, for ZnO cone structures (**Figure 4.6 and 4.7**), ammonia with pH ~ 9 was used as a source of OH^- ions, which spontaneously react with Zn^{2+} ions to form $[Zn(OH)_2]$ on g-C_3N_4 surface. Afterwards, the $[Zn(OH)_2]$ complex further reacts with excess OH^- ions to form $[Zn(OH)_4]^{2-}$ ions. During reflux, dehydration of $[Zn(OH)_4]^{2-}$ takes place and finally gives rise to ZnO formation.

Apart from the OH^- ion supply, as the rate of hydrolysis decreases with increasing pH and vice-versa, HMT also acts as a buffer [35]. Dutta and co-workers [35] nicely represented the role of HMT for the growth of ZnO nanowire and nanorod. Due to the presence of a long chain polymer and a nonpolar chelating agent in HMT, it prefers to attach with the nonpolar facets of zincite crystal for epitaxial growth through a polar (001) face only [36,37]. Therefore, instead of buffer like behaviour, HMT behaves more like a shape-inducing polymer surfactant. However, in this study, HMT was used for dual purposes. Firstly, a source of OH^- ions and secondly a shape inducing polymer surfactant along with CTAB for the growth of ZnO dumbbells on the surface of g-C_3N_4. Finally, the surrounding of ZnO dumbbells on g-C_3N_4 surface is covered by the CTAB, which is confirmed by a positive surface charge (+5.14±0.8 mV) from zeta potential analysis. There is no shape inducing agent for the synthesis of ZnO cones, the morphology was obtained solely due to the presence of cationic surfactant (CTAB) in the solution, a growth controlling agent. This phenomena was confirmed by a positive surface charge (+14.3±1.2 mV) of g-C_3N_4/ZnO cone heterostructures from zeta potential analysis. Therefore, we can conclude that the CTAB and the available OH^- ions from ammonia solution can favour the formation of ZnO cones on g-C_3N_4 surface. Due to relatively higher concentration of OH^- ions from ammonia, the surface coverage of ZnO cones on g-C_3N_4 is found significantly more, whereas the coverage of ZnO dumbbells appears less with the HMT (**Figure 4.6 and 4.7**). This relatively higher surface coverage of ZnO cones over dumbbell structures was also confirmed by XPS and SEM analysis. The overall formation mechanisms of ZnO in presence of both HMT and ammonia are given below.

$$Zn^{+2} + 2OH^- \rightarrow Zn(OH)_2$$
$$Zn(OH)_2 + 2OH^- \rightarrow [Zn(OH)_4\ ]^{2-}$$
$$[Zn(OH)_4\ ]^{2-} \rightarrow ZnO + OH^- + H_2O$$
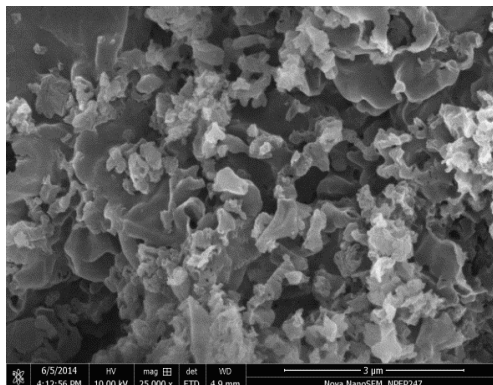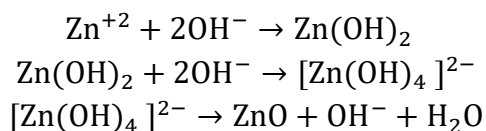
Figure 4.12 FESEM image of g-C$_3$N$_4$/ZnO aggregated form, synthesized without using CTAB keeping all other conditions same

Additionally, some control experiments were carried out to determine the role of CTAB, HMT, ammonia, for the formation of different ZnO morphologies on g-C$_3$N$_4$ substrate. At first, without any CTAB aggregated ZnO particles were obtained on the surface of g-C$_3$N$_4$ keeping all other conditions unaltered. FESEM image of aggregated ZnO particles is shown in **Figure 4.12**.

Secondly, in absence of any hydrolyzing agent (HMT or ammonia) it was impossible to grow any ZnO on the g-C$_3$N$_4$ surface. In an alternate approach, without using any C$_3$N$_4$ while keeping the CTAB and ammonia concentration unaltered, flower shaped ZnO structures were observed [33]. However, other morphological shapes of ZnO such as nanorod, nanowire, nanotube etc. have been reported for HMT hydrolyser, without C$_3$N$_4$ substrate [38,39]. Therefore, it can be concluded that presumably, C$_3$N$_4$ can provide many active centres for the initial nucleation of ZnO. This effect helps to grow ZnO randomly on C$_3$N$_4$ surface in spite of growing on a single centre which finally gives rise to the flower, rod, wire etc like morphology. Therefore, for the synthesis of ZnO dumbbell and cone structures on g-C$_3$N$_4$ surface, CTAB, HMT, ammonia, and g-C$_3$N$_4$ play very important roles. The overall formation of shape-dependent ZnO nanostructure on g-C$_3$N$_4$ surface is shown in **Scheme 4.1**.
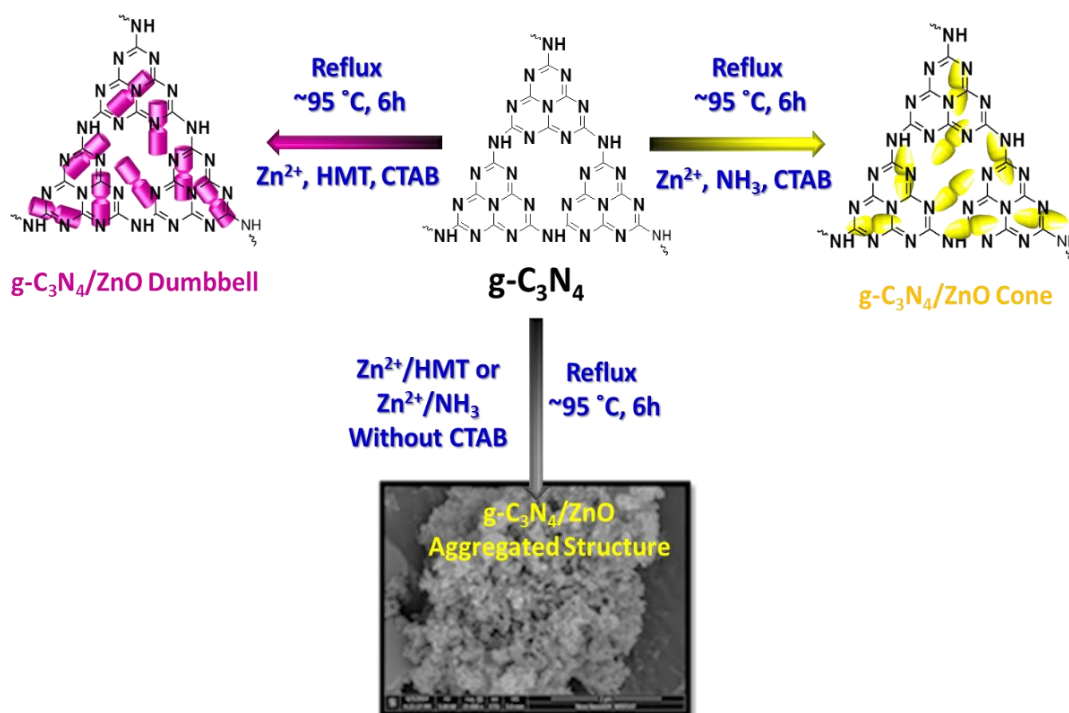
Scheme 4.1 The overall mechanism for the formation of bulk g-C$_3$N$_4$, g-C$_3$N$_4$/ZnO heterostructure (dumbbell and cone), and aggregated ZnO on g-C$_3$N$_4$ surface

4.3.3 Determination of Photocatalytic Activity

For photocatalytic activity of the as-synthesized materials, 1 mL of 3×10^{-4} M MB solution and 5.0 mg of g-C$_3$N$_4$/ZnO catalysts (dumbbell and cone) were taken in 9 mL water so that the final concentration of MB was 3×10^{-5} M in 10 mL water. Prior to irradiation, the aqueous solution was stirred continuously for ~20 min in the dark to confirm the saturation of dye on g-C$_3$N$_4$/ZnO catalyst surface. After saturation, the reaction mixture was placed under visible light with constant stirring to initiate the degradation reaction. The source of visible light was a tungsten bulb of 60 W, which emits mainly visible light. At regular irradiation time or interval (~ 20 min), 3.0 mL of aliquot was taken from the reaction mixture, centrifuged at 1000 rpm for UV-vis measurement, and re-added carefully (3.0 mL solution and catalyst) to the original reaction container. Photodegradation kinetics of MB dye was monitored by observing the change in absorbance intensity at 664 nm (maximum intense peak for MB dye) with time by UV-vis spectroscopy.

Similar procedure was applied with phenol degradation using visible light, 0.4 mL of 5×10^{-3} M aqueous phenol solution and 5.0 mg of catalyst were used for the decomposition reaction so that the final concentration of phenol in 10 ml water was 2×10^{-4} M.

For MB and phenol dye % degradation or degradation yield was calculated using initial and time-dependent absorbance values:

$$\% \text{ Degradation} = (A_0 - A_t)/A_0 \times 100$$

Where, A_0 = initial absorbance and A_t = absorbance at time 't'.

The main characteristic peaks for MB and phenol at 664 nm and 270 nm were used to monitor the photocatalytic reaction. Tungsten bulb with a wavelength range of 300-1200 nm was used as a visible light source for the photocatalytic study. There was no degradation of MB and phenol in absence of visible light as well as without any catalyst. To check the dye adsorption on catalyst surface, the reaction mixture of MB solution and catalyst was agitated in the dark with continuous stirring, prior to any irradiation with visible light. In the dark, maximum adsorption of dye was found to be 20% (within 20 min) on the catalyst surface (**Figure 4.13**) and afterwards it remained constant till 140 min. Therefore, to stabilize the adsorption-desorption equilibrium, the reaction mixture (dye and catalyst) was stirred 20 min in dark condition prior to any use.
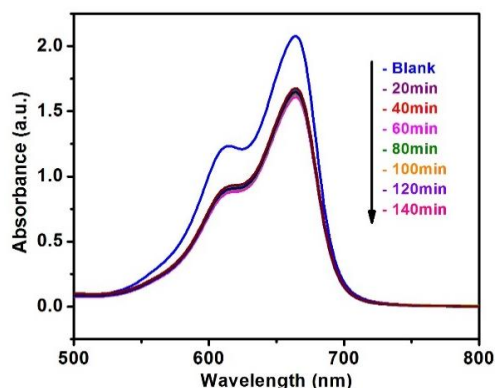
Figure 4.13 UV-vis absorption spectra of MB adsorption-desorption equilibrium in dark with g-C$_3$N$_4$/ZnO heterostructure catalyst

It can be seen from **Figure 4.14** that the degradation of MB with bare g-C$_3$N$_4$ was reached ~ 55% decomposition under visible light irradiation. The rate constant (k_{bare}) value with

bare g-C$_3$N$_4$ is observed 0.6×10^{-2} min^{-1} and showed pseudo-first order kinetics.
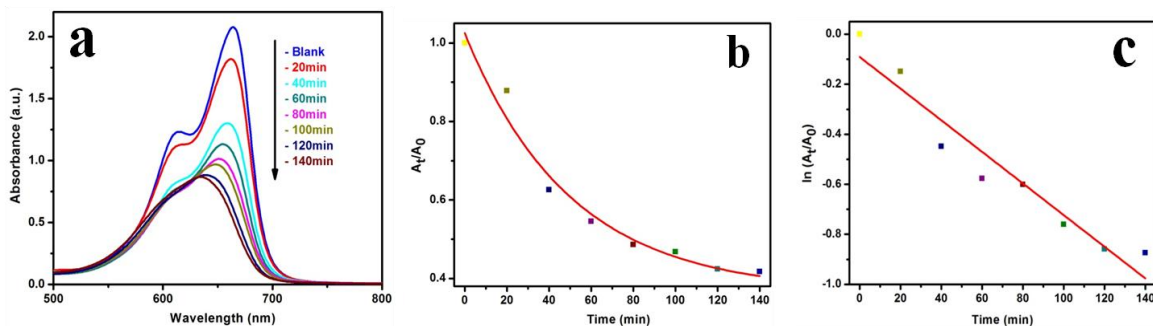
Figure 4.14 (a) UV-vis absorption spectra to show degradation of MB in presence of g-C$_3$N$_4$, (b) A$_t$/A$_0$ vs. time (min) plot, and (c) ln (A$_t$/A$_0$) vs. time (min) plot. Conditions: [MB] = 3×10^{-5} M and amount of catalyst = 5.0 mg. In all cases water was used as reference solution

Figure 4.15.a shows the degradation of the MB using dumbbell shape of g-C$_3$N$_4$/ZnO heterostructures. After 140 min., the reaction was almost over and ~99% of dye degradation was achieved. Within **Figure 4.15.b**, A$_t$/A$_0$ vs. time (min) has been plotted, which shows an exponential behaviour with time. The rate constant (k_{ND}) of 2.4×10^{-2} min^{-1} was determined from the slope of ln(A$_t$/A$_0$) vs. time (min) plot (**Figure 4.15.c**), which is four times higher than that of bare g-C$_3$N$_4$. **Figure 4.15.c** also confirms pseudo-first-order kinetics of MB degradation using g-C$_3$N$_4$/ZnO dumbbell catalyst.
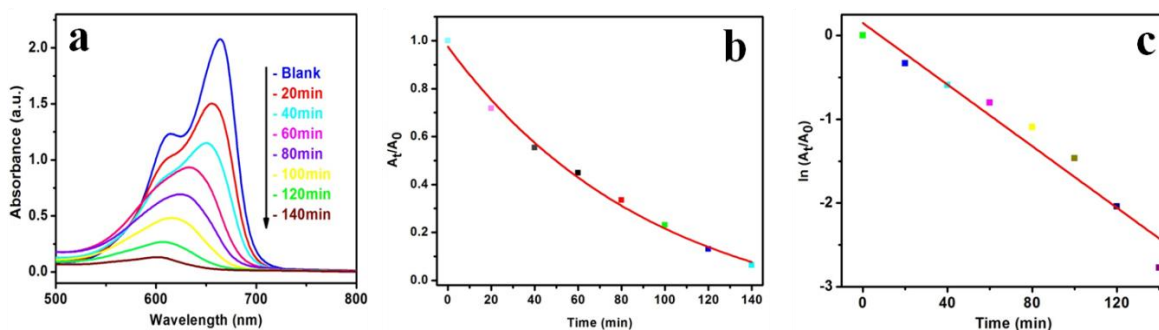
Figure 4.15 (a) UV-vis absorption spectra to show visible light degradation of MB in presence of g-C$_3$N$_4$/ZnO (dumbbells) (b) A$_t$/A$_0$ vs. time (min) plot and (c) ln(A$_t$/A$_0$) vs. time (min) plot. During the photocatalysis measurements, reaction mixture was stirred continuously
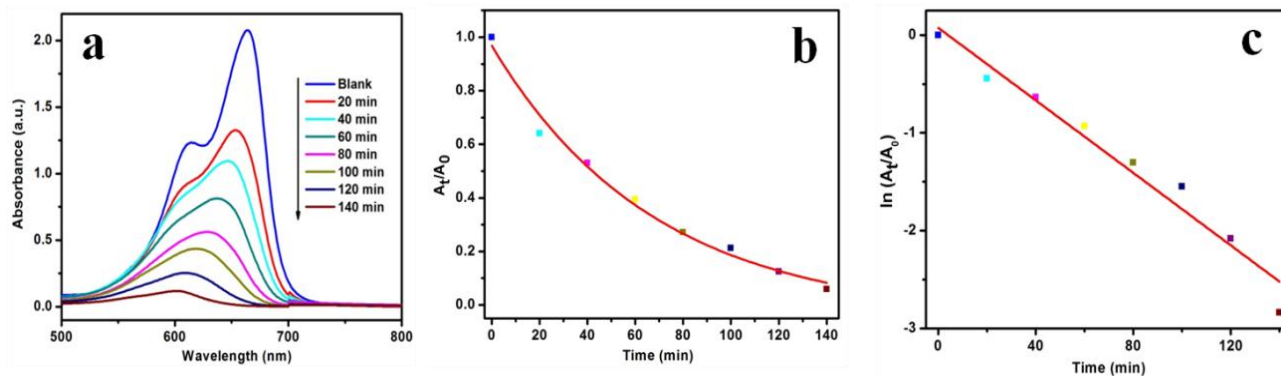
Figure 4.16 (a) UV-vis absorption spectra to show degradation of MB in presence of g-C$_3$N$_4$/ZnO (cone), (b) A$_t$/A$_0$ vs. time (min) plot, and (c) ln(A$_t$/A$_0$) vs. time (min) plot

Figure 4.16.a shows the UV-vis absorption spectra of MB degradation using cone shaped g-C$_3$N$_4$/ZnO heterostructures. At the end of 140 min, ~99% of the dye was already degraded. Similar to earlier result, the A$_t$/A$_0$ vs. time (min) plot also appears in exponential nature (**Figure 4.16.b**) and from the slope of ln(A$_t$/A$_0$) vs. time (min) plot (**Figure 4.16.c**), the rate constant (k_{NC}) was calculated to be 1.8×10^{-2} min^{-1}, which is three times higher than that of bare g-C$_3$N$_4$. Pseudo-first-order kinetics of MB degradation was also observed with cone structures of ZnO. After the completion of 1st cycle, the catalyst was removed from the reaction mixture and washed for the re-use purpose.

Furthermore, to prove the visible light activity of g-C$_3$N$_4$/ZnO (dumbbell and cone) heterostructures, a pure UV light active material phenol was used for degradation reaction. The UV-vis spectra of phenol degradation using dumbbell and cone shaped ZnO heterostructures are shown in **Figure 4.17.a** and **b**, respectively.

It can be seen from **Figure 4.17.a** and **b** that the complete phenol degradation was reached under a visible light irradiation in 150 and 170 min for dumbbell and cone structure of ZnO, respectively. Whereas, 300 min is required for complete degradation of the phenol with bare g-C$_3$N$_4$ catalyst. The rate constant values for g-C$_3$N$_4$/ZnO dumbbell and cone heterostructure are found 2.0×10^{-2} min^{-1} and 1.5×10^{-2} min^{-1}, respectively, which is significantly higher than that of pure g-C$_3$N$_4$. Hence, phenol degradation result also confirms the higher photo-activity of the dumbbell and cone structure of ZnO on g-C$_3$N$_4$ surface as compared to the bare g-C$_3$N$_4$ catalyst.
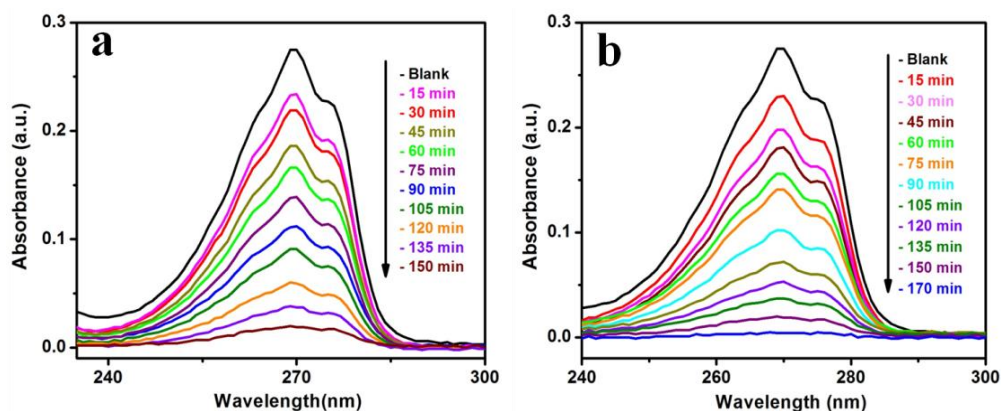
Figure 4.17 UV-vis absorption spectra of phenol decomposition using (a) g-C₃N4/ZnO (dumbbell) and (b) g-C₃N₄/ZnO (cone) catalyst, under irradiation of visible light Conditions: [phenol] = 2×10⁻⁴ M and amount of catalyst = 5.0 mg

Figure 4.18 shows the comparative study of MB dye degradation using ZnO, bare g-C₃N₄, and g-C₃N₄/ZnO (dumbbell and cone) heterostructure catalysts under visible light irradiation. Pure ZnO nanoparticles are UV light active and does not have any role on MB dye degradation under visible light illumination [33]. Bare g-C₃N₄ is known as a visible light active material and electron-hole pairs are generated after irradiation with visible light.
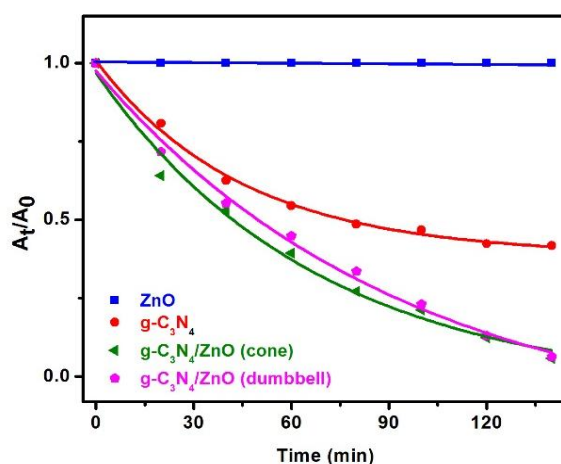
Figure 4.18 Comparative studies of degradation of MB dye in presence of ZnO, bulk g-C₃N₄, g-C₃N₄/ZnO (dumbbells), and g-C₃N₄/ZnO (cones) under visible light

It can be seen from **Figure 4.18** that the degradation of MB occurred with bare g-C$_3$N$_4$ with a slowest rate (k$_{bare}$ = 0.6×10^{-2} min^{-1}), which is due to the fast recombination of the photogenerated charged species (e$^-$ and h$^+$). Therefore, to suppress this problem of recombination, a heterojunction was created by modifying the surface of g-C$_3$N$_4$ with dumbbell and cone structures of ZnO. In case of heterostructures, the photo-activity is higher (k_{ND} = 2.4×10^{-2} min^{-1} and k_{NC} = 1.8×10^{-2} min^{-1}) due to the decreased recombination of e$^-$ and h$^+$. This diminished recombination of e$^-$-h$^+$ pairs has also been proved from the decreased intensity in photoluminescence spectra (**Figure 4.2**) of g-C$_3$N$_4$/ZnO heterostructures as compared to bare g-C$_3$N$_4$.

Sun and co-workers reported 3 times better activity in visible light dye degradation with g-C$_3$N$_4$-ZnO spherical particles as compared to bare g-C$_3$N$_4$ for methyl orange and *p*-nitrophenol degradation [20]. Kumar and co-workers also reported 5 times higher rate constant value for N-doped ZnO nanoplates than bare g-C$_3$N$_4$ nanosheets [30]. Li and co-workers reported 3.8 times higher rate constant value with g-C$_3$N$_4$/ZnO composite than the pure g-C$_3$N$_4$, during Rhodamine B dye degradation [41]. However, both dumbbell and cone structures of ZnO on g-C$_3$N$_4$ surface shows 3-4 times higher activity in MB and phenol dye degradation than bare g-C$_3$N$_4$, under illumination with the visible light and the rate constants order is found as $k_{ND} > k_{NC} > k_{bare}$. The higher rate constant with g-C$_3$N$_4$/ZnO dumbbell structures is mainly due to the larger surface area of dumbbells (45.35 m^2/g) as compared to that of cones (23.67 m^2/g). Larger surface area of the catalyst particles absorb more organic dye molecules, which further confirms the faster dye degradation rate of ZnO dumbbells than cone structures. Therefore, the as-obtained morphologies of ZnO in g-C$_3$N$_4$/ZnO heterostructures show better photo-activity than other reported ZnO morphologies.

4.3.3.1 Mechanism for Enhanced Photoactivity with g-C$_3$N$_4$/ZnO Heterostructure

In case of heterogeneous photocatalysis, two important parameters are the adsorption of dye on catalyst surface and the degradation of dye with the help of photogenerated electron-hole separation. In this study, dumbbell and cone morphologies of g-C$_3$N$_4$/ZnO heterostructures and negative surface charge of g-C$_3$N$_4$ enhance the adsorption process of dye on its surface. The efficient photo-activity of g-C$_3$N$_4$/ZnO heterojunctions can be explained in terms of the

alignment of the valence band (VB) and the conduction band (CB) positions of both g-C$_3$N$_4$ and ZnO separately. Both the g-C$_3$N$_4$ and ZnO are examples of type-II semiconductor, which can be verified by potential energy level calculations as shown in the following equation: [42-47].

$$E_{VB} = \chi - E_c + 0.5E_g$$

E_{VB} = VB edge potential, χ = electronegativity of the semiconductor, E_c = energy of free electrons in hydrogen scale (~ 4.5 eV), and E_g = band gap energy of the semiconductor. The edge potential for CB (E_{CB}) can be calculated by:

$$E_{CB} = E_{VB} - E_g$$

The value of χ for ZnO is 5.79 eV and the band gap energy (E_g) of the as-synthesized ZnO material is 3.12 eV. The E_{VB} of ZnO was calculated to be +2.85 eV. Hence, the E_{CB} of ZnO can be estimated to −0.27 eV. Based on the reported data, the CB and the VB edge potential values of g-C$_3$N$_4$ are −1.1 eV and +1.6 eV, respectively [43,46]. All the potential energy values for both ZnO and g-C$_3$N$_4$ are shown in **Scheme 4.2**. It can be seen from scheme 4.2 that the CB potential energy or LUMO for g-C$_3$N$_4$ (E_{CB} = −1.1 eV) is lower than the ZnO (E_{CB} = −0.27 eV). Hence, the excited e$^-$ from the CB of g-C$_3$N$_4$ can easily inject to the CB of ZnO upon irradiation with visible light [21,30-32,42]. Therefore, the potential energy match in the heterojunction of g-C$_3$N$_4$/ZnO is a driving force for the transportation of photogenerated e$^-$ from the CB of g-C$_3$N$_4$ towards the CB of ZnO, which effectively reduces the recombination of e$^-$-h$^+$ pairs [32,42].

Upon irradiation of visible light on g-C$_3$N$_4$/ZnO heterostructures, the e$^-$ on g-C$_3$N$_4$ can easily move from VB to CB (e$_{CB}^-$) leaving behind h$^+$ on VB (h$_{VB}^+$) of g-C$_3$N$_4$. Now, the excited electrons may easily transfer from the CB of g-C$_3$N$_4$ to the CB of ZnO. Afterwards, the electrons on the CB of ZnO react with O$_2$ and generate superoxide radicals (O$_2^{-\bullet}$), which further generate hydroxyl radicals (OH$^\bullet$) [21,30-33,48]. These $^\bullet$OH radicals are responsible for the photodecomposition of MB and phenol. On the other hand, h$^+$ in VB of g-C$_3$N$_4$ is also responsible for the generation of OH$^\bullet$ radicals from OH$^-$ ions, which are the active species in dye degradation [20,21,33,48]. As ZnO is an UV light active material, photo-excitation of it is not possible under visible light irradiation. The overall electronic transition and dye degradation

reaction in g-C$_3$N$_4$/ZnO heterostructures are shown below:
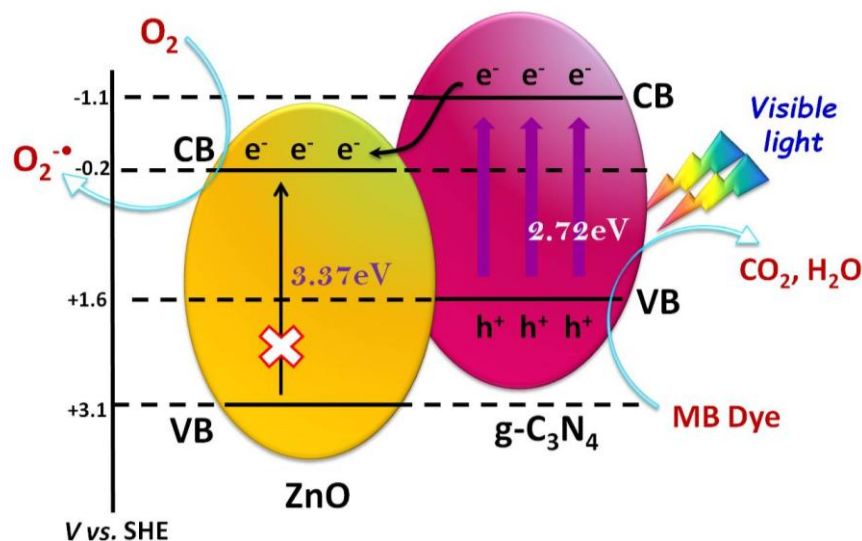
Scheme 4.2 The VB and CB energy levels and the mechanism of charge transfer in g-C$_3$N$_4$/ZnO heterostructure under visible light irradiation during organic pollutant degradation

$$g\text{-}C_3N_4 \xrightarrow[\text{light}]{\text{Visible}} g\text{-}C_3N_4 (e_{CB}^- + h_{VB}^+) \xrightarrow[\text{towards CB of ZnO}]{\text{Movement of e-}} ZnO (e_{CB}^-)$$

$$ZnO(e_{CB}^-) + O_2 \longrightarrow O_2^{-\bullet}$$

$$O_2^{-\bullet} + 2H^+ \longrightarrow 2OH^\bullet$$

$$h^+ + OH^- \longrightarrow OH^\bullet$$

$$OH^\bullet + MB/Phenol \longrightarrow decomposed\ products$$
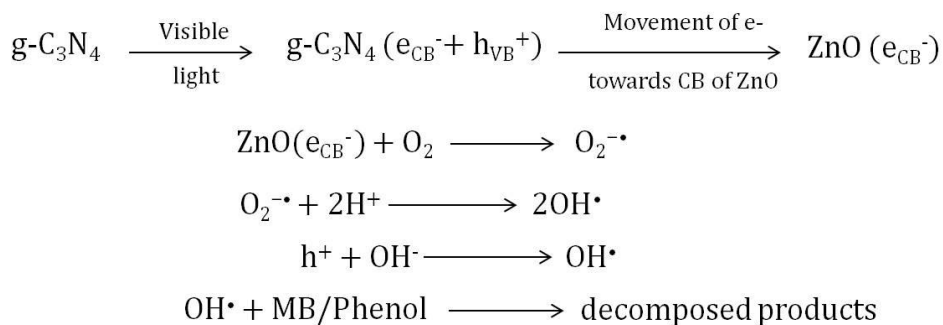
It can be seen from the above reactions that the species like e$^-$, O$_2^{-\bullet}$, OH$^\bullet$, and h$^+$ are directly involved in the photocatalytic process [49,50]. Therefore, to confirm the role of electrons and holes in visible light photocatalysis, scavenging experiment has been carried out with *t*-BuOH and ammonium oxalate (AO) for MB degradation, using g-C$_3$N$_4$/ZnO heterostructure catalyst. *t*-BuOH was used as OH$^-$ scavenger and AO as a hole scavenger [30,33]. For scavenging experiments, 1 mL of *t*-BuOH and 0.2 g of AO were used, keeping the other reaction parameters unaltered, to trap the electron/radical and holes, respectively. Incorporation of *t*-

BuOH in the reaction mixture prevented the presence of OH^- and the formation of $O_2^{-\bullet}$ and $OH^\bullet$ radicals, which largely affected the visible light dye degradation and results in ~ 27% degradation. On the other hand, h^+ was promptly scavenged with the addition of AO and ~ 88% degradation was achieved. Therefore, it can be concluded that % degradation of dye is not greatly affected due to the h^+ scavenger. Altogether, the formation of $O_2^{-\bullet}$ and $OH^\bullet$ radicals play a major role in photocatalysis under the visible light. This scavenging experiment findings are also supported by earlier reported values [21,30,31].

4.3.3.2 Reusability of g-C$_3$N$_4$/ZnO Catalyst

Reusability of g-C$_3$N$_4$/ZnO catalyst has been tested in MB degradation reaction, under the irradiation of visible light source. **Figure 4.19.a** shows the reusability histogram using ZnO dumbbell for MB degradation. After the 1st cycle, catalyst particles were collected and washed thoroughly with water for further use. Using same condition, the experiments were repeated thrice and the % of degradation results show 98%, 94%, and 92% for 1st, 2nd, and 3rd cycles, respectively. This degradation result confirms that the catalysts remain chemically stable even after several recycles. Similar reusability test was also conducted with ZnO cones and the % degradation demonstrate 98%, 92%, and 90% for 1st, 2nd, and 3rd cycles, respectively (**Figure 4.19.b**).
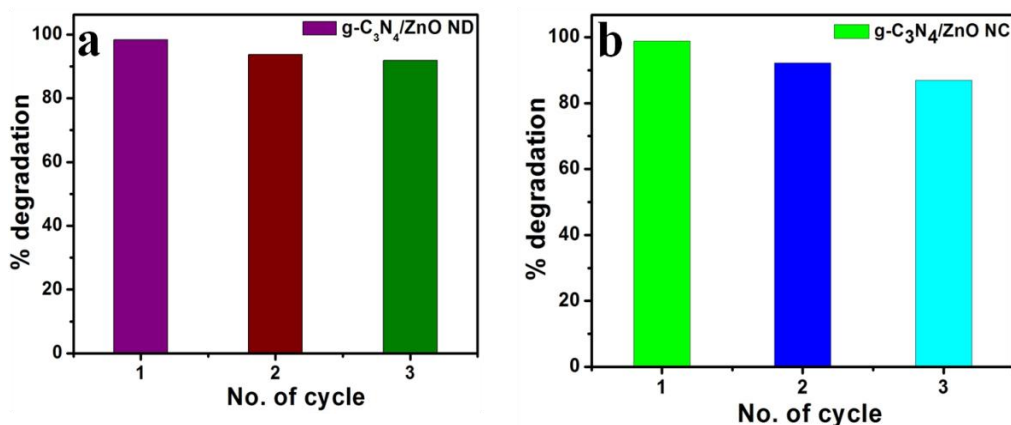
Figure 4.19 Histogram between % degradation vs. number of cycle for (a) g-C$_3$N$_4$/ZnO (dumbbell), (b) g-C$_3$N$_4$/ZnO (cone) catalyst after 140 min exposure (for each cycle) under a visible light source. The catalyst particles were centrifuged and washed well before reuse

After the 3rd cycle of photocatalysis reaction, both (dumbbell and cone) morphologies of ZnO in g-C$_3$N$_4$/ZnO heterostructures were checked with the help of FESEM which also confirmed the morphological stability of the ZnO structures (**Figure 4.20**).
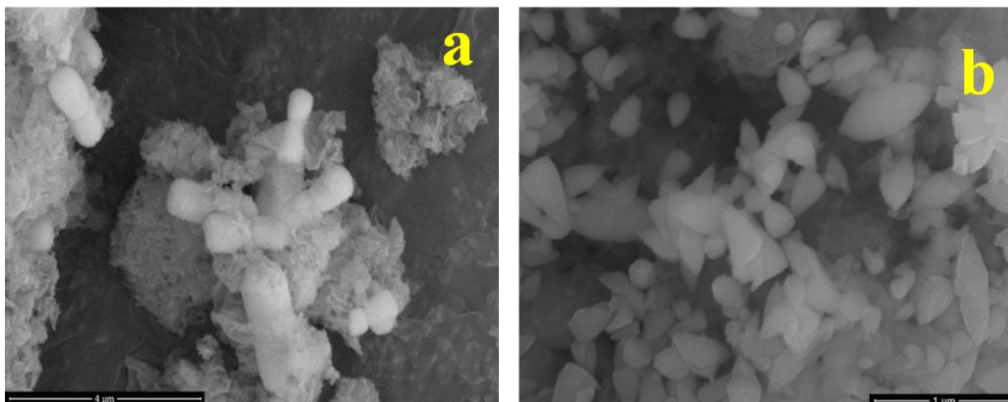
Figure 4.20 FESEM image of reused (A) g-C$_3$N$_4$/ZnO (dumbbell) and (B) g-C$_3$N$_4$/ZnO (cone) catalyst after 3rd cycle
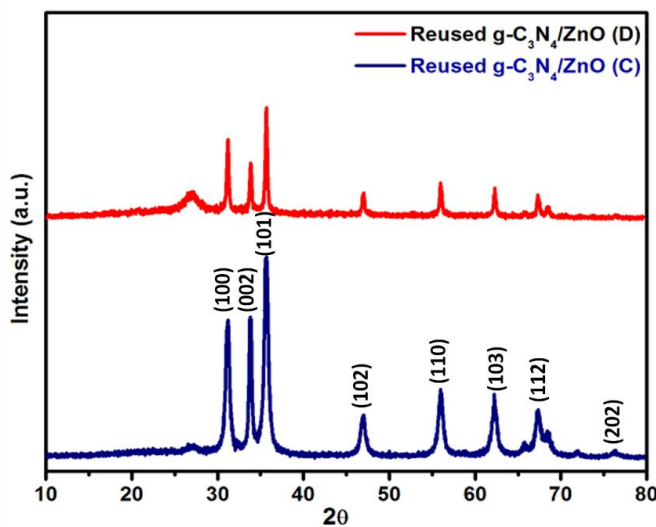
Figure 4.21 PXRD patterns of reused g-C$_3$N$_4$/ZnO (dumbbell) and g-C$_3$N$_4$/ZnO (cone) catalyst after 3rd cycle

Structural stability of the ZnO catalysts after several reuses was also verified using XRD

analysis. **Figure 4.21** represents eight major reflection peaks of ZnO in both dumbbell and cone shaped particles appear at 31.78°, 34.42°, 36.19°, 47.40°, 56.47°, 62.63°, 68.85°, and 76.71° confirm the presence of (100), (002), (101), (102), (110), (103), (112), and (202) crystal planes of ZnO, respectively. The other 2θ value at 27.6° is due to the (002) plane of g-C_3N_4. These findings are very much in line with earlier XRD data of the ZnO structures before any dye degradation. Therefore, it can be concluded that the structural purity and phase stability of dumbbell and cone shaped ZnO remain unchanged even after several cycles of the degradation process.

4.4 Conclusion

In conclusion, we have successfully developed a simple and facile wet-chemical approach for the synthesis of morphology-dependent ZnO on g-C_3N_4 surface. Dumbbell and cone structures of ZnO were synthesized using HMT and ammonia as hydrolyzing agents. As characterizing techniques, FESEM, XRD, TEM, XPS, and EDS were used to verify the formation of dumbbell and cone morphology of ZnO on g-C_3N_4 surface and phase purity as well as investigate their structural and chemical properties. On the other hand, UV-vis, PL, and FTIR were used to confirm the existence and increased lifetime of the photogenerated carriers in g-C_3N_4/ZnO heterostructures. The shape-dependent mechanism using HMT and ammonia hydrolyzing agent was discussed thoroughly. The as-prepared heterostructures were used in organic pollutants degradation under visible light irradiation which shows a higher visible light photo-activity for g-C_3N_4/ZnO heterostructures than bare ZnO particles and g-C_3N_4. Moreover, a better photo-activity was observed with the g-C_3N_4/ZnO dumbbells than the g-C_3N_4/ZnO cone structure. This simple, environmental friendly and the unique hybrid structures of g-C_3N_4/ZnO make the composite material a greater perspective in the field of energy and environment. Finally, this result provides a new visible light driven environmentally benign catalyst with high stability and shows a new pathway for fabricating an efficient heterostructure photocatalyst.

References

[1]   Zhang, Y.; Pan, Q.; Chai, G.; Liang, M.; Dong, G.; Zhang, Q.; Qiu, J. Synthesis and Luminescence Mechanism of Multicolor-Emitting g-C₃N₄ Nanopowders by Low Temperature Thermal Condensation of Melamine. *Sci. Rep.* **2013**, *3*, 1943.

[2]   Shang, L.; Bian, T.; Zhang, B.; Zhang, D.; Wu, L.-Z.; Tung, C.; Yin, Y., Zhang, T. Graphene-Supported Ultrafine Metal Nanoparticles Encapsulated by Mesoporous Silica: Robust Catalysts for Oxidation and Reduction Reactions. *Angew. Chem. Int. Ed.* **2014**, *53*, 250-254.

[3]   Yang, J.; Wu, X.; Li, X.; Liu, Y.; Gao, M.; Liu, X.; Kong, L.; Yang, S. Synthesis And Characterization of Nitrogen-Rich Carbon Nitride Nanobelts by Pyrolysis of Melamine. *Appl. Phys. A* **2011**, *105*, 161-166.

[4]   Iwano, Y.; Kittaka, T.; Tabuchi, H.; Soukawa, M.; Kunitsugu, S.; Takarabe, K.; Itoh, K. Study of Amorphous Carbon Nitride Films Aiming at White Light Emitting Devices. *Jpn. J. Appl. Phys.* **2008**, *47*, 7842-7844.

[5]   Hong, J.; Xia, X.; Wang, Y.; Xu, R. Mesoporous Carbon Nitride with In Situ Sulfur Doping for Enhanced Photocatalytic Hydrogen Evolution from Water Under Visible Light. *J. Mater. Chem.* **2012**, *22*, 15006-15012.

[6]   Zhang, X.; Xie, X.; Wang, H.; Zhang, J.; Pan, B.; Xie, Y. Enhanced Photoresponsive Ultrathin Graphitic-phase C₃N₄ Nanosheets for Bioimaging. *J. Am. Chem. Soc.* **2013**, *135*, 18-21.

[7]   Li, Y.; Zhang, J.; Wang, Q.; Jin, Y.; Huang, D.; Cui, Q.; Zou, G. Nitrogen-Rich Carbon Nitride Hollow Vessels: Synthesis, Characterization, and their Properties. *J. Phys. Chem. B.* **2010**, *114*, 9429-9434.

[8]   Wang, Y.; Wang, X.; Antonietti, M. Polymeric Graphitic Carbon Nitride as a Heterogeneous Organocatalyst: From Photochemistry to Multipurpose Catalysis to Sustainable Chemistry. *Angew. Chem. Int. Ed.* **2012**, *51*, 68-89.

[9]   Wang, X.; Maeda, K.; Thomas, A.; Takanabe, K.; Xin, G.; Carlsson, J.M.; Domen, K.; Antonietti, M. A Metal-Free Polymeric Photocatalyst for Hydrogen Production from Water under Visible Light. *Nat. Mater.* **2009**, *8*, 76-80.

[10]   Wang, X.; Chen, X.; Thomas, A.; Fu, X.; Antonietti, M. Metal-Containing Carbon

Nitride Compounds: A New Functional Organic-Metal Hybrid Material. *Adv. Mater.* **2009**, *21*, 1609-1612.

[11]   Wang, Y.; Li, H.; Yao, J.; Wang, X.; Antonietti, M. Synthesis of Boron Doped Polymeric Carbon Nitride Solids and their Use as Metal-Free Catalysts for Aliphatic C–H Bond Oxidation. *Chem. Sci.* **2011**, *2*, 446-450.

[12]   Dong, F.; Wu, L.; Sun, Y.; Fu, M.; Wu, Z.; Lee, S. C. Efficient Synthesis of Polymeric g-C_3N_4 Layered Materials as Novel Efficient Visible Light Driven Photocatalysts. *J. Mater. Chem.* **2011**, *21*, 15171-15174.

[13]   Liu, J.; Zhang, T.; Wang, Z.; Dawson, G.; Chen, W. Simple Pyrolysis of Urea into Graphitic Carbon Nitride with Recyclable Adsorption and Photocatalytic Activity. *J. Mater. Chem.* **2011**, *21*, 14398-14401.

[14]   Thomas, A.; Fischer, A.; Goettmann, F.; Antonietti, M.; Muller, J. O.; Schlogl, R.; Carlsson, J. M. Graphitic Carbon Nitride Materials: Variation of Structure and Morphology and their Use as Metal-Free Catalysts. *J. Mater. Chem.* **2008**, *18*, 4893-4908.

[15]   Zhang, X.; Wang, H.; Wang, H.; Zhang, Q.; Xie, J.; Tian, Y.; Wang, J.; Xie, Y. Single-Layered Graphitic-C_3N_4 Quantum Dots for Two-Photon Fluorescence Imaging of Cellular Nucleus. *Adv. Mater.* **2014**, *26*, 4438-4443.

[16]   Yan, H. Soft-Templating Synthesis of Mesoporous Graphitic Carbon Nitride with Enhanced Photocatalytic H_2 Evolution under Visible Light. *Chem. Commun.* **2012**, *48*, 3430-3432.

[17]   Takanabe, K.; Kamata, K.; Wang, X.; Antonietti, M.; Kubota, J.; Domen, K. Photocatalytic Hydrogen Evolution on Dye-Sensitized Mesoporous Carbon Nitride Photocatalyst with Magnesium Phthalocyanine. *Phys. Chem. Chem. Phys.* **2010**, *12*, 13020-13025.

[18]   Di, Y.; Wang, X.; Thomas, A.; Antonietti, M. Making Metal- Carbon Nitride Heterojunctions for Improved Photocatalytic Hydrogen Evolution with Visible Light. *ChemCatChem* **2010**, *2*, 834-838.

[19]   Yan, S. C.; Li, Z. S.; Zou, Z. G. Photodegradation of Rhodamine B and Methyl Orange Over Boron-Doped g-C_3N_4 Under Visible Light Irradiation. *Langmuir* **2010**, *26*, 3894-3901.

[20] Sun, J. X.; Yuan, Y. P.; Qiu, L. G.; Jiang, X.; Xie, A. J.; Shen, Y. H.; Zhu, J. F. Fabrication of Composite Photocatalyst g-C$_3$N$_4$-ZnO and Enhancement of Photocatalytic Activity Under Visible Light. *Dalton Trans.* **2012**, *41*, 6756-6763.

[21] Wang, Y.; Shi, R.; Lin, J.; Zhu, Y. Enhancement of Photocurrent and Photocatalytic Activity of ZnO Hybridized with Graphite-like C$_3$N$_4$. *Energy Environ. Sci.* **2011**, *4*, 2922-2929.

[22] Zhang, J.; Chen, X.; Takanabe, K.; Maeda, K.; Domen, K.; Epping, J.D.; Fu, X.; Antonietti, M.; Wang, X. Synthesis of a Carbon Nitride Structure for Visible-Light Catalysis by Copolymerization. *Angew. Chem. Int. Ed.* **2010**, *49*, 441-444.

[23] Wang, X.; Maeda, K.; Chen, X.; Takanabe, K.; Domen, K.; Hou, Y.; Fu, X.; Antonietti, M. Polymer Semiconductors for Artificial Photosynthesis: Hydrogen Evolution by Mesoporous Graphitic Carbon Nitride with Visible Light. *J. Am. Chem. Soc.* **2009**, *131*, 1680-1681.

[24] Jo, W. K.; Selvam, N. C. S. Enhanced Visible Light-Driven Photocatalytic Performance of ZnO-gC$_3$N$_4$ Coupled with Graphene Oxide as a Novel Ternary Nanocomposite. *J. Hazard. Mater.,* **2015**, *299*, 462-470.

[25] Zhang, Y.; Mori, T.; Ye, J.; Antonietti, M. Phosphorus-Doped Carbon Nitride Solid: Enhanced Electrical Conductivity and Photocurrent Generation. *J. Am. Chem. Soc.* **2010**, *132*, 6294-6295.

[26] Liu, G.; Niu, P.; Sun, C.; Smith, S. C.; Chen, Z.; Lu, G. Q.; Cheng, H. M. Unique Electronic Structure Induced High Photoreactivity of Sulfur-Doped Graphitic C$_3$N$_4$. *J. Am. Chem. Soc.* **2010**, *132*, 11642-11648.

[27] Wang, Y.; Di, Y.; Antonietti, M.; Li, H.; Chen, X.; Wang, X. Excellent Visible-Light Photocatalysis of Fluorinated Polymeric Carbon Nitride Solids. *Chem. Mater.* **2010**, *22*, 5119-5121.

[28] Zhu, Y. P.; Li, M.; Liu, Y. L.; Ren, T. Z.; Yuan, Z. Y. Carbon-Doped ZnO Hybridized Homogeneously with Graphitic Carbon Nitride Nanocomposites for Photocatalysis. *J. Phys. Chem. C* **2014**, *118*, 10963-10971.

[29] Yan, H.; Yang, H. TiO$_2$-gC$_3$N$_4$ Composite Materials for Photocatalytic H$_2$ Evolution under Visible Light Irradiation. *J Alloy Compd.* **2011**, *509*, L26-L29.

[30] Kumar, S.; Baruah, A.; Tonda, S.; Kumar, B.; Shanker, V.; Sreedhar, B. Cost-Effective

and Eco-Friendly Synthesis of Novel and Stable N-Doped ZnO/gC$_3$N$_4$ Core–Shell Nanoplates with Excellent Visible-Light Responsive Photocatalysis. *Nanoscale* **2014**, *6*, 4830-4842.

[31]   Liu, W.; Wang, M.; Xu, C.; Chen, S. Facile Synthesis of g-C$_3$N$_4$/ZnO Composite with Enhanced Visible Light Photooxidation and Photoreduction Properties. *Chem. Eng. J.* **2012**, *209*, 386-393.

[32]   Wang, J.; Su, F. Y.; Zhang, W. D. Preparation and Enhanced Visible Light Photoelectrochemical Activity of g-C$_3$N$_4$/ZnO Nanotube Arrays. *J. Solid State Electrochem.* **2014**, *18*, 2921-2929.

[33]   Fageria, P.; Gangopadhyay, S.; Pande, S. Synthesis of ZnO/Au and ZnO/Ag Nanoparticles and their Photocatalytic Application Using UV and Visible Light. *RSC Adv.* **2014**, *4*, 24962-24972.

[34]   Ashfold, M. N. R.; Doherty, R. P.; Angwafor, N. G. N.; Riley D. J.; Sun, Y. The Kinetics of the Hydrothermal Growth of ZnO Nanostructures. *Thin Solid Films* **2007**, *515*, 8679-8683.

[35]   Baruah, S.; Dutta, J. Hydrothermal Growth of ZnO Nanostructures. *Sci. Technol. Adv. Mater.* **2009**, *10*, 013001.

[36]   Govender, K.; Boyle, D. S.; Kenway, P. B.; O'Brien, P. Understanding the Factors that Govern the Deposition and Morphology of Thin Films of ZnO from Aqueous Solution. *J. Mater. Chem.* **2004**, *14*, 2575-2591.

[37]   Sugunan, A.; Warad, H. C.; Boman, M.; Dutta, J. Zinc Oxide Nanowires in Chemical Bath on Seeded Substrates: Role of Hexamine. *J. Sol-Gel Sci. Technol.* **2006**, *39*, 49-56.

[38]   Vayssieres, L.; Keis, K.; Lindquist, S. E.; Hagfeldt, A. Purpose-Built Anisotropic Metal Oxide Material: 3D Highly Oriented Microrod Array of ZnO. *J. Phys. Chem. B* **2001**, *105*, 3350-3352.

[39]   Vayssieres, L. Growth of Arrayed Nanorods and Nanowires of ZnO From Aqueous Solutions. *Adv. Mater.* **2003**, *15*, 464-466.

[40]   Ong, C. B.; Ng, L. Y.; Mohammad, A. W. A Review of ZnO Nanoparticles as Solar Photocatalysts: Synthesis, Mechanisms and Applications. *Renew. Sust. Energ. Rev.* **2018**, *81*, 536-551.

[41]   Li, X.; Li, M.; Yang, J.; Li, X.; Hu, T.; Wang, J.; Sui, Y.; Wu, X.; Kong, L. Synergistic

Effect of Efficient Adsorption g-C$_3$N$_4$/ZnO Composite for Photocatalytic Property. *J. Phys. Chem. Solids* **2014**, *75*, 441-446.

[42]   Zhou, J.; Zhang, M.; Zhu, Y. Preparation of Visible Light-Driven g-C$_3$N$_4$@ ZnO Hybrid Photocatalyst via Mechanochemistry. *Phys. Chem. Chem. Phys.* **2014**, *16*, 17627-17633.

[43]   Wang, X. J.; Yang, W. Y.; Li, F. T.; Xue, Y. B.; Liu, R. H.; Hao, Y. J. In Situ Microwave-Assisted Synthesis of Porous N-TiO$_2$/g-C$_3$N$_4$ Heterojunctions with Enhanced Visible-Light Photocatalytic Properties. *Ind. Eng. Chem. Res.* **2013**, *52*, 17140.

[44]   Xu, Y.; Schoonen, M. A. The Absolute Energy Positions of Conduction and Valence Bands of Selected Semiconducting Minerals. *Am. Mineral.* **2000**, *85*, 543-556.

[45]   Samal, A.; Das, D. P. Transfiguring UV Light Active "Metal Oxides" to Visible Light Active Photocatayst by Reduced Graphene Oxide Hypostatization. *Catal. Today* **2018**, *300*, 124-13.

[46]   Wang, Y.; Wang, Z.; Muhammad, S.; He, J. Graphite-like C$_3$N$_4$ Hybridized ZnWO$_4$ Nanorods: Synthesis and its Enhanced Photocatalysis in Visible Light. *CrystEngComm* **2012**, *14*, 5065-5070.

[47]   Lin, X.; Guo, X.; Shi, W.; Zhao, L.; Yan, Y.; Wang, Q. Ternary Heterostructured Ag-BiVO$_4$/InVO$_4$ Composites: Synthesis and Enhanced Visible-Light-Driven Photocatalytic Activity. *J. Alloys Compd.* **2015**, *635*, 256-264.

[48]   Ravichandran, K.; Kalpana, K.; Uma, R.; Sindhuja, E.; Seelan, K. S. Cost-Effective Fabrication of ZnO/g-C$_3$N$_4$ Composite Film Coated Stainless Steel Meshes for Visible Light Responsive Photocatalysis. *Mater. Res. Bull.* **2018**, *99*, 268-280.

[49]   Park, T. J.; Pawar, R. C. Kang, S.; Lee, C. S. Ultra-Thin Coating of g-C$_3$N$_4$ on an Aligned ZnO Nanorod Film for Rapid Charge Separation and Improved Photodegradation Performance. *RSC Adv.* **2016**, *6*, 89944-89952.

[50]   Sivalingam, M. M.; Balasubramanian, K. Morphological Tuned Preparation of Zinc Oxide: Reduced Graphene Oxide Composites for Non-Enzymatic Fluorescence Glucose Sensing and Enhanced Photocatalysis. *Appl. Phys. A* **2016**, *122*, 694.

Carbon Nitride (C₃N₄) Quantum Dots: A Material for the Synthesis and Stabilization of Monometallic (Au & Pd) and Bimetallic (AuPd) Nanoparticles for Nitrophenol Reduction

✿ *Synthesis of mono- (Au and Pd) and bimetallic (AuPd) nanoparticles using carbon nitride (C₃N₄) quantum dots (QDs) as a photoreducing and stabilizing agents is reported.*

✿ *In addition, catalytic efficiency of mono- (Au and Pd) and bimetallic (AuPd) nanoparticles were tested using a model reduction reaction, 4-NP to 4-AP and AuPd was observed to be a superior catalyst.*
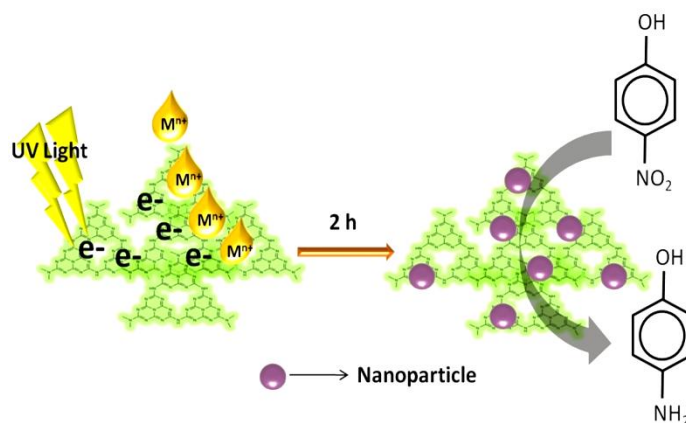
Abstract

In this study, we report the synthesis of monometallic (Au and Pd) and bimetallic (AuPd) nanoparticles (NPs) using graphitic carbon nitride (g-C$_3$N$_4$) quantum dots (QDs) and photochemical routes. Eliminating the necessity of any extra stabilizer or reducing agent, the photochemical reactions have been carried out using a UV light source of 365 nm where C$_3$N$_4$ QD itself functions as a suitable stabilizer as well as a reducing agent. The C$_3$N$_4$ QDs are excited upon irradiation with UV light and produce photogenerated electrons, which further facilitate the reduction of metal ions. The successful formation of Au, Pd, and AuPd alloy nanoparticles is evidenced by UV-vis, powder X-ray diffraction, X-ray photon spectroscopy, and energy-dispersive spectroscopy techniques. The morphology and distribution of metal nanoparticles over the C$_3$N$_4$ QD surface has been systematically investigated by high-resolution transmission electron microscopy and SAED analysis. To explore the catalytic activity of the as-prepared samples, the reduction reaction of 4-nitrophenol with excellent performance is also investigated. It is noteworthy that the synthesis of both monometallic and bimetallic NPs can be accomplished by using a very small amount of C$_3$N$_4$, which can be used as a promising photoreducing material as well as a stabilizer for the synthesis of various metal nanoparticles.

5.1 Introduction

In the past decade, a plethora of reports have been documented, stating the wide range of applications of the noble metal nanoparticles (NPs). Metal NPs have been proved as efficient catalysts due to their high optical absorption in UV and visible light regime (a major part of solar spectrum), which makes them greatly significant for practical applications [1]. Metal NPs, *e.g.,* Au, Ag, Pd and Pt are well known for harvesting light energy [2]. to perform as an active catalyst in cross coupling reactions [3,4,5], redox reactions [6,7,8] and photocatalytic reactions [4-10]. Most of the metal NPs are also used in biological applications such as a sensor to the cancer therapy, [11] light emitting devices [12] as well as in surface enhanced Raman spectroscopy (SERS) studies [13]. The synthesis of noble metal nanoparticles (NPs) using greener routes is a major agenda of nowadays scientific research [14,15]. Indeed, many reports on the synthesis of metal NPs using various methods, like thermal reduction of metal ion, electrochemical methods, [16] radiolytic, sonochemical process, [17] and photochemicaly [18,19] abound in the literature [18-21]. The one pot synthesis and in-situ assembly of fluorescent gold nanodots using photochemical method was reported by Zhang and co-workers [22]. El-Sayed and co-workers also reported the photochemical reduction of gold chloride in presence of ethylene glycol (EG) and polyvinylpyrrolidone (PVP) to Au NPs [23]. Sun and co-workers reported the synthesis of Au NPs using graphitic carbon nitride (g-C_3N_4) quantum dots (QDs) under UV irradiation, which shows the photocatalytic property of g-C_3N_4 QD for the synthesis of metal NPs [24]. The same group also reported the use of g-C_3N_4 nanosheets as a support and visible light driven photocatalyst for the green synthesis of Au NPs/g-C_3N_4 hybrid using methanol as a reducing agent and their enhanced photocatalytic performance in pollutant degradation [25]. Barman and co-workers demonstrated ultrasound mediated synthesis of Au-CN_x composite, where the dispersed Au NPs are very small in size (1-3 nm), and their superior catalytic properties towards the reduction of 4-NP [26].

Graphitic carbon nitride (g-C_3N_4), a graphene derivative with a delocalized pi-conjugated structure, of band gap ~ 2.70 eV has been turned out to be a fascinating choice in the field of photocatalysis [27]. The wide catalytic applications of g-C_3N_4 include the degradation of hazardous dyes, water splitting, hydrogen storage, bioimaging, Friedel-Craft reactions, NO decomposition and CO_2 reduction etc. [28]. Recently, g-C_3N_4 is identified as a polymeric organic

metal-free semiconductor of visible light photocatalyst and electrocatalyst for oxygen and hydrogen evolution reaction (OER & HER) [29-32]. g-C_3N_4 has many intriguing features such as chemical and thermal stability, high in plane nitrogen content, low cost, easy preparation and environment benign [31-34]. Low specific surface area and poor quantum yield significantly limits the performance of bulk g-C_3N_4 which demands a further improvement [31-33]. To resolve the above mentioned shortcomings of g-C_3N_4 in the bulk form, quantum dots of graphitic carbon nitrite with significantly enhanced surface to volume ratio with better quantum confinement have been prepared. However, C_3N_4 quantum dot has recently attracted tremendous attention because of its excellent reactivity, good stability, effectivity as fluorescent probe for the biological samples and environmental detection, water solubility, sensing ability, resistivity against corrosion, low cytotoxicity as well as wide range of applicability as catalysis [26,35-39].

Being inspired from the above studies, we have introduced a facile photochemical reduction approach for the synthesis of mono- (Au and Pd) and bimetallic (AuPd) nanoparticles using the C_3N_4 QD. Initially, C_3N_4 QD was illuminated with a UV light source of $\lambda = 365$ nm and to excite electrons, which were further utilized for the reduction of metal ions to metal nanoparticles. The type of synthesis is quite prominent as it uses very less amount of C_3N_4 QDs as a photoreducing agent as well as provides support for the growth of metal nanoparticles. Monometallic (Au & Pd) and bimetallic (AuPd) nanoparticles of size starting from 13 down to 5 nm were synthesized. The as-synthesized materials were characterized using UV-vis, XPS, TEM, EDS, and PXRD techniques to confirm their formation, size, shape, oxidation states and phase purity. In addition, to probe the catalytic efficiency of these mono-(Au and Pd) and bimetallic (AuPd) nanoparticles reduction reaction using 4-nitrophenol (4-NP) to 4-aminophenol (4-AP) was also tested. Interestingly, superior photocatalytic efficiency was observed for bimetallic nanoparticles as compare to monometallic and bare C_3N_4 QD. Hence, it can be concluded that the advantages for this synthesis are in manifold. Firstly, a metal free fluorescent semiconductor (C_3N_4 QD) is used as a photoreducing agent. Secondly, a simple and highly reproducible method for the synthesis of mono- and bimetallic NPs is reported. Finally, the necessity of any external stabilizing and reducing agent can also be eliminated.

5.2 Experimental Section

5.2.1 Synthesis of C₃N₄ Quantum Dot

Solid powder of C_3N_4 QDs was synthesized using urea and trisodium citrate and reported elsewhere [40]. In brief, 0.101 g urea and 0.081 g trisodium citrate were well grinded and properly mixed in a mortar pestle. Afterwards, the grinded powder was kept in a covered crucible and heated at 180 °C for 1 hour in a muffle furnace. After the furnace heating, dark brown coloured QDs powder was obtained which further washed with methanol 3-4 times to remove the extra impurities and dried in oven. Thereafter, 100 mg of dry C_3N_4 QDs powder was dissolved in 10 mL water and dialyzed against Milli-Q water using 10,000 kDa MW cut off dialysis membrane. The dialysed solution was then preserved and used as photocatalyst for the synthesis of metal nanoparticles. After dialysis, C_3N_4 QDs showed a strong green fluorescence colour under the UV irradiation ($\lambda = 365$ nm).

5.2.2 Synthesis of Mono- (Au and Pd) and Bimetallic (AuPd) Nanoparticles

Synthesis of Au and Pd nanoparticles were carried out by using dialyzed C_3N_4 solution as a photo-reducing agent. Dialyzed solution 40.0 µL of C_3N_4 and 100.0 µL of 10^{-2} M $HAuCl_4$ were added in 30% (volume ratio) ethanol solution. The total volume of the reaction mixture was 5.0 mL (1.5 mL absolute EtOH + 3.38 mL water) and kept under the UV lamp ($\lambda = 365$ nm) for 2 h in a closed system. The solution was continuously stirred during the UV light irradiation. After 2 h, the colour of the UV light exposed solution was changed to pink, indicating the formation of gold nanoparticles. However, Pd nanoparticles were also synthesised following a similar method of Au NP, except 100.0 µL of K_2PdCl_4 (10^{-2} M) was used instead of $HAuCl_4$. In this case, black coloured Pd nanoparticles were obtained after the UV light irradiation for 2 h.

In case of AuPd alloy nanoparticles synthesis, a co-reduction technique was followed, where both $HAuCl_4$ (50 µL of 10^{-2} M) and K_2PdCl_4 (50 µL of 10^{-2} M) were added instead of using only one metal precursor. Finally, a pinkish black solution was obtained for AuPd alloy after 2 h of UV light illumination. It can be noted that during the synthesis of mono- and bimetallic NPs no extra reducing agent was added. Both the as-synthesized Au and Pd NPs were very much stable for long time, whereas AuPd bimetallic alloy showed a relatively less stability

and appeared with a black precipitate after 24 h of synthesis. Hence, to avoid any kind of agglomeration in AuPd alloy, polyvinylpyrrolidone (2.8 mL of 2×10^{-3} M) was added as stabilizer after the formation of NP, *i.e.,* after 2 h of UV light irradiation. The overall synthetic procedure of mono- and bimetallic NPs is schematically shown in **Scheme 5.1**.

5.3 Results and Discussion

5.3.1 Characterization

5.3.1.1 UV-visible Absorption Study of Mono- and Bimetallic NPs

UV-vis absorption spectrum of the dialysed C_3N_4 solution is shown in **Figure 5.1**. It can be seen from **Figure 5.1** that the C_3N_4 QDs shows a clear band at 330 nm with a rising baseline around 450 nm, which can be related to the characteristic absorption peak of the graphite like stacked layered structure as well as the π-π conjugation in C_3N_4 [40,41]. Similar kind of UV-vis pattern for C_3N_4 solution *i.e.*, stacked layer structure and π-π conjugation is also reported in the literature [40,42,43]. Using classical tauc approach, energy band gap (E_g) for the C_3N_4 QDs was calculated to be 3.24 eV (**inset** of **Figure 5.1**), which is nicely matching with the reported literature values. The widening of the HOMO-LUMO energy gap depends upon the quantum confinement effect of smaller size nanoparticles [42].

UV-vis spectrum for Au NP exhibits characteristic plasmon band at 532 nm, as can be seen in **Figure 5.1**. This region of UV-vis study clearly indicates the formation of Au NPs and the surface plasmon band of Au is greatly affected by the particle size, shape, surrounding environment, and interparticle interactions [24,44,45]. As there is no characteristic peak for the case of Pd NPs, a featureless nature is attained. AuPd bimetallic NPs show an absorption band at 532 nm for Au(0), also indicates the presence of Au within the solution. During the synthesis of metal NPs, only 40.0 µL of C_3N_4 dialyzed solution was used which does not any characteristic peak in the plasmon band of mono- and bimetallic NPs.
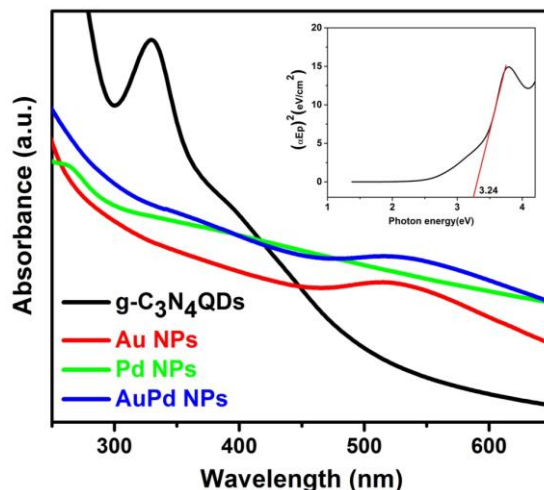
Figure 5.1 UV-vis absorption spectra of C$_3$N$_4$ QDs, Au, Pd, and AuPd NPs. 30% ethanol solution was used as a reference. Inset shows $(\alpha E_p)^2$ vs. E$_p$ plot for band gap (E$_g$) calculation of C$_3$N$_4$ QDs

5.3.1.2 Powder X-ray Diffraction Study of Mono- and Bimetallic NPs

The structural identity and phase purity of the as-obtained C$_3$N$_4$ QDs as well as all Au, Pd, AuPd NPs were confirmed using the powder X-ray diffraction (PXRD) patterns, as shown in **Figure 5.2**.**a**. The XRD pattern of pure C$_3$N$_4$ QDs reveals distinct reflections at 2θ = 13.1° and 27.7°, correspond to the (100) equivalent planes and interlayer stacking of aromatic segments, which can be indexed to (002) reflection plane, (**Figure 5.2.b**). This result is consistent with the previous reports [40,42]. In case of Au samples, the PXRD pattern shows four separate reflections at 2θ = 38.11°, 44.29°, 64.81°, and 77.60°, corresponding to (111), (200), (220), and (311) planes of Au NPs, respectively (JCPDS No. 89-3697) [44]. Two reflection peaks at 39.94° and 46.28° assigned to (111) and (200) planes of face centered cubic Pd NPs (JCPDS No. 87-0645) were observed [6,7]. Subsequently, in AuPd bimetallics, PXRD spectrum shows the presence of both Au and Pd with a minor shift and significant broadening of the Au reflection planes. The 2θ values are at 38.63, 44.74, 65.18, and 77.98 corresponds to (111), (200), (220), and (311) crystal planes. This peak shift and broadening may originate due to the interaction between Au and Pd atoms and associate lattice strain which confirms the formation of bimetallic alloy NPs [3,8,46].
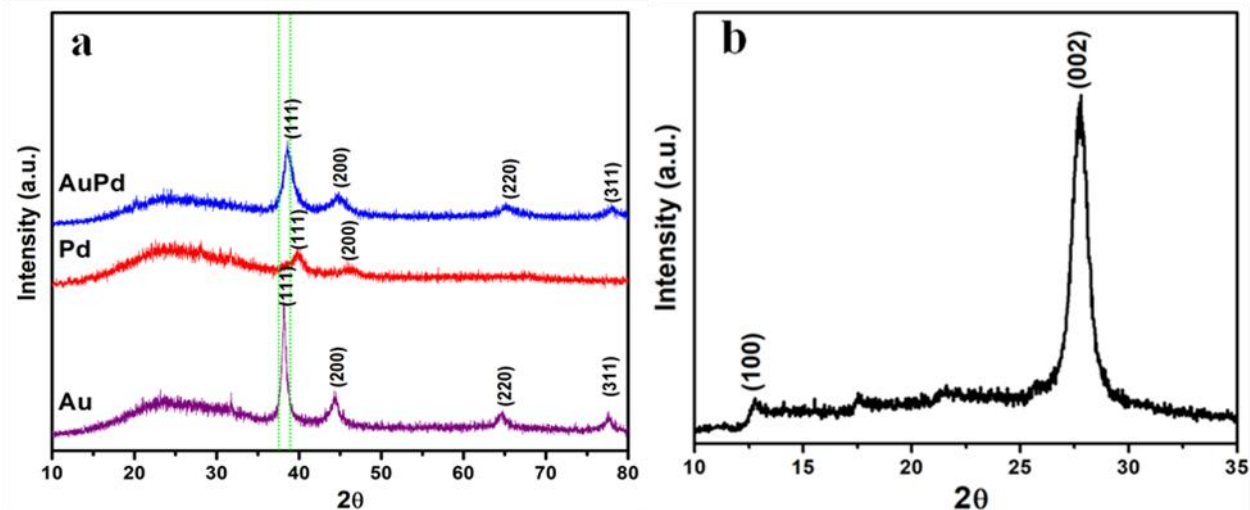
Figure 5.2 (a) Powder X-ray diffraction patterns of Au, Pd, and AuPd NPs. During PXRD measurement scan rate was fixed at 2° per min and (b) PXRD patterns for C$_3$N$_4$ QDs powder before dialysis

5.3.1.3 Morphological Analysis of Mono- and Bimetallic NPs

In order to confirm size, shape, and morphology of the photochemically synthesized C$_3$N$_4$ QDs, Au, Pd, and AuPd NPs, TEM studies were performed, which are depicted in **Figure 5.3-5.6**. TEM image and the size-distribution histogram of bare C$_3$N$_4$ QDs (**Figure 5.3**), shows well dispersed particles of uniform in size 4.5±1.1 nm.
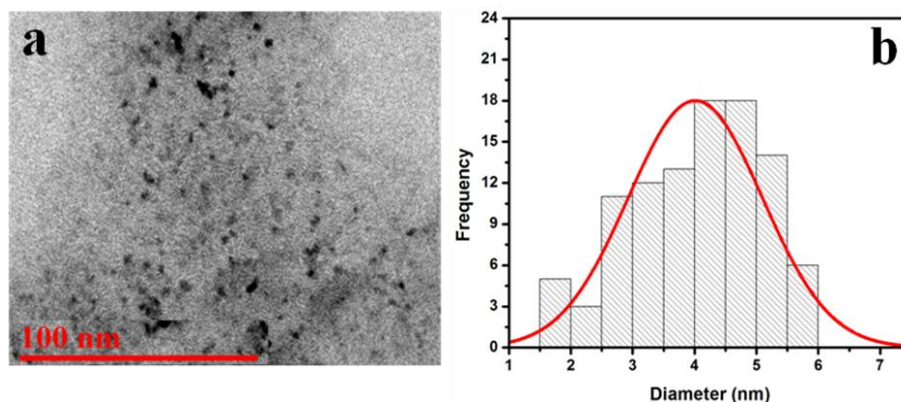
Figure 5.3 (a) TEM image of dialysed C$_3$N$_4$ QDs solution prepared by urea and trisodium citrate and (b) size-distribution histogram (4.5±1.1 nm)

Figure 5.4.a, b and **c** represent the TEM images at low and high resolution of Au NPs of average sizes 6.8±1.3 nm and of spherical shape. The corresponding size distribution histogram for Au NPs is shown in **Figure 5.3.a**. High-Resolution TEM image (**Figure 5.4.c**) reveals the d-spacing value of 0.24 nm corresponds to (111) lattice plane of Au NPs. The presence of (111) and (200) diffraction planes for Au NPs are also confirmed from SAED analysis shown in **Figure 5.6.a**.
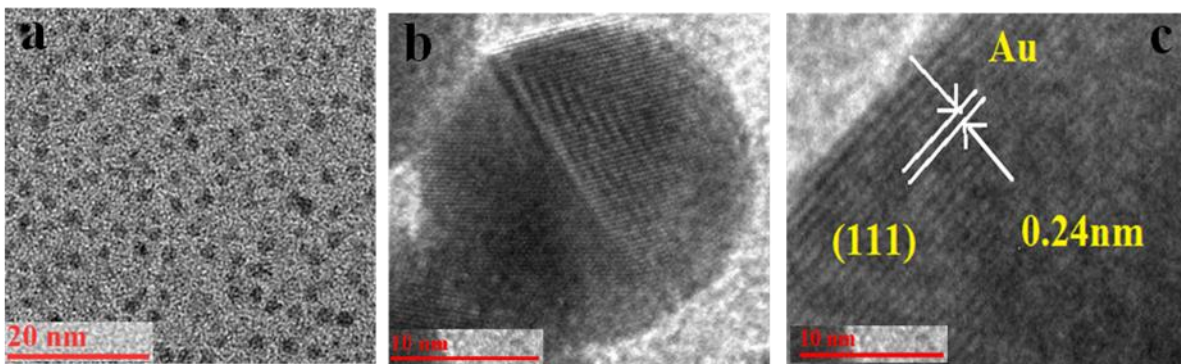
Figure 5.4 (a) TEM image of Au NPs and (b) High Resolution TEM images of Au NPs and (c) d-spacing calculation of Au NPs
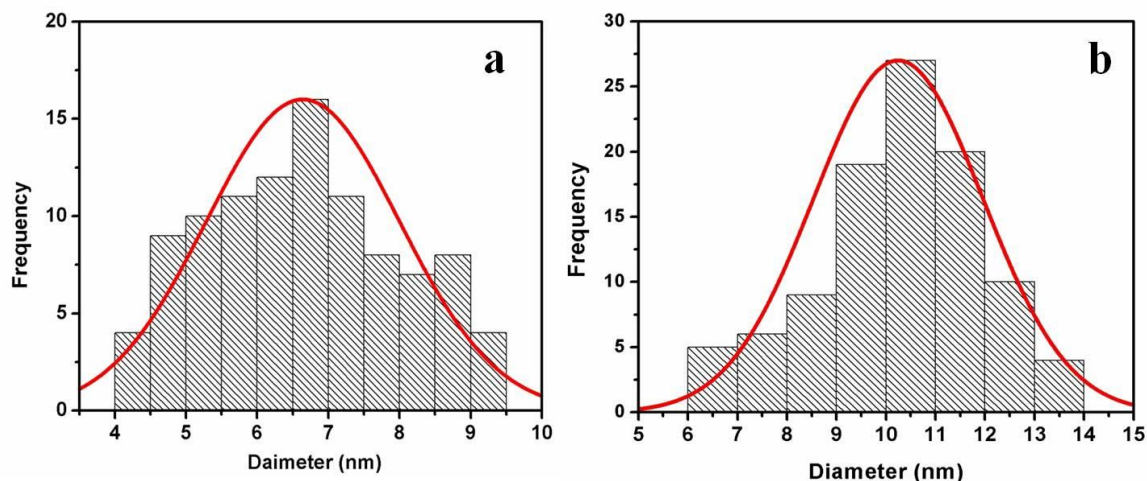
Figure 5.5 (a) Size-distribution histogram of Au NPs (6.8±1.3 nm) and (b) size-distribution histogram of Pd NPs (10.1±1.2 nm)

Plain view TEM and HRTEM images of Pd NPs are shown by **Figure 5.7.a, b** and **c**,

which illustrate that Pd NPs are not fully monodispersed like Au NPs. However, as illustrated in the size distribution histogram in **Figure 5.5.b** the average particle size for Pd is 10.1±1.2 nm. HRTEM image shows a d-spacing value of 0.23 nm correspond to the (111) plane of Pd NPs, which is also supported by the SAED analysis (**Figure 5.6.b**).
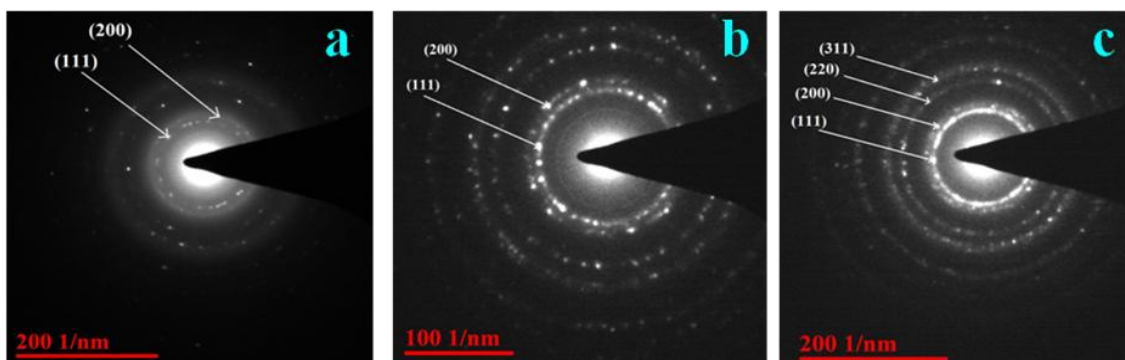
Figure 5.6 Selected area electron diffraction patterns in (a) Au, (b) Pd and (c) AuPd NPs
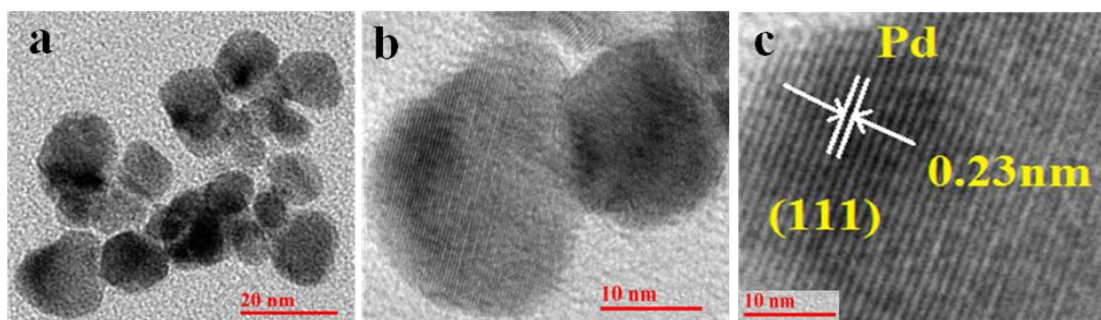
Figure 5.7 (a) TEM image of Pd NPs and (b) High Resolution TEM images of Pd NPs and (c) d-spacing calculation of Pd NPs

Figure 5.8.a, b and **c** shows low & high resolution TEM image of AuPd alloy nanoparticles which are spherical in shape. The average diameter of AuPd alloy is calculated to be 9.6±1.9 nm and the size-distribution histogram is shown in **Figure 5.8.d**. The interplanar spacing of 0.24 nm is due to the spacing of (111) crystal plane for alloy nanoparticles. The equivalent planes can be seen from SAED pattern shown in **Figure 5.6.c**. All the interplanar spacing value for Au and Pd NPs are in good agreement with previously reported values [6,7,24].
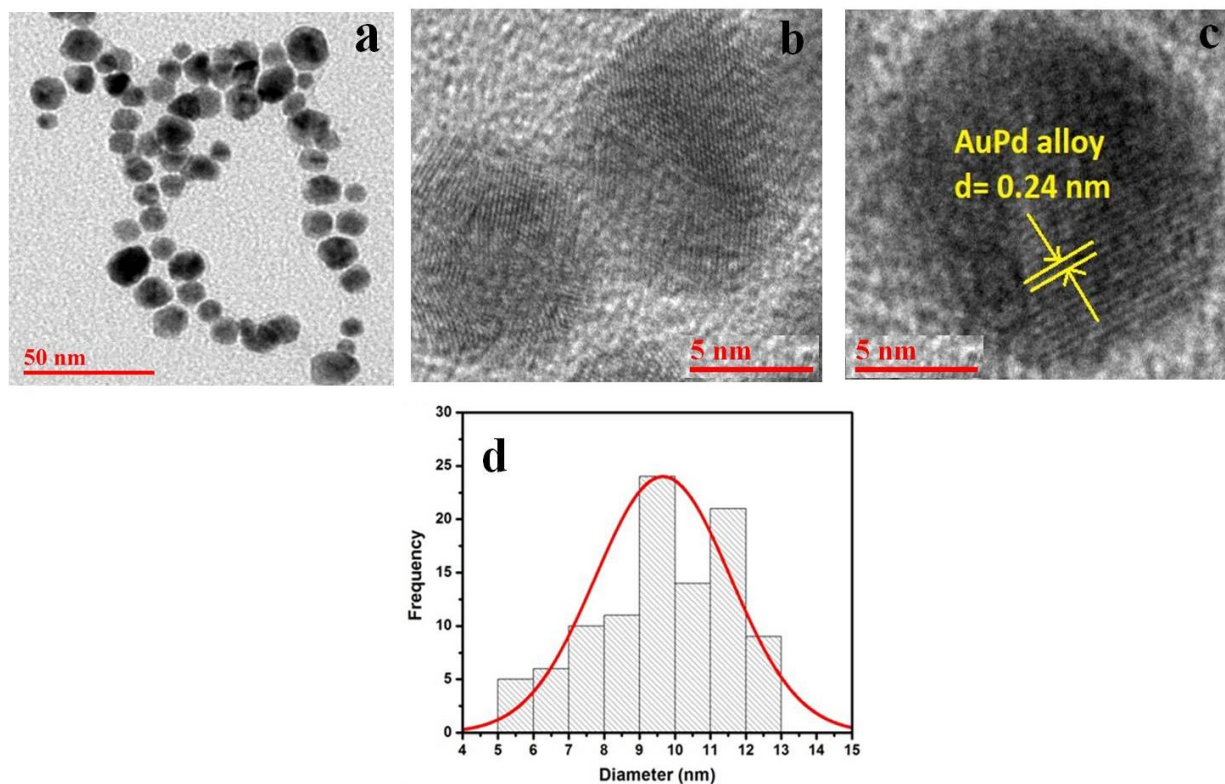
Figure 5.8 (a) TEM image of AuPd NPs, (b) High Resolution TEM images of AuPd NPs, (c) d-spacing calculation of AuPd NPs and (d) size-distribution histogram for AuPd NPs
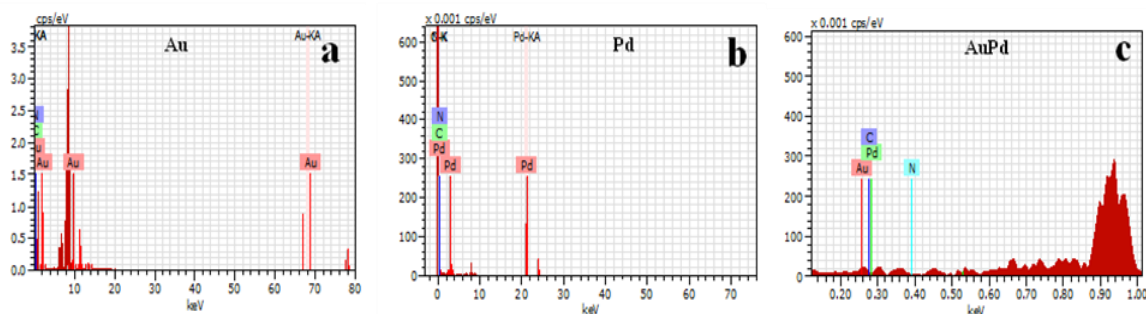
Figure 5.9 EDS spectra of (a) Au, (b) Pd and (c) AuPd NPs

Furthermore, the EDS analysis of the Au, Pd and AuPd NPs are shown in **Figure 5.9.a, b and c** to further ensure the presence of Au and Pd metals. Peaks correspond to C and N also confirms the presence of C_3N_4 surrounding metal NPs. EDS line mapping of AuPd alloy clearly illustrates the presence of both Au and Pd along with C and N. The line mapping results Au:Pd =

1:1, which further confirms the combination of Au and Pd in AuPd alloy, as shown in **Figure 5.10**.
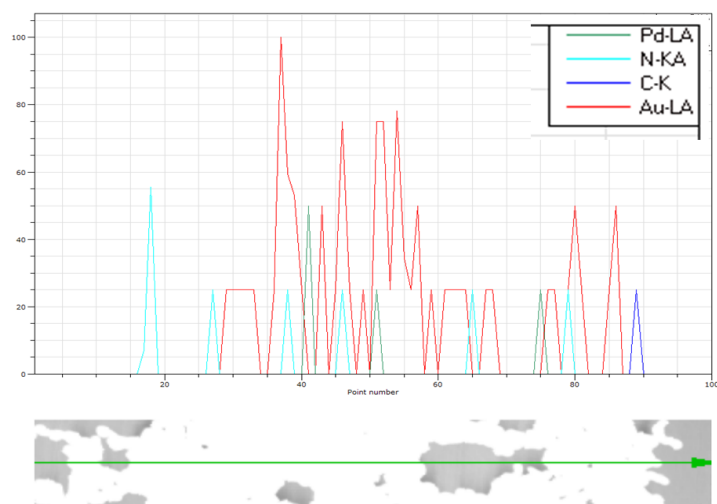
Figure 5.10 Line spectrum of AuPd NPs solution shows the presence of both Au and Pd nanoparticles with C and N from g-C$_3$N$_4$
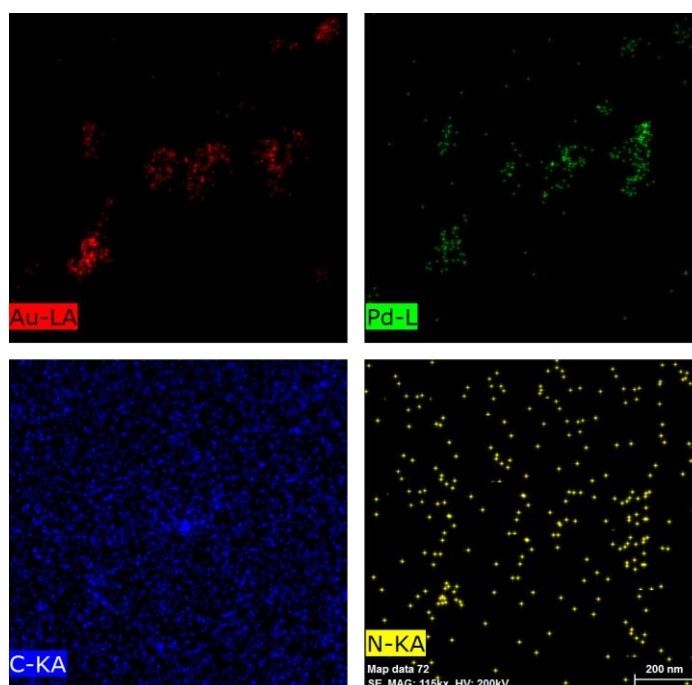
Figure 5.11 EDS mapping of AuPd alloy NPs shows the presence of both Au and Pd nanoparticles with C and N from C$_3$N$_4$

To demonstrate the space distribution of Au and Pd in AuPd alloy NPs, EDS area mapping analysis is performed (**Figure 5.11**), which confirms the presence of Au and Pd nanocrystals within the alloy NPs.

5.3.1.4 Surface Chemical Analysis of Au, Pd and AuPd Nanoparticles on C_3N_4 Surface

To investigate the surface chemical properties, material compositions and the oxidation states of the metal (Au, Pd, and AuPd) nanoparticles synthesized on C_3N_4 surface, XPS technique was employed as a characterizing tool. Successful formation of all types of metal nanoparticles on g-C_3N_4 surface as well as their oxidation states are depicted in **Figure 5.12**. **Figure 5.12.a** shows a comparison of the survey spectra for bare and bimetallic AuPd nanoparticles decorated graphitic carbon nitride surface. Both spectra appear with strong existence of C 1s (285 eV), N 1s (399 eV) and O 1s (532 eV) core level binding energy peaks along with Si 2p (100 eV) and Si 2s (150 eV) BEs, originated from the Si substrate. In addition, clear existence of Au 4f (87.3 eV and 83.6 eV) as well as Pd 3d (340 eV and 335 eV) doublets within the AuPd nanostructure confirms the successful formation of bimetallic nanoparticles of AuPd alloy on the C_3N_4 surface. High resolution scans of C 1s and N 1s core level spectra with various deconvolution components are shown for a clean C_3N_4 surface in **Figure 5.12.b** and **Figure 5.12.c**, respectively.

The deconvoluted C 1s binding energy spectrum is fitted into four peaks at around 284.6 eV, 286.2 eV, 288 eV and 289.2 eV, which can be attributed to C-C, C-N (or C-O), C=N and C=O bonding, respectively (**Figure 5.12.b**). Similarly, the N 1s BE spectrum of C_3N_4 is also deconvoluted into four peaks centering around 400.6 eV, 399.8 eV, 398.6 eV and 397.4 eV, corresponding to N-O (or N-H), N-(C)$_3$, C-N-C, and C=N-C, respectively (**Figure 5.12.c**). These findings are in good agreement with earlier reported values of carbon nitrides [24-26]. High resolution Au 4f binding energy spectrum of the AuPd NPs synthesized on C_3N_4 surface is presented in **Figure 5.12.d**. Two binding energy peaks, positioned at 83.6 and 87.3 eV, appear with an energy separation was 3.7 eV and an intensity ratio of 0.75, which clearly represent the spin orbit splitting of metallic Au(0), *i.e.*, zero oxidation state of Au4f$_{7/2}$ and Au4f$_{5/2}$, respectively. Similarly, the high resolution Pd 3d B.E. spectrum of AuPd/C_3N_4, with various deconvolution components is presented in **Figure 5.12.e**.
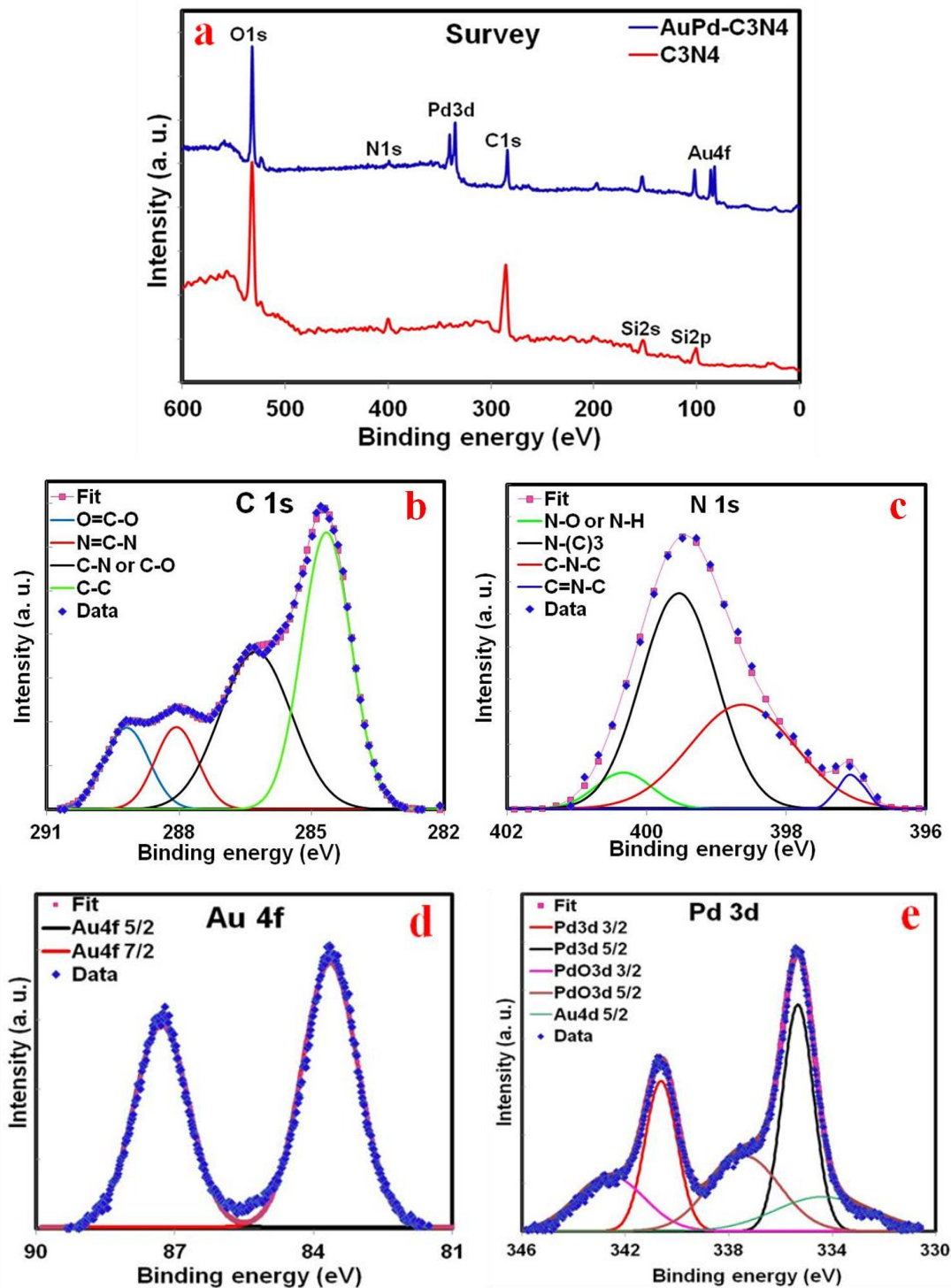
Figure 5.12 XP spectra of (a) wide scan survey of g-C₃N₄ and AuPd structure. High resolution scans of (b) C 1s, (c) N 1s spectra for g-C₃N₄, (d) Au 4f and (e) Pd 3d for Au-Pd structure

Deconvolution data mainly appears with two sets of Pd 3d doublets with an intensity ratio of about 68% for both cases. One pair centered at 335.3 eV and 340.6 eV corresponds to the metallic Pd(0) state of Pd $3d_{5/2}$ and Pd $3d_{3/2}$, respectively. Whereas, the other Pd doublet positioned at 337.4 and 342.6 eV can be attributed to the Pd(II) oxidation state, suggesting that the Pd surface is partially oxidized [47]. However, a small amount of Au $4d_{5/2}$ component centered at 334.2 eV can also be observed within the deconvoluted part. High resolution scans of monometallic Au and Pd nanoparticles on C_3N_4 show very similar kind of results as can be seen in **Figure 5.13**.
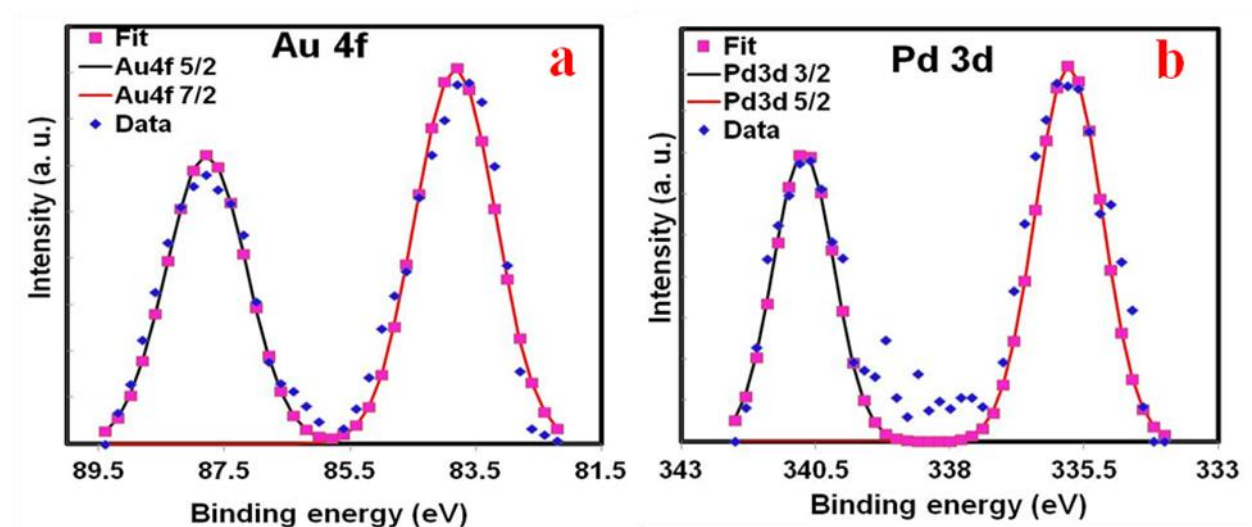
Figure 5.13 High resolution XP spectra (a) Au 4f and (b) Pd 3d for Au and Pd NPs on g-C_3N_4 structure, respectively

Figure 5.13.a represents the Au 4f scan of Au whereas for Pd, Pd 3d scan is presented in **Figure 5.13.b**. Both the monometallic nanoparticles appear with zero oxidation states. However, minor shifts in binding energy peak positions towards the higher energy for monometallic particles as compared to the bimetallic one have also been noticed. This observation is consistent with the exchange of electrons between Au and Pd NPs which may further result in more efficient transfer of electrons from the C_3N_4 substrate to the metal nanoparticles [48]. For a better understanding and clarity, every detail of all the deconvoluted spectra is summarized in **Table 5.1**.

Table 5.1 Binding Energy positions and relative intensities of deconvoluted C 1s and N 1s spectra for g-C$_3$N$_4$ QDs and Au 4f and Pd 3d for AuPd, respectively

Samples	B. E. peaks	Sub-peaks	Area	Position
C$_3$N$_4$	C 1s	O=C-O	4769.405	289.196
		N=C-N	4523.938	288.064
		C-N or C-O	14633.09	286.263
		C-C	17741.68	284.66
	N 1s	N-O or N-H	225.975	400.332
		N-(C)$_3$	1801.691	399.54
		C-N-C	1210.976	398.63
		C=N-C	103.305	397.07
AuPd bimetallics	Au 4f	Au 4f$_{5/2}$	217359.3	87.291
		Au 4f$_{7/2}$	288833.3	83.649
	Pd 3d	Pd 3d$_{3/2}$	243274.2	340.622
		Pd 3d$_{5/2}$	357513.7	335.329
		PdO 3d$_{3/2}$	185230.6	342.567
		PdO 3d$_{5/2}$	265672.2	337.394
		Au 4d$_{5/2}$	160017.6	334.392

5.3.2 Formation Mechanism of Au, Pd, and AuPd NPs using C$_3$N$_4$ Photoreducing Agent

The mechanism of Au, Pd, and AuPd NPs formation using C$_3$N$_4$ as a photoreducing agent has been shown in **Scheme 5.1**.

In brief, urea and sodium citrate in 6:1 was used to get a bright fluorescent C$_3$N$_4$ QDs at 180 °C, using a muffle furnace. The purified QDs were consumed for the synthesis of mono- and bimetallic NPs under the illumination of UV light (λ = 365 nm). During the synthesis of metal NPs, 30% ethanolic solution was utilized as a solvent. Gold and palladium salts were taken with 40.0 μL of C$_3$N$_4$ QD solution. Digital photographs of all the synthesized NPs have been shown in the **Figure 5.14**.
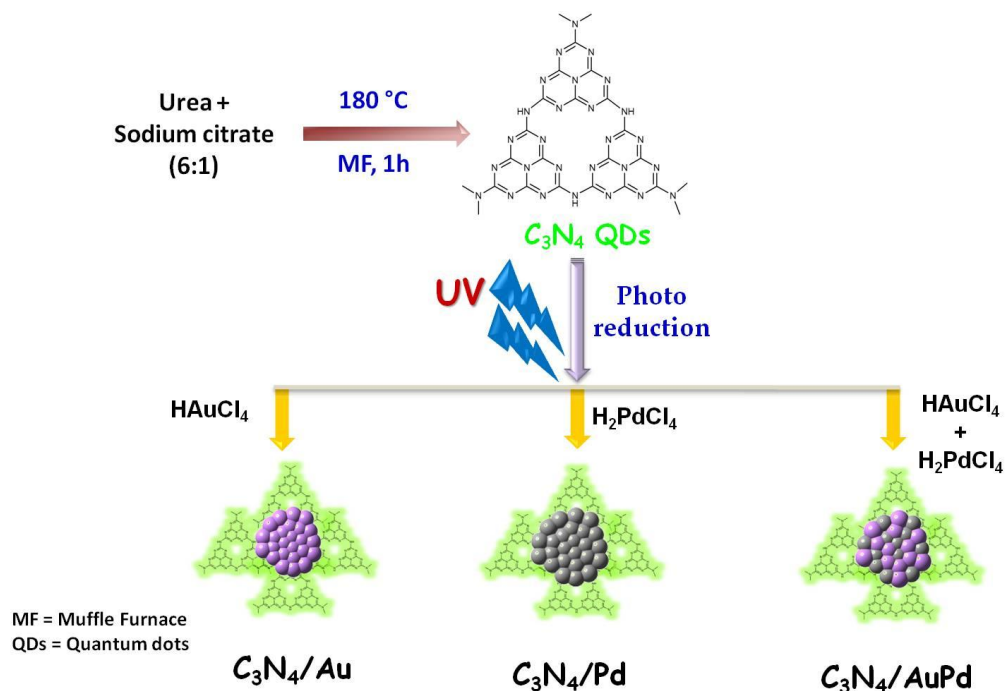
Scheme 5.1 Schematic representation for the formation of C$_3$N$_4$ QDs, Au, Pd, and AuPd NPs under UV light irradiation
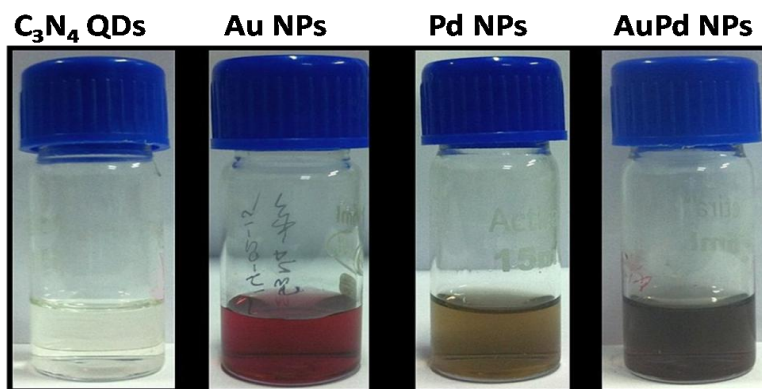
Figure 5.14 Digital photograph of C$_3$N$_4$ QDs, Au, Pd and AuPd NPs

C$_3$N$_4$ QDs have stacked layer structure, which are analogues to the graphite structure. Like graphite, electrons circulation is also present in C$_3$N$_4$ QDs due to $\pi-\pi^*$ charge transfer and the lone pair electrons of nitrogen which also participate in the conjugation [28,40,49]. C$_3$N$_4$ QDs is also known as a metal free semiconductor photocatalyst with relatively higher band gap

of E_g = 3.24 eV, which makes it a UV light active material. Therefore, upon UV light irradiation on C_3N_4, electron and hole pairs can be generated within C_3N_4. Electrons situated in the valence band of C_3N_4 get excited and move to conduction band which are finally trapped by the metal ions and leads the reduction to synthesize metal nanoparticles. On the other hand, holes are scavenged by ethanol solvent (**Scheme 5.2**). Here, C_3N_4 is acting as a photoreducing agent, which sensitizes itself in the presence of UV light and provides electrons for reduction. The phenomena of photochemical synthesis of metal nanoparticles using a photoreducing agent are well supported in literature [23,50]. The probable mechanism for the formation of metal nanoparticles using a semiconductor photoreducing agent is illustrated below:
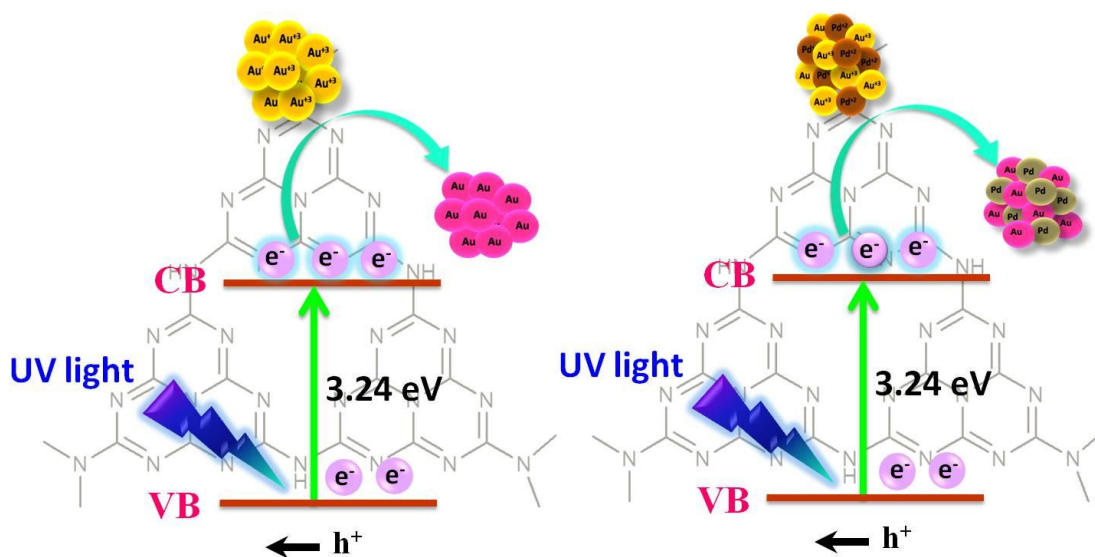
Scheme 5.2 Schematic representation for the mechanism of charge transfer and the movement of electrons during the formation of Au, and AuPd NPs via photochemical route using C_3N_4 QDs as a photocatalyst

The above mentioned mechanism consists of six steps. At first, C_3N_4 QDs get excited upon illumination with UV light and electron-hole pair formation initiates. Secondly, the excited electrons in conduction band combine with $AuCl_4^-$ to provide $[Au^{3+}Cl_4^-]^*(e^-)$ and reduce it to $[Au^{2+}Cl_3^-]$. In third step, reduced metal ions become unstable and undergo fast disproportionation reaction to get the stability. Afterwards, $[Au^+Cl_2^-]$ species again undergoes slow disproportionation to form $[Au^{2+}Cl_3^-]$ ions and Au(0), which is reduced easily. Thereafter,

net disproportionation reaction leads to the formation of the metal nanoparticles, which increases with time by continuing the same reactions. Finally, the reduced metal atoms (Au, Pd and AuPd) associated to form metal nanoparticles, which are investigated by their specific surface plasmon bands.

$$C_3N_4 \xrightarrow{\ \mathbf{h\nu}\ } [C_3N_4]^* (h^+ e^-) \qquad\qquad \{excitation\} \quad (1)$$

$$[C_3N_4]^* (e\text{-}) + Au^{+3}Cl_4^- \longrightarrow C_3N_4 + [Au^{+3}Cl_4^-]^* (e\text{-})$$

$$C_3N_4 + [Au^{+3}Cl_4^-]^* (e\text{-}) \longrightarrow [Au^{+2}Cl_3^-] + Cl^- \qquad \{reduction\} \quad (2)$$

$$2\,Au^{+2}Cl_3^- \longrightarrow Au^+Cl_2^- + Au^{+3}Cl_4^- \qquad \{fast\ disproportionation\} \quad (3)$$

$$4\,Au^+Cl_2^- \longrightarrow 2\,Au^{+2}Cl_3^- + 2Au^0 + 2Cl^- \quad \{slow\ disproportionation\} \quad (4)$$

$$3\,Au^+Cl_2^- \longrightarrow Au^{+3}Cl_4^- + 2Au^0 + 2Cl^- \qquad \{net\ disproportionation\} \quad (5)$$

$$nAu^0 \longrightarrow (Au^0)n \qquad\qquad \{nanoparticle\ formation\} \quad (6)$$
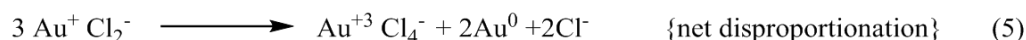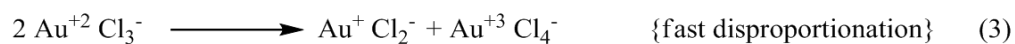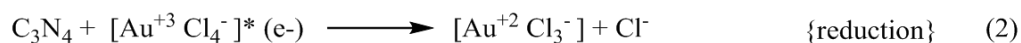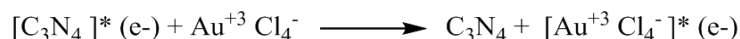
To investigate the role of C_3N_4 QD, UV light, and electrons in conduction band during the synthesis of metal NPs, various control experiments were performed and monitored by UV-vis spectroscopy. Firstly, synthesis of gold nanoparticles was carried out without any C_3N_4 QDs while other conditions were remain unaltered. All the control experiments were performed up to 5 h, which is far beyond our experimental time scale (2 h). In the absence of C_3N_4, the yield of nanoparticle formation is found to be close to zero. However, **Figure 5.15** shows a small broad peak at 510-570 nm, which presumably due to presence of ethanol and water solvent.

El-Sayed and co-workers have also reported similar kind of observation when ethylene glycol was used as a photoreducing agent in presence of PVP and water solvent [23]. Secondly, same synthetic route was followed for gold nanoparticles without using any UV-irradiation. The whole reaction was performed in presence of visible light. The yield of NP formation is found to be zero and no pink colour was observed, which proves the significance of the UV light to excite the electrons from the valence band to the conduction band. Similar experiment was also carried out in the dark and the yield of NP formation is found absolutely zero. A very small peak due to the reduction of $HAuCl_4$ in ethanol water mixed solvent is observed. Therefore, we can conclude that to synthesize metal NPs both C_3N_4 and UV light are essential and an overall study is

depicted in **Figure 5.15.** To confirm the role of photoexcited electrons during the synthesis of metal NPs, scavenging experiment was performed where electrons were trapped by using an established electron scavenger tertiary-butyl alcohol (TBA), keeping all others experimental parameters unchanged except 0.5 mL of TBA added in the reaction solution and monitored the formation of metal nanoparticles in presence of UV light.
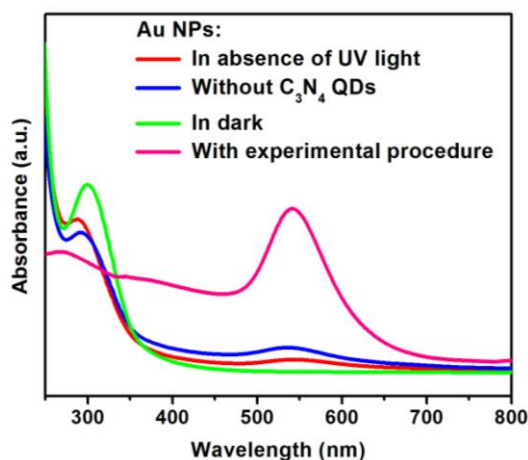
Figure 5.15 UV-vis absorption spectra of Au solution synthesized in different conditions (in absence of UV light, without C_3N_4 QDs, in dark, and with experimental procedure)
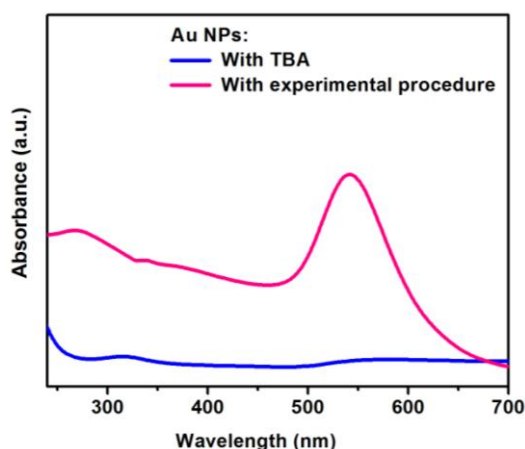
Figure 5.16 UV-vis absorption spectra of Au NPs solution synthesized in presence of an electron scavenger, tert-butyl alcohol (TBA) and with experimental procedure (without electron scavenger)

It can be seen from **Figure 5.16** that there is no formation of metal nanoparticles as all the photogenerated electrons were scavenged by TBA. This phenomenon clearly validates the

contribution of excited electron in C_3N_4 for the synthesis of metal nanoparticles. Synthesis of metal NPs was also carried out in water instead of ethanol water mixed solvent, which significantly decreases the rate of disappearance of the Au^{3+} ion. Therefore, it is obvious that for photoreduction reaction ethanol acts as hole scavenger to restrict recombination of photo-generated electron-hole pairs. Sun and co-workers also reported the hole scavenging property of ethanol during the Au NP synthesis [24].

All the as-synthesized monometallic NPs are very stable, whereas, AuPd bimetallic NP agglomerated within 24 h. To prove the stabilizing nature of C_3N_4, zeta potential measurements were performed. The zeta potential value of bare C_3N_4 QDs is measured as 71.2±2.8 mV. While, zeta potential values for Au, Pd, and AuPd NPs (without PVP) show 37.8±2.3 mV, 30.9±1.6 mV, and 26.3±3.3 mV, respectively. Lowering the zeta potential values for metal NPs is due to the adsorption of negatively charged counter ions, i.e., Cl^- ions. Sun and co-workers also reported a lowering of zeta potential when the Cl^- counter ion was adsorbed onto the metal NP surface [24]. Therefore, the presence of C_3N_4 surrounding metal NPs confirms that C_3N_4 may act as a support for the growth of metal nanoparticles. Less stability of AuPd alloy as compared to monometallic Au and Pd NPs, presumably due to the small amount of C_3N_4 present in the solution which also reflects from the lowering of zeta potential value. Furthermore, to stabilize AuPd alloy NPs PVP (2.8 ml of 2×10^{-3} M) was added just after the formation of bimetallic NPs, *i.e.*, after 2 h of UV light illumination. Addition of stabilizer after the formation of NPs was also reported by Pal and co-workers during the synthesis of Se NPs [51]. Presence of C_3N_4 surrounding the NPs also confirmed from photoluminescence study. It is well known that metal NPs are good quencher of electrons when a mixture of metal and fluorescent molecule brings in close proximity. The fluorescence quenching was observed when Au, Pd, and AuPd NPs were prepared using C_3N_4, which further proves that C_3N_4 was directly anchored with metal NPs as shown in **Figure 5.17**.

C_3N_4 appears with a broad PL band in between 400-650 nm at λ_{exc} = 400 nm, whereas with metal NPs the PL intensity is significantly reduced [40]. In case of bare C_3N_4, electrons and holes are less separated and recombination process takes place quite easily. Whereas, metal NPs behave as an electron sink which efficiently block the recombination process of electron-hole pair and further reduce the PL intensity for enhanced reactivity [21].
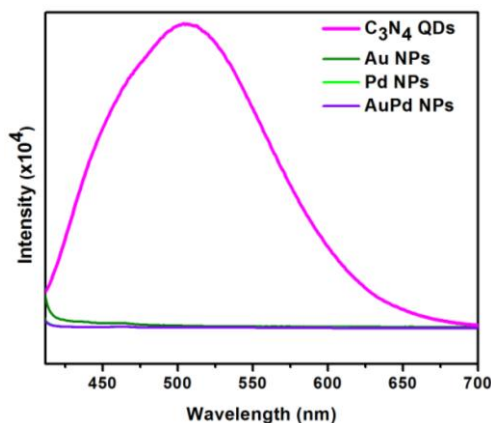
Figure 5.17 Comparative photoluminescence spectra of C_3N_4 QD, Au, Pd, and AuPd NPs

5.3.3 Application of Mono- and Bimetallic NPs in Nitrophenol Reduction

5.3.3.1 Para-nitrophenol Reduction

Water pollution by phenolic and nitrophenol compounds is of immense global concern and the most sensitive area of environmental research. Nitrophenols are the most obstinate pollutants that found mainly within the waste water materials. Moreover, nitrophenol compounds and their derivatives can also be originated from industrial wastes, herbicides, pesticides, insecticides and various synthetic dyes, which deteriorate the environment to a great extent.

To check the reactivity of the as-prepared mono- and bimetallic NPs, a model reduction reaction of 4-nitrophenol (4-NP) was carried out. Total 3.0 mL solution was prepared using water, 4-NP, $NaBH_4$, and catalyst. Freshly prepared 300.0 μL of 10^{-1} M $NaBH_4$ solution and 30.0 μL of 10^{-2} M 4-NP solution were used for this reduction reaction. 30.0 μL of catalyst was added in each case. The overall reaction was monitored in a quartz cuvette. The peak centered at ~ 400 nm was monitored indicating the conversion of 4-NP to 4-aminophenol (4-AP). The percentage of conversion of the 4-NP to the 4-AP can be calculated using the following equation:

$$\% \text{ Degradation} = (A_0 - A_t)/A_0 \times 100$$

where, A_0 = initial absorbance and A_t = absorbance at time 't'.

A significant absorption peak at 315 nm was appeared in pure 4-NP. When a freshly

prepared $NaBH_4$ (10^{-1} M) solution was added into the 4-NP, the absorption peak was shifted to 400 nm, analogous to the 4-nitrophenolate ions where, nitrophenolate ion behave as an oxidant and BH_4^- as a reductant. In absence of any catalyst, BH_4^- is incapable of reducing 4-NP to the corresponding amino compound and the peak intensity of nitrophenolate at 400 nm remains unaffected with time, which verifies that the reduction reaction doesn't occur. It is established by a control experiment that after addition of $NaBH_4$, 4-NP converted to the phenolate ion with a shift in 315 nm peak. The new peak at 400 nm appeared due to the formation of phenolate ion from 4-NP. The phenolate ion solution is very stable and the peak intensity at 400 nm is unaltered with time, which is confirmed from UV-vis spectra, shown in **Figure 5.18.**
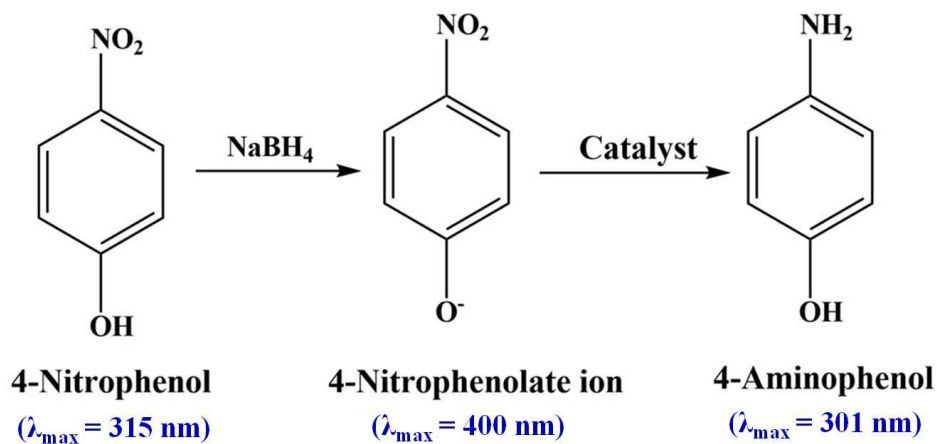
Scheme 5.3 Schematic representation for the conversion of 4-NP to 4-AP with their corresponding λ_{max} values

Hence, our as-prepared NPs are employed as a catalyst for the reduction of 4-NP to 4-AP. After addition of a catalyst, the reduction of 4-NP was initiated, which can be visualised by tracking the gradual decrease in absorption intensity of 4-nitrophenolate ions at 400 nm, accompanying the appearance of a new peak of 4-AP at 301 nm. The conversion of 4-NP to 4-AP via the formation of phenolate ion and their respective λ_{max} values are represented in **Scheme 5.3**. This successive decrease in the peak intensity at 400 nm was taken into consideration for the kinetic study of the reaction. The overall reduction reaction and kinetics can easily be monitored by using the UV-vis spectroscopy.
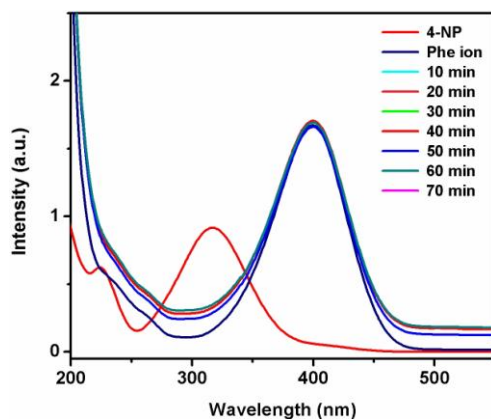
Figure 5.18 UV-vis absorption spectra of 4-nitrophenol and 4-nitrophenolate ion after addition of NaBH$_4$ in the absence of any catalyst

The conversion process is directly studied by UV-vis spectra at different time intervals. The ratio of the concentrations of nitrophenolate ion at different time intervals will be helpful to get the values of A_t/A_0. The exponential nature of A_t/A_0 vs. time (min.) plot specify the pseudo first order reaction. Since, the NaBH$_4$ is present in excess amount than 4-NP, the rate of reduction reaction is supposed to be independent of borohydride concentration. From the linear plot of $\ln(A_t/A_0)$ vs. time (min.), it is confirmed that the reduction reaction follows the pseudo-first order kinetics and the conclusion about the reactivity can be made by calculating the rate constants from the slop using the following equation.

$$\ln(A_0/A_t) = kt$$

The plot of A_t/A_0 vs. time (t) for the reduction of 4-NP using C$_3$N$_4$ QDs is shown in **Figure 5.19.a**, which shows ~ 60% reduction of 4-NP to 4-AP within 70 min. The exponential nature of A_t/A_0 vs. time (min.) plot demonstrate the pseudo first order kinetics as shown in **Figure 5.19.b**. The rate constant for the reduction reaction is calculated from the slope of $\ln(A_t/A_0)$ vs. time (min.), as shown in **Figure 5.19.c**. The rate constant (k_1) for the C$_3$N$_4$ QDs is calculated to be 0.1×10^{-1} min^{-1}.

In case of Au NPs, the reactivity increases as compare to the bare C$_3$N$_4$ quantum dots. **Figure 5.20.a** exhibits ~ 99% conversion of 4-NP to 4-AP within 40 min in presence of Au nanoparticle. The exponential nature and straight line in **Figure 5.20.b** and **c** illustrates the pseudo first order reaction. The value of rate constant obtained from the slope of **Figure 5.20.c** is

$0.9{\times}10^{-1}$ min^{-1}, which is ~ 9 times higher than bare C_3N_4.
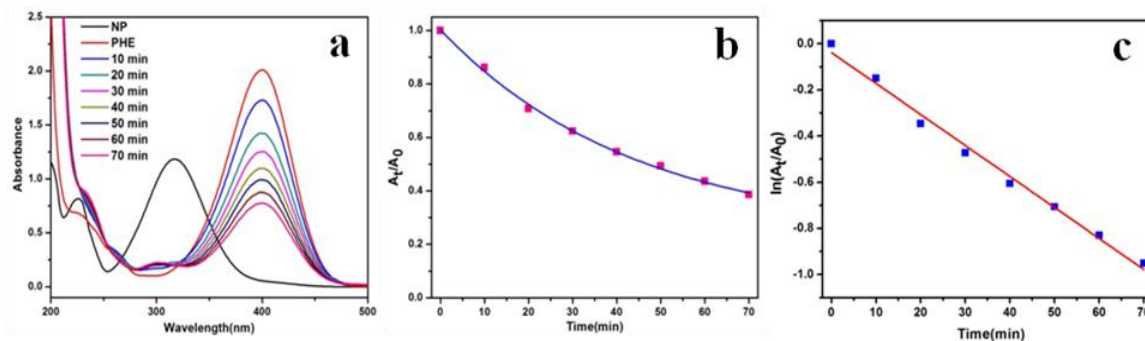
Figure 5.19 UV-vis absorption spectra of (a) 4-nitrophenol reduction in presence of C_3N_4 (b) A_t/A_0 vs. time (min) plot and (c) ln (A_t/A_0) vs. time (min) plot. Conditions: [4-NP] = 10^{-4} M and amount of catalyst = 30 µL
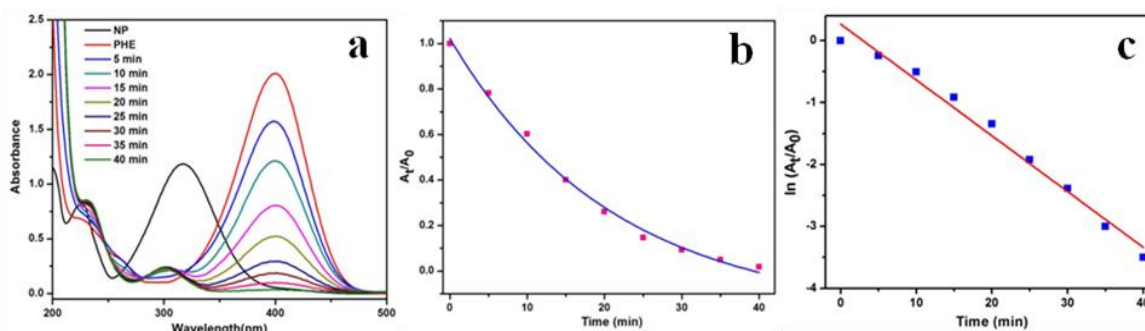
Figure 5.20 UV-vis absorption spectra of (a) 4-nitrophenol reduction in presence of Au NPs, (b) A_t/A_0 vs. time (min) plot and (c) ln (A_t/A_0) vs. time (min) plot. Conditions: [4-NP] = 10^{-4} M and amount of catalyst = 30 µL

Further, the catalytic reaction was carried out using Pd NPs which shows a higher rate of the reaction with a rate constant value is $1.5{\times}10^{-1}$ min^{-1}. **Figure 5.21.a** shows ~ 99% of conversion within 25 min and exponential curve is obtained from A_t/A_0 vs. time (min.) plot (**Figure 5.21.b**). The higher rate constant value using Pd is also reported in the literature for various organic reactions like hydrogenation of phenol, hydrogenation of nitroarenes etc. [6,7,9]. ln(A_t/A_0) vs. time (min.) graph shows a straight line, shown in **Figure 5.21.c**, which further explains similar kinetics.
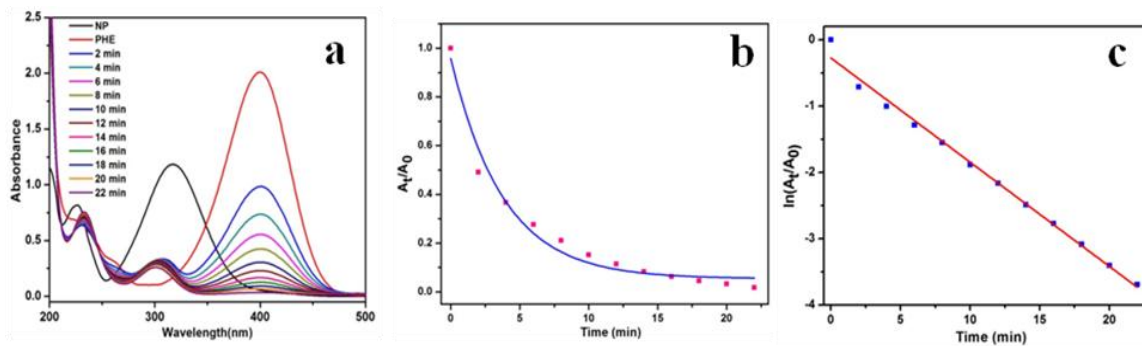
Figure 5.21 UV-vis absorption spectra of (a) 4-nitrophenol reduction in presence of Pd NPs, (b) A_t/A_0 vs. time (min) plot and (c) ln (A_t/A_0) vs. time (min) plot. Conditions: [4-NP] = 10^{-4} M and amount of catalyst = 30 µL
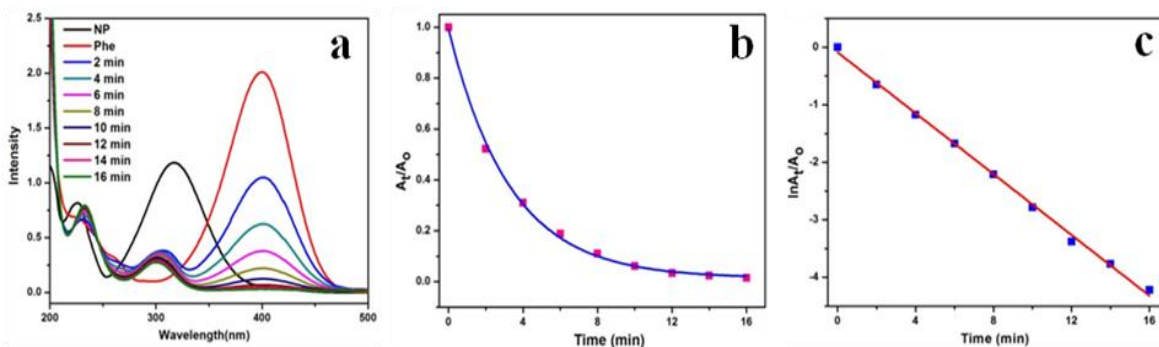
Figure 5.22 UV-vis absorption spectra of (a) 4-nitrophenol reduction in presence of AuPd NPs, (b) A_t/A_0 vs. time (min) plot and (c) ln (A_t/A_0) vs. time (min) plot. Conditions: [4-NP] = 10^{-4} M, [NaBH$_4$] = 0.1 M, and amount of catalyst = 30 µL

In case of AuPd NPs, the reduction reaction proceeds very quickly and gives ~ 99% conversion within 15 min (Figure **5.22.a**), which exhibits a rate constant value of 2.6×10^{-1} min^{-1} from the slope of Figure **5.22.c**. The straight line nature in ln(A_t/A_0) vs. time (min.) graph (**Figure 5.22.c**) further explains the kinetics of the reaction, which also observed in C$_3$N$_4$, Au and Pd NPs.

Based on the above findings it can be deduced that the reactivity towards the conversion of 4-NP to 4-AP remarkably superior with AuPd. Therefore, the descending order of rate constant for 4-NP to 4-AP conversion is $k_{AuPd} > k_{Pd} > k_{Au} > k_{C3N4}$. The comparative study in rate

constants and percent conversion after 15 min from 4-NP to 4-AP (using all the NPs) are presented in **Figure 5.23.a** and **b**, respectively. The final product is further scrutinized by UV-vis as well as mass spectroscopy.
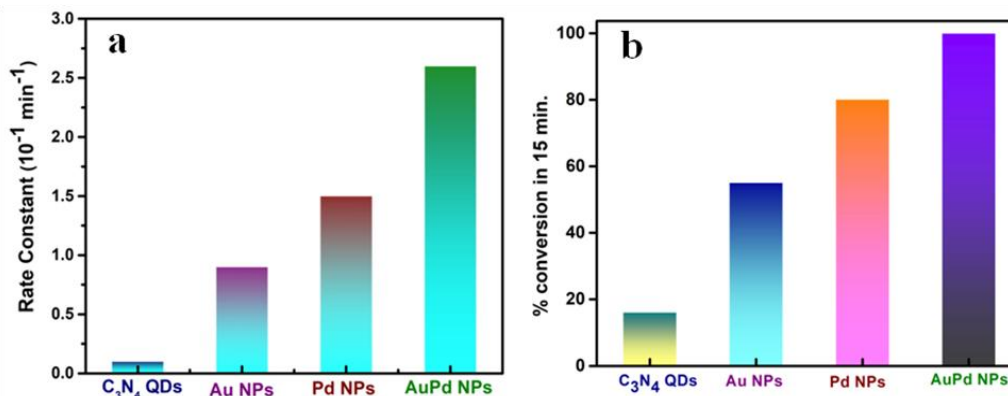
Figure 5.23 (a) Comparative study of rate constants (*k*) using C$_3$N$_4$ QDs, Au, Pd, and AuPd NPs for the nitrophenol reduction reaction and (b) comparative study of percent conversion from 4-NP to 4-AP in 15 min C$_3$N$_4$ QDs, Au, Pd & AuPd NPs
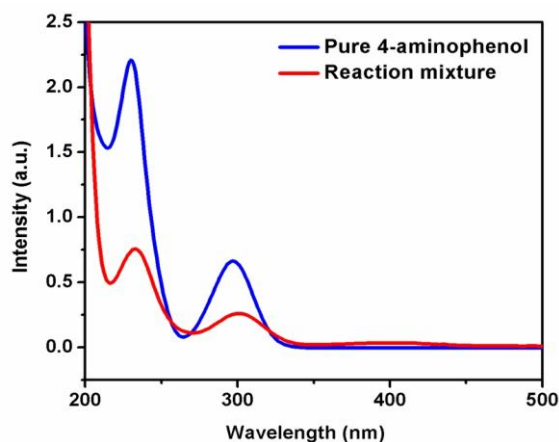
Figure 5.24 UV-vis absorption spectra of pure 4-aminophenol and reaction mixture

The UV-vis spectra of standard aqueous solution of 4-AP and reaction mixture are compared and shown in **Figure 5.24**. It is clearly visible from UV-vis spectra (**Figure 5.24**) that standard 4-AP shows a peak at 297 nm. Whereas, reaction mixture exhibits a peak at 301 nm,

which is well matched with standard 4-AP, further prove for the formation of 4-AP. Standard 4-NP, standard 4-AP, and reaction mixture was further analysed by mass spectroscopy to confirm the presence of molecular ion (m/z) peak of the compound (**Figure 5.25**). Characteristic m/z = 139.0443, 109.9740, 109.9084 are observed for standard 4-NP, 4-AP, and reaction mixture, respectively which confirm the formation of 4-AP in the reaction mixture (**Figure 5.25**).
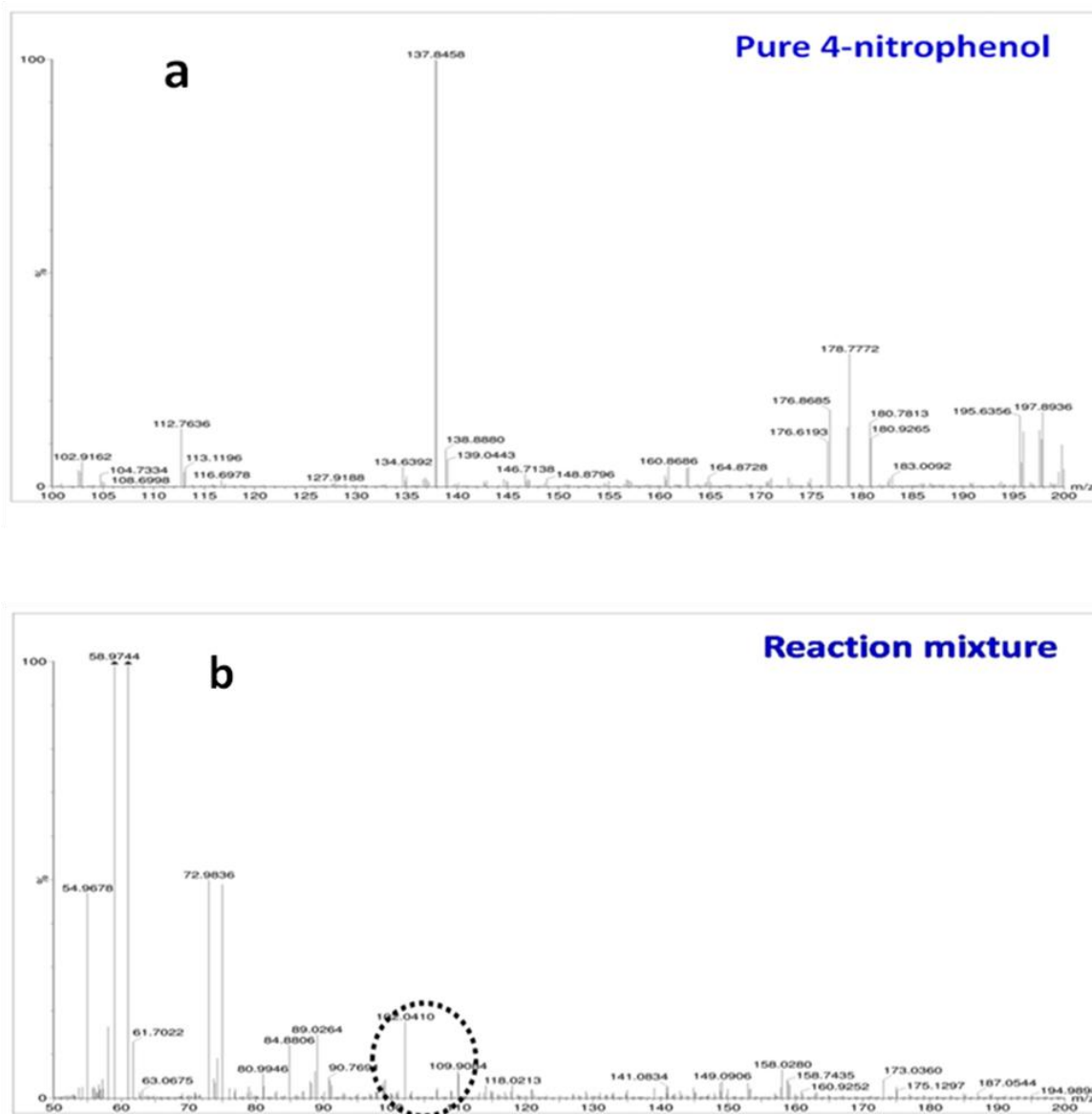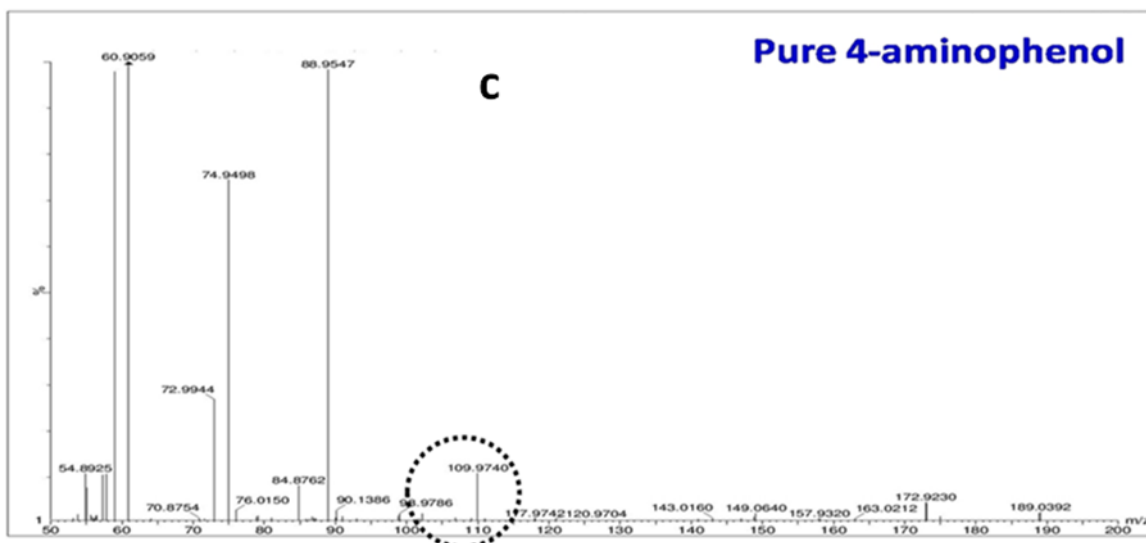
Figure 5.25 Mass spectra of (a) pure 4-nitrophenol, (b) reaction mixture and (c) pure 4-aminophenol. The molecular ion peak for all is encircled

In general, catalytic activities of the noble metal nanoparticles (Au, Pd, and AuPd) can quantitatively be determined by the reduction process of 4-nitrophenolate ions to 4-AP via electron transfer mechanism (**Scheme 5.3**). Recent trend shows that the bimetallic nanoparticles are even superior catalysts as compared to the monometallic ones [52]. Our findings of enhanced catalytic activity of AuPd alloy with respect to the individual Au and Pd nanoparticles are very much in line with recent reports, which can be explained in terms of complete miscibility of Au and Pd atoms with little lattice mismatch, significantly differ electro-negativities as well as vastly different catalytic properties. Relatively higher electro-negativity of Au (2.54) as compared to Pd (2.2) may influence in partial transfer of electrons from the Pd atoms towards the Au atoms within the alloy nanoparticles. This process causes an overall decrease of electron affinity of Au atoms within the bimetallic alloys as compared to that of monometallic. Hence, it will resultantly enhance the reduction process of 4-nitrophenolate ion to 4-AP (**Scheme 5.3**). High resolution XPS scans of Au 4f spectra strongly support the partial electron transfer mechanism where a little shift of Au $4f_{7/2}$ binding energy peak from 87.7 eV (monometallic) to 87.3 eV (bimetallic) can also be observed. In contrast to Au, a slight increase in electro-negativity may occur for Pd atoms within the alloy nanoparticles due the partial transfer of charge, although it will be far lower than that of Au and hardly effect on 4-NP reduction process. However, the enhanced

catalytic activity of Pd within the alloy compound can be explained in terms of lattice strain. As the gold atoms (144 pm) are slightly bigger in size as compare to the palladium atoms (137 pm), usually Pd nanocrystals experience a tensile stress within the alloy nanoparticles. Significant broadening in AuPd XRD peaks (**Figure 5.2**) also indicates a strained lattice condition. However, this tensile strain can significantly alter the position and width of the *d*-band energy configurations of Pd atoms leading to a reduction of the *d* orbitals overlapping. As a consequence, band narrowing as well as decrease in ionization potential may also occur. This effect is also complementary with our high resolution XPS scans, where a peak shift (0.8 eV) towards the lower energy for Pd $3d_{3/2}$ BE spectra has been observed for bimetallic as compared to monometallic Pd nanoparticles. A similar kind of peak shifts for core-shell structures have recently been reported by Chen and co-workers [53]. The density functional theory (DFT) calculations reported by Norskov and co-workers [54] also explained how the effect of structure (ensemble) and electronic (ligand) properties can modify the catalytic effect of Au/Pd (111) surface. Moreover, the substrate effect (C_3N_4 QD) on different nanoparticles has to be taken in account as well. Therefore, all the above mentioned reasons can lead the bimetallic alloy a superior catalyst as compared to monometallic ones.

5.4 Conclusion

In conclusion, we have developed a facile method for the synthesis of mono- and bimetallic alloy nanoparticles via photoreduction using C_3N_4 quantum dots as a photocatalyst. The role of C_3N_4 QDs in the synthetic procedure was explained by performing several controlled experiments. The present study has revealed that very less amount (40 μL) of g-C_3N_4 may act like a stabilizer in the synthetic procedure. The probable mechanism behind the NPs formation has been illustrated clearly and the as-synthesized samples were efficiently used for the 4-NP reduction. It was demonstrated that bimetallic AuPd alloy is a superior catalyst to convert 4-NP to 4-AP as compared to others with higher rate constant (*k*) value. This superior activity is consistent with the exchange of electrons between Au and Pd NPs in AuPd alloy, which may further result in more efficient transfer of electrons from the g-C_3N_4 substrate to the metal nanoparticles. Future efforts are being directed towards the synthesis of other mono- and bimetallic nanoparticles with long term stability as well as the effective reactivity.

References

[1] Beydoun, D.; Amal, R.; Low, G.; McEvoy, S. Role of Nanoparticles in Photocatalysis. *J. Nanopart. Res.* **1999**, *1*, 439-458.

[2] Sarina, S.; Waclawik, E. R.; Zhu, H. Photocatalysis on Supported Gold and Silver Nanoparticles under Ultraviolet and Visible Light Irradiation. *Green Chem.* **2013**, *15*, 1814-1833.

[3] Xiao, Qi.; Sarina, S.; Jaatinen, E.; Jia, J.; Arnold, D. P.; Liuc, H.; Zhu, H. Efficient Photocatalytic Suzuki Cross-Coupling Reactions on Au-Pd Alloy Nanoparticles Under Visible Light Irradiation. *Green Chem.* **2014**, *16*, 4272-4285.

[4] Ganguly, M.; Jana, J.; Pal, A.; Pal, T. Synergism of Gold and Silver Invites Enhanced fluorescence for Practical Applications. *RSC Adv.* **2016**, *6*, 17683-17703.

[5] Samanta, S.; Martha, S.; Parida, K. Facile Synthesis of Au/g-C$_3$N$_4$ Nanocomposites: An Inorganic/Organic Hybrid Plasmonic Photocatalyst with Enhanced Hydrogen Gas Evolution under Visible-Light Irradiation. *ChemCatChem* **2014**, *6*, 1453-1462.

[6] Wang, Y.; Yao, J.; Li, H.; Su, D.; Antonietti, M. Highly Selective Hydrogenation of Phenol and Derivatives over a Pd@Carbon Nitride Catalyst in Aqueous Media. *J. Am. Chem. Soc.* **2011**, *133*, 2362-2365.

[7] Long, J.; Liu, H.; Wu, S.; Liao, S.; Li, Y. Selective Oxidation of Saturated Hydrocarbons Using Au-Pd Alloy Nanoparticles Supported on Metal-Organic Frameworks. *ACS Catal.* **2013**, *3*, 647-654.

[8] Chai, J.; Li, F.; Hu, Y.; Zhang, Q.; Hana, D.; Niu, L. Hollow Flower-Like AuPd Alloy Nanoparticles: One Step Synthesis, Self-Assembly on Ionic Liquid-Functionalized Graphene, and Electrooxidation of Formic Acid. *J. Mater. Chem.* **2011**, *21*, 17922-17929.

[9] Takasaki, M.; Motoyama, Y.; Higashi, K.; Yoon, S.; Mochida, I.; Nagashima, H. Chemoselective Hydrogenation of Nitroarenes with Carbon Nanofiber-Supported Platinum and Palladium Nanoparticles. *Org. Lett.* **2008**, *10*, 1601-1604.

[10] Liu, J.; Zhang, Y.; Lu, L.; Wu, G.; Chen, W. Self Regenerated Solar Driven Photocatalytic Water Splitting by Urea Derived Graphitic Carbon Nitride with Platinum Nanoparticles. *Chem Commun.* **2012**, *48*, 8826-8828.

[11] Peer, D.; Karp, J. M.; Hong, S.; Farokhzad, O. C.; Margalit, R.; Langer, R. Nanocarriers

as an Emerging Platform for Cancer Therapy. *Nat. Nanotechnol.* **2007**, *2*, 751-760.

[12]   Sung, H.; Lee, J.; Han, K.; Lee. J. K.; Sung, J.; Kim, J.; Choi, M.; Kim, C. Controlled Positioning of Metal Nanoparticles in an Organic Light-Emitting Device for Enhanced Quantum Efficiency. *Org Electron* **2014**, *15*, 491-499.

[13]   Pande, S.; Ghosh, S. K.; Praharaj, S.; Panigrahi, S.; Basu, S.; Jana, S.; Pal, A.; Tsukuda, T.; Pal, T. Synthesis of Normal and Inverted Gold-Silver Core-Shell Architectures in β-Cyclodextrin and their Applications in SERS. *J. Phys. Chem. C* **2007**, *111*, 10806-10813.

[14]   Dahl, J. A.; Maddux, B. L. S.; Hutchison, J. E. Toward Greener Nanosynthesis. *Chem Rev.* **2007**, *107*, 2228-2269.

[15]   Quaresma, P; Soares, L.; Contar, L.; Miranda, A.; Osório, I.; Carvalho, P. A.; Franco, R.; Pereira, E. Green Photocatalytic Synthesis of Stable Au and Ag Nanoparticles. *Green Chem.* **2009**, *11*, 1889-1893.

[16]   Khaydarov, R. A.; Khaydarov, R. R.; Gapurova, O.; Estrin, Y.; Scheper T. Electrochemical Method for the Synthesis of Silver Nanoparticles. *J Nanopart Res.* **2009**, *11*, 1193-1200.

[17]   Park, J.; Atobe, M.; Fuchigami, T. Sonochemical Synthesis of Conducting Polymer-Metal Nanoparticles Nanocomposite. *Electrochim. Acta.* **2005**, *51*, 849-854.

[18]   Huang, X.; Qi, X.; Huang, Y.; Li, S.; Xue, C.; Gan, C. L.; Boey, F.; Zhang, H. Photochemically Controlled Synthesis of Anisotropic Au Nanostructures: Platelet-like Au Nanorods and Six-Star Au Nanoparticles. *ACS Nano* **2010**, *4*, 6196-6202.

[19]   Kim, F.; Song, J. H.; Yang, P. Photochemical Synthesis of Gold Nanorods. *J. Am. Chem. Soc.* **2002**, *124*, 14316-14317.

[20]   Fageria, P.; Nazir, R.; Gangopadhyay, S.; Barshilia, H. C.; Pande, S. Graphitic-Carbon Nitride Support for the Synthesis of Shape-Dependent ZnO and their Application in Visible Light Photocatalysts. *RSC Adv.* **2015**, *5*, 80397-80409.

[21]   Fageria, P.; Gangopadhyay, S.; Pande, S. Synthesis of ZnO/Au and ZnO/Ag Nanoparticles and their Photocatalytic Application Using UV and Visible Light. *RSC Adv.* **2014**, *4*, 24962-24972.

[22]   Huang, X.; Zhou, X.; Wu, S.; Wei, Y.; Qi, X.; Zhang, J.; Boey, F.; Zhang, H. Reduced Graphene Oxide-Templated Photochemical Synthesis and In Situ Assembly of Au Nanodots to Orderly Patterned Au Nanodot Chains. *Small* **2010**, *6*, 513-516.

[23]   Eustis, S.; Hsu, H.; El-Sayed, M. A. Gold Nanoparticle Formation from Photochemical Reduction of Au^{3+} by Continuous Excitation in Colloidal Solutions. A Proposed Molecular Mechanism. *J. Phy. Chem. B* **2005**, *109*, 4811-4815.

[24]   Qin, X.; Lu, W.; Chang, G.; Luo, Y.; Asiri, A. M.; Al-Youbi, A. O.; Sun, X. Novel Synthesis of Au Nanoparticles Using Fluorescent Carbon Nitride Dots as Photocatalyst. *Gold Bull.* **2012**, *45*, 61-67.

[25]   Cheng, N.; Tian, J.; Liu, Q.; Ge, C.; Qusti, A. H.; Asiri, A. M.; Al-Youbi, A. O.; Sun, X. Au-Nanoparticle-Loaded Graphitic Carbon Nitride Nanosheets: Green Photocatalytic Synthesis and Application toward the Degradation of Organic Pollutants. *ACS Appl. Mater. Interfaces* **2013**, *5*, 6815-6819.

[26]   Bhowmik, T.; Kundu, M. K.; Barman, S. Ultra Small Gold Nanoparticles- Graphitic Carbon Nitride Composite: An Efficient Catalyst for Ultrafast Reduction of 4-Nitrophenol and Removal of Organic Dyes from Water. *RSC Adv.* **2015**, *5*, 38760-38773.

[27]   Wang, X.; Blechert, S.; Antonietti, M. Polymeric Graphitic Carbon Nitride for Heterogeneous Photocatalysis. *ACS Catal*. **2012**, *2*, 1596-1606.

[28]   Han, C.; Gao, Y.; Liu, S.; Ge, L.; Xiao, N.; Dai, D.; Xu, B.; Chen, C. Facile Synthesis of AuPd/g-C_3N_4 Nanocomposite: An Effective Strategy to Enhance Photocatalytic Hydrogen Evolution Activity. *Int. J. Hydrog. Energy* **2017**, *42*, 22765-22775.

[29]   Ma, Z.; Sa, R.; Li, Q.; Wu, K. Interfacial Electronic Structure and Charge Transfer of Hybrid Graphene Quantum Dot and Graphitic Carbon Nitride Nanocomposites: Insights into High Efficiency for Photocatalytic Solar Water Splitting. *Phys. Chem. Chem. Phys.* **2016**, *18*, 1050-1058.

[30]   Xu, C.; Han, Q.; Zhao, Y.; Wang, L.; Lia, Y.; Qu, L. Sulfur-Doped Graphitic Carbon Nitride Decorated with Graphene Quantum Dots for an Efficient Metal-Free Electrocatalyst. *J. Mater. Chem. A* **2015**, *3*, 1841-1846.

[31]   Wang, X.; Wang, L.; Zhao, F.; Hu, C.; Zhao, Y.; Zhang, Z.; Chen, S.; Shib, G.; Qu, L. Monoatomic-Thick Graphitic Carbon Nitride Dots on Graphene Sheets as an Efficient Catalyst in the Oxygen Reduction Reaction. *Nanoscale* **2015**, *7*, 3035-3042.

[32]   Xu, M.; Han, L.; Dong, S. Facile Fabrication of Highly Efficient g-C_3N_4/Ag_2O Heterostructured Photocatalysts with Enhanced Visible-Light Photocatalytic Activity. *ACS Appl. Mater. Interfaces* **2013**, *5*, 12533-12540.

[33]   Zhao, F.; Cheng, H.; Hu, Y.; Song, L.; Zhang, Z.; Jiang, L.; Qu, L. Functionalized Graphitic Carbon Nitride for Metal-free, Flexible and Rewritable Nonvolatile Memory Device via Direct Laser-Writing. *Sci. Rep.* **2014**, *4*, 5882.

[34]   Zhao, Y.; Liu, Z.; Chu, W.; Song, L.; Zhang, Z.; Yu, D.; Tian, Y.; Xie, S.; Sun, L. Large-Scale Synthesis of Nitrogen-Rich Carbon Nitride Microfibers by Using Graphitic Carbon Nitride as Precursor. *Adv. Mater.* **2008**, *9999*, 1-5.

[35]   Lia, G.; Liana, Z.; Wanga, W.; Zhang, D.; Lia, H. Nanotube-Confinement Induced Size-Controllable g-C$_3$N$_4$ Quantum Dots Modified Single-Crystalline TiO$_2$ Nanotube Arrays for Stable Synergetic Photoelectrocatalysis. *Nano Energy* **2016**, *19*, 446-454.

[36]   Zhang, X.; Wang, H.; Wang, H.; Zhang, Q.; Xie, J.; Tian, Y.; Wang, J.; Xie, Yi. Single Layered Graphitic-C$_3$N$_4$ Quantum Dots for Two-Photon Fluorescence Imaging of Cellular Nucleus. *Adv. Mater.* **2014**, *26*, 4438-4443.

[37]   Tang, Y.; Su, Y.; Yang, N.; Zhang, L.; Lv, Y. Carbon Nitride Quantum Dots: A Novel Chemiluminescence System for Selective Detection of Free Chlorine in Water. *Anal. Chem.* **2014**, *86*, 4528-4535.

[38]   Fan, X.; Feng, Y.; Su, Y.; Zhang L.; Lv, Y. A Green Solid-Phase Method for Preparation of Carbon Nitride Quantum Dots and their Applications in Chemiluminescent Dopamine Sensing. *RSC Adv.* **2015**, *5*, 55158-55164.

[39]   Song, Z.; Lin, T.; Lin, L.; Lin, S.; Fu, F.; Wang, X.; Guo, L. Invisible Security Ink Based on Water-Soluble Graphitic Carbon Nitride Quantum Dots. *Angew. Chem. Int. Ed.* **2016**, *55*, 2773-2777.

[40]   Zhou, J.; Yang, Y.; Zhang, C. A Low-Temperature Solid-Phase Method to Synthesize Highly Fluorescent Carbon Nitride Dots with Tunable Emission. *Chem. Commun.* **2013**, *49*, 8605-8607.

[41]   Barman, S.; Sadhukhan, M. Facile Bulk Production of Highly Blue Fluorescent Graphitic Carbon Nitride Quantum Dots and their Application as Highly Selective and Sensitive Sensors for the Detection of Mercuric and Iodide Ions in Aqueous Media. *J. Mater. Chem.* **2012**, *22*, 21832-21837.

[42]   An, T.; Tang, J.; Zhang, Y.; Quan, Y.; Gong, X.; Al-Enizi, A. M.; Elzatahry, A. A.; Zhang, L.; Zheng, G. Photoelectrochemical Conversion from Graphitic C$_3$N$_4$ Quantum Dot Decorated Semiconductor Nanowires. *ACS Appl. Mater. Interfaces* **2016**, *8*, 12772-

12779.

[43] Liu, J.; Zhang, T.; Wang, Z.; Dawson, G.; Chen, W. Simple Pyrolysis of Urea into Graphitic Carbon Nitride with Recyclable Adsorption and Photocatalytic Activity. *J. Mater. Chem.* **2011**, *21*, 14398-14401.

[44] Xiao, Q.; Sarina, S.; Bo, A.; Jia, J.; Liu, H.; Arnold, D. P.; Huang, Y.; Wu, H.; Zhu, H. Visible Light-Driven Cross-Coupling Reactions at Lower Temperatures Using a Photocatalyst of Palladium and Gold Alloy Nanoparticles. *ACS Catal.* **2014**, *4*, 1725-1734.

[45] Pozun, Z. D.; Rodenbusch, S. E.; Keller, E.; Tran, K.; Tang, W.; Stevenson, K. J.; Henkelman, G. A. Systematic Investigation of p‑Nitrophenol Reduction by Bimetallic Dendrimer Encapsulated Nanoparticles *J. Phys. Chem. C.* **2013**, *117*, 7598-7604.

[46] Ding, Y.; Fan, F.; Tian, Z.; Wang, Z. L. Atomic Structure of Au-Pd Bimetallic Alloyed Nanoparticles. *J. Am. Chem. Soc.* **2010**, *132*, 12480-12486.

[47] Darabdhara, G.; Amin, M. A.; Mersal, G. A. M.; Ahmed, E. M.; Das, M. R.; Zakaria, M. B.; Malgras,V.; Alshehri, S. M.; Yamauchi, Y.; Szunerits, S.; Boukherroub, R. Reduced Graphene Oxide Nanosheets Decorated with Au, Pd and Au-Pd Bimetallic Nanoparticles as Highly Efficient Catalysts for Electrochemical Hydrogen Generation. *J. Mater. Chem. A* **2015**, *3*, 20254-20266.

[48] Zhang, Y.; Ge, J.; Wang, L.; Wang, D.; Ding, F.; Tao, X.; Chen, W. Manageable N-doped Graphene for High Performance Oxygen Reduction Reaction. *Sci. Rep.* **2007**, *3*, 2771.

[49] Wang, W.; Yu, J. C.; Shen, Z.; Chan, D. K. L.; Gu, T. g-C_3N_4 Quantum Dots: Direct Synthesis, Upconversion Properties and Photocatalytic Application. *Chem. Commun.* **2014**, *50*, 10148-10150.

[50] Jakob, M.; Levanon, H.; Kamat, P. V. Charge Distribution between UV-Irradiated TiO_2 and Gold Nanoparticles: Determination of Shift in the Fermi Level. *Nano Lett.* **2003**, *3*, 353-358.

[51] Nath, S.; Ghosh, S. K.; Panigahi, S.; Thundat, T.; Pal, T. Synthesis of Selenium Nanoparticle and its Photocatalytic Application for Decolorization of Methylene Blue under UV Irradiation. *Langmuir* **2004**, *20*, 7880-7883.

[52] Chu, C.; Su, Z. Facile Synthesis of AuPt Alloy Nanoparticles in Polyelectrolyte

Multilayers with Enhanced Catalytic Activity for Reduction of 4-Nitrophenol. *Langmuir* **2014,** *30,* 15345-15350.

[53]   Chen, D.; Li, C.; Liu, H.; Ye, F.; Yang, J. Core-shell Au@Pd Nanoparticles with Enhanced Catalytic Activity for Oxygen Reduction Reaction *via* Core-Shell Au@Ag/Pd Constructions. *Sci. Rep.* **2015**, *5*, 11949.

[54]   Liu, P.; Nørskov, J. K. Ligand and Ensemble Effects in Adsorption on Alloy Surfaces. *Phys. Chem. Chem. Phys.* **2001**, *3*, 3814-3818.

Decoration of MoS₂ on g-C₃N₄ for Enhanced Electrochemical Hydrogen Evolution Reaction and RhB Dye Degradation

✿ *A facile hydrothermal approach for the decoration of molybdenum disulfide on g-C₃N₄ surface has been introduced and MoS₂/g-C₃N₄ heterostructure has been synthesized.*

✿ *The heterostructure of MoS₂/g-C₃N₄ utilized as visible light active catalyst for RhB degradation and as electrocatalyst for hydrogen evolution reaction and demonstrated higher activity.*
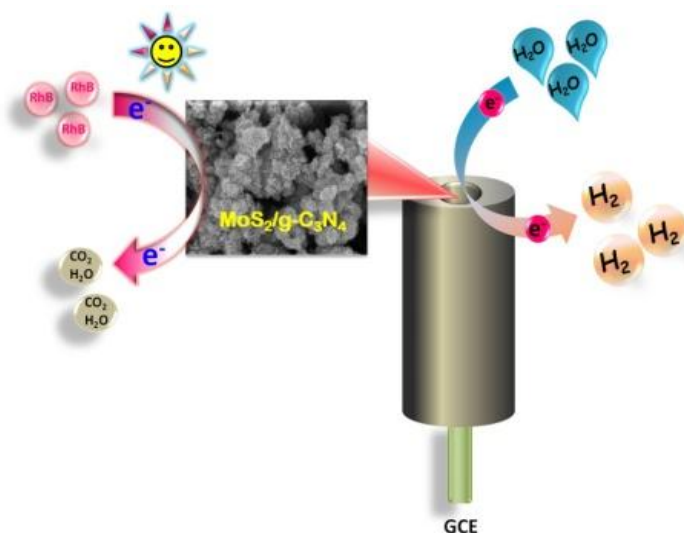
Abstract

The increasing demand for energy and strain on the environment due to human activities has led to an increased focus on the development of cleaner alternative fuels. Hydrogen gas is found as a substitute in the progress of sustainable energy sources due to its high calorific values and clean combustion products. In this work molybdenum disulfide (MoS_2) decorated on graphitic carbon nitride (g-C_3N_4) was synthesized via a simple hydrothermal route. The morphology and surface structure of MoS_2/g-C_3N_4 were analyzed by SEM, TEM, and EDS techniques. The crystal structure, optical properties, and elemental composition of the catalyst were investigated by PXRD, UV-vis, RAMAN, and XPS. BET analysis is carried out to determine the surface area of both MoS_2 and MoS_2/g-C_3N_4. The catalyst material, MoS_2/g-C_3N_4 demonstrates enormous improvement in production of H_2 with low onset potentials (−0.24 V vs. RHE), small Tafel slope (63 mV/dec), and excellent cycling stability as compared with bare MoS_2. The enhanced electrochemical performance of the MoS_2/g-C_3N_4 heterostructure could be attributed to higher charge carrier mobility in heterostructure interface, improved specific activity and large surface area. Moreover, it also exhibited visible-light driven photocatalytic activity in Rhodamine B (RhB) dye degradation. The focus of this study is to construct a new MoS_2 based semiconductor heterostructure electrocatalyst with improved HER activity and photocatalyst with higher degradation efficiency.

6.1 Introduction

Energy is one of the most important contributors to the growth of the human economy. In 2013, the total power consumption in the world exceeded exponentially (18 TW) [1-3]. Huge increasing energy crises in the near future and issues of environmental pollution, semiconductor photocatalyst have fascinated the attention of researchers and offered "green" route for hydrogen production [4-6]. Nearly 86% of this energy was produced by the use of fossil fuels such as oil, coal, and gas. Apart from the production of large quantities of CO_2, which is linked to the increasing global temperature, this activity has also caused the depletion of the earth's reserves of these fuels [3]. This has accelerated the research on green and renewable sources of energy such as the wind, hydro, solar power, and alternative fuels [1-4]. Among the various renewable sources of energy being investigated, hydrogen gas has been put forth as the most viable alternative fuel for the future. H_2 gas is a carbon-free fuel, having high calorific value (142 MJ/kg), an ideal energy carrier and avoid the elimination of any waste product when combined with O_2 in a fuel cell [1-3]. During the past few years, a range of catalysts have been developed for H_2 production, but the activity is hindered due to wide band gap and stability issues. Therefore, the effectiveness is still far from practical applications and there is a requirement to design more efficient alternatives for HER [3-6].

Graphitic carbon nitride (g-C_3N_4), has emerged as a metal-free semiconductor with intensive application in electrocatalysis to produce H_2 from water [6]. g-C_3N_4 attracted the attention of many researchers as it is an n-type semiconductor acquiring stacked 2D layered structure with high thermal and chemical stability, low cost and environment benign [6-11]. In addition, it has an appealing electronic structure with 2.7 eV band gap, has endowed its light absorption range to visible region [8-11]. The drawbacks associated with bare g-C_3N_4 are low quantum efficiency, limited delocalized conductivity and spontaneous recombination between the photogenerated electron-hole pair, which lead to low photocatalytic efficiency [7,10]. However, there are numerous methods to improve the performance of g-C_3N_4 for optimal photocatalysis including the deposition of noble metals [12], doping of non-metals [13,14], coupling with the other functional materials [9-11]. These modified routes enhance the surface area and restrict the recombination of charge carriers, which extensively increase the catalytic activity than bare materials [13-20]. Wang and co-workers developed a low-cost, robust, non-

toxic, and metal free 2D nanosheets of C_3N_4, a conjugated polymer for hydrogen evolution photocatalytically and other application purposes [21-24]. The same group has also reported the decoration of cocatalysts (Pt and Co_3O_4) on C_3N_4 surface for overall water splitting [25,26]. The presence of cocatalysts reduces the activation energy barrier and increases the reaction kinetics of g-C_3N_4 polymers. They have also reported $CoSe_2$ as a versatile cocatalyst for efficient water oxidation photocatalytically under the illumination of visible light [27].

Molybdenum sulfide (MoS_2), a transition metal dichalcogenide has attracted attention as an electrocatalyst for hydrogen evolution [14-18]. Molybdenum (Mo) metal is relatively earth-abundant and therefore much cheaper than noble metal which is widely used in hydrogen evolution reaction (HER). Thus, Mo based catalysts offer significant advantages over noble metal catalysts as electrocatalysts [14-17]. It has also been considered an ideal cocatalyst as it possesses large specific surface area, narrow band gap (1.9 eV) and proper band edge potential for the interfacial charge transfer in heterostructure [14-17]. In the hexagonal close packed structure of MoS_2, Mo atoms are located between two layers of sulfur atoms like a sandwich. It also acquires layered structure similar to graphene, displays peculiar physical, optical, and electrical properties associated with its diverse structures [16-18]. The analogous layered structure of MoS_2 and g-C_3N_4 also reduce the lattice mismatch, the planar growth of MoS_2 could be accomplished on the g-C_3N_4 surface [18-19]. Despite considerable success, the design and fabrication of MoS_2-based catalysts for HER with remarkable activity and durability remain a huge concern.

The coupling of g-C_3N_4 and layered MoS_2 could significantly reduce the charge carrier recombination and shows enhanced activity than those bare materials [19,20,28-30]. MoS_2/g-C_3N_4 heterostructures have been previously reported by researchers for electrocatalytic hydrogen production reaction and photodegradation of the pollutants [16]. Dickon and co-workers reported MoS_2/g-C_3N_4 heterostructure for rhodamine B (RhB) and methyl orange (MO) dye degradation reaction. They have synthesized MoS_2 nanosheets coupled into the carbon nitride via ultrasonication and reported 3.6 times higher reaction rate constant towards dye degradation than bare g-C_3N_4 [16]. Tian and co-workers described a facile impregnation and heating method for the synthesis of MoS_2/g-C_3N_4 for H_2 evolution under visible light irradiation. According to their photocatalysis results 11.3 times higher H_2 evolution rate was achieved in case of 0.5 wt.% MoS_2/g-C_3N_4 sample as compared to bare g-C_3N_4 with the production of 2.03 µmol h^{-1} H_2 [19].

Zhang and co-workers decorated the surface of g-C_3N_4 with MoS_2 quantum dots via a wetness impregnation route. The catalytic activity was evaluated by HER using visible light illumination and 19.66 μmol h^{-1} yield of H_2 was achieved [31]. Jiang and co-workers also reported MoS_2/g-C_3N_4 for enhanced photocatalytic H_2 production [32]. Synthesis of layered MoS_2 on hollow g-C_3N_4 substrate for photocatalytic hydrogen evolution has been reported by Zheng and co-workers. The enhanced activity is due the formation of layered junction between MoS_2 and hollow C_3N_4, for efficient charge separation and active site formation [33]. Hou and co-workers also reported enhanced hydrogen production under visible light by developing layers of MoS_2 on C_3N_4 surface [34]. Liu and co-workers synthesized ultrathin MoS_2 on carbon nanospheres via solvothermal technique for enhanced hydrogen evolution reaction [35,36]. The same group also reported the pH effect on the growth of MoS_2 and its application for hydrogen evolution [37].

Considering the prompt advancement and development of molybdenum based materials as promising electrocatalyst for sustainable hydrogen evolution, we were inspired to construct MoS_2/g-C_3N_4 heterostructure, a semiconductor heterostructure with suitable band structure for hydrogen evolution reaction. MoS_2 microstructures were decorated on g-C_3N_4 surface via the hydrothermal route in order to provide an improved framework for MoS_2 and efficient production of H_2. The morphology, chemical composition, and crystal structure were characterized systematically. The mechanism of HER and synergistic electron transfer were also discussed. In case of MoS_2/g-C_3N_4, 10 mA/cm^2 current density can be generated applying −0.26 V vs. RHE applied potential, which is comparatively lower than bare MoS_2 (−0.43 V vs. RHE). The superior electrocatalytic activity of MoS_2/g-C_3N_4 is elucidated with the help of impedance spectroscopy, Tafel plots, and electrochemically active surface area measurements. In addition, MoS_2/g-C_3N_4 also demonstrated better performance in photocatalysis and achieved 91% degradation within 30 min with rate constant (*k*) value is 7.4x10^{-2} min^{-1}. The synergistic interaction and flow of charge carrier species between MoS_2 and g-C_3N_4 during photocatalysis have also been discussed. Therefore, the advantages of this work are multifold. First, this is a very convenient preparation method for the chemical coupling of two different layered materials to construct a new heterostructure. Second, the HER and dye degradation result strongly suggest the promise of an earth-abundant, robust, economic and extremely proficient metal-free hybrid catalyst based on MoS_2 and g-C_3N_4. Furthermore, the enhanced activity towards HER suggests that the heterostructure has increased exposed active sites for catalytic reactions than bare

structure. Electrochemically active surface area is successfully calculated from the CV curve for both MoS_2 and MoS_2/g-C_3N_4 which shows that ECSA of MoS_2/g-C_3N_4 is nearly 13 times higher compared to bare MoS_2. This enhanced activity may be attributed to the intercalated structure of both the layered materials. BET surface area also supports the ECSA results. This finding may shed light towards substitution of noble metals by 2D-layered transition metal dichalcogenide and provide an insight to design performance-oriented structure for renewable energy applications.

6.2 Experimental Section

6.2.1 Synthesis of MoS_2

For the synthesis of MoS_2, a facile hydrothermal route was followed. 1.5 g ammonium molybdate as a molybdenum precursor and 0.75 g thiourea as a sulfur source were used. The precursors were dissolved in 70 mL water and the reaction mixture was poured into the Teflon lined autoclave reaction vessel for 24 h at 180 °C. Black colored MoS_2 NPs was obtained after 24 h. The final product was washed with water followed by ethanol and dried on a hot water bath.

6.2.2 Synthesis of MoS_2/g-C_3N_4 Heterostructure

g-C_3N_4 was synthesized using our previously reported method [20]. Briefly, 10 g of dried urea powder was treated thermally at 550 °C for 2.5 h in a muffle furnace using a covered crucible and yellow powder was collected as a product. The product was washed with 0.1 M HNO_3 for the removal of impurities and grinded into powder. In 70 mL water, 0.05 g of g-C_3N_4 powder was mixed with 1.5 g of ammonium molybdate and 0.75 g of thiourea. The reaction mixture was sonicated for 30 min. and poured into the Teflon lined autoclave vessel for 24 h at 180 °C. Finally, the brown color product was extracted and cleaned with water and ethanol and dried in an oven. The overall synthetic procedure is shown in **Scheme 6.1**. To check the stability of bare g-C_3N_4, hydrothermal reaction was carried out at 180 °C for 24 h only dispersing g-C_3N_4 in 70 mL water.
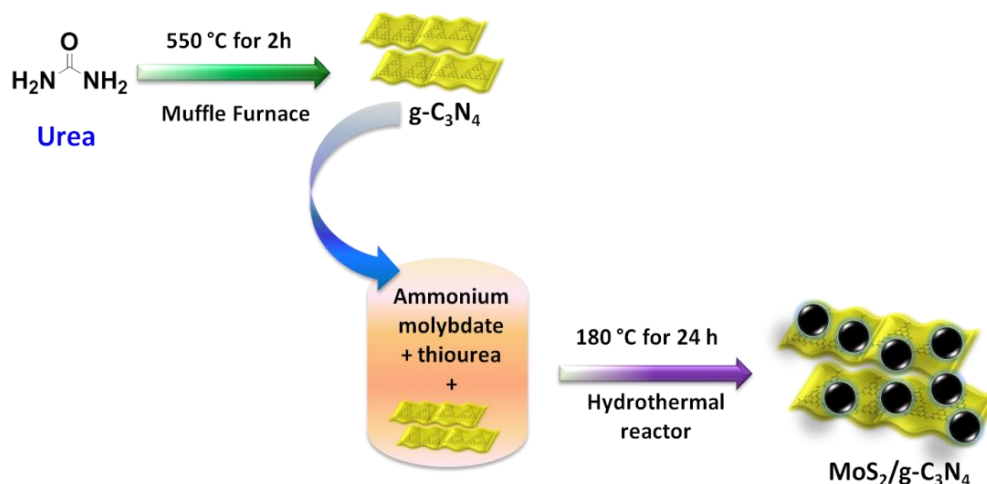
Scheme 6.1 Schematic representation of the formation of MoS₂, and MoS₂/g-C₃N₄ under hydrothermal conditions at 180 °C for 24 h

6.3 Results and Discussion

Hydrothermal method was followed for synthesizing molybdenum sulfide using thiourea, and ammonium molybdate tetrahydrate as starting materials at 180 °C for 24 h. Using similar reaction conditions with the addition of g-C₃N₄, the heterostructure (MoS₂/g-C₃N₄) was synthesized.

6.3.1 Characterization

The synthesized materials were used for characterization using various characterization techniques and discussed below.

6.3.1.1 X-ray Diffraction Study

In order to determine the phase and purity of the synthesized material, XRD analysis has been performed and the result is shown in **Figure 6.1.a**. In the XRD pattern of MoS₂/g-C₃N₄ the peaks for MoS₂ appeared at $2\theta = 13.9°$, $33.9°$, $39.8°$, and $59.7°$ could be assigned to (002), (100), (103), and (110) crystal planes, respectively (JCPDS 37-1492) [16,38-41]. It can be seen from

Figure 6.1 that all the peaks are well indexed to hexagonal structure of MoS_2. No obvious peaks for g-C_3N_4 ($2\theta = 13.3^o$ and 27.6^o) have been obtained from XRD patterns, which presumably due to the higher crystalllinity of MoS_2 on the g-C_3N_4 surface [19-20]. In case of MoS_2, the peaks for MoS_2 appeared at $2\theta = 13.9°$, $33.9°$, $39.8°$, and $59.7°$ corresponds to (002), (100), (103), and (110) crystal planes, respectively.
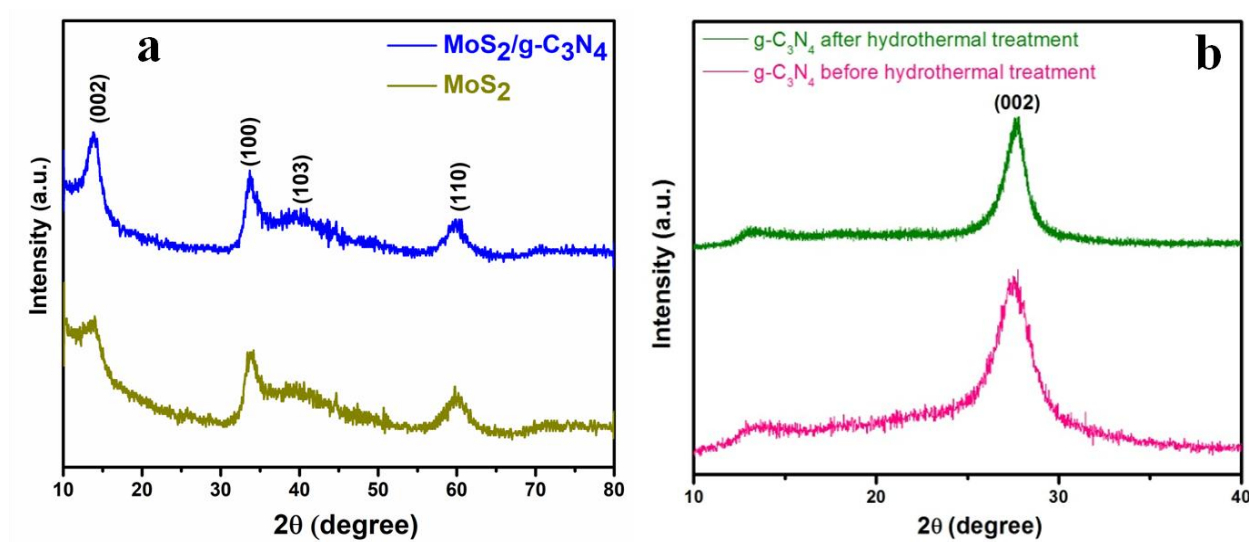
Figure 6.1 Powder X-ray diffraction patterns of (a) MoS_2/g-C_3N_4, and MoS_2 at 2° per min scanning rate and (b) PXRD pattern of g-C_3N_4 before and after hydrothermal treatment at 180 ^{o}C for 24 h

The PXRD pattern of bare g-C_3N_4 (before hydrothermal treatment) shown in **Figure 6.1.b** which shows the peaks at 27.6^o and $13.3°$ corresponding to the (002) and (100) crystal planes, respectively. The initial peak due to the interlayer stacking of the conjugated aromatic system of g-C_3N_4 and later represents the presence of tri-s-triazine units [19,20,28]. However, absence of any other peaks represent the as-synthesized sample is pure. Similarly, the PXRD pattern of g-C_3N_4 after hydrothermal treatment shows the strongest XRD peak at 27.6^o corresponding to the stacking of the conjugated aromatic system and weak at 13.3 due to the in-plane ordering of tri-s-triazine units [21-23]. The analogous peak positions before and after hydrothermal treatment suggested that g-C_3N_4 does not go through further condensation reactions at 180 °C shown in **Figure 6.1.b**.

6.3.1.2 Morphology Analysis

Field emission scanning electron microscopy (FESEM) analysis has been conducted to check the morphology of the as-synthesized materials, shown in **Figure 6.2.a** and **b**.
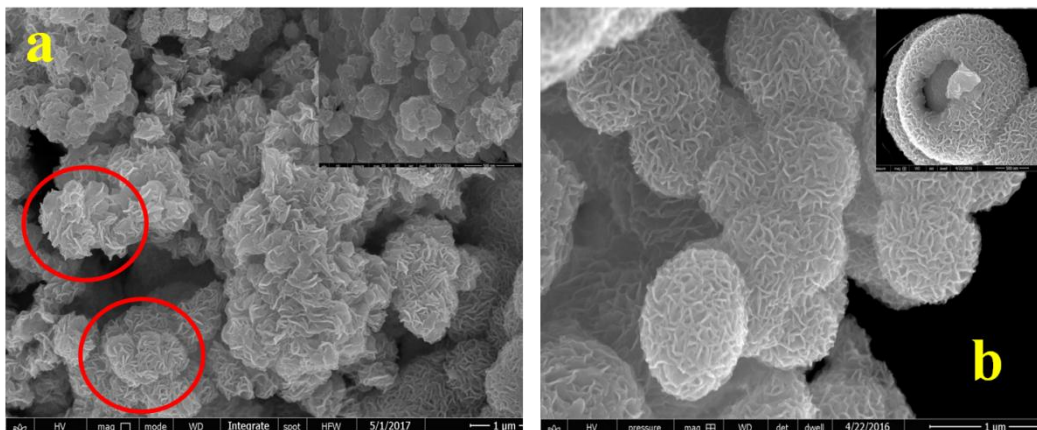
Figure 6.2 FESEM image of (a) MoS$_2$/g-C$_3$N$_4$ heterostructure and (b) MoS$_2$ microstructures. Inset figure shows high resolution FESEM images

The FESEM images of MoS$_2$/g-C$_3$N$_4$ show that MoS$_2$ are evenly decorated on g-C$_3$N$_4$ substrate and heterostructure is made up from two different layered materials shown in **Figure 6.2.a**. The layered structure signifies the aggregation of g-C$_3$N$_4$ sheets to form plates. It can also be noted that the plate has a flake like topography similar to that observed from the FESEM images of bare MoS$_2$ (**Figure 6.2.b**). The structure shows the more exposed edges with edge length of ~ 120-150 nm. The FESEM image in **Figure 6.3** shows that bare MoS$_2$ has a 3D microstructure with a flaky texture. The microstructures consist of numerous thin nanoflakes, shown in high resolution SEM image, (inset of **Figure 6.2.b**). The approximate length of a single flake of MoS$_2$ is ~ 120-150 nm with the edge width of ~ 20 nm. The sheet like structure of g-C$_3$N$_4$ is shown in the **Figure 6.3**.

More insights into the structure and morphology have been gained via TEM analysis of MoS$_2$/g-C$_3$N$_4$ and MoS$_2$. TEM analysis of MoS$_2$/g-C$_3$N$_4$ heterostructure indicates the presence of MoS$_2$ on the surface of g-C$_3$N$_4$ shown in **Figure 6.4.a**. HRTEM image (**Figure 6.4.b**) of MoS$_2$/g-C$_3$N$_4$ clearly shows intimate interface formation between MoS$_2$ and g-C$_3$N$_4$,

semiconductors. From HRTEM the d-spacing value has been calculated and observed that d=0.62 nm for (002) plane of hexagonal MoS_2, illustrates the presence of MoS_2 on g-C_3N_4 surface (**Figure 6.4.b**) [18,19,40,41].
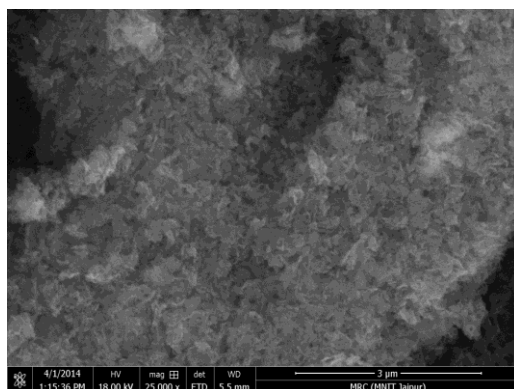
Figure 6.3 FESEM image of bare g-C$_3$N$_4$ surface
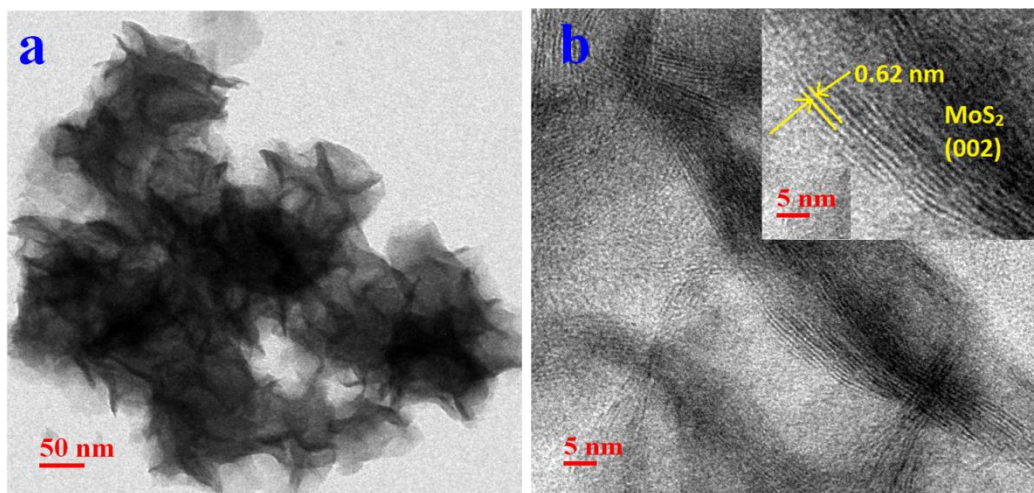
Figure 6.4 (a) TEM image and (b) High-resolution TEM image of MoS$_2$/g-C$_3$N$_4$ heterostructure, d-spacing calculation is shown in inset figure

TEM-EDS area mapping of MoS_2/g-C_3N_4 shown in **Figure 6.5.a-e** exhibits the existence of Mo, S, C, and N.
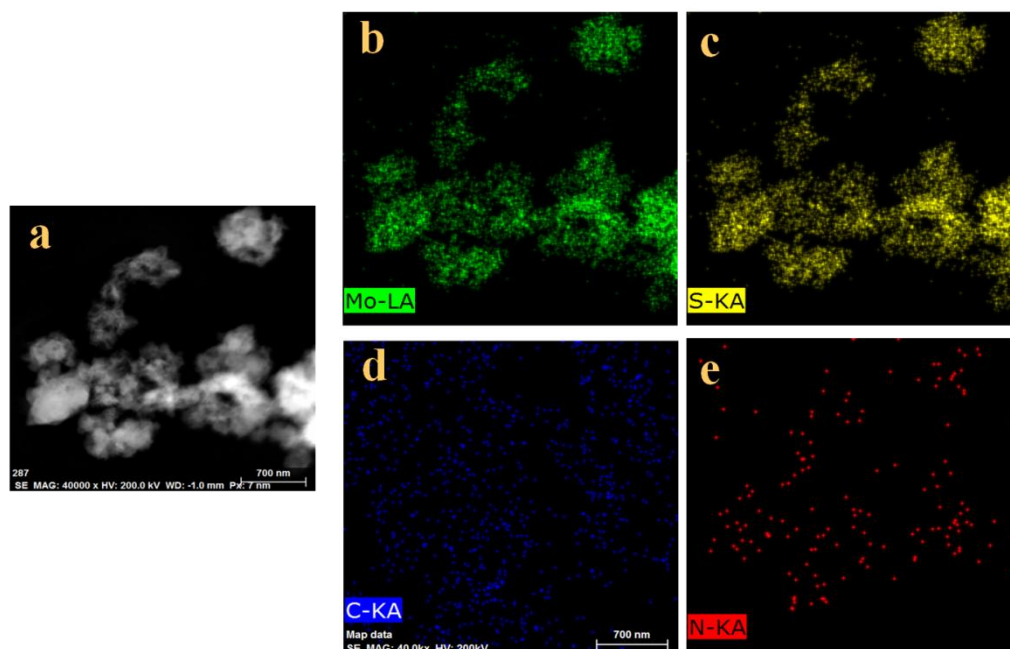
Figure 6.5 EDS area mapping of MoS$_2$/g-C$_3$N$_4$ (a) FESEM image and (b, c, d, e) mapping analysis of Mo, S, C, and N, respectively in MoS$_2$/g-C$_3$N$_4$ heterostructure
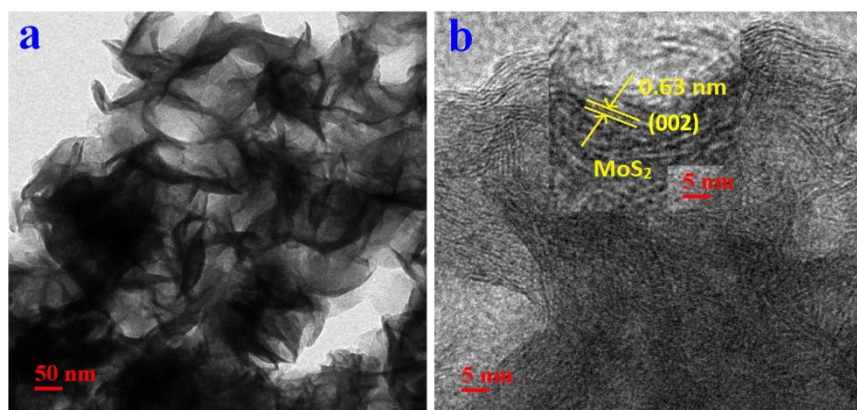
Figure 6.6 (a) TEM image and (b) High-resolution TEM image of MoS$_2$ microstructures. Inset figure shows d-spacing calculation

Figure 6.6.a shows the low magnification TEM images of MoS$_2$ microstructures made up of well-defined, rounded and loosely connected flake like structures.

It can be seen from **Figure 6.6.a** that layered structures of MoS$_2$ are stacked with each other. The edge length of a single flake of MoS$_2$ is ~ 120-150 nm, which is well matched with SEM analysis. It can be seen from HRTEM (**Figure 6.6.b**) that the d-spacing value is 0.62 nm attributed to the (002) plane of hexagonal close packed MoS$_2$ [18,19].

TEM-EDS area mapping analysis of MoS$_2$ shows the uniform distribution of Mo and S elements (**Figure 6.7.a-c**).
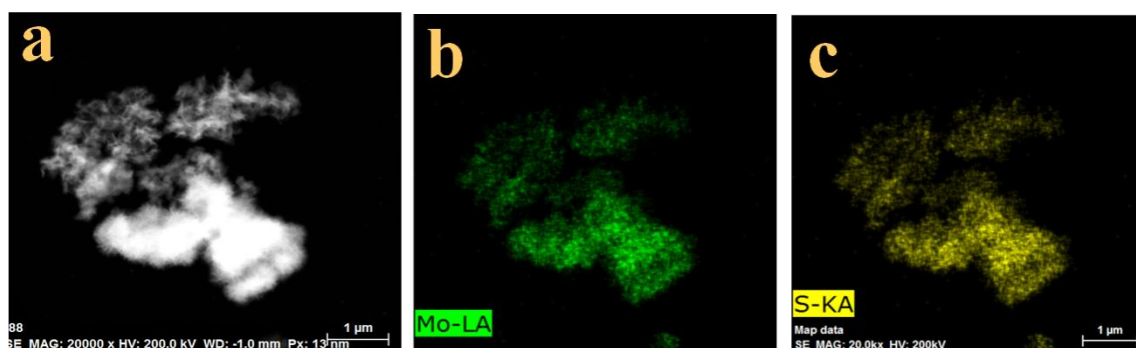
Figure 6.7 EDS area mapping of MoS$_2$ (a) FESEM image and (b, c) area mapping of Mo and S, respectively in MoS$_2$

6.3.1.3 X-ray Photoelectron Spectroscopy

To ensure the components of the as synthesized samples and oxidation states of the elements in MoS$_2$/g-C$_3$N$_4$, X-ray photoelectron spectroscopy (XPS) analysis has been executed. Survey spectrum of the heterostructure and the high-resolution XP spectra of C, N, and O elements are shown in **Figure 6.8.a** and **Figure 6.9**. The high-resolution XP spectra of Mo and S elements are presented in **Figure 6.8.b-d**. The peaks have been deconvoluted into several Gaussian-Lorentzian peaks shown in **Figure 6.8.c-d** and **Figure 6.9.a-c**. The C 1s core level spectrum in **Figure 6.9.a** deconvoltued into two Gaussian peaks. The peak located at 284.39 eV could be assigned to the graphitic carbon (C-C) and peak centered at 287.18 eV is for sp^2-hybridized carbon in N-containing triazine rings (N–C=N) [19,20,42]. The peak centered at 394.54, and 399.33 eV from high-resolution XPS spectrum of N 1s (**Figure 6.9.b**) is usually ascribed to the C–N=C, and N–(C$_3$) bonds respectively, corresponds with the pyridinic and

graphic N atoms of triazine structure of g-C_3N_4 [4,20]. The spectrum in **Figure 6.9.c** of O 1s shows two peaks at 531.16 and 533.23 eV related to Mo-O bond and chemisorbed oxygen. The high resolution XP spectra of Mo 3d and S 2p for MoS_2 displayed in **Figure 6.8.b-d**.
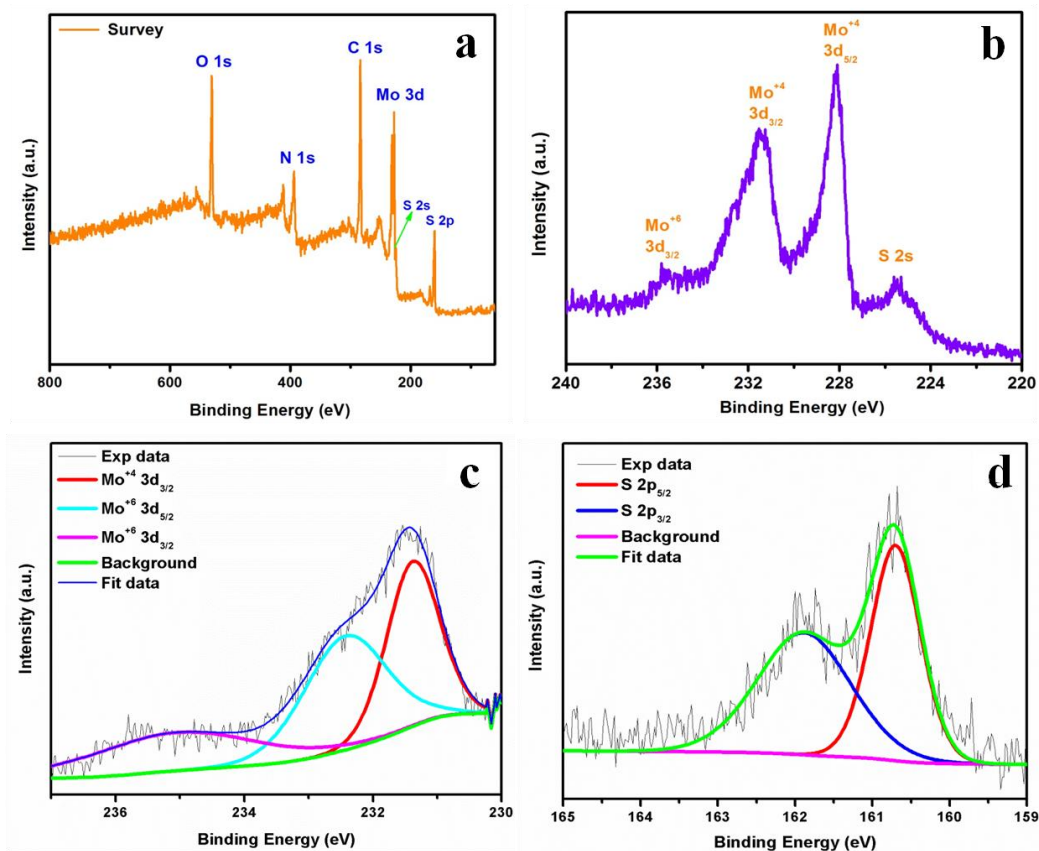
Figure 6.8 XP spectra of (a) survey spectrum, (b) Mo-3d core level, (c) deconvoluted spectra of Mo^{+4} 3d$_{3/2}$ and Mo^{+6} 3d$_{3/2}$ and 3d$_{5/2}$ region, and (d) deconvoluted spectra of S-2p core level

Figure 6.8.b shows the binding energy peaks of the Mo 3d$_{5/2}$ and 3d$_{3/2}$ at 228.27, and 231.38 eV, respectively, which corresponds to Mo^{+4} species in Molybdenum [40-42]. The peak located at 225.43 eV is recognized for S 2s and the peak for Mo^{+6} species is asymmetric hence it has been deconvoluted and the spectrum shown in **Figure 6.8.c.** Now, the peaks are clearly distinct, which is attributed to Mo^{+6} (3d$_{3/2}$) at 235.05 eV and for Mo^{+6} (3d$_{5/2}$) at 232.42 eV revealing the presence of oxide species of molybdenum due to aerial oxidation [17-19,42]. The S

2p peak is splited into two peaks centered at 161.89 eV and 160.69 eV, assigned to S $2p_{1/2}$ and S $2p_{3/2}$, respectively shown in **Figure 6.8.d** [16,19,42]. All the binding energy values are summarized in **Table 6.1**. XPS results confirm the formation of MoS_2 on g-C_3N_4.
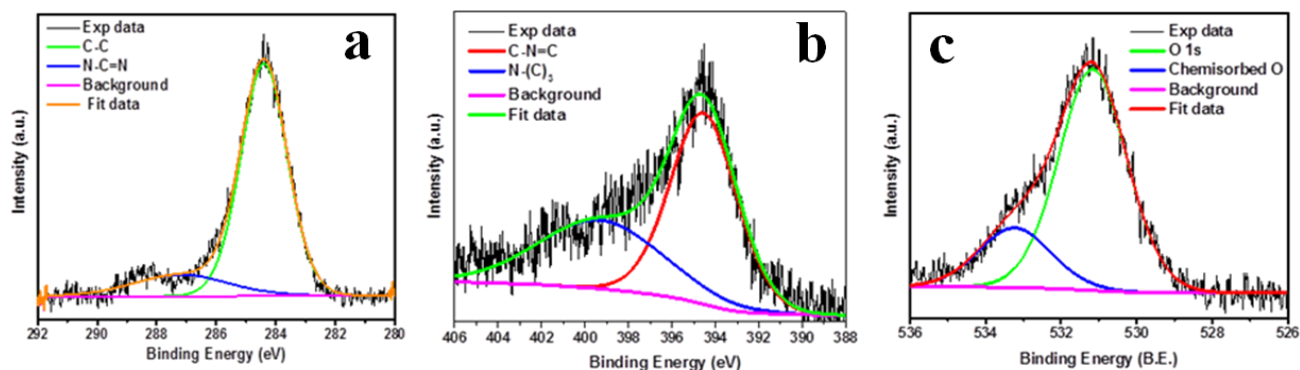
Figure 6.9 High resolution XP spectra of MoS_2/g-C_3N_4 (a) C 1s, (b) N 1s and (c) O 1s

Table 6.1 Binding energy peak positions of Mo 3d and S 2p from XP spectra of the MoS_2/g-C_3N_4

MoS_2/g-C_3N_4		
B.E. peaks	**Sub-peaks**	**Positions**
C 1s	C-C	284.39
	N-C=N	287.18
N 1s	C-N=C	394.54
	N-(C_3)	399.33
O 1s	Mo-O	531.16
	O-O	533.23
Mo^{+4}	$3d_{5/2}$	228.27
	$3d_{3/2}$	231.38
Mo^{+6}	$3d_{5/2}$	232.42
	$3d_{3/2}$	235.05
	S2s	225.43
S	$2p_{3/2}$	160.69
	$2p_{1/2}$	161.89

6.3.1.4 Raman and UV-visible Analysis

Raman analysis of MoS_2 and MoS_2/g-C_3N_4 is performed and shown in **Figure 6.10.a**. It reveals two characteristic peaks in both the samples positioned at 374 and 405 cm^{-1} and recognized as E^1_{2g} and A^1_g Raman active vibration modes of MoS_2. Both the Raman peaks are generated from in-plane and out-of-plane motion of the sandwiched S-Mo-S layer, which is well coordinated with literature reports [16-19]. The Raman study further confirms the existence of MoS_2 on the surface of g-C_3N_4.

The optical properties of MoS_2/g-C_3N_4 heterostructure and bare MoS_2 and g-C_3N_4 have been determined by UV-vis diffuse reflectance spectra and shown in **Figure 6.10.b**. An enhanced absorption in the visible region has been observed in MoS_2/g-C_3N_4 heterostructure as compared to bare g-C_3N_4. The increased absorption intensity supports the successful introduction of MoS_2 on g-C_3N_4 surface in heterostructure [6,18,31]. The absorption band for pure g-C_3N_4 displays absorption from the UV to visible range ~ 200 to 450 nm which corresponds to 2.87 eV band gap of g-C_3N_4, calculated by classical Tauc approach and shown in the inset of **Figure 6.10.b** [18,20].
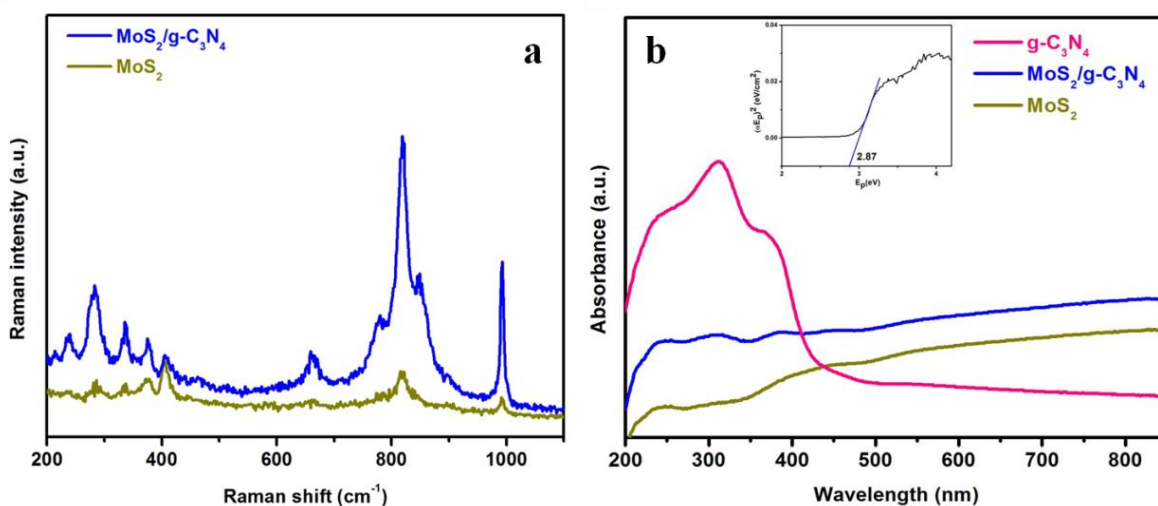
Figure 6.10 (a) Raman spectra of MoS_2/g-C_3N_4 and MoS_2 (b) DRS for MoS_2/g-C_3N_4, MoS_2 and g-C_3N_4. Inset shows $(\alpha Ep)^2$ *vs.* Ep plot for band gap (E_g) calculation of g-C_3N_4

6.3.2 Electrocatalytic Study for Hydrogen Evolution Reaction

Electrochemical performance was examined in a three-electrode system and 0.5 M H_2SO_4 was used as the electrolyte. For this study, glassy carbon electrode (GCE) was used as a working electrode, graphite rod as a counter electrode, and Ag/AgCl used as reference electrode. Typically, the working electrode was prepared as follows: 5 mg MoS_2/g-C_3N_4 was dispersed in 300 µL iso-propyl alcohol and 30 µL Nafion (adhesive). Then, the mixture was sonicated for 10 min in order to obtain a homogeneous suspension. Finally, 5.0 µL of the homogeneous mixture was dropped onto GCE and allowed to dry. CH Instrument (CHI 604E) was used to measure all the electrochemical data at room temperature. The blank GCE was tested for a baseline.

Impedance measurements were performed using the same three-electrode system and at the frequency of 0.1-100 Hz with a 10 mV ac dither. The electrochemical capacitance study was performed between 0.0 and 0.2 V vs. RHE at varied scan rates from 10-100 V/s. The electrochemical surface area (ECSA) was calculated by the specific capacitance. The calculation method of mass activity and specific activity is done according to the literature [3,28,32]. The mass activity value (A/g) was calculated from the catalyst loading and the observed current density (mA/cm^2) at a potential of −0.333 V vs. RHE. The specific activity was calculated by normalizing the current at a fixed potential (−0.333 V vs. RHE) by the electrochemically active surface area.

6.3.2.1 Linear Sweep Voltammetry

The electrocatalytic performance of as-synthesized catalysts has been carried out with the help of linear sweep voltammogram technique. The electrochemical experiment was carried out in a three-electrode system using 0.5 M H_2SO_4 was used as electrolyte. Ag/AgCl electrode was used as a reference to record the data but presented with respect to reverse hydrogen electrode (RHE). The activity for electrochemical hydrogen evolution reaction, bare GC, MoS_2, MoS_2/g-C_3N_4, and Pt/C (5%) are checked and presented in **Figure 6.11**. **Figure 6.11.a-b** depicts the polarization curves of bare GC, MoS_2, MoS_2/g-C_3N_4, and Pt/C (5%) electrode recorded at a scan rate of 2 mV/sec.
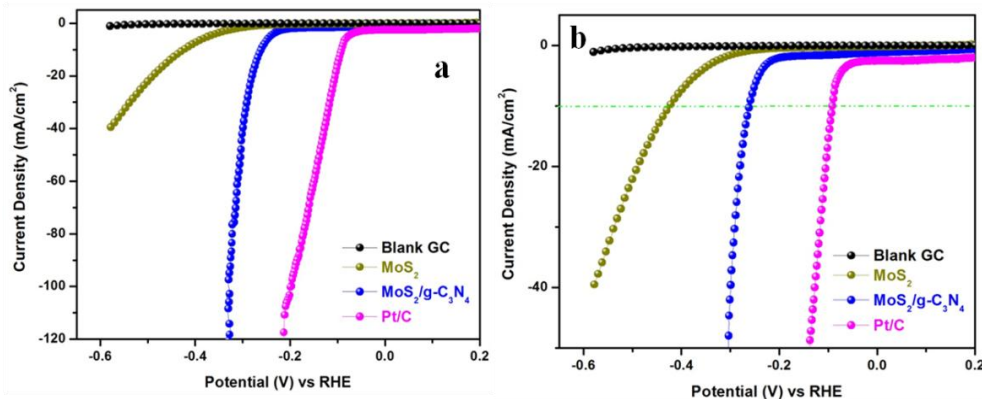
Figure 6.11 (a, b) Polarization curve for blank GCE, Pt/C, MoS$_2$ and MoS$_2$/g-C$_3$N$_4$ in 0.5 M H$_2$SO$_4$ (iR corrected)

All the polarization curves are shown after iR correction. In case of MoS$_2$/g-C$_3$N$_4$ the observed LSV and iR corrected LSV are shown in **Figure 6.12**.
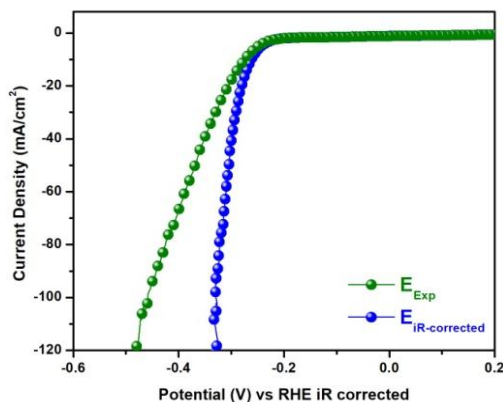
Figure 6.12 LSV curve of MoS$_2$/g-C$_3$N$_4$ before and after iR correction

Bare GC electrode doesn't show any catalytic activity in the recorded potential window and pure MoS$_2$ shows poor catalytic activity for HER. As shown in **Figure 6.11.a** the polarization curves revealed that the as-prepared MoS$_2$/g-C$_3$N$_4$ displayed a small onset potential of -0.24 V vs. RHE. In contrast, the lower onset potential in MoS$_2$ (-0.37 V vs. RHE) indicates lesser electrocatalytic activity. In order to generate a current density of 10 mA/cm^2, -0.43 V vs. RHE potential is needed for bare MoS$_2$ whereas relatively smaller potential (-0.26 V vs. RHE) is required for MoS$_2$/g-C$_3$N$_4$. The result clearly reveals that MoS$_2$/g-C$_3$N$_4$ can facilitate the HER

process and has higher electrocatalytic activity. HER catalytic activity of $MoS_2/g\text{-}C_3N_4$ is compared with Pt/C (5%), where it requires only 92 mV potential to generate current density of 10 mA/cm^2.

6.3.2.2 Surface Area of $MoS_2/g\text{-}C_3N_4$

ECSA is an important parameter to determine the effectiveness of the catalyst. It has been determined for MoS_2 and $MoS_2/g\text{-}C_3N_4$ following some literature to provide the further insights [3,28,29]. **Figure 6.13.a** and **b** revealed the CV curves of MoS_2 and $MoS_2/g\text{-}C_3N_4$ using a potential range of +0.2157 to +0.4157 V vs. RHE at a different scan rates of 10-100 mV/s 0.5 M H_2SO_4 electrolyte. At a potential of +0.3157 V vs. RHE, double-layer charging currents are measured from the CV curves and are plotted against scan rates and shown in **Figure 6.13.c**.
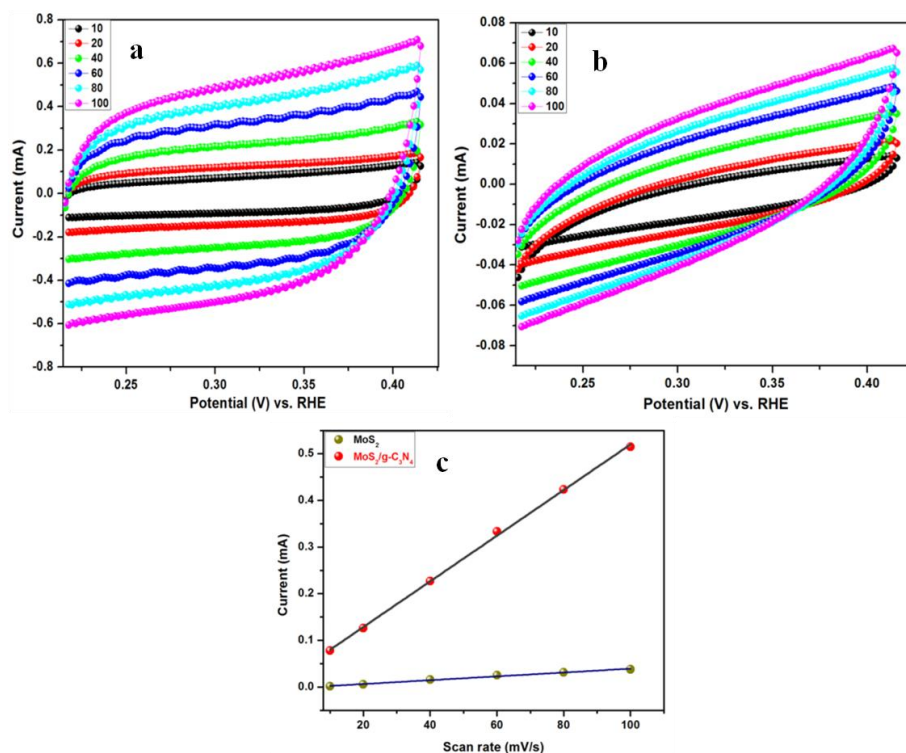
Figure 6.13 Cyclic voltammetry curves of (a) MoS_2, (b) $MoS_2/g\text{-}C_3N_4$ recorded in 0.5 M H_2SO_4 recorded with different scan rates, (c) capacitive current at +0.3157 (V vs. RHE) as a function of scan rate for MoS_2, $MoS_2/g\text{-}C_3N_4$

The double-layer capacitance (C_{dl}) is calculated from the slope, and the values are 0.41 mF and 4.89 mF for MoS_2 and $MoS_2/g-C_3N_4$, respectively. Consequently, the roughness factor (R_f) is calculated from ECSA. Therefore, the calculated ECSA and R_f values for $MoS_2/g-C_3N_4$ and MoS_2 are 81.5 cm^2, 6.83 cm^2, and 1147.8, 96.2, respectively. Higher values of ECSA and R_f for $MoS_2/g-C_3N_4$ proves that it has more exposed electrochemically active surface area toward the HER reaction compared to bare MoS_2. The inclusion of $g-C_3N_4$ increases the conductivity of the material via charge transportation, which further results in superior activity of $MoS_2/g-C_3N_4$. Mass activity and specific activity (with respect to ECSA surface area and with respect to BET surface area) are also helpful to determine the efficiency of the catalyst. Here mass activities of $MoS_2/g-C_3N_4$ and MoS_2 are estimated at a fixed potential of −0.333 V vs. RHE and the corresponding values are 97.81, and 2.60 A/g, respectively, which claims $MoS_2/g-C_3N_4$ as an efficient electrocatalyst compared to the bare material. In addition, the value of specific activity (ECSA) for $MoS_2/g-C_3N_4$ is 0.09 mA/cm$^2_{ECSA}$ which is higher than that of bare MoS_2 (0.03 mA/ cm$^2_{ECSA}$) which further support the higher electrocatalytic activity of heterostructure. The specific activities (ECSA) are 0.03 and, for MoS_2 and $MoS_2/g-C_3N_4$ respectively, calculated from the ECSA. All the values (mass activity and specific activity) are summarized in **Table 6.2**.

Table 6.2 Comparative results of the overall electrocatalytic performance for MoS₂, MoS₂/g-C₃N₄, MoS₂/CNT, and MoS₂/C

Cathode	ECSA (cm^2)	R.F.	Mass activity (A/g)	Tafel slope (mV/dec)	Specific activity (ECSA) (mA/cm^2)	Specific activity (BET) (mA/cm^2)
MoS_2	6.83	96.24	2.60	149	0.03	0.056
$MoS_2/g-C_3N_4$	81.50	1147.89	97.81	63	0.09	0.601
MoS_2/C	-	-	12.67	109	-	
MoS_2/CNT	-	-	36.53	67	-	

To support the higher electrocatalytic activity of $MoS_2/g-C_3N_4$, BET surface area for MoS_2 and $MoS_2/g-C_3N_4$ is determined. BET surface area of MoS_2 is 4.66 m^{2}g^{-1} where as in case of $MoS_2/g-C_3N_4$, the value is 16.26 m^{2}g^{-1} which suggest the successive increase in the surface area after synthesis of the intercalated heterostructure (**Figure 6.14.a**). Specific activity of both

MoS_2 and $MoS_2/g\text{-}C_3N_4$ is calculated from the BET surface area (S_{BET}) and the values are 0.056 mA/cm^2 and 0.601 mA/cm^2 which are shown in **Table 6.2**.
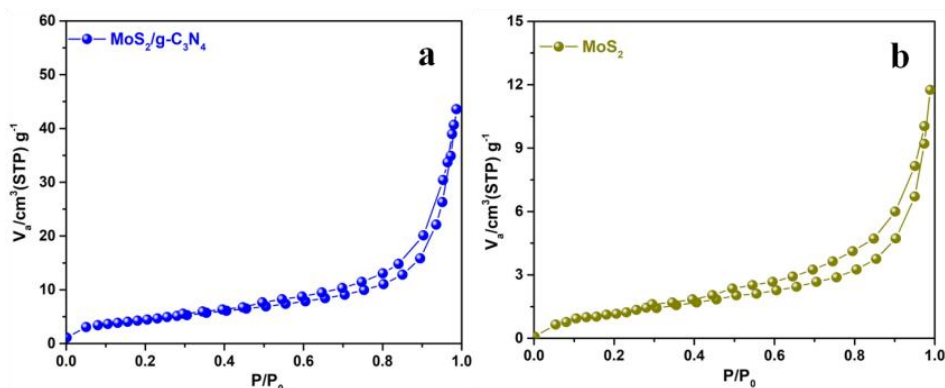
Figure 6.14 N$_2$ adsorption-desorption isotherms of (a) MoS$_2$/g-C$_3$N$_4$ and (b) MoS$_2$

6.3.2.3 Stability of the MoS$_2$/g-C$_3$N$_4$ after Electrocatalysis

In case of $MoS_2/g\text{-}C_3N_4$, after 1000 cycles of LSV the current density remained unchanged, demonstrating the excellent durability of the catalyst shown in **Figure 6.15.a**. After electrocatalysis, the morphology of $MoS_2/g\text{-}C_3N_4$ has been investigated by FESEM analysis (**Figure 6.15.b**) and it remains unaffected even after 1000 cycles. All these results reveal the excellent catalytic performance of $MoS_2/g\text{-}C_3N_4$ heterostructure with remarkable stability.
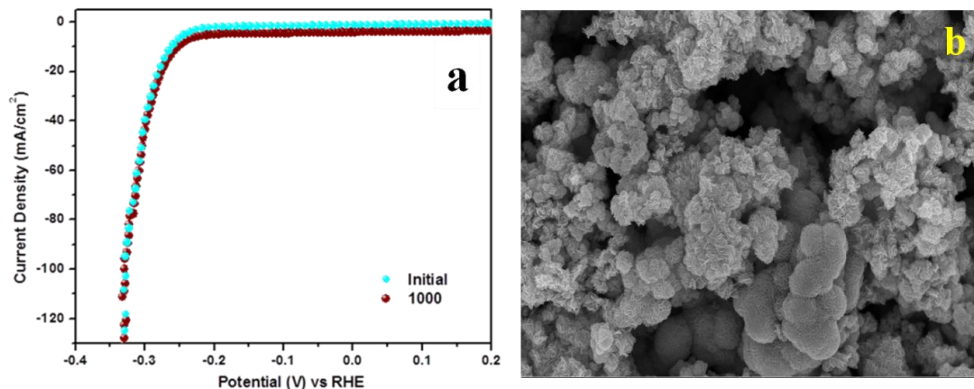
Figure 6.15 (a) Stability after 1000 cycles of repetitive LSV scans, (b) FESEM image of MoS$_2$/g-C$_3$N$_4$ after 1000 cycles of electrocatalysis

6.3.2.4 Tafel Slope

To further investigate the performance of a catalyst, and to determine the exact mechanism of HER, Tafel slope has been calculated from Tafel plots. For Tafel slope calculation, the linear portion of the Tafel plots has been fitted to the Tafel equation (η = a + b log J, where η = overpotential, J = current density, a = exchange current density at zero overpotential, and b = Tafel slope) [3,28-32]. The Tafel plot is shown in the **Figure 6.16** and the values are concluded in **Table 6.2**.

The Pt/C (5%) shows the Tafel slope value 37 mV dec^{-1}. The synthesized MoS$_2$/g-C$_3$N$_4$ and MoS$_2$ exhibit 63, and 149 mV dec^{-1}, Tafel slopes respectively. A lower Tafel slope of MoS$_2$/g-C$_3$N$_4$ signifies the improved reaction kinetics for HER [28,40]. The calculated Tafel slope values for MoS$_2$/CNT and MoS$_2$/C are 67 and 109 mV dec^{-1}, respectively.

The HER kinetics in case of MoS$_2$/g-C$_3$N$_4$ and MoS$_2$ has been studied in details and explored. Generally, Volmer-Heyrovsky and Volmer-Tafel reactions are two accepted HER mechanisms, where Volmer, Heyrovsky, and Tafel anyone can be the rate-determining step: [3,28-32].

$$\text{MoS}_2/\text{g} - \text{C}_3\text{N}_4 + \text{H}_3\text{O}^+ + \text{e}^- \rightarrow \text{MoS}_2/\text{g} - \text{C}_3\text{N}_4 - \text{H}_{abs} + \text{H}_2\text{O} \quad \text{(Volmer reaction)}$$

$$\text{MoS}_2/\text{g} - \text{C}_3\text{N}_4 - \text{H}_{abs} + \text{H}_3\text{O}^+ + \text{e}^- \rightarrow \text{MoS}_2/\text{g} - \text{C}_3\text{N}_4 + \text{H}_2 + \text{H}_2\text{O} \text{ (Heyrovsky reaction)}$$

$$\text{MoS}_2/\text{g} - \text{C}_3\text{N}_4 - \text{H}_{abs} + \text{MoS}_2/\text{g} - \text{C}_3\text{N}_4 - \text{H}_{abs} \rightarrow \text{H}_2 + \text{MoS}_2/\text{g} - \text{C}_3\text{N}_4 \text{ (Tafel reaction)}$$
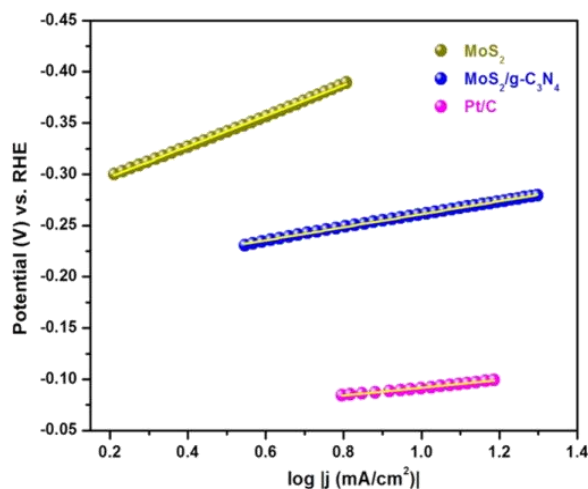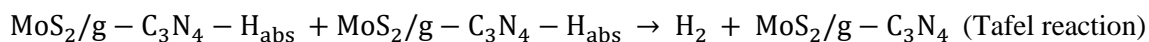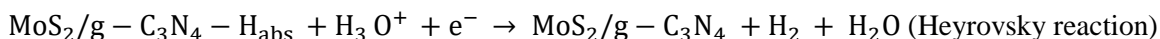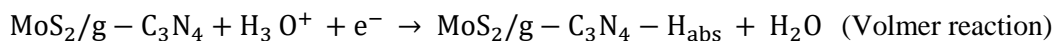
Figure 6.16 Tafel plots of Pt/C, MoS$_2$, and MoS$_2$/g-C$_3$N$_4$

In the first step hydrogen gets adsorb via a combination of the proton with an electron: Volmer reaction. Now adsorbed H atom has two possible ways to form H_2 molecule. First is the reaction with hydrated proton generated by an acidic electrolyte (0.5 M H_2SO_4) and with an electron provided from the catalyst (Heyrovsky mechanism), and second is the direct combination with an additional H atom which is absorbed on the catalyst surface (Tafel mechanism) [28,29,32]. The Tafel slopes value for the Volmer, Heyrovsky, and Tafel reactions have been calculated under standard conditions are 118, 39, and 29 mV dec^{-1}, respectively [3,43,44]. In this work, the obtained Tafel slope value for MoS_2/g-C_3N_4, MoS_2/CNT, and MoS_2/C, is 63, 66 and 109 mV dec^{-1}, respectively, which authenticates that the hydrogen evolution reaction proceeds via the Volmer-Heyrovsky mechanism.

Table 6.3 summarizes the electrochemical results of MoS_2/g-C_3N_4 catalyst and the earlier reported MoS_2 and g-C_3N_4 based HER catalysts. One can see that the onset value (−0.24 V vs. RHE) for MoS_2/g-C_3N_4 heterostructure is lower than previously reported MoS_2 based catalysts, which reveals the effect of g-C_3N_4.

Table 6.3 Comparative study of HER activity of reported references

Material	Loading amount (mg/cm^2)	Medium	Overpotential to generate 10 mA/cm^2 current	Tafel slope (mV/decade)	Reference
C-MoS_2	-	0.5 M H_2SO_4	80 mV (onset)	47	40
MoS_2 nanosheet on C_3N_4	-	0.5 M H_2SO_4	158 mV	52	30
GQDs-MoS_2	-	0.5 M H_2SO_4	200 mV	43	46
O-MoS_2	0.29	0.5 M H_2SO_4	120 mV (onset)	55	47
MoS_2 /CNFs	-	0.5 M H_2SO_4	120 mV (onset)	44	48
C_3N_4@NG	0.10	0.5 M H_2SO_4	240 mV	51.5	8
C_3N_4-MoS_2 (mixture)	-	0.5 M H_2SO_4	330 mV (5 mA/cm^2)	95	15

MoS$_2$/MoO$_2$	0.22	0.5 M H$_2$SO$_4$	240 mV	76.1	17
Ultrathin MoS$_2$-coated carbon nanospheres	~ 0.31	0.5 M H$_2$SO$_4$	200 mV	53	35
MoS$_2$/g-C$_3$N$_4$	1.06	0.5 M H$_2$SO$_4$	260 mV	63	*This work*

6.3.2.5 Electrochemical Impedance Spectroscopy

To understand the HER mechanism clearly the electrochemical impedance spectroscopy (EIS) of the MoS$_2$ and MoS$_2$/g-C$_3$N$_4$ heterostructure have been carried out. The arc of the EIS Nyquist plot indicates the charge transfer resistance [4,29]. The smaller arc radius means reduced charge transfer resistance and there will be faster charge transportation from electrode to electrolyte [29,32,45]. For both the samples, the impedance has been measured at their respective onset potentials and shown in **Figure 6.17**.

The Nyquist plot of the MoS$_2$/g-C$_3$N$_4$ heterostructure demonstrates smaller arc radius attributing to the reduced resistance and increased conductivity due to having the intercalated layered structure of conductive g-C$_3$N$_4$ and MoS$_2$ as compared to bare MoS$_2$. Experimental data is fitted with an equivalent circuit which is composed of R$_1$, R$_2$ and a constant phase element (CPE1) and shown as the inset of **Figure 6.17** and the corresponding parameters are shown in **Table 6.4**. Here R$_1$ is the solution resistance; R$_2$ is the charge transfer resistance. For MoS$_2$/g-C$_3$N$_4$ heterostructure the resistance of electrolyte R$_1$ which is 18.19 Ω, and the charge transfer resistance R$_2$ is 66.19 Ω. By contrast, for MoS$_2$, R$_1$ is 2.03 Ω and R$_2$ is 410.47 Ω., mentioned in **Table 6.4**. The subsequent decrease in the charge transfer resistance (R$_2$) in MoS$_2$/g-C$_3$N$_4$ compared to the MoS$_2$ suggested that there is faster interfacial charge transfer in heterostructure. Overall, the superior long-term durability, higher surface area, lower Tafel slope and higher current density at lower onset potential in MoS$_2$/g-C$_3$N$_4$ catalyst implies the great possibility of executed this new catalyst for efficient hydrogen evolution reaction.
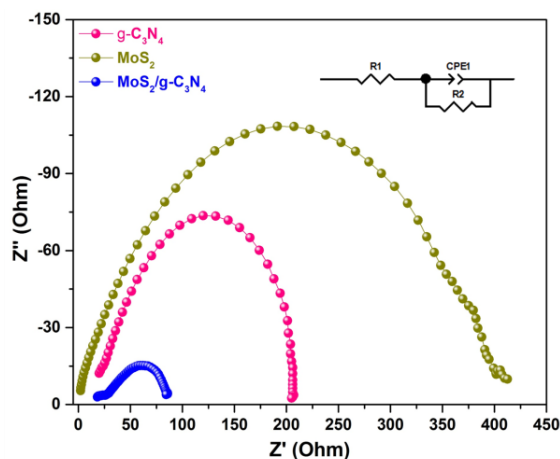
Figure 6.17 Nyquist plots of MoS$_2$, g-C$_3$N$_4$ and MoS$_2$/g-C$_3$N$_4$. Inset shows equivalent circuit used to fit the Nyquist plot

Table 6.4 Values of solution resistance (R$_1$) and charge transfer resistance (R$_2$) for both MoS$_2$/g-C$_3$N$_4$ and MoS$_2$ from Nyquist plots

Cathode	R$_1$(Ω)	R$_2$ (Ω)
MoS$_2$	2.03	410.47
MoS$_2$/g-C$_3$N$_4$	18.19	66.19

6.3.2.6 Role of the Support

To study the role of g-C$_3$N$_4$ surface, MoS$_2$ microstructures have been synthesized on multi-walled carbon nanotube (CNT) and mesoporous carbon nanopowder (C) substrates. The electrocatalytic activity of MoS$_2$/CNT and MoS$_2$/C have been compared with MoS$_2$/g-C$_3$N$_4$ heterostructure. For the synthesis of MoS$_2$/CNT and MoS$_2$/C, similar experimental procedure, which was used for MoS$_2$/g-C$_3$N$_4$ was followed. The formation of MoS$_2$ on the surface of CNT and carbon was confirmed by X-ray diffraction patterns shown in **Figure 6.18.a**. The crystal planes (002), (100), (103), and (110) corresponding to MoS$_2$ are present in the XRD patterns of both MoS$_2$/CNT and MoS$_2$/C, respectively. Potential required to generate 10 mA/cm^2 current

density in MoS_2/CNT and MoS_2/C is −0.28 and −0.32 V vs. RHE, respectively (**Figure 6.18.b**), which is higher than the $MoS_2/g-C_3N_4$ (−0.26 V).

Therefore, it can be confirmed that MoS_2 microstructure on both $g-C_3N_4$ and CNT substrates is comparable for HER. The advantages of $g-C_3N_4$ substrate are multifold. First, the electrocatalytic activity of $MoS_2/g-C_3N_4$ is related to the flake like topography of MoS_2 on $g-C_3N_4$ surface. The flake like structure has more exposed surface area, which is helpful for HER reaction. Flake like morphology of $MoS_2/g-C_3N_4$ heterostructure have been confirmed by FESEM and TEM analysis. Second, the intimate contact between MoS_2 and $g-C_3N_4$ is pronounced, which allows the ease of electronic transportation between the materials. Therefore, the improvement in the charge transfer may be due to the ready penetration of the electrolyte in the porous structure of $g-C_3N_4$ which gets saturated with time [9,12]. Third, the chemisorption and dissociation of hydrogen molecules on catalyst surface also play an important role. The dissociated H atoms migrate to the support through surface diffusion, called spillover effect of hydrogen [9]. The spillover effect is increased due to the formation of N-H bonds between pyridinic and graphitic N atoms of $g-C_3N_4$ and dissociated H atom. Therefore, a better quantity of hydrogen can be accumulated on $MoS_2/g-C_3N_4$ surface, which also supports the improved activity of $g-C_3N_4$ substrate [9-12,20].

Literatures also reports for the poor conductivity of pristine carbon nitride due to the high nitrogen doping intensity and abundance of defects. In our present study, MoS_2 is synthesized on $g-C_3N_4$ substrate at 180 °C for 24 h hydrothermal reaction. Therefore, to check the transfer behavior and the carrier mobility, impedance study was carried out for bare $g-C_3N_4$ at the onset potential of (−0.68 V vs. RHE). From the impedance result it is clear that R_2 value i.e., the charge transfer resistance of $g-C_3N_4$ is lower than that of MoS_2 (**Figure 6.17**). So, it can be claimed that $g-C_3N_4$ itself helps to decrease the charge transfer resistance in the heterostructure which results in higher current density with improved onset potential.
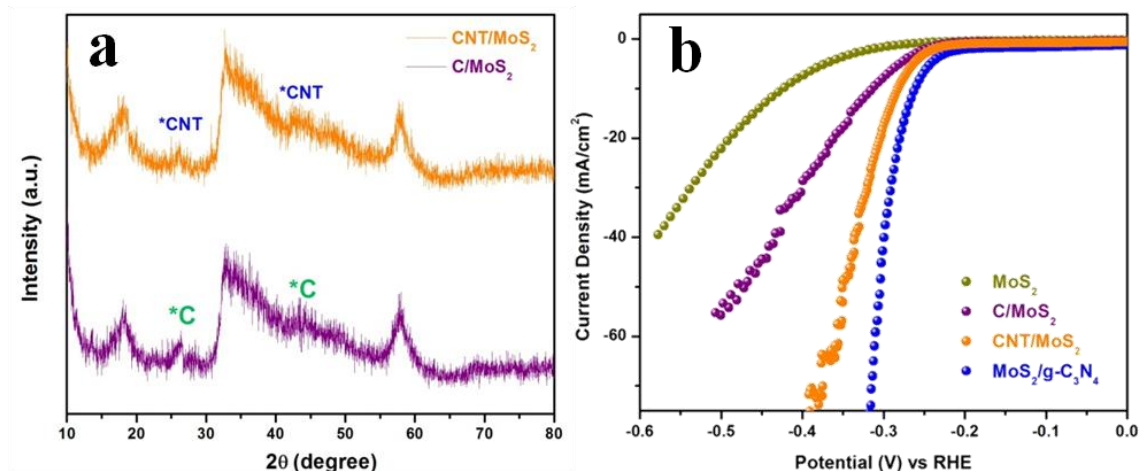
Figure 6.18 (a) PXRD pattern of MoS$_2$/CNT and MoS$_2$/C at 2° per min scanning rate, (b) Polarization curve for MoS$_2$, MoS$_2$/g-C$_3$N$_4$, MoS$_2$/CNT, MoS$_2$/C (iR free) [CNT= Fullerene carbon nanotube multi-walled, C= Mesoporous carbon powder]

6.3.3 Photocatalytic Study using g-C$_3$N$_4$ and MoS$_2$/g-C$_3$N$_4$ Catalyst

To assess the photocatalytic performance of the as-prepared catalyst, RhB dye was degraded under irradiation of visible light. Prior to photoirradiation to establish the adsorption-desorption equilibrium between dye and catalyst, 10^{-5} M RhB and 5.0 mg catalyst were kept in dark for 30 min. Subsequently, the suspension was irradiated under visible light source (Tungsten lamp, 60 W). The reaction mixture was magnetically stirred throughout the experiment. At the given irradiation time, 2.0 mL sample was collected and centrifuged to remove the catalyst. The degradation efficiency of RhB dye was recorded on a UV-visible spectrophotometer.

RhB dye has absorbance maxima at 553 nm and decreased with time when degraded in presence of catalyst. Before irradiation, the reaction has been continued in the dark condition, where 75 % RhB was adsorbed on the catalyst surface in case of MoS$_2$/g-C$_3$N$_4$ and 12% in bare g-C$_3$N$_4$. Once the adsorption process over then the reaction has been illuminated with a tungsten bulb ($\lambda > 300$ nm). The dye adsorbed on the catalyst surface as well as dye present in the solution degraded with time and solution becomes colorless from pink.
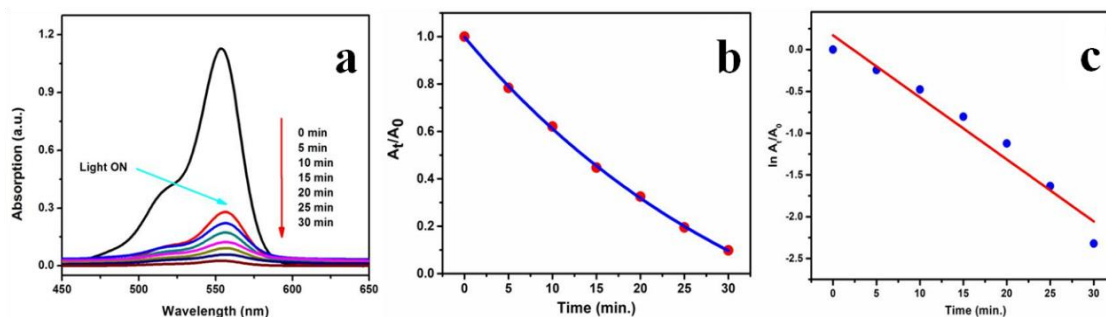
Figure 6.19 Plot of (a) absorbance vs. wavelength, (b) (A_t/A_0) vs. time, and (c) ln(A_t/A_0) vs. time for photocatalytic decomposition of RhB dye using MoS$_2$/g-C$_3$N$_4$ heterostructure. Conditions: [RhB] = 10^{-5} M and catalyst = 5.0 mg

The MoS$_2$/g-C$_3$N$_4$ heterostructure improved photoactivity and degraded 91 % dye within 30 min of light irradiation, shown in **Figure 6.19.a**. Whereas, under the similar experimental condition, bare g-C$_3$N$_4$ undergo 54 % dye degradation (**Figure 6.20.a**). Therefore, MoS$_2$/g-C$_3$N$_4$ demonstrated 3.3 times higher photocatalytic performance than bare g-C$_3$N$_4$. The plot of (A_t/A_0) *vs.* t (**Figure 6.19.b**.) shows the exponential decay in case of MoS$_2$/g-C$_3$N$_4$. From the plot of ln (A_t/A_0) *vs.* t, the value of the rate constant '*k*' was determined and the value is 7.4×10^{-2} min^{-1} shown in **Figure 6.19.c**. The (A_t/A_0) *vs.* t and ln(A_t/A_0) *vs.* t plot for pure g-C$_3$N$_4$ shown in **Figure 6.19.b** and **c** and the rate constant was calculated to be 2.2×10^{-2} min^{-1}. Therefore, the rate constant order is MoS$_2$/g-C$_3$N$_4$ > g-C$_3$N$_4$. The straight line in ln(A_t/A_0) *vs.* t shows that the degradation reaction follows pseudo-first order kinetics.
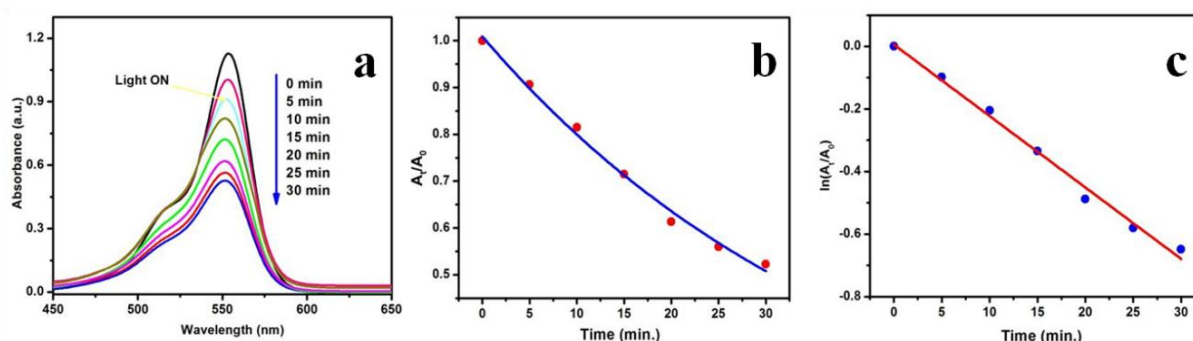
Figure 6.20 UV-vis absorption spectra of (a) RhB degradation where g-C$_3$N$_4$ is the catalyst, (b) A_t/A_0 *vs*. time (min) plot and (c) ln(A_t/A_0) *vs*. time (min) plot

The comparative photocatalytic activity has been shown in **Figure 6.21**, which indicates improved activity of MoS$_2$/g-C$_3$N$_4$. This higher degradation efficiency in case of MoS$_2$/g-C$_3$N$_4$ is attributed to the stronger visible light absorption, easy transportation of photogenerated species between material interface, and separation of photoinduced e$^-$-h$^+$ pairs than bare g-C$_3$N$_4$ [4,6,16].
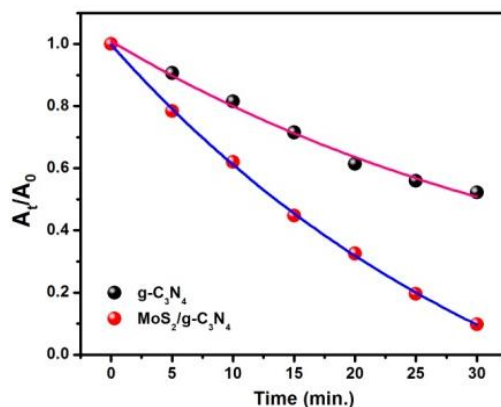
Figure 6.21 Comparative study of photodegradation using both MoS$_2$/g-C$_3$N$_4$ and g-C$_3$N$_4$

6.3.3.1 Mechanism of Photocatalysis

The MoS$_2$/g-C$_3$N$_4$ heterostructure is illustrated in **Scheme 6.2** to gain more insight into migration and flow of charge carriers at the heterojunction interface during photocatalysis reaction. The redox capacity of a semiconductor during photodegradation reaction is evaluated by the positions of conduction and valence band. The band edge potentials of VB and CB of g-C$_3$N$_4$ were calculated according to the following equations [20]:

$$E_{VB} = \chi - E_e + 0.5E_g$$
$$E_{CB} = E_{VB} - E_g$$

Where χ is the absolute electronegativity of the semiconductor. The χ values for g-C$_3$N$_4$ is 4.73 [30,33]. E_e is the energy of free electron on the hydrogen scale (4.5 eV). E_g is the band gap of the semiconductor. The calculated band gap for g-C$_3$N$_4$ is 2.87 eV which indicates the visible light activity of the g-C$_3$N$_4$. On the basis of above equations, the band edge positions of

CB and VB of g-C$_3$N$_4$ are -1.21 and 1.66 eV, respectively, versus the normal hydrogen electrode (NHE). Under visible light irradiation electron and hole, pairs are generated in g-C$_3$N$_4$ [4,6,20]. However, the enhanced photocatalytic activity in MoS$_2$/g-C$_3$N$_4$ heterostructure may be attributed to the successful formation of the intimate contact between g-C$_3$N$_4$ and MoS$_2$, which lead to improved charge separation as compared to bare g-C$_3$N$_4$.

Upon irradiation, with light, the electrons get excited from the VB of g-C$_3$N$_4$ [4,16,33]. The excited electrons on g-C$_3$N$_4$ undergo vectorial transfer to MoS$_2$. Wang and co-workers reported the band alignment in MoS$_2$/g-C$_3$N$_4$ heterostructure, which promotes the effective separation of charge carriers and a built-in polarized field between g-C$_3$N$_4$ and MoS$_2$ might suppress the recombination of electron-hole [31,46].
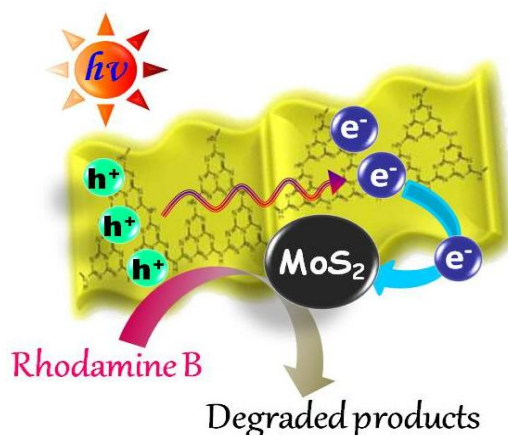
Scheme 6.2 Schematic representation of the photocatalysis in MoS$_2$/g-C$_3$N$_4$ under irradiation of visible light

In this study, higher activity of MoS$_2$/g-C$_3$N$_4$ heterostructure than g-C$_3$N$_4$ shows that band alignment is the dominant factor to promote the separation of photogenerated species [19,39,49]. The restricted recombination provides an excess availability of electrons at MoS$_2$ and holes at VB of g-C$_3$N$_4$ endorsed the reductive and oxidative reactions for the dye degradation. It is already mentioned in several reports that hydroxyl radicals ($^{\cdot}$OH) are mainly responsible for the degradation of dyes [4,16,46]. The electrons of CBs have been used for the formation of $^{\cdot}$OH which further degrade the RhB dye and generate the decomposed products. Simultaneously, the accumulated holes at the VB of g-C$_3$N$_4$ would degrade the RhB dye generating $^{\cdot}$OH radical species [6,16]. The degradation steps are as follows:

$$MoS_2/g - C_3N_4 + hv \rightarrow (e^-_{CB} + h^+_{VB})$$

$$e^-_{CB} + O_2 \rightarrow O_2^{-\cdot}$$

$$O_2^{-\cdot} + 2H^+ \rightarrow 2OH^{\cdot}$$

$$h^+_{VB} + OH^- \rightarrow OH^{\cdot}$$

$$^{\cdot}OH + RhB\ dye \rightarrow Decomposed\ Products$$
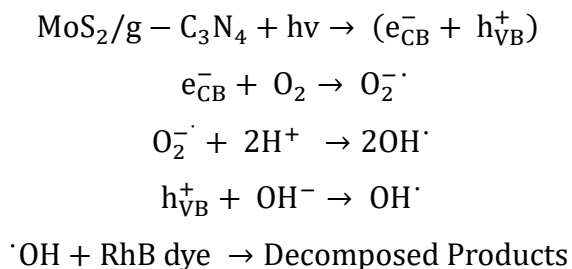
6.4 Conclusions

MoS_2/g-C_3N_4 has been successfully synthesized by decorating MoS_2 on the g-C_3N_4 surface via a facile and inexpensive hydrothermal route. The structure and morphology of as-prepared MoS_2/g-C_3N_4 have been examined by PXRD, RAMAN, UV-vis, FESEM, HRTEM, and XPS techniques. To check the catalytic activity, all the samples have been utilized for electrocatalytic hydrogen evolution reaction and in the photodegradation of RhB dye. The MoS_2/g-C_3N_4 showed higher electrocatalytic behavior than bare MoS_2 with remarkable stability. The morphology of MoS_2/g-C_3N_4 has been unaltered after electrocatalysis. MoS_2/g-C_3N_4 requires -0.26 V vs. RHE potential for the successful generation of 10 mA/cm^2 current density. In addition, heterostructured photocatalyst exhibited enhanced activity than bare g-C_3N_4 towards degradation of RhB dye. The morphology of MoS_2/g-C_3N_4 heterostructure enclosed with more exposed edges and increased active sites leads to the superior catalytic activity. ECSA and BET results support the observed current density for both MoS_2 and MoS_2/g-C_3N_4. This work expands our vision for the designing of proficient and sun-light driven electrocatalyst for production of H$_2$ from water splitting.

References

[1]   Turner, J. A. A Realizable Renewable Energy Future. *Science* **1999**, *285*, 687-689.

[2]   Dresselhaus, M. S.; Thomas, I.L. Alternative Energy Technologies. *Nature* **2001**, *414*, 332-337.

[3]   Anantharaj, S.; Ede, S. R.; Sakthikumar, K.; Karthick, K.; Mishra, S.; Kundu, S. Recent Trends and Perspectives in Electrochemical, Electrochemical Water Splitting with an Emphasis on Sulfide, Selenide, and Phosphide catalysts of Fe, Co, and Ni: A Review. *ACS Catal.* **2016**, *6*, 8069-8097.

[4]   Ansari, S. A.; Cho, M. H. Simple and Large Scale Construction of MoS_2-g-C_3N_4 Heterostructures Using Mechanochemistry for High Performance Electrochemical Supercapacitor and Visible Light Photocatalytic Applications. *Sci. Rep.* **2017**, *7*, 43055.

[5]   Basu, M.; Nazir, R.; Fageria, P.; Pande, S. Construction of CuS/Au Heterostructure Through a Simple Photoreduction Route for Enhanced Electrochemical Hydrogen Evolution and Photocatalysis. *Sci. Rep.* **2016**, *6*, 34738.

[6]   Lu, D.; Wang, H.; Zhao, X.; Kondamareddy, K. K.; Ding, J.; Li, C.; Fang, P. Highly Efficient Visible-Light-Induced Photoactivity of Z-Scheme g-C_3N_4/Ag/MoS_2 Ternary Photocatalysts for Organic Pollutant Degradation and Production of Hydrogen. *ACS Sustainable Chem. Eng.* **2017**, *5*, 1436-1445.

[7]   Zhao, Z.; Sun, Y.; Dong, F. Graphitic Carbon Nitride based Nanocomposites: A Review. *Nanoscale* **2015**, *7*, 15-37.

[8]   Zheng, Y.; Jiao, Y.; Zhu, Y.; Li, L. H.; Han, Y.; Chen, Y.; Du, A.; Jaroniec, M.; Qiao, S. Z. Hydrogen Evolution by a Metal-Free Electrocatalysts. *Nat. Commun.* **2014**, *5*, 3783.

[9]   Bhowmik, T.; Kundu, M. K.; Barman, S. Palladium Nanoparticles-Graphitic Carbon Nitride Porous Synergistic Catalyst for Hydrogen Evolution/Oxidation Reactions over a Broad Range of pH and Correlation of its Catalytic Activity with Measured Hydrogen Binding Energy. *ACS Catal.* **2016**, *6*, 1929-1941.

[10]   Bai, S.; Wang, X.; Hu, C.; Xie, M.; Jiang, J.; Xiong, Y. Two-Dimensional g-C_3N_4: An Ideal Platform for Examining Facet Selectivity of Metal Co-catalysts in Photocatalysis. *Chem. Commun.* **2014**, *50*, 6094-6097.

[11]   Wen, J.; Xie, J.; Chen, X.; Li, X. A Review on g-C$_3$N$_4$-Based Photocatalysts. *Appl. Surf. Sci.* **2017**, *391*, 72-123.

[12]   Nazir, R.; Fageria, P.; Basu, M.; Pande, S. Decoration of Carbon Nitride Surface with Bimetallic Nanoparticles (Ag/Pt, Ag/Pd, and Ag/Au) via Galvanic Exchange for Hydrogen Evolution Reaction. *J. Phys. Chem. C* **2017**, *121*, 19548-19558.

[13]   Ye, L.; Wang, D.; Chen, S. Fabrication and Enhanced Photoelectrochemical Performance of MoS$_2$/S-Doped g-C$_3$N$_4$ Heterojunction Film. *ACS Appl. Mater. Interfaces* **2016**, *8*, 5280-5289.

[14]   Dong, H.; Liu, C.; Ye, H.; Hu, L.; Fugetsu, B.; Dai, W.; Cao, Y.; Qi, X.; Lu, H.; Zhang, X. Three-Dimensional Nitrogen-Doped Graphene Supported Molybdenum Disulfide Nanoparticles as an Advanced Catalyst for Hydrogen Evolution Reaction. *Sci. Rep.* **2015**, *5*, 17542.

[15]   Pramoda, K.; Gupta, U.; Chhetri, M.; Bandyopadhyay, A.; Pati, S.K.; Rao, C.N.R. Nanocomposites of C$_3$N$_4$ with Layers of MoS$_2$ and Nitrogenated RGO, Obtained by Covalent Cross-linking: Synthesis, Characterization, and HER Activity. *ACS Appl. Mater. Interfaces* **2017**, *9*, 10664-10672.

[16]   Li, Q.; Zhang, N.; Yang, Y.; Wang, G.; Ng, D.H. High Efficiency Photocatalysis for Pollutant Degradation with MoS$_2$/C$_3$N$_4$ Heterostructures. *Langmuir* **2014**, *30*, 8965-8972.

[17]   Yang, L.; Zhou, W.; Hou, D.; Zhou, K.; Li, G.; Tang, Z.; Li, L.; Chen, S. Porous Metallic MoO$_2$-Supported MoS$_2$ Nanosheets for Enhanced Electrolytic Activity in Hydrogen Evolution Reaction. Nanoscale **2015**, *7*, 5203-5208.

[18]   Tian, Y.; Ge, L.; Wang, K.; Chai, Y. Synthesis of Novel MoS$_2$/g-C$_3$N$_4$ Heterojunction Photocatalysts with Enhanced Hydrogen Evolution Activity. *Mater. Charact.* **2014**, *87*, 70-73.

[19]   Ge, L.; Han, C.; Xiao, X.; Guo, L. Synthesis and Characterization of Composite Visible Light Active Photocatalysts MoS$_2$-g-C$_3$N$_4$ with Enhanced Hydrogen Evolution Activity. *Int. J. Hydrogen Energy* **2013**, *38*, 6960-6969.

[20]   Fageria, P.; Nazir, R.; Gangopadhyay, S.; Barshilia, H. C.; Pande, S. Graphitic-Carbon Nitride Support for the Synthesis of Shape-Dependent ZnO and their Application in Visible Light Photocatalysts. *RSC Adv.* **2015**, *5*, 80397-80409.

[21]   Zhang, G.; Lan, Z. A.; Wang, X. Conjugated Polymers: Catalysts for Photocatalytic

Hydrogen Evolution. *Angew. Chem. Int. Ed.* **2016**, *55*, 15712-15727.

[22]   Zhang, J.; Chen, Y.; Wang, X. Two-Dimensional Covalent Carbon Nitride Nanosheets: Synthesis, Functionalization, and Applications. *Energy Environ. Sci.* **2015**, *8*, 3092-3108.

[23]   Zheng, Y.; Lin, L.; Wang, B.; Wang, X. Graphitic Carbon Nitride Polymers Toward Sustainable Photoredox Catalysis. *Angew. Chem. Int. Ed.* **2015**, *54*, 12868-12884.

[24]   Wang, X.; Maeda, K.; Thomas, A.; Takanabe, K.; Xin, G.; Carlsson, J.M.; Domen, K.; Antonietti, M. A Metal-Free Polymeric Photocatalyst for Hydrogen Production from Water Under Visible Light. *Nat. Mater.* **2009**, *8*, 76-80.

[25]   Zhang, G.; Lan, Z. A.; Wang, X. Surface Engineering of Graphitic Carbon Nitride Polymers with Cocatalysts for Photocatalytic Overall Water Splitting. *Chem. Sci.* **2017**, *8*, 5261-5174.

[26]   Zhang, G.; Zang, S.; Lin, L.; Lan, Z. A.; Li, G.; Wang, X. Ultrafine Cobalt Catalysts on Covalent Carbon Nitride Frameworks for Oxygenic Photosynthesis. *ACS Appl. Mater. Interfaces* **2016**, *8*, 2287-2296.

[27]   Zhang, G.; Zang, S.; Lan, Z. A.; Huang, C.; Li, G.; Wang, X. Cobalt Selenide: A Versatile Cocatalyst for Photocatalytic Water Oxidation with Visible Light. *J. Mater. Chem. A* **2015**, *3*, 17946-17950.

[28]   Basu, M.; Nazir, R.; Mahala, C.; Fageria, P.; Chaudhary, S.; Gangopadhyay, S.; Pande, S. Ag_2S/Ag Heterostructure: A Promising Electrocatalyst for the Hydrogen Evolution Reaction. *Langmuir* **2017**, *33*, 3178-3186.

[29]   Shi, H.; Zhao, G. Water Oxidation on Spinel $NiCo_2O_4$ Nanoneedles Anode: Microstructures, Specific Surface Character, and the Enhanced Electrocatalytic Performance. *J. Phys. Chem. C* **2014**, *118*, 25939-25946.

[30]   Zhang, X.; Ding, P.; Sun, Y.; Wang, Y.; Li, J.; Guo, J. MoS_2 Nanosheets on C_3N_4 Realizing improved Electrochemical Hydrogen Evolution. *Mater. Lett.* **2017**, *197*, 41-44.

[31]   Zhao, H.; Dong, Y.; Jiang, P.; Miao, H.; Wang, G.; Zhang, J. In Situ Light-Assisted Preparation of MoS_2 on Graphitic C_3N_4 Nanosheets for Enhanced Photocatalytic H_2 Production from Water. *J. Mater. Chem. A* **2015**, *3*, 7375-7381.

[32]   Gao, M.; Sheng, W.; Zhuang, Z.; Fang, Q.; Gu, S.; Jiang, J.; Yan, Y. Efficient Water Oxidation using Nanostructured α-Nickel- Hydroxide as an Electrocatalyst. *J. Am. Chem. Soc.* **2014**, *136*, 7077-7084.

[33]   Zheng, D.; Zhang, G.; Hou, Y.; Wang, X. Layering MoS$_2$ on Soft Hollow g-C$_3$N$_4$ Nanostructures for Photocatalytic Hydrogen Evolution. *Appl. Catal. A-General* **2016**, *52*, 2-8.

[34]   Hou, Y.; Laursen, A.B.; Zhang, J.; Zhang, G.; Zhu, Y.; Wang, X.; Dahl, S.; Chorkendorff, I. Layered Nano Junctions for Hydrogen-Evolution Catalysis. *Angew. Chem. Int. Ed.* **2013**, *52*, 3621-3625.

[35]   Hu, W.-H.; Han, G.-Q.; Liu, Y.-R.; Dong, B.; Chai, Y.-M.; Liu, Y.-Q.; Liu, C.-G. Ultrathin MoS$_2$-Coated Carbon Nanospheres as Highly Efficient Electrocatalyts for Hydrogen Evolution Reaction. *Int. J. Hydrog. Energy* **2015**, *40*, 6552-9558.

[36]   Shang, X.; Hu, W.-H.; Li, X.; Dong, B.; Liu, Y.-R., Han, G.-Q.; Chai, Y.-M.; Liu, C.-G. Oriented Stacking Along Vertical (002) Planes of MoS$_2$: A Novel Assembling Style to Enhance Activity for Hydrogen Evolution. *Electrochim. Acta* **2017**, *224*, 25-31.

[37]   Hu, W.-H.; Han, G.-Q.; Dai, F.-N.; Liu, Y.-R.; Shang, X.; Dong, B.; Chai, Y.-M.; Liu, Y.-Q.; Liu, C.-G. Effect of pH on the Growth of MoS$_2$ (002) Plane and Electrocatalytic Activity for HER. *Int. J. Hydrog. Energy* **2016**, *41*, 294-299.

[38]   Dominique, D.; Ste´phane, B.; Le´vy-Cle´ment, C. Chemical Synthesis of Molybdenum Disulfide Nanoparticles in an Organic Solution. *J. Mater. Chem.* **2002**, *12*, 2430-2432.

[39]   Yan, J.; Chen, Z.; Ji, H.; Liu, Z.; Wang, X.; Xu, Y.; She, X.; Huang, L.; Xu, L.; Xu, H.; Li, H. Construction of a 2D Graphene-like MoS$_2$/C$_3$N$_4$ Heterojunction with Enhanced Visible-Light Photocatalytic Activity and Photoelectrochemical Activity. *Chem. Eur. J.* **2016**, *22*, 4764-4773.

[40]   Dou, S.; Wu, J.; Tao, L.; Shen, A.; Huo, J.; Wang, S. Carbon-Coated MoS$_2$ Nanosheets as Highly Efficient Electrocatalysts for the Hydrogen Evolution Reaction. *Nanotechnol.* **2016**, *27*, 045402.

[41]   Lin, Y. C.; Zhang, W.; Huang, J. K.; Liu, K. K.; Lee, Y. H.; Liang, C. T.; Chu, C. W.; Li, L. J. Wafer-Scale MoS$_2$ Thin Layers Prepared by MoO$_3$ Sulfurization. *Nanoscale* **2012**, *4*, 6637-6641.

[42]   Wang, X.; Hong, M.; Zhang, F.; Zhuang, Z.; Yu, Y. Recyclable Nanoscale Zero Valent Iron Doped g-C$_3$N$_4$/MoS$_2$ for Efficient Photocatalysis of RhB and Cr (VI) Driven by Visible Light. *ACS Sustainable Chem. Eng.* **2016**, *4*, 4055-4063.

[43]   Vrubel, H.; Moehl, T.; Gratzel, M.; Hu, X. Revealing and Accelerating Slow Electron

Transport in Amorphous Molybdenum Sulphide Particles for Hydrogen Evolution Reaction. *Chem. Commun.* **2013**, *49*, 8985-8987.

[44]   Cao, Y.; Li, Q.; Wang, W. Construction of a Crossed-Layer-Structure MoS_2/g-C_3N_4 Heterojunction with Enhanced Photocatalytic Performance. *RSC Adv.* **2017**, *7*, 6131-6139.

[45]   Wang, J.; Guan, Z.; Huang, J.; Li, Q.; Yang, J. Enhanced Photocatalytic Mechanism for the Hybrid g-C_3N_4/MoS_2 Nanocomposite. *J. Mater. Chem. A* **2014**, *2*, 7960-7966.

[46]   Guo, J.; Zhu, H.; Sun, Y.; Tang, L.; Zhang, X. Doping MoS_2 with Graphene Quantum Dots: Structural and Electrical Engineering Towards Enhanced Electrochemical Hydrogen Evolution. *Electrochim. Acta* **2016**, *212*, 603-610.

[47]   Xie, J.; Zhang, J.; Li, S.; Grote, F.; Zhang, X.; Zhang, H.; Wang, R.; Lei, Y.; Pan, B.; Xie, Y. Controllable Disorder Engineering in Oxygen-Incorporated MoS_2 Ultrathin Nanosheets for Efficient Hydrogen Evolution. *J. Am. Chem. Soc.* **2013**, *135*, 17881-17888.

[48]   Guo, X.; Cao, G.L.; Ding, F.; Li, X.; Zhen, S.; Xue, Y.F.; Yan, Y.M.; Liu, T.; Sun, K.N. A Bulky and Flexible Electrocatalyst for Efficient Hydrogen Evolution Based on the Growth of MoS_2 Nanoparticles on Carbon Nanofiber Foam**. *J. Mater. Chem. A* **2015,** *3*, 5041-5046.

[49]   Shi, L.; Ding, W.; Yang, S.; He, Z.; Liu S. Rationally Designed MoS_2/protonated g-C_3N_4 Nanosheet Composites as Photocatalysts with an Excellent Synergistic Effect Toward Photocatalytic Degradation of Organic Pollutants. *J. Hazard. Mater.* **2018,** *347*, 431-441.

Synthesis of ZnO/ZnS Hollow Nanostructure via Kirkendall Effect for Adsorptive Dye Removal

✿ *In this chapter wet chemical synthesis of ZnO/ZnS hollow structure has been reported via Kirkendall effect.*

✿ *The as-synthesized hollow structure has been used for the removal of dyes from waste water.*

ZnO nanorods

Kirkendall

Dyes

Removal

ZnO/ZnS hollow structure
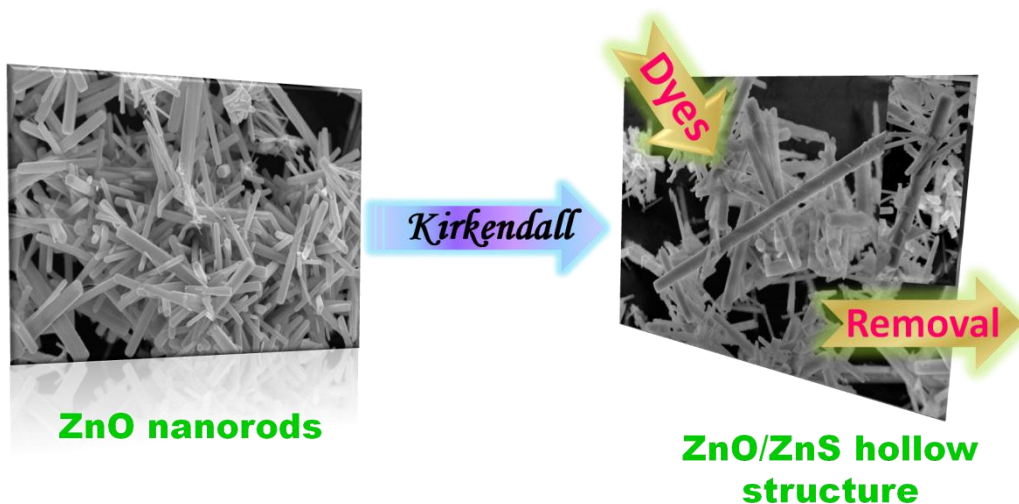
Abstract

The search of proficient semiconductor catalysts for pollutants removal from contaminated water is one of the interesting areas of research, due to the growing concern about environmental issues. Nanomaterials with hollow interior represent a class of significant materials that exhibit variety of applications in catalysis due to their large surface area. Synthesis via Kirkendall effect is a promising approach for hollow nanostructures and it occurs due to the difference in the diffusion rates of two materials. Here, we have introduced the wet chemical synthesis of hollow nanostructure of ZnO/ZnS via Kirkendall effect using ZnO nanorods wherein ZnO, ZnS and ZnO/ZnS nanostructures have been synthesized in the reflux conditions. The surface morphologies, optical characteristics, elemental compositions, and crystal structures of the as synthesized materials are systematically studied using FESEM, TEM, UV-vis, EDS, PXRD and XPS etc. A detailed growth mechanism of hollow ZnO/ZnS hollow structure is proposed based on the Kirkendall effect. A hollow nanomaterial, envisaged being highly efficient for molecule adsorption on its surface, which has been utilized for the removal of textile dyes from the waste water using methylene blue, rhodamine B and malachite green dyes.

7.1 Introduction

The earth's most valuable and essential natural resource, water, is in danger as its consumption has been increased to multifold with the population growth. Simultaneously, due to the excess release of contaminants in water, this is a serious threat to the environment as well as for the human. Semiconductor nanomaterials are popular and have the great potential to degrade and remove the pollutants from water. Semiconductor nanomaterials are the subject of intense research in the present scenario. According to their electronic properties, they are the intermediate molecular species and macro entities. Numerous shaped semiconductor nanostructures like nanowires, nanorods, and nanoribbons have fascinated the attention owing to higher surface to volume ratio and quantum confinement [1-5]. The use of ZnO as a semiconductor photocatalyst has gained special interest due to its high electron mobility and stability [2,5-12]. ZnO nanomaterials exhibit vast functionality in the catalysis due to a high surface area and photosensitivity but wide band gap (3.37 eV) renders its activity exclusively under visible light [5-9]. The easy recombination of photogenerated charge carriers limits the utilization of pure ZnO for photocatalytic applications [5,12,13]. Recently, ZnS has been utilized extensively in solar cells, sensors, and photocatalysis because of its tunable size, optical, and electronic properties [6-9]. However, it should be noted that, although ZnO and ZnS have been widely studied, but never established as an effective photocatalyst because of its restricted light-harvesting property and their resistance to photo-corrosion [2,3,5-12].

To date, heterostructures consisting of two important semiconductor materials have drawn increasing awareness because of their tunable electronic and optical properties [11-16]. Hence, there is a significant progress for the synthesis of various heterostructure including Ag_2S-ZnS [15], g-C_3N_4/ZnO [10], ZnO/ZnTe [16], and ZnO/CuS [12] for a variety of applications. Notably, amongst various semiconductor heterostructure, ZnO/ZnS is considered to be the most promising as it possesses excellent optoelectronic properties [3,6-9,17-18]. The band structure of ZnO and ZnS is favorable to facilitate the electron transfer process and creates the semiconductor heterostructure. It is also studied from the theoretical calculations that ZnO and ZnS can form a coupled heterostructure having lesser photoexcitation threshold energy than the individual materials [14,16-17]. Moreover, coupled semiconductors are considered to be superior photocatalysts than bare materials owing to charge separation efficiency, less carrier

recombination along with improving visible light absorption by the formation of interface contact potentials [15-17].

Currently, intense research has been devoted in the direction of design and fabrication of hollow structures with specific morphologies [19-20]. Hollow nanomaterials acquire the distinctive properties of special hollow geometrical shapes, small density, larger specific surface area, and porous nature [21]. These materials have gained considerable interest due to their widespread applications in solar cells, catalysis, sensors, drug delivery, nanoscale chemical reactors, and energy storage medium [19-22]. There are a variety of methods presently utilized to design a large range of stable, hollow spheres of different compositions [20-24]. So far, spherical hollow structures have been synthesized by utilizing only template-assisted method [20-23]. The etching of the template requires enormously complex synthetic procedures which not only increases the production cost and but also influences the purity of the samples [19-23]. Therefore, it is highly desirable to fabricate a facile, economical and adaptable synthetic strategy to synthesize semiconductor hollow nanomaterials.

Over the past decade, it has been known that formation of hollow structure may result from differential solid-state diffusion of the reactants in an oxidation reaction [21-24]. This phenomenon was studied by Kirkendall in 1947 and recently a variety of hollow nanostructures has been synthesized using the same effect [19,21-26]. In the Kirkendall effect, the diffusion rate differ by a considerable amount for the two different component and it leads to the void formation inside the structure [19,21]. Shen *et al.* reported the synthesis of ZnO/ZnS core/shell nanorods and nanotubes of other metal sulfides including ZnS, Ag_2S, CuS, PbS, and Bi_2S_3 *via* sulfidation exchange and the Kirkendall effect [17]. The Reported study revealed that ZnO nanowire, ZnO/ZnS core/shell nanorod, and metal sulfide nanotube can be effectively synthesized with almost 100 % morphological yield and having a wide range of applications [17]. Synthesis of ZnO nanotube using ZnO nanowires and nanotubes of other metal oxides and chalcogenides ($ZnCr_2O_4$, Co_3O_4, ZnS, CdS and CdSe) using their elemental nanowires via Kirkendall effect were explained by C. N. R. Rao *et al*. [25] Kirkendall effect was also reported for the synthesis of ZnS hollow nanoneedles at a low-temperature hydrothermal route with lower symmetry structures by Wang *et al*. [26] Alivisatos *et al.* prepared Cd/CdSe core-shell nanoparticles via the Kirkendall effect and explained various reaction conditions for this synthesis [27].

It is obvious that adsorbents with high surface area play an essential role in the catalytic reactions. The consumption of dyes in textile industries is increasing incessantly which is a severe concern for the environment due to the toxic nature of the dyes [28-32]. The dyes are released in the water after its utilization which pollutes the water leading to a serious hazard. Therefore, recently, the removal of dyes from contaminated water using an efficient catalyst is an active area of research. Various physical, chemical, and biological methods have been studied previously to purify the contaminated water [30-32]. Amongst all, removal of dyes by physical adsorption technologies is a remarkable method because of its high effectiveness, economic viability and facile synthesis [30-33]. Thus, for dye removal, it is desirable to explore new adsorbents with high adsorption capacity.

In this chapter, we have demonstrated the successful synthesis of ZnO/ZnS hollow nanorods (NRs) using ZnO nanorods via Kirkendall approach. Sodium sulfide has been used as a source for sulphidation. The optical, structural, elemental and systematic morphological characterizations were performed for all the synthesized materials using UV-vis, PXRD, FESEM, HRTEM, XPS, EDS, SAED techniques. The structure of the ZnO nanorods, ZnS NPs and hollow ZnO/ZnS structures are studied extensively and a growth mechanism for hollow morphology via Kirkendall effect is proposed. Hollow ZnO/ZnS nanostructures have been used as an effective adsorbent for methylene blue, rhodamine B, and malachite green dyes. The advantages of this hollow nanostructure study are multifold. First, ZnO and ZnS are inexpensive semiconductors with high band gap energy which fulfilling the requirement band edge potential for the semiconductor type-II structure (**Figure 1.10**). Second, hollow structures allow an enhanced surface area for the adsorptive catalysis reactions. Third, hollow morphology is a favorable morphology to recover and recycle the catalyst after utilization.

7.2 Experimental Section

7.2.1 Synthesis of ZnO Nanorods

ZnO nanorods were synthesized using zinc nitrate $Zn(NO_3)_2$, hexamethylenetetramine (HMT) and cetyltrimethyl ammonium bromide (CTAB) by following procedure. Initially, in a 100 mL round bottom flask equal volume (5 mL) of zinc nitrate (0.1 M), HMT (0.1 M) and

CTAB (0.5 M) solutions were dissolved in 35 mL water. The final concentration of $Zn(NO_3)_2$, HMT, and CTAB were 0.01 M, 0.01 M and 0.05 M, respectively. The pH of the solution was alkaline (pH ~ 7.5). After that the solution was agitated well on a stirrer for 30 min. Subsequently, the whole solution was kept at ~ 90 °C for 4 h in reflux condition without stirring during which the ZnO nanorods were formed and settled down in the bottom. The resulting white powder was collected and washed with ethanol and finally air dried in oven.

7.2.2 Synthesis of ZnS

ZnS NPs were synthesized by the similar approach depicted for ZnO NPs. Additionally, sodium sulfide (Na_2S) was added for sulphidation process. 5.0 mL of Zinc nitrate (0.1 M), HMT (0.1 M), Na_2S (0.5 M), and CTAB (0.5 M) solutions were added in 30 mL water. Final concentration of $Zn(NO_3)_2$ and HMT was 0.01 M and Na_2S and CTAB was 0.05 M. The reaction mixture was stirred constantly for 30 min and followed by reflux at ~ 90 °C for 4 h without stirring. Finally, white color ZnS powder was collected and impurities were removed by washing with ethanol and air dried in oven.

7.2.3 Synthesis of ZnO/ZnS Hollow Nanostructure

30.0 mg of synthesized ZnO nanorod was dispersed properly in water via sonication up to 30 min. 5.0 mL of Na_2S (0.5 M) solution was added in 50 ml water so that the final concentration of Na_2S was maintained 0.05 M. The pH of the solution was ~ 8-9. The reaction mixture was sonicated for 15 min and kept for reflux at ~ 90 °C for 12 h without stirring. The final product was obtained by washing with ethanol to remove the extra sulfur impurities and dried in oven.

7.2.4 Dye Removal

In a typical experiment, 50 mg of the as-prepared ZnO/ZnS catalyst was added and dispersed in 10 mL of aqueous solutions of dyes (Methylene blue, Rhodamine B, Malachite green). Final concentration of the dye was 10^{-5} M in 10 mL. After stirring at room temperature for 1 h, the catalyst was separated by centrifugation (10,000 rpm) and the supernatant solutions were analyzed with UV-vis spectroscopy to obtain the concentration of dye in solution. To

evaluate the % adsorption, the initial concentrations of dye solutions were measured, and the dosage of ZnO/ZnS catalyst was kept same for each dye.

The percentage of adsorption of the dye can be calculated using:

$$\% \text{ Adsorption} = (A_0 - A_t)/A_0 \times 100$$

where, initial absorbance $= A_0$ and absorbance at time 't' $= A_t$.

7.3 Results and Discussion

All the synthesized nanomaterials were washed carefully and utilized further for characterization and application purposes. Here, the formation mechanism of the ZnO/ZnS nanostructure is proposed according to Kirkendall effect using ZnO NRs. In the following sections complete physical characterization, mechanism of Kirkendall effect and application will be discussed.

7.3.1 Characterization

7.3.1.1 UV-vis Diffuse Reflectance Spectra

UV-vis analysis is an effective tool to study the optical properties of the as-synthesized samples. **Figure 7.1** shows UV-vis spectrum of as-synthesized ZnO/ZnS, ZnO, and ZnS respectively measured in the range of 260-500 nm. ZnS NPs demonstrated a steep edge at about 360 nm and the peak is intensified in case of ZnS which corresponds to the wider band gap of ZnS [9,11,26]. The bare ZnO NR shows the characteristic band for ZnO at 370 nm. Whereas, for ZnO/ZnS heterostructure the first peak at 370 nm for ZnO and a steep edge at ~ 340 nm represents the presence of ZnS. The wavelength values for both ZnO and ZnS are in different position as compared to bare ZnO and ZnS. This spectrum deduced the formation of ZnO/ZnS nanostructure. UV-vis study apprises that ZnO/ZnS nanostructure can be applicable in many photon induced reactions due to their broad absorption range [2,34]. Using classical Tauc approach, from the plot of $(\alpha E_p)^2$ vs. photon energy (E_p) the band gap energy (E_g) of ZnO and ZnS can be calculated (**Figure 7.2.a** and **b**). The calculated E_g value for ZnO and ZnS is ~ 3.2 and ~ 3.6 eV, respectively, which is well coordinated with previous reports [5,9-10].
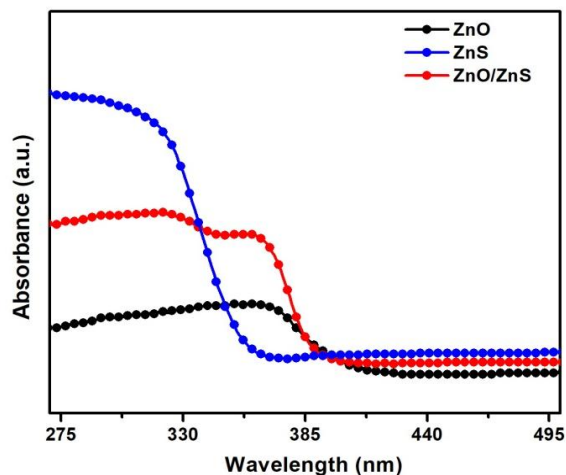
Figure 7.1 UV-vis DRS spectra of as-synthesized ZnO, ZnS, and ZnO/ZnS, where BaSO₄ was used as a reference
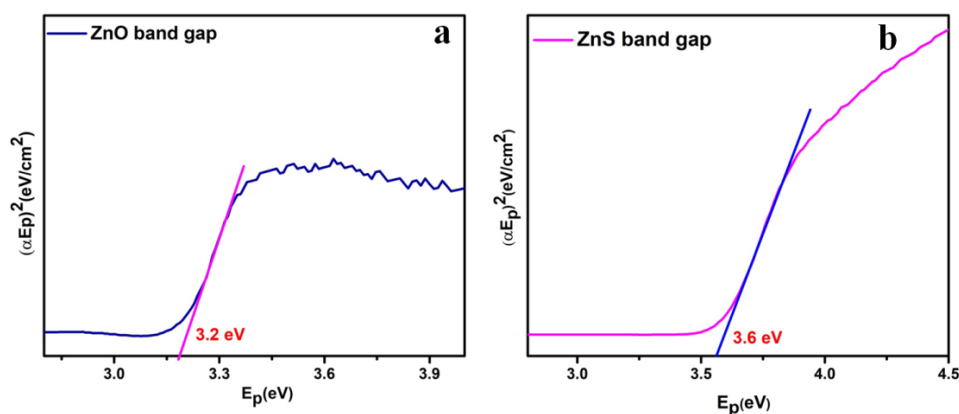
Figure 7.2 $(\alpha Ep)^2$ vs. E_p plot for band gap (E_g) calculation of (a) ZnO and (b) ZnS nanoparticles from their respective UV-vis absorption spectra

7.3.1.2 X-ray Diffraction Analysis of ZnO/ZnS, ZnO and ZnS

The structural identity and phase purity of the as-synthesized nanostructure were studied by PXRD analysis. **Figure 7.3** shows the PXRD patterns of ZnO, ZnS and ZnO/ZnS. It can be seen that peaks corresponding to ZnO, ZnS and ZnO/ZnS are identified in the sample according to their standard diffraction peaks. The ZnO/ZnS nanostructure, shows the characteristic peaks for ZnO NRs at 2θ values of 31.74°, 34.34°, 36.24°, 47.51°, 56.52°, 62.78°, 67.78°, and 76.85°

which corresponds to the (100), (002), (101), (102), (110), (103), (201) and (202) which are well consistent with the reported literature [5,10]. Moreover, in same diffraction pattern the peak for ZnS at 2θ values of 28.8° indexed to (111) plane is present in the PXRD pattern of ZnO/ZnS. This pattern signifies the successful synthesis of the nanostructure. The PXRD pattern of bare ZnO shows all the aforesaid characteristic peaks for the ZnO NR [6-8,34]. The observed diffraction peaks are assigned to the wurtzite ZnO structure with lattice constants a = 3.249 Å and c = 5.206 Å, which is in agreement with the literature (JCPDS 99-0111) [5,10,35]. The high intense peak in (101) plane can be evidently observed as a result of the vertical growth of ZnO NRs [35]. The 2θ values indicate that the as-prepared ZnO NRs are of high quality and purity. The PXRD of pure ZnS NPs shows diffraction peaks centred at 2θ = 28.8°, 48.23°, and 56.90° which can be indexed to (111), (220) and (311) planes of a typical zinc blende crystal phase of ZnS (JCPDS 80-0020) [17-21,35].
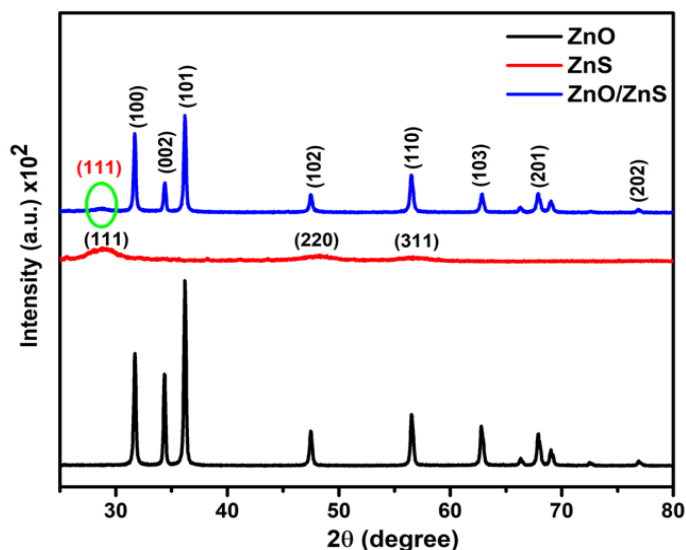
Figure 7.3 Powder X-ray diffraction patterns of ZnO NRs, ZnS NPs, and ZnO/ZnS hollow nanostructure. During PXRD measurement, 2θ is kept 10-80° and the scan rate was 2° per min

7.3.1.3 Morphological Analysis

To analyze the surface morphology and structure of the as-synthesized sample, FESEM analysis has been performed. FESEM micrographs display the shape and size of the as-

synthesized samples which is shown in **Figure 7.4**.
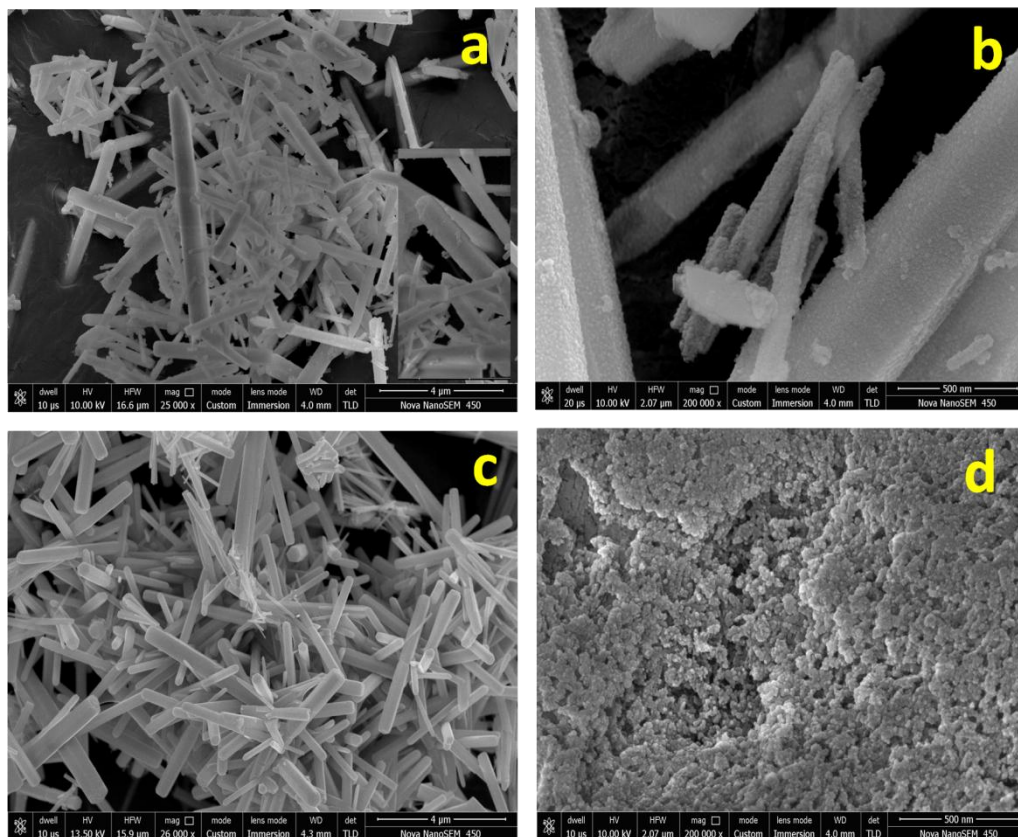
Figure 7.4 FESEM images of (a) ZnO/ZnS hollow nanostructure at low resolution (b) at high resolution (c) ZnO NRs and, (d) ZnS NPs

Low magnification FESEM image in **Figure 7.4.a** shows the hollow structure of ZnO/ZnS whereas high magnification FESEM image in **Figure 7.4.b** shows etched surface structure of nanorods which supports the formation of hollow structure. FESEM image of ZnO nanorods shown in the **Figure 7.4.c**. and the thickness is 316 nm and width is 148 nm. The rod shaped morphology of ZnO is generally observed and ascribed to the inherent anisotropy of the Wurtzite crystal structure. The image shows smooth surface hexagonal shaped rods of ZnO with tip sized of 120 nm. We have observed the highest growth rate along the (001) facet direction of wurtzite structure which is most common in the hydrothermal treatments and it can associate with the PXRD patterns [36]. The surface structure comparison of ZnO NRs and ZnO/ZnS shows that there is etching of oxygen ions from ZnO NRs by the replacement of sulfur ions.

FESEM image in **Figure 7.4.d** demonstrate the agglomeration of spherical ZnS NPs which are polydisperse in the nature.
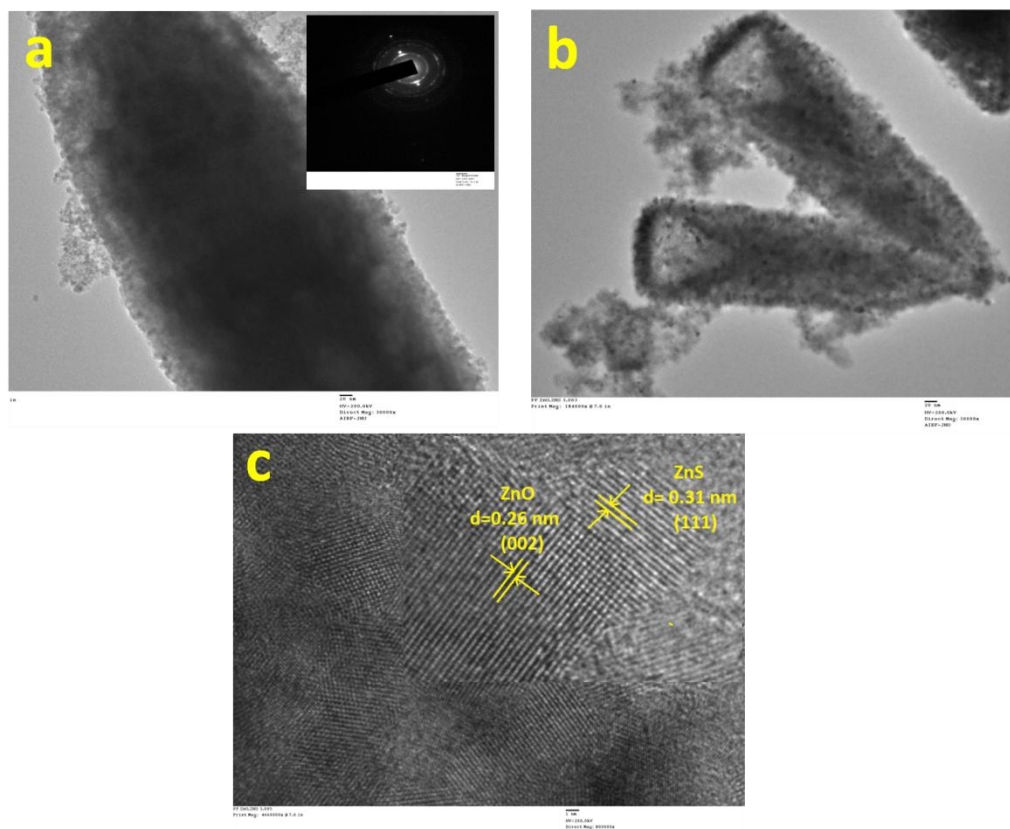
Figure 7.5 TEM image of hollow ZnO/ZnS nanostructure (a) at low resolution (inset) SAED pattern (b) at high-resolution (c) HRTEM images of ZnO/ZnS nanostructure where d-spacing calculated at different places for ZnO and ZnS

To give deep insight into the crystal structures and hollow morphologies of the as-prepared products, further HRTEM and EDS characterization of the as-synthesized materials have been performed. The TEM image of the ZnO/ZnS displayed in **Figure 7.5.a-c** obtained after 12 h sulfidation time, where the hollow structure can be detected. **Figure 7.5.a** and **b** show the low magnification and high magnification TEM image of ZnO/ZnS that two sets of lattice fringes were found on the surface, revealing the presence of ZnO/ZnS. The SAED pattern shown in **inset** of **Figure 7.5.a** reveals a spotted pattern that corresponds to the single crystalline nature of ZnO, and a set of diffraction rings that are consistent with the polycrystalline nature of ZnS

nanoparticles. All the TEM images validated the presence of ZnO and ZnS in ZnO/ZnS nanostructure. Therefore, TEM analysis of ZnO, ZnS and ZnO/ZnS is well acquainted with their FESEM analysis.
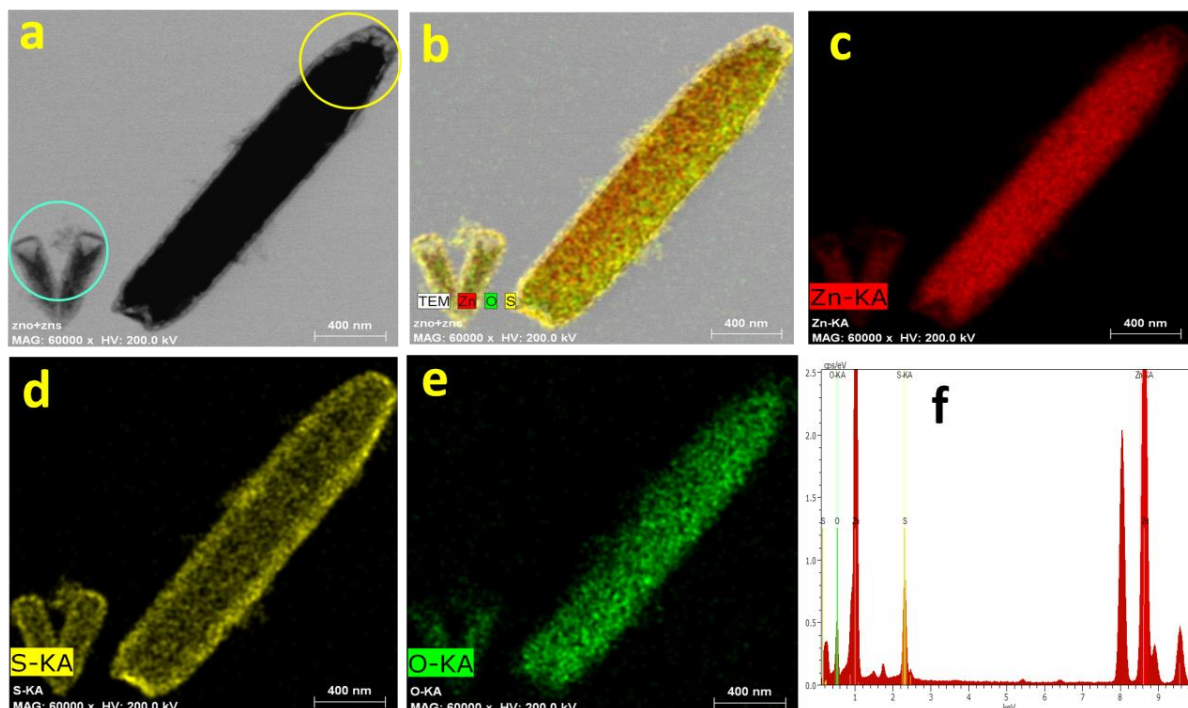
Figure 7.6 (a-e) EDS area mapping of ZnO/ZnS hollow nanostructure, hollow parts have been circled in the mapping, and (f) EDS Spectrum of ZnO/ZnS nanostructure

Moreover, to elucidate the presence of all the elements (Zn, O, and S) the EDS area mapping has been performed and shown in **Figure 7.6.a-e** and EDS spectra for the same has shown in **Figure 7.6.f**. In the hollow structure oxygen is getting released slowly so the outer layer is blurred but obviously a core is made up with sulfur which indicates the formation of hollow structure.

The typical low resolution and high resolution TEM images of ZnO NRs shown in **Figure 7.7.a** and **b**. The aspect ratio of a rod is ~ 0.47. The SAED pattern of the nanorods shown in **Figure 7.7.c** also established its single crystal nature. Therefore, the observation exhibited that the ZnO NRs grow along the (001) plane which is responsible for the growth of rod shape. The SAED pattern shown in **Figure 7.8.c** also reveals the single crystalline nature of ZnO NRs and

bright spots corresponding to hexagonal wurtzite ZnO. **Figure 7.7.d** shows the HRTEM image of ZnO NRs where the interplaner spacing (d) value is 0.26 nm corresponding to (002) plane, which indicates that the preferred growth of hexagonal structure of ZnO, well matched with the literature [5,10].
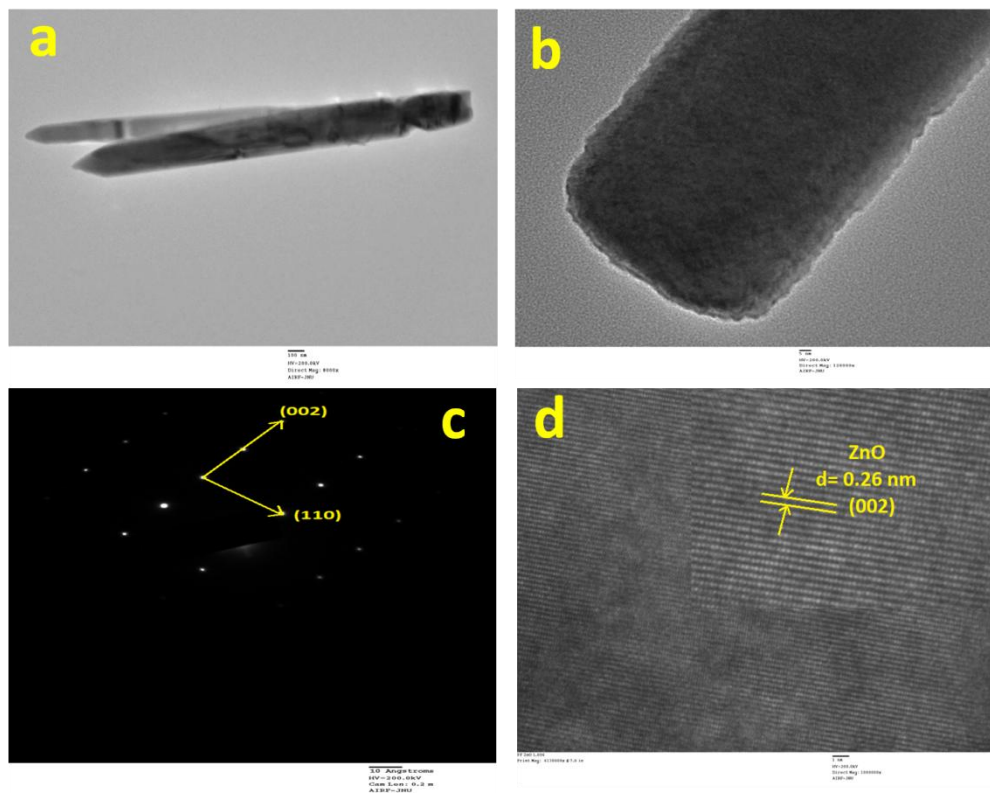
Figure 7.7 TEM images of ZnO nanorods (a) at low resolution and (b) at high-resolution (c) SAED pattern (d) HRTEM images of ZnO nanorods where d-spacing calculated for ZnO rods

Figure 7.8 is a representative TEM image of the as-prepared ZnS nanoparticles. The spherical morphology can be observed from the Figure and lattice fringe spacing was calculated 0.31 nm which corresponds to (111) plane shown in **Figure 7.8.a** and **b** and the results are well consistent with the earlier reports [36-38].
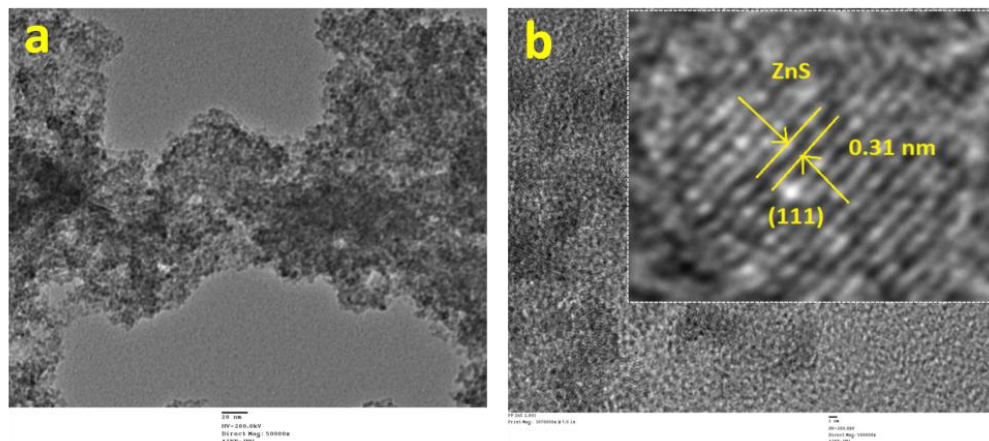
Figure 7.8 (a) TEM image of ZnS nanoparticles (b) HRTEM images of ZnS where d-spacing is calculated for ZnS NPs

7.3.1.4 Surface Chemical Analysis of ZnO/ZnS

XPS technique was employed to analyze the surface chemical composition of the metal oxide and metal sulfide NPs as well as oxidation states of metal. Successful formation of ZnO/ZnS structure has been observed by the individual wide scan XPS spectrum of Zn, S and O. A wide scan survey spectrum of ZnO/ZnS shows the presence of Zn, S, O and C elements in **Figure 7.9.a**. In ZnO/ZnS, the zinc is present as Zn(+2) oxidation state, which is evident from the binding energy (BE) value of Zn $2p_{3/2}$ peak at 1023.72 eV and Zn $2p_{1/2}$ is 1047.05 eV [5,10]. The difference in binding energy between two Zn peaks is about 23.0 eV, which matches well with the earlier reports [5]. Similarly, the S2p binding energy spectrum shows the peak centered at 163.09 eV implies that sulfur is exist as sulfide (S^{2-}), suggests the formation of ZnS. No supplementary peaks were noticed from 165 to 170 eV, which clearly displayed the absence of an oxidized form of sulfur shown in **Figure 7.9.c** [12,17,35]. Further, the O1s peak shows the binding energy position at 533.51 eV shown in **Figure 7.9.d**. The oxygen species commonly show in (−2) oxidation state within the ZnO matrix, with a negligible portion of surface hydroxides [5,10]. All these findings clearly suggest the presence of Zn^{+2}, O^{-2}, and S^{2-} ions in the ZnO/ZnS hereostructure [34-35]. The XPS spectrum for C1s is shown in **Figure 7.9.e** with binding energy at 286.6 eV. Details of all the BE of ZnO/ZnS nanostructure is summarized in **Table 7.1**.
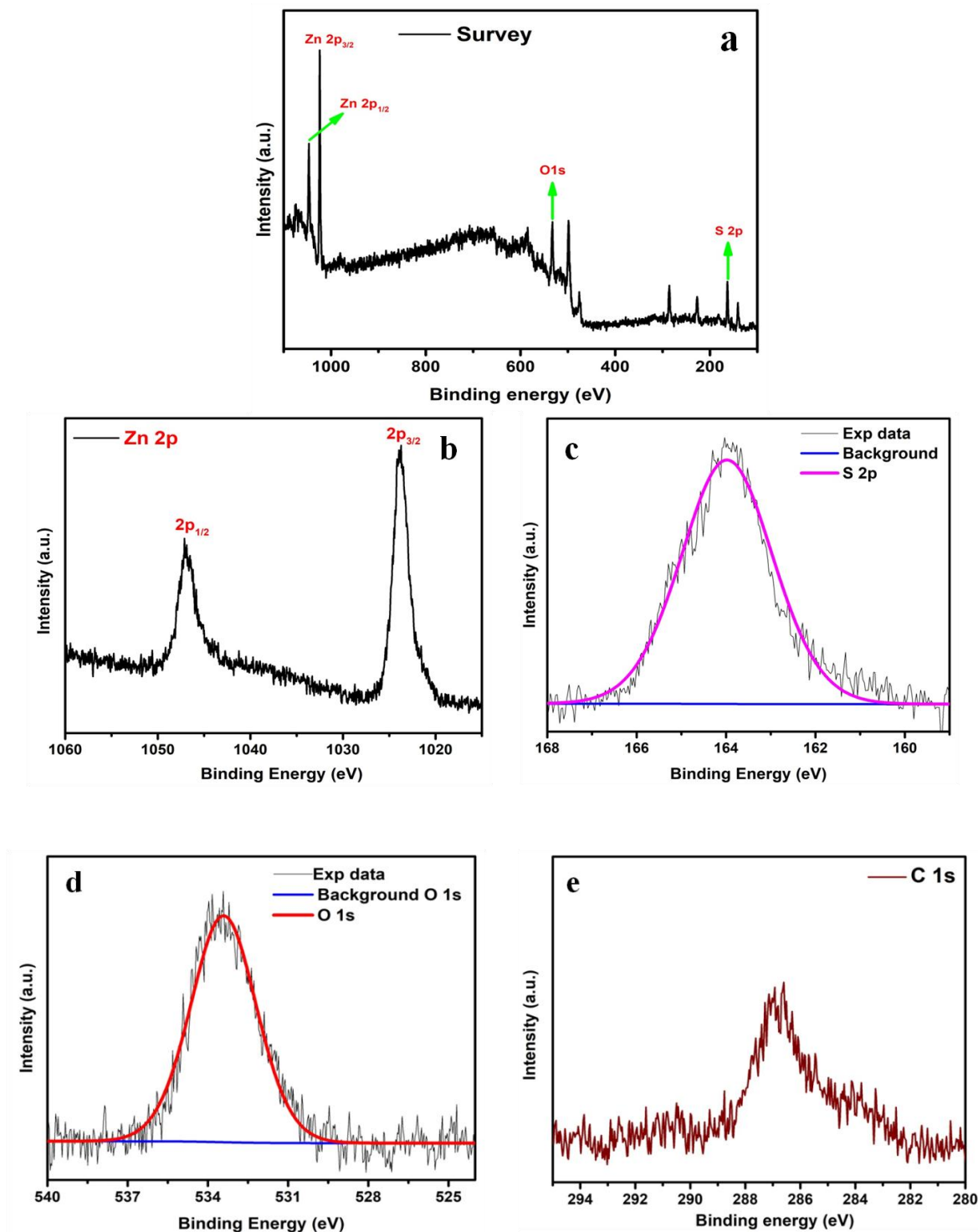
Figure 7.9 XP spectra of high resolution scans of (a) wide scan survey of ZnO/ZnS hollow nanostructure (b) Zn 2p and XPS spectrum for (c) S-2p core level (d) O 1s (e) C 1s

Table 7.1 Details of all the binding energies of ZnO/ZnS nanostructure from XP spectra

ZnO/ZnS	Peaks	Binding Energy (eV)
Zinc	$2p_{3/2}$	1023.72
	$2p_{1/2}$	1047.05
Sulfur	2p	163.96
Oxygen	1s	533.51
Carbon	1s	286.92

7.3.2 Mechanism of Formation

Here, ZnO nanorods were first synthesized by a hydrothermal process using HMT and CTAB. CTAB was used as stabilizer and growth controlling agent and HMT as a hydrolyzing agent for the synthesis [10,36-37]. Railey *et al.* suggested that HMT is a highly water soluble, non-ionic tetradentate cyclic tertiary amine and it provides hydroxyl ion during the reaction. When HMT decompose thermally, it generates ammonia and formaldehyde which further release hydroxyl ion in aqueous medium [10,37]. HMT provides the OH$^-$ ions during reflux conditions to drive the precipitation reaction reported by Dutta and co-workers [36,39]. According to these reports, in the hydrothermal condition firstly, Zn^{+2} ions react with OH– ions and forms [Zn(OH)$_2$], afterward the [Zn(OH)$_2$] complex reacts with excess OH$^-$ ions to form [Zn(OH)$_4$]$^{2-}$ ions. The dehydration of [Zn(OH)$_4$]$^{2-}$ takes place in hydrothermal conditions, which results in the formation of ZnO [5,10]. This mechanism is well explained and reported in previous reports and can be summarized as follows:

$$(CH_2)_6N_4 + 6H_2O \rightarrow 6HCHO + 4NH_3$$
$$NH_3 + H_2O \rightarrow NH_4^+ + OH^-$$
$$2OH^- + Zn^{2+} \rightarrow Zn(OH)_2 + H_2O$$
$$2OH^- + Zn(OH)_2 \rightarrow [Zn(OH)_4]^{2-} + H_2O$$
$$[Zn(OH)_4]^{2-} \rightarrow ZnO + OH^- + H_2O$$
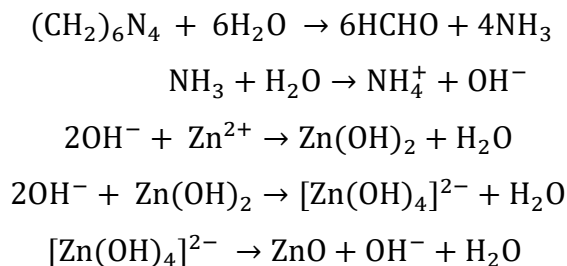
There are many literature reports suggesting the growth mechanism of ZnO rods in the presence of HMT using zinc nitrate as a zinc precursor. Dutta *et al.* explained the attachment of HMT on the (001) facet which directs the growth along the same facet [36,39]. Sugunan *et al.* suggested that according to the theoretical study, the non polar surface of ZnO has smaller energy than the polar surface. Furthermore they reveal the role of HMT in the growth of ZnO nanowire [36]. From these reports it is clear that in ZnO, HMT is attached preferentially to the non-polar facets and allows the Zn^{2+} ions to approach the polar (001) face. HMT therefore can be said as a morphology inducing polymer surfactant.

The intense peak corresponds to (101) plane is attributed to ZnO NRs which is in well agreement with the literature report. It is also evident from the control experiments that the synthesis of ZnO without HMT and CTAB always ended with agglomerated particles [10,36-40]. Moreover, for the synthesis of ZnS NPs, Na_2S is added as a sulfur precursor in the reaction mixture and kept it at 90 °C in heating condition where it provides S^{2-} ions. The ZnS nanoparticles formation starts in the solution following below reaction and aggregate to form spherical shape [38,40]. Presence of HMT creates the basic environment where HMT behaves as a buffer to control the release rate of Zn^{2+} ions and consequently the rate of ZnS nuclei formation is controlled [4,10,39].

$$Zn^{2+} + Na_2S \rightarrow ZnS + 2Na^+$$
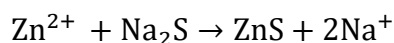
The synthesis of ZnO/ZnS hollow nanorods takes place via Kirkendall phenomena. To synthesize ZnO/ZnS hollow structure, ZnO nanorods were dispersed in 0.05 M Na_2S solution. The sulfur ions released by Na_2S at 90 °C reacts with ZnO at the interface of nanorods to form ZnO/ZnS [2,38-40].

$$Na_2S \rightarrow S^{2-} + 2Na^+$$
$$S^{2-} + H_2O \rightarrow HS^- + OH^-$$
$$ZnO + 2OH^- \rightarrow ZnO_2^{2-} + H_2O$$
$$ZnO_2^{2-} + S^{2-} + 2H_2O \rightarrow ZnS \downarrow + OH^-$$
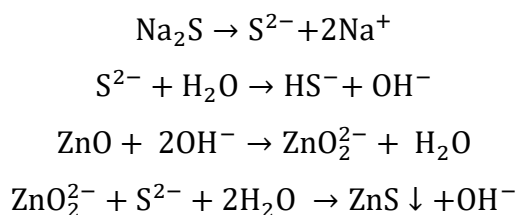
Owing to these results mentioned above, the mechanism of formation of hollow ZnO/ZnS structure [1-3,26] can be explained as follows, shown in **Scheme 7.1**.

In the ion exchange step initially Na_2S releases S^{2-} ions which hydrolyze to give OH^-

ions. ZnO NRs present in the solution react with OH$^-$ ions to be converted in the more reactive form ZnO$_2$$^{2-}$. Now the active species, ZnO$_2$$^{2-}$ reacts with released S^{2-} and formation of ZnS starts. In sulphidation process, initially S^{2-} ions loaded on the surface of the ZnO rod. The availability of S^{2-} ions leads to the formation of hollow ZnO/ZnS nanostructure. Now, by the diffusion of the Zn^{2+} ions from inside and preferable bonding with S^{2-} ions development of hollow ZnO/ZnS occur. Lastly, after 12 h of sulfidation under reflux condition, the continuous diffusion of Zn^{+2} ions from the central region results in the hollow structure represented in **Scheme 7.1**.
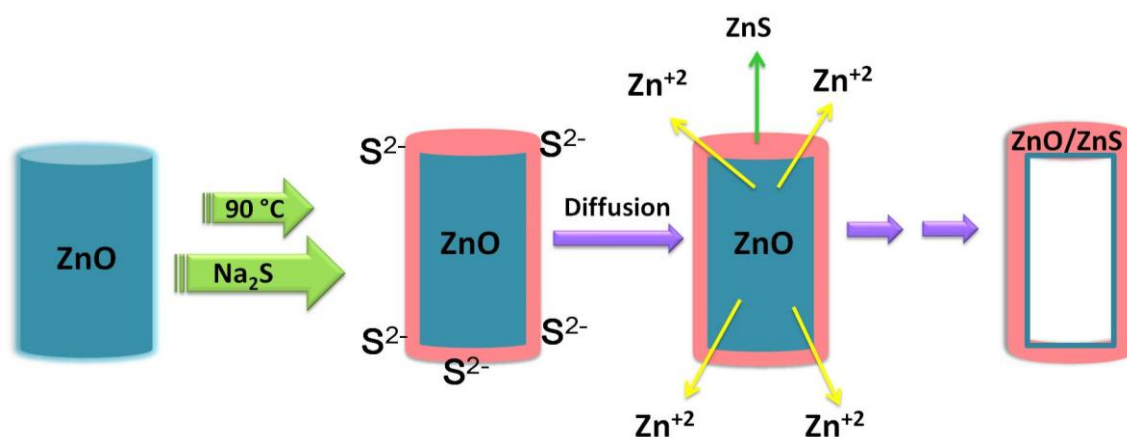
Scheme 7.1 Overall mechanism of formation of ZnO/ZnS hollow nanostructure via Kirkendall effect

Figure 7.4 shows the FESEM image of the as-synthesized hollow ZnO/ZnS core-shell structure. We can see that some of the structures have an etched surface, as compared to smooth surface of ZnO NRs clearly indicates the hollow structure of the prepared nanorods. The overall formation mechanism of the ZnO/ZnS hollow core-shell structure can be explained by the Kirkendall process, which generally refers to relative diffusive migrations of dissimilar ions under different temperature conditions [17-21].

The elemental compositions of ZnO/ZnS structures are Zn^{+2}, O^{2-} and S^{2-}. Initially the solid nanoparticles including one of the elements of end product (ZnO/ZnS) have been synthesized which is known as starting material [20-25]. Here, ZnO nanorods have been used as a starting material. Now, the second element is allowed to react with the starting material to achieve the heterostructure. The solution of Na$_2$S is added which provides the second element

S^{2-} for the reaction with ZnO and a layer of ZnS form on the top surface. During this step the morphology is similar like core-shell where ZnO is present as an inner core material which is covered by outer shell of ZnS. The direct conversion of core to shell is restricted by the layer and now the reaction is carried out by diffusion of ions from the interface. The rate of diffusion is faster in case of core ions O^{2-} as compared to the shell S^{2-} ions which results in the formation of a net material flux across the heterostructure interface. This leads to a flow of fast-moving vacancies to the vicinity of the solid-liquid interface; consequently, the hollow voids are produced through coalescence of the vacancies via the Kirkendall effect [17-22].

7.3.3 Adsorption of Dye Molecules

To check the catalytic ability of the as-synthesized hollow structure, adsorption experiment was performed. For this 50 mg ZnO/ZnS catalyst is dispersed into 10 mL of dye solution with an initial concentration of 10^{-5} M by slow stirring. The reaction mixture was kept for 1 h and after that supernatant was collected by centrifugation. To calculate the adsorption % UV-vis absorption spectroscopy measurements were executed.
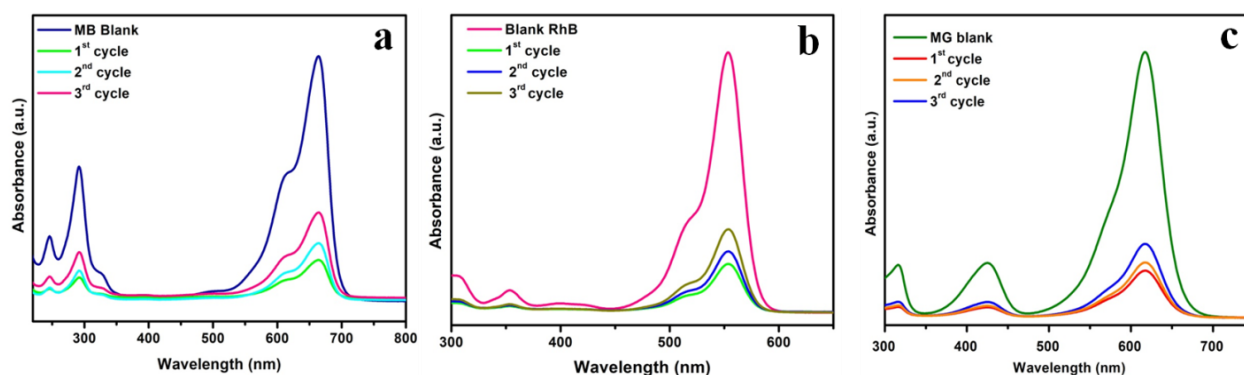
Figure 7.10 UV-vis spectra of dye absorption by recycling the ZnO/ZnS catalyst three times (a) MB: methylene blue, (b) RhB: rhodamine B and (c) MG: malachite green. Conditions: [dye] = 10^{-5} M and catalyst used: 50 mg

The UV-vis absorption spectra in **Figure 7.10** show the dye solutions, before and after adsorption in the presence of hollow ZnO/ZnS. For the each experiment 50 mg of catalyst was

taken and three dyes: methylene blue, rhodamine B and malachite green were used to adsorb. First, methylene blue dye was dispersed in the solution with catalyst and in first cycle ~ 84% dye was adsorbed. After that catalyst was recollected by decanting the supernatant solution and washed with ethanol 2-3 times to remove the adsorbed dye molecules. Two more cycles were repeated with the same catalyst and ~ 76 and ~ 64 % MB dye was adsorbed in the repetitive cycles. The UV-vis analysis of adsorption of MB dye is shown in **Figure 7.10.a**. Similar approach was followed with rhodamine B and 86, 77, 69 % adsorption was achieved for the RhB dye within three cycles and UV-Vis shown in **Figure 7.10.b**. Furthermore, the malachite green dye was also used and 83, 79, 72 % adsorption takes place within the same time, **Figure 7.10.c**. The comparative adsorption study and recyclability of the ZnO/ZnS catalyst has been shown in the **Figure 7.11**.
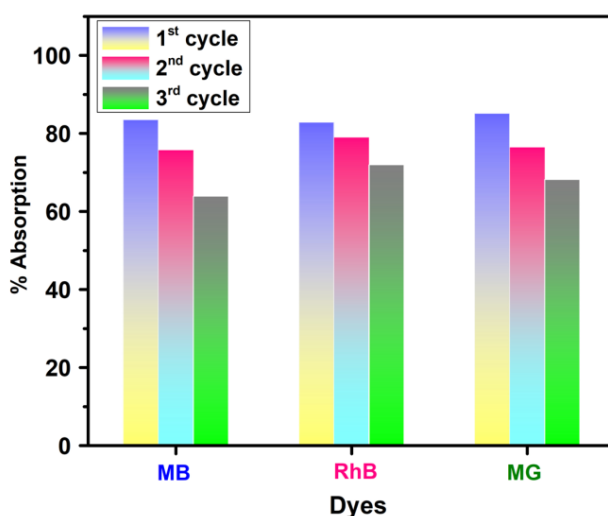
Figure 7.11 Comparative study of dye absorption (MB: methylene blue, RhB: rhodamine B and MG: malachite green) by recycling of the ZnO/ZnS nanostructure three times

7.4 Conclusion

In summary, we have successfully demonstrated the synthesis of ZnO nanorods using HMT and CTAB as a hydrolyzing and growth controlling agent. Successful synthesis of hexagonal nanorod has been observed in the FESEM and TEM images. Furthermore, synthesis of ZnS NPs has also been performed utilizing the similar synthetic approach and characterized. Using ZnO nanorods as sacrificial templates, synthesis of ZnO/ZnS hollow nanorod has been carried out at low temperature via Kirkendall effect. The formation of hollow structures has been described using Kirkendall phenomena and etching of the ions was observed in SEM and TEM images. Thus, based on as-synthesized ZnO/ZnS hollow nanostructure, a new paradigm to design effective material as adsorbent using two wide band gap semiconductor nanomaterials, via Kirkendall effect is possible.

References

[1]   Huang, X.; Willinger, M. G.; Fan, H.; Xie, Z. L.; Wang, L.; Klein-Hoffmann, A.; Girgsdies, F.; Lee, C. S.; Meng, X. M. Single Crystalline Wurtzite ZnO/Zinc Blende ZnS Coaxial Heterojunctions and Hollow Zinc Blende ZnS Nanotubes: Synthesis, Structural Characterization and Optical Properties. *Nanoscale* **2014**, *6*, 8787-8795.

[2]   Wu, D.; Jiang, Y.; Yuan, Y.; Wu, J.; Jiang, K. ZnO-ZnS Heterostructures with Enhanced Optical and Photocatalytic Properties. *J. Nanopart Res.* **2011**, *13*, 2875-2886.

[3]   Guo, P.; Jiang, J.; Shen, S.; Guo, L. ZnS/ZnO Heterojunction as Photoelectrode: Type-II Band Alignment towards Enhanced Photoelectrochemical Performance. *Int. J. Hydrog. Energy* **2013**, *38*, 13097-13103.

[4]   Chen, X.; Li, Y.; Pan, X.; Cortie, D.; Huang, X.; Yi, Z. Photocatalytic Oxidation of Methane over Silver Decorated Zinc Oxide Nanocatalysts. *Nat. Commun.* **2016**, *7*, 12273.

[5]   Fageria, P.; Gangopadhyay, S.; Pande, S. Synthesis of ZnO/Au and ZnO/Ag Nanoparticles and their Photocatalytic Application using UV and Visible Light. *RSC Adv.* **2014**, *4*, 24962-24972.

[6]   Huang, X.; Wang, M.; Willinger, M. G.; Shao, L.; Su, D. S.; Meng, X. M. Assembly of Three-Dimensional Hetero-Epitaxial ZnO/ZnS Core/Shell Nanorod and Single Crystalline Hollow ZnS Nanotube Arrays. *ACS Nano* **2012**, *6*, 7333-7339.

[7]   Hu, Y.; Qian, H.; Liu, Y.; Du, G.; Zhang, F.; Wang, L.; Hu, X. A Microwave-Assisted Rapid Route to Synthesize ZnO/ZnS Core-Shell Nanostructures via Controllable Surface Sulfidation of ZnO Nanorods. *CrystEngComm* **2011**, *13*, 3438-3443.

[8]   Murphy, M. W.; Zhou, X. T.; Ko, J. Y.; Zhou, J. G.; Heigl, F.; Sham, T. K. Optical Emission of Biaxial ZnO-ZnS Nanoribbon Heterostructures. *J. Chem. Phys.* **2009**, *130*, 084707-8.

[9]   Sanchez-Tovar, R.; Fernandez-Domene, R. M.; Montanes, M. T.; Sanz-Marco, A.; Garcia-Anton, J. ZnO/ZnS Heterostructures for Hydrogen Production by Photoelectrochemical Water Splitting. *RSC Adv.* **2016**, *6*, 30425-30435.

[10]   Zhang, W.; Wang, S.; Wang, Y.; Zhu, Z.; Gao, X.; Yang, J.; Xin Zhang, H. ZnO@ ZnS Core/Shell Microrods with Enhanced Gas Sensing Properties. *RSC Adv.* **2015**, *5*, 2620-2629.

[11]   Ranjith, K. S.; Senthamizhan, A.; Balusamy, B.; Uyar, T. Nanograined Surface Shell Wall Controlled ZnO-ZnS Core-Shell Nanofibers and their Shell Wall Thickness Dependent Visible Photocatalytic Properties. *Catal. Sci. Technol.* **2017**, *7*, 1167-1180.

[12]   Basu, M.; Garg, N.; Ganguli, A. K. A Type-II Semiconductor (ZnO/CuS Heterostructure) for Visible Light Photocatalysis. *J. Mater. Chem. A* **2014**, *2*, 7517-7525.

[13]   Zhu, Y. F.; Fan, D. H.; Shen, W. Z. Chemical Conversion Synthesis and Optical Properties of Metal Sulfide Hollow Microspheres. *Langmuir* **2008**, *24*, 11131-11136

[14]   Gao, X.; Wang, J.; Yu, J.; Xu, H. Novel ZnO-ZnS Nanowire Arrays with Heterostructures and Enhanced Photocatalytic Properties. *CrystEngComm* **2015**, *17*, 6328-6337.

[15]   Wang, G.; Li, Z.; Li, M.; Chen, C.; Lv, S.; Liao, J. Aqueous Phase Synthesis and Enhanced Field Emission Properties of ZnO-Sulfide Heterojunction Nanowires. *Sci. Rep.* **2016**, *6*, 29470.

[16]   Schrier, J.; Demchenko, D. O.; Wang, L. W.; Alivisatos, A. P. Optical Properties of ZnO/ZnS and ZnO/ZnTe Heterostructures for Photovoltaic Applications. *Nano Lett.* **2007**, *7*, 2377-2382.

[17]   Shuai, X. M.; Shen, W. Z. A Facile Chemical Conversion Synthesis of ZnO/ZnS Core/Shell Nanorods and Diverse Metal Sulfide Nanotubes. *J. Phys. Chem. C* **2011**, *115*, 6415-6422.

[18]   Li, F.; Jiang, Y.; Hu, L.; Liu, L.; Li, Z.; Huang, X. Structural and Luminescent Properties of ZnO Nanorods and ZnO/ZnS Nanocomposites. *J. Alloys Compd.* **2009**, *474*, 531-535.

[19]   Lu, Q.; Gao, F. Synthesis and Property Studies of Hollow Nanostructures. *CrystEngComm* **2016**, *18*, 7399-7409.

[20]   Dhas, N. A., Suslick, K. A. Sonochemical Preparation of Hollow Nanospheres and Hollow Nanocrystals. *J. Am. Chem. Soc.* **2005**, *127*, 2368-2369.

[21]   Fan, H. J.; Gcsele, U.; Zacharias, M. Formation of Nanotubes and Hollow Nanoparticles Based on Kirkendall and Diffusion Processes: A Review. *Small* **2007**, *3*, 1660-1671

[22]   Kirkendall, E. O. Diffusion of Zinc in Alpha Brass. *Trans. Am. Inst. Min. Metall. Eng.* **1942**, *147*, 104-109.

[23]   Wang, W.; Dahl, M.; Yin, Y. Hollow Nanocrystals through the Nanoscale Kirkendall Effect. *Chem. Mater.* **2013**, *25*, 1179-1189.

[24]   Yang, Z.; Yang, N.; Pileni, M. P. Nano Kirkendall Effect Related to Nanocrystallinity of Metal Nanocrystals: Influence of the Outward and Inward Atomic Diffusion on the Final Nanoparticle Structure. *J. Phys. Chem. C* **2015**, *119*, 22249-22260.

[25]   Raidongia, K.; Rao, C. N. R. Study of the Transformations of Elemental Nanowires to Nanotubes of Metal Oxides and Chalcogenides through the Kirkendall Effect. *J. Phys. Chem. C* **2008**, *112*, 13366-13371.

[26]   Sun, H.; Chen, Y.; Wang, X. Synthesis of ZnS Hollow Nanoneedles via the Nanoscale Kirkendall Effect. *J. Nanopart Res.* **2011**, *13*, 97-103.

[27]   Cabot, A.; Ibanez, M.; Guardia, P.; Alivisatos, A. P. Reaction Regimes on the Synthesis of Hollow Particles by the Kirkendall Effect. *J. Am. Chem. Soc.* **2009**, *131*, 11326-11328.

[28]   Liu, L.; Zhang, B.; Zhang, Y.; He, Y.; Huang, L.; Tan, S.; Cai, X. Simultaneous Removal of Cationic and Anionic Dyes from Environmental Water Using Montmorillonite-Pillared Graphene Oxide. *J. Chem. Eng. Data* **2015**, *60*, 1270-1278.

[29]   Rafatullah, M.; Sulaiman, O.; Hashim, R.; Ahmad, A. Adsorption of Methylene Blue on Low-cost Adsorbents: A Review. *J. Hazard. Mater.* **2010**, *177*, 70-80.

[30]   Zhu, T.; Chen, J. S.; Lou, X. W. Highly Efficient Removal of Organic Dyes from Waste Water using Hierarchical NiO Spheres with High Surface Area. *J. Phys. Chem. C* **2012**, *116*, 6873-6878.

[31]   Luo, Y.; Duan, G.; Ye, M.; Zhang, Y.; Li, G. Poly(ethylene glycol)-Mediated Synthesis of Hollow ZnS Microspheres. *J. Phys. Chem. C* **2008**, *112*, 2349-2352.

[32]   Chowdhury, R.; Barah, N.; Rashid, M. Facile Biopolymer Assisted Synthesis of Hollow SnO_2 Nanostructures and their Application in Dye Removal. *Chemistry Select* **2016**, *1*, 4682-4689.

[33]   Yang, S.; Wu, Z.; Huang, L.; Zhou, B.; Lei, M.; Sun, L.; Tian, Q.; Pan, J.; Wu, W.; Zhang, H. Significantly Enhanced Dye Removal Performance of Hollow Tin Oxide Nanoparticles via Carbon Coating in Dark Environment and Study of its Mechanism. *Nanoscale Res. Lett.* **2014**, *9*, 442-451.

[34]   Li, F.; Jiang, Y.; Hu, L.; Liu, L.; Li, Z.; Huang, X. Structural and Luminescent Properties of ZnO Nanorods and ZnO/ZnS Nanocomposites. *J. Alloys Compd.* **2009**, *474*, 531-535.

[35]   Park, J. Y.; Park, S. J.; Lee, J. H.; Hwang, C. H.; Hwang, K. J.; Jin, S.; Choi, D. Y.; Yoon, S. D.; Lee, I. H. Synthesis and Characterization of Cauliflower-like ZnS

Microspheres by Simple Self-Assembly Method. *Mater. Lett.* **2014**, *121*, 97-100.

[36]   Sugunan, A.; Warad, H. C.; Boman, M.; Dutta, J. Zinc Oxide Nanowires in Chemical Bath on Seeded Substrates: Role of Hexamine. *J. Sol-Gel Sci. Technol.* **2006**, *39*, 49-56

[37]   Ashfold, M. N.; Doherty, R. P.; Ndifor-Angwafor, N. G.; Riley, D. J.; Sun, Y. The Kinetics of the Hydrothermal Growth of ZnO Nanostructures. *Thin Solid Films* **2007**, *515*, 8679-8683.

[38]   She, Y. Y.; Juan, Y. A. N. G.; Qiu, K. Q. Synthesis of ZnS Nanoparticles by Solid-liquid Chemical Reaction with ZnO and Na$_2$S under Ultrasonic. *Trans. Nonferrous Met. Soc. China* **2010**, *20*, s211-s215.

[39]   Baruah, S.; Dutta, J. Hydrothermal Growth of ZnO Nanostructures. *Sci. Technol. Adv. Mater.* **2009**, *10*, 013001-18.

[40]   Liu, W.; Wang, N. Wang, R. Atom-Resolved Evidence of Anisotropic Growth in ZnS Nanotetrapods. *Nano Lett.* **2011**, *11*, 2983-2988.

[41]   Wu, A.; Jing, L.; Wang, J.; Qu, Y.; Xie, Y.; Jiang, B.; Tian, C.; Fu, H. ZnO-Dotted Porous ZnS Cluster Microspheres for High Efficient, Pt-free Photocatalytic Hydrogen Evolution. *Sci. Rep.* **2015**, *5*, 8858.

Chapter 8

Summary and Future Avenues

✿ This chapter recapitulates the work carried out in this thesis by highlighting the prominent attributes of the work.

✿ The future avenues of the work that can be carried out using this thesis are also established.

Chapter 1: This chapter describes a brief introduction on origin and history of nanosciences, synthetic methods for the nanomaterials, stabilizers, metal nanoparticles, type of materials, semiconductor nanomaterials and application of semiconductor nanomaterials in catalysis.

Chapter 2: This chapter illustrates all the chemicals, reagents, instruments, and techniques for the synthesis, methods, calculations, and detection from an analytical chemistry point of view.

Chapter 3: In this chapter, a wet-chemical approach for the synthesis of ZnO nanoflower and deposition of Au and Ag nanoparticles on ZnO surface has been reported. Their application and photoactivity were investigated by degradation of phenol and methylene blue under visible and UV light. The mechanism of degradation, reaction kinetics, and study of involved species has been presented properly.

Chapter 4: A simple wet-chemical approach for the synthesis of morphology-dependent (dumbbell and cone) ZnO nanostructure on g-C_3N_4 surface using different hydrolyzing agent has been reported in this chapter. The visible light photoactivity of g-C_3N_4/ZnO dumbbell and cone has been performed via photo mineralization of phenol and methylene blue and activities have been compared.

Chapter 5: In this chapter, we have reported the synthesis of mono- (Au and Pd) and bimetallic (AuPd) nanoparticles using carbon nitride (C_3N_4) quantum dots as a photoreducing and stabilizing agents. In addition, the catalytic efficiency of mono- (Au and Pd) and bimetallic (AuPd) nanoparticles have been tested using a model reduction reaction, 4-NP to 4-AP and AuPd bimetallics has been observed a superior catalyst.

Chapter 6: This chapter demonstrates a facile hydrothermal approach for the decoration of molybdenum disulfide on g-C_3N_4 surface. The heterostructure of MoS_2/g-C_3N_4 has been utilized in electrocatalysis for hydrogen evolution reaction and as a photocatalyst to degrade rhodamine B dye and demonstrated higher activity of MoS_2/g-C_3N_4 as compared to bare g-C_3N_4 and MoS_2.

Chapter 7: In this last chapter we have described the synthesis of ZnO/ZnS hollow struture via

Kirkendall effect and mechanism of formation has been discussed. The dye removal has been successfully carried out using as-synthesized heterostructure.

The following work is suggested for the future research:

1. Synthesis of other semiconductor heterostructure using new wide band gap nanomaterials and their reactivity tuning using similar approach reported in the thesis.
2. The photocatalytic performance can be further evaluated to degrade more organic pollutant and the method can be used in industrial scale.
3. The technique of total organic carbon (TOC) can be employed to investigate the mineralization of dyes used in the entire thesis. The end product (CO_2) of dye and pollutant degradation reaction can convert into other hydrocarbons which are less hazardous.
4. The techniques, HPLC, LC/MS/MS, and GC/MS can be utilized to further study the intermediate products and monitor the temporal course of the reaction in detail during the photocatalytic degradation.
5. Using photoexcited electron many other mono- and bimetallic NP combination and tuning of bimetallic NP can be performed.
6. The reported nanomaterials in the thesis can be applied in the photoelectrochemical water splitting reaction, especially, hollow ZnO-ZnS nanostructure.

Appendices

1. **Fageria, P.**; Gangopadhyay, S.; Pande, S. Synthesis of ZnO/Au and ZnO/Ag nanoparticles and their photocatalytic application using UV and visible light. *RSC Adv.* **2014**, *4*, 24962-24972.

2. **Fageria, P.**; Nazir, R.; Gangopadhyay, S.; Barshilia, H. C.; Pande, S. Graphitic-Carbon Nitride Support for the Synthesis of Shape- Dependent ZnO and their Application in Visible Light Photocatalysts. *RSC Adv.* **2015**, *5*, 80397-80409.

3. **Fageria, P.**; Uppala, S.; Nazir, R.; Gangopadhyay, S.; Chang C. H.; Basu, M.; Pande, S. Synthesis of Monometallic (Au and Pd) and Bimetallic (AuPd) Nanoparticles using Carbon Nitride (C_3N_4) Quantum Dots via the Photochemical Route for Nitrophenol Reduction. *Langmuir* **2016**, *32*, 10054-10064.

4. **Fageria, P.**; Sudharshana, K.Y.; Nazir, R.; Basu, M., Pande, S.; Decoration of MoS_2 on g-C_3N_4 surface for efficient hydrogen evolution reaction. *Electrochim. Acta* **2017**, *258*, 1273-1283.

5. **Fageria, P.**; Basu, M., Pande, S.; Hydrothermal Synthesis of ZnO/ZnS Hollow Nanorods via Kirkendall Effect for Adsorptive Dye Removal (MS under preparation)

6. Nazir, R.; **Fageria, P.**; Basu, M.; Gangopadhyay, S.; Pande, S. Decoration of Pd and Pt Nanoparticles on a Carbon Nitride (C_3N_4) Surface for Nitro-Compounds Reduction and Hydrogen Evolution Reaction. *New J. Chem.* **2017**, *41*, 9658-9667.

7. Nazir, R.; **Fageria, P.**; Basu, M.; Pande, S. Decoration of Carbon Nitride Surface with Bimetallic Nanoparticles (Ag/Pt, Ag/Pd, and Ag/Au) via Galvanic Exchange for Hydrogen Evolution Reaction. *J. Phys. Chem. C.* **2017**, *121*, 19548-19558.

8. Basu, M.; Nazir, R.; **Fageria, P.**; Pande, S. Construction of CuS/Au Heterostructure through a Simple Photoreduction Route for Enhanced Electrochemical Hydrogen Evolution and Photocatalysis. *Sci. Rep.* **2016**, *6*, 34738.

9. Basu, M.; Nazir, R.; Mahala, C.; **Fageria, P.**; Chaudhary, S.; Gangopadhyay, S.; Pande, S. Ag_2S/Ag Heterostructure: A Promising Electrocatalyst for the Hydrogen Evolution Reaction. *Langmuir* **2017**, *33*, 3178.

10. Mandal, H.; Shyamal, S.; Hajra, P.; Samanta, B.; **Fageria, P.**; Pande, S.; Bhattacharya, C. Improved photoelectrochemical water oxidation using wurtzite ZnO semiconductors synthesized through simple chemical bath reaction. *Electrochim. Acta*. **2014**, *141*, 294-301.

11. Hajra, P.; Shyamal, S.; Mandal, H.; **Fageria, P.**; Pande, S.; Bhattacharyaa, C.; Photocatalytic activity of Bi_2O_3 Nanocrystalline Semiconductor developed via Chemical-bath Synthesis. *Electrochim. Acta.* **2014**, *123*, 494-500.

** Embodied in the Thesis

1. International Conference on Nanoscience and Technology (ICONSAT-2014) at Mohali, Punjab, organized by Institute of Nanoscience and Technology and Punjab University, during 2-5 March, 2014. **(poster)**

2. National Conference on Nano-and Functional Materials (NFM-2014) at BITS Pilani, organized by Department of Chemistry, Birla Institute of Technology and Sciences, BITS Pilani, Rajasthan during 7-8 November, 2014. **(Best poster award)**

3. National Conference on Recent Advancements in Chemical Sciences (RAICS-2015) organized by Department of Chemistry, Malaviya National Institute of Technology, MNIT Jaipur, during 21-23 August, 2015. **(poster)**

4. 2nd International Conference on Emerging Technologies-Micro to Nano (ETMN-2015) Organized By Manipal University Jaipur, CSIR-CEERI Pilani and BITS Pilani, during 24-25 October 2015. **(poster)**

5. International Conference on Nanoscience and Technology (ICONSAT-2016) organized by the Indian Institute of Science Education and Research (IISER), Pune during February 29-2 March 2016. **(poster)**

6. International Conference on Advances in Nanomaterials and Nanotechnology (ICANN-2016), Organized by Centre for Nanoscience and Nanotechnology, Jamia millia Islamia, New Delhi, India during 4-5 November, 2016. **(poster)**

7. International Conference on Soft Materials (ICSM-2016) organized by Department of Physics Malaviya National Institute of Technology Jaipur during 12-16 Dec., 2016. **(oral)**

8. International Conference on Frontiers at the Chemistry - Allied Sciences Interface (FCASI-2017) at University of Rajasthan, Jaipur, organized by Center for Advanced Studies, Department of Chemistry, University of Rajasthan, Jaipur, during 22-23 July, 2017. **(oral)**

9. International National Conference on Nano-and Functional Materials (NFM-2017) at BITS Pilani, organized by Department of Chemistry, Birla Institute of Technology and Sciences, BITS Pilani, Rajasthan during 16-18 November, 2017. **(Best oral award)**

10. International Conference on Nano-materials for Energy Conversion and Storage Applications (NECSA-2018) at Pandit Deendayal Petroleum University, Gandhinagar, Gujarat, organized by The Solar Research & Development Center (SRDC), PDPU Gujarat during 29- 31 January 2018. **(oral)**

Name : Pragati Fageria

Born at Sikar, Rajasthan, India

Bachelor of Science in Chemistry Honors from Banasthali Vidyapeeth, Rajasthan, India in 2009

Master in Science from University of Rajasthan, Jaipur (India) in 2011 with the specialization in Inorganic and Physical Chemistry

Permanent Address

Pragati Fageria
D/O Baldev Singh Fageria
Chaudhary Charan Singh Nagar
Nawalgarh Road
Dist: Sikar
State: Rajasthan
India
Pin: 332001

Email: pragati.fageria@gmail.com

Dr. SUROJIT PANDE
Associate Professor, Department of Chemistry,
BITS Pilani, Pilani campus, Rajasthan, 333031

Dr. Pande did his M.Sc. in Inorganic Chemistry, Kayani University, Kalyani, West Bengal and Ph. D. from Indian Institute of Technology, Kharagpur. During Ph. D., he worked on metal and metal oxide nanoparticles and their application in catalysis and surface enhanced Raman spectroscopy. He worked on application of metal and metal oxide nanoparticles in catalysis, analytical and environmental chemistry, and surface enhance Raman scattering (SERS) studies using DOPAMINE, 1,10 Phenanthroline, and various dyes as a SERS probe. Before joining BITS on March 2012, Dr. Pande was a postdoctoral fellow in the Richard M. Crooks research group at The University of Texas at Austin, Texas, USA with research interests in homogeneous catalysis using dendrimer-encapsulated nanoparticles. He was experienced on spectroscopic study of sixth and fourth generation of hydroxy-terminated poly(amidoamine) (PAMAM) dendrimer. Synthesis of mono- (Au, Pd, and Pt) and bimetallic (Au@Pd and Pd@Au) dendrimer-encapsulated nanoparticles of definite cluster size and atoms (magic no cluster) and their application in electrocatalyst.

Email: surojitpande@gmail.com, spande@pilani.bits-pilani.ac.in

"We must have perseverance and above all confidence in ourselves. We must believe that we are gifted for something and that this thing must be attained.

MARIE CURIE